DOE/ER/45278--T2

DE-FG02-86ER45278

DOE/ER/45278

Final Report

Nucleation, Propagation, Electronic Levels and Elimination of Misfit Dislocations in III-V Semiconductor Interfaces

by

D.G. Ast, G.P. Watson and M. Matragrano

Cornell University

Ithaca NY

14853-1501

March 1995

TABLE OF CONTENTS

LIST OF TABLES

LIST OF FIGURES

Chapter 1

Overview of Strained Layer Defects

1.1 Heterojunctions

Heterojunctions are powerful elements in semiconductor device technology. As the term *bandgap engineering* suggests, the difference between the electron energy states of adjacent layers of different semiconductors is exploited to control carrier densities and other properties, creating many new types of electronic and optoelectronic devices.

To create semiconductor crystals in intimate contact with each other, many techniques have been developed: liquid phase epitaxy, vapor phase epitaxy, molecular beam epitaxy (MBE), and organo-metallic chemical vapor deposition (OMCVD) are among the more important ones. In each technique, a single crystal substrate is used as a template to grow (epitaxial) layers of ordered arrays of different compounds.

Two important requirements for a good substrate/epitaxial layer system are

that the crystal structures be compatible and the interatomic distances of both be at least approximately the same. If the lattice parameters of the two materials are not precisely equal, defects can form at the interface or in the epitaxial layer to relieve the strain caused by the necessity of the epitaxial layer to otherwise register to the substrate crystal dimensions in the interface plane [Pea91]. An important defect is the misfit dislocation, that lies at a strained layer interface. Studies of the properties of these linear defects are discussed in this thesis.

1.1.1 Strained Layers and Misfit Dislocations

Why are misfit dislocations important? The primary reason is because dislocations destroy the periodicity of the semiconductor crystal lattice, which creates electron energy states that lie in the normally forbidden gap between the valence and conduction bands [Rea54]. These localized electron states are responsible for poor device performance and reliability.

Dislocation electron states can act as recombination centers that annihilate electron hole pairs. Optoelectronic devices such as light emitting diodes (LED's) and lasers are known to degrade by the formation of dark line defects (DLD's), dislocations in the device active area that non-radiatively recombine injected electron-hole pairs [Zip85,UKYK81,BYC+89]. It is clear that these defects also adversely effect other devices such as heterojunction bipolar transistors (HBT's) and field effect transistors [AAS+88,MIIN83]. Charged dislocation trap states create localized, charged cylinders that reduce carrier mobility as well [Ger79].

Besides the electronic nature of the misfit dislocation, the strain relief it cre-

ates can also be unwanted. As described below, it is sometimes advantageous to intentionally strain a semiconductor crystal to modify its bulk electronic properties. Misfit dislocations always lower (as much as possible) the strain in epitaxial layers to their natural state and thus reduce the changes in electronic properties affected by the strain.

1.1.2 Carrier Injection

Two semiconductor systems that possess technologically important electronic properties and are virtually lattice parameter matched to readily available substrates are AlGaAs on GaAs and InGaAsP on InP. The AlGaAs alloys are essentially lattice matched to GaAs throughout the composition range and have a well developed epitaxial growth technology [Cho83]. The bandgap, conduction and valence band offsets are controlled by the Al content. The quaternary alloy InGaAsP is not necessarily lattice matched to InP, but since the In/Ga and the As/P ratios can be independently varied, it is possible to choose a composition that does have the same lattice parameter as InP with a relatively wide range of bandgaps [Sze81, ND85]. One or both of these systems have been successfully used to produce commercially available LED's, lasers, and HBT's. However, because of limitations in these materials, a large effort has gone into developing heterojunctions made from semiconductors that are not precisely lattice matched [STFE91].

Two such non-lattice matched systems are InGaAs/GaAs and SiGe/Si. InGaAs, which can differ in natural lattice parameter by several percent compared to GaAs, has been used to produce bipolar transistors superior to homojunction devices, in

spite of the fact that the strained layer induces electrically active defects [AAS+88, REC+87]. Devices have also been produced in SiGe alloy epitaxial layers, again with improved properties [KHG89,IMW91].

1.1.3 Charge Accumulation

The conduction and valence band offsets of InGaAs/GaAs may also be exploited to produce 2-dimensional electron gases used in modulation doped field-effect transistors (MODFET's). The larger conduction band offset of InGaAs/GaAs compared to AlGaAs/GaAs makes it an attractive material system [STFE91,LTLA89]. But the fact that misfit dislocations form at the strained layer interfaces interferes with the improvements in performance.

1.1.4 Strain and Electron Band Effects

The fact that one or more epitaxial layers are elastically strained is not necessarily a hindrance; in some material systems, strain may create new properties that can be exploited in new devices. Strain in the epitaxial layers changes the crystal symmetry, creating tetragonal or orthorhombic crystal structures from the diamond cubic and zincblende (cubic) lattices. The lower symmetry leads to loss of degeneracy of electron bands and shifts the conduction band minimums and/or the valence band maximums. One instance is the Si/SiGe system in which both components are strained (in opposite directions). Abstreiter et al. showed that this material system possesses conduction band offsets not present in strained SiGe on unstrained Si [ABW85]. Another example is the partial elimination of the valence band degeneracy and the ensuing increase of hole mobility in strained InGaAs on

GaAs [REC+87]. In both cases, it is believed that the strain in these layers (if defect densities are limited) may lead to improved device characteristics.

1.2 Strain Relief and Misfit Dislocations

It has long been recognized that lattice mismatched epitaxial layers can be grown defect free up to a *critical thickness* that depends on the degree of mismatch. Beyond the critical thickness, misfit dislocations can form at the interface to relieve some of the strain in the epitaxial layer. The conditions for the onset of misfit dislocation formation is an important element of this thesis and is introduced in this section.

1.2.1 Matthew's Theory

Matthews et al. proposed and further developed a simple quantitative model to estimate the critical thickness of strained epitaxial layers [MML70,MBM76,Mat75b, MB74,Mat75a]. The concept is based on elementary dislocation theory; a dislocation that threads through an epitaxial layer from the substrate will glide in the presence of a driving force. The glide will lay out a misfit dislocation at the interface. The net driving force is a competition between the reduction in free energy as the epitaxial layer is relaxed by the misfit dislocation and the gain in energy caused by the extension of the dislocation. Only when the epitaxial layer is of sufficient thickness (the critical thickness) does the net free energy drop as a threading dislocation glides (a thermodynamically favored process). Matthews' theory is considered in detail in Chapter 2.

1.2.2 Misfit Dislocation Sources

Matthews' theory is based on the assumption that misfit dislocations form by glide of dislocation segments that extend through an epitaxial layer. How these segments themselves form is an important issue in the growth of strained layers.

As will be shown in Chapter 2, Matthews' theory correctly predicts the layer thickness at which misfit dislocations begin to form. However, the predicted maximum defect density for a given mismatch and thickness is much higher that found empirically. Experimentally, the misfit dislocation density varies widely, depending on mismatch, growth temperature, substrate processing, etc. Matthews et al. proposed that misfit dislocations nucleated from threading dislocations in the substrate [MML70]. These dislocations thread through the substrate and are copied into the epitaxial layer during growth. Matthews envisioned the copied threads to be the glide segments that form a misfit dislocation once the critical thickness is exceeded.

As expected from Matthews' theory, a rough correlation has been found between the substrate defect density and the misfit dislocation density in strained epitaxial layers. Fitzgerald et al. measured the misfit dislocation density of InGaAs grown on patterned GaAs substrates and found that a substrate with the highest etch pit density (EPD) did indeed have more misfit dislocations at the heterojunction interface than similar material with a lower EPD [FWP+89]. However, one substrate with a nominal EPD of less than 500 cm^{-2} (extremely low for GaAs) appeared to possess many more misfit dislocations than would be expected. Klem et al. observed that the misfit dislocation density in InGaAs on unpatterned GaAs was higher, and

the electronic properties were poorer, on higher EPD substrates as well [KFG+90].

Threading dislocations are not the only active source, and in some cases they are not even the predominant nucleation source. For instance, large numbers of misfit dislocations can be found at the interface of Si_xGe_{1-x} strained layers on Si substrates, even though Si wafers are virtually dislocation-free. Other substrate surface defects such as scratches or contaminant particles can concentrate stress,leading to the formation of small dislocation half-loops. If the Burgers vector of the loop is correct, the loop may expand by the glide of one of its segments and form a misfit dislocation. Chapters 3 and 4 are devoted in part to aspects of this form of dislocation nucleation.

Other nucleation mechanisms have been proposed, most notably the dislocation multiplication mechanism of Hagan and Strunk and another form by Tuppen et al. [HS78,TGHR90]. The basic idea is that two perpendicular misfit dislocations react and form two additional thread segments that subsequently glide and form new misfit dislocations adjacent to the old ones.

To quantitatively account for the fraction of layer strain that is relaxed by misfit dislocations, Dodson and Tsao proposed a semi-empirical model based on dislocation multiplication and misfit dislocation velocities that leads to a time dependent strain relaxation [DT87]. It has been applied to the experimental data of the SiGe/Si and the InGaAs/GaAs material systems with mixed success [DT87,Hou91,WC90, Wie89]. Houghton extended this theory, including the spontaneous nucleation of misfit dislocations by an unknown mechanism [Hou91,Hou90].

Matthews and Blakeslee also observed the *re-use* of misfit dislocation glide seg-

ments in strained multi-layers [MB74]. As the multi-layer is grown, a glide segment would move in one direction, leaving a misfit dislocation at the first interface and then glide back, leaving another one at the new interface. The final structure consisted of loops of the same dislocations alternately relieving compressive and tensile strain.

It should be noted that the above nucleation mechanisms are important only for strained layers with less than about 1 to 2% lattice parameter mismatch. Above this value, it is possible to spontaneously form a dislocation half-loop at the epitaxial layer surface that glides to become a misfit dislocation. Studies by others have shown that this homogeneous nucleation mechanism is probable only at high strains [Mat75b,FWP+89]. In addition, in systems with greater than about 1.5% mismatch, 3-D island growth commences, allowing surface steps to form sessile edge dislocations [FAI+90]. All of the material described in this thesis possessed strains well below the homogeneous nucleation and 3-D growth limits, so these regimes will not be considered in subsequent chapters.

Restricting strained layers to below the critical thickness severely limits the design of electronic devices. Since in most device structures the layer thicknesses are set by electrical considerations, this requirement translates into a limit on alloy composition and hence a limit on the available band offsets. In the next section, a technique developed by Fitzgerald is described that allows one to create epitaxial layers that are several times their critical thickness with few or no misfit dislocations.

1.3 Misfit Dislocation Density Control

1.3.1 Patterning and Defect Control

Matthews realized that if only *fixed* nucleation sources are active in material with less than 1% mismatch, then the misfit dislocation density can be reduced simply be using smaller substrates [MML70]. The nucleation sites due to threading dislocations or other imperfections are constant per unit area of substrate, and therefore less sites will be present if the size of the substrate is reduced. Fitzgerald exploited this idea in an ingenious way; by patterning and etching deep trenches between mesas on a substrate before epitaxial growth of a strained layer, a series of small substrates are made, each isolated from each other as far as misfit dislocation glide is concerned [FWP$^+$89,Fit89,Fit88,FXM$^+$90]. The small area of each mesa ensures that only a few misfit dislocation nucleation sites are available and that only a small density of misfit dislocations may form. Fitzgerald et al. demonstrated the effectiveness of patterning on MBE InGaAs strained layers grown on GaAs [FWP$^+$89]. This concept has been later demonstrated on other material systems and using different isolation techniques by Watson et al., Fitzgerald et al., and Noble et al. [WAAH90b, FXM$^+$90,NHK$^+$90]

The basic principle of patterning is illustrated in Figure 1.1. A rectangular substrate with a strained epitaxial layer is shown on the left in plan view. The black circles represent nucleation sources and the lines are misfit dislocations emanating from these sources. For simplicity, the misfit dislocations are assumed to glide only in the up-down direction. The misfit dislocation density is defined as the number of

dislocations that cross the dotted line per unit length of that line, resulting in units of length^{-1}. On the right is the same wafer with the same density of nucleation sites as before. In this case, however, the substrate was patterned and etched before growth, creating two mesas separated by a deep trench. Misfit dislocations nucleating on the top portion of the substrate are blocked from reaching the lower portion by the trench. The misfit dislocation density is now about half of what it was before.

The average misfit dislocation density is expected to decrease linearly with decreasing isolation dimension. This was demonstrated by Fitzgerald et al. and later by Watson et al., who studied a larger number of mesas so that the statistical fluctuations were minimized [FWP$^+$89,WAAH90a]. Hence patterning can not only be used to minimize the defect density at strained layer interfaces (and create better devices), but it can be used to adjust the average misfit dislocation density in a controlled way. This feature is exploited in Chapter 8; the average dislocation density is changed simply by varying the size of the mesa on a substrate before growth. The electronic properties of dislocations can then be separated from those due to other defects because only the dislocation induced properties should change with mesa dimension.

Misfit dislocation reduction by patterning as developed by Fitzgerald has been demonstrated for low strain epitaxial layers, but there are conditions where this technique can reduce the misfit dislocation density in homogeneous nucleation epitaxial layers as well. If the average time interval between nucleation of dislocation half loops in a patterned mesa is very long compared to the time it takes for a

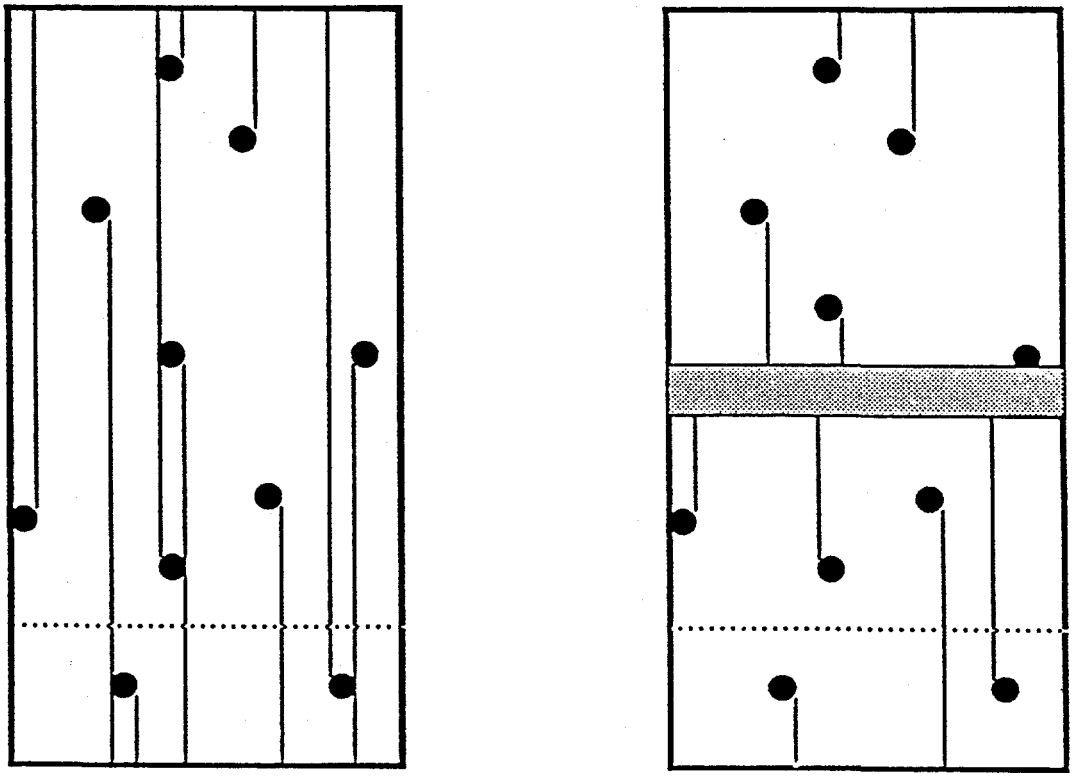

Figure 1.1: A schematic diagram of misfit dislocations forming in unpatterned (left) and patterned (right) substrates.

dislocation to glide to a mesa edge, then a quick epitaxial growth on a patterned substrate should still significantly reduce the interface defect density compared to unpatterned material. It is only when the nucleation rate is high and the time at high (growth) temperatures is long that patterning has little effect on interface defect density.

1.3.2 Device Performance and Patterning

Recent work has shown improved performance of devices constructed on patterned strained layer material. Kamins et al. have described work done at Stanford University and Hewlett Packard regarding the fabrication of SiGe HBT's with properties that improved as the pattern dimension is reduced (and the misfit dislocation density as well) [KNJ+91]. Li et al. recently looked at InGaAs/GaAs photodetectors on patterned substrates and found that the performance of the devices improved significantly as the mesa dimensions were reduced [LBT91]. Hence the adverse effects of misfit dislocations can be reduced without limiting the composition and thickness of the strained epitaxial layers.

1.4 Overview of Report

There are three main directions taken in the research described in this report. After the basic properties of dislocations in compound semiconductors is described in Chapter 2, aspects of misfit dislocations nucleation are described in Chapters 3 (fixed nucleation sites), 4 (ion damaged substrates) and 6 (thermal stability of patterned material). Second, the propagation of misfit dislocations are studied in

OMCVD InGaAs grown on patterned GaAs in Chapter 5, and in ZnSe in Chapter 7. Finally, new information pertaining to the electronic properties misfit dislocations is discussed in Chapter 8 (and in parts of Chapter 2 as well).

The Chapters are organized roughly in chronological order of the research carried out by the author. However, they also arrange naturally along the lines of the three categories described above. The one exception is Chapter 6, which appears after the description of OMCVD grown InGaAs on patterned GaAs substrates (Chapter 5) because important information dealing with the characteristics of material used in 6 is described in the previous chapter.

Chapter 2

Structural and Electronic Characteristics of Misfit Dislocations

2.1 Introduction

In this chapter we define and discuss some basic properties of misfit dislocations. The theory of Matthews and others is first presented in detail, based on minimizing energies instead of the usual force balance approach. While the minimization of strain energy approach is not new, it facilitates modifications made in later chapters. It is also, in the opinion of the author, much simpler to understand conceptually. Limitations of this model, other theoretical approaches, and experimental verification are discussed as well.

The structures of misfit dislocations are described, concentrating exclusively on those defects found in the zincblende crystal structure. The fact that GaAs is a non-centrosymmetric crystal leads to interesting effects concerning the activity of the

misfit dislocations. The experimental method used by the author to assign the dislocation character and specimen crystallographic orientation is reported at this point. The final section deals with the carrier recombination properties misfit dislocations, describing some simple calculations dealing with the optimum specimen characteristics for dislocation detection using the non-radiative recombination properties of the defects. Some experimental results showing the effect of dislocation Burgers vector and dislocation reactions on carrier recombination are also presented.

2.2 Misfit Dislocation Formation

2.2.1 Basic Concepts

The formation of misfit dislocations is driven by the strain relief that they impart on the epitaxial layer. They exist only because the complete epitaxial layer/substrate system possesses a lower free energy when the dislocations are present. Experiments showed that for strained epitaxial layers below a critical thickness, no misfit dislocations form; only when that critical thickness (which is a function of the mismatch) is exceeded are misfit dislocations found. Others, such as Van der Merwe, had previously calculated the critical thickness, based on the balance between the energy of dislocation formation and the energy release caused by the (plastic) relaxation of the epitaxial layer [vdM63]. Matthew's et al., however, recognized the importance of dislocation glide in misfit dislocation formation and used a simple model to relate mismatch to critical thickness [MML70,MBM76,Mat75b,MB74,Mat75a].

Misfit dislocations in moderately mismatched materials form by the glide of a small dislocation segment that threads through the epitaxial layer from the interface

to the free surface. The misfit dislocation at the interface (connected to the segment) does not move itself; it simply extends as the segment moves in a direction perpendicular to the interface normal. The small segment is called the *threading segment* or *glide segment* throughout this thesis. Figure 2.1 is a schematic representing a misfit dislocation and its threading segment.

Since the misfit dislocations must lie in the {111} glide planes and also in the strained layer interface plane (the (001) plane), their line directions are determined by the intersection of these two plane types, which are the [110] and [1$\bar{1}$0] directions. Consequently, in all of the images seen in this thesis, misfit dislocations are oriented in two perpendicular directions.

Figure 2.2 is a diagram showing a 60° misfit dislocation and its Burgers vector separated into 3 orthogonal components: the screw component, the in-plane edge component, and the out of plane edge component. Only the in-plane edge component actually relieves epitaxial layer strain. The others cannot change the in-plane interatomic distances between atoms in the epitaxial layer (to first order, according to infinitesimal elastic strain theory). The in-plane edge component, b_e, is related to the Burgers vector magnitude, b, by

$$b_e = b \sin\theta \cos\phi \tag{2.1}$$

where $\theta = 60°$ is the angle between the Burgers vector and the line direction and $\phi = 54.736°$ is the angle between the {111} and (001) planes.

It is important to note that a misfit dislocation may relieve compressive or tensile strain in the epitaxial layer in only the direction *perpendicular* to the dislocation line

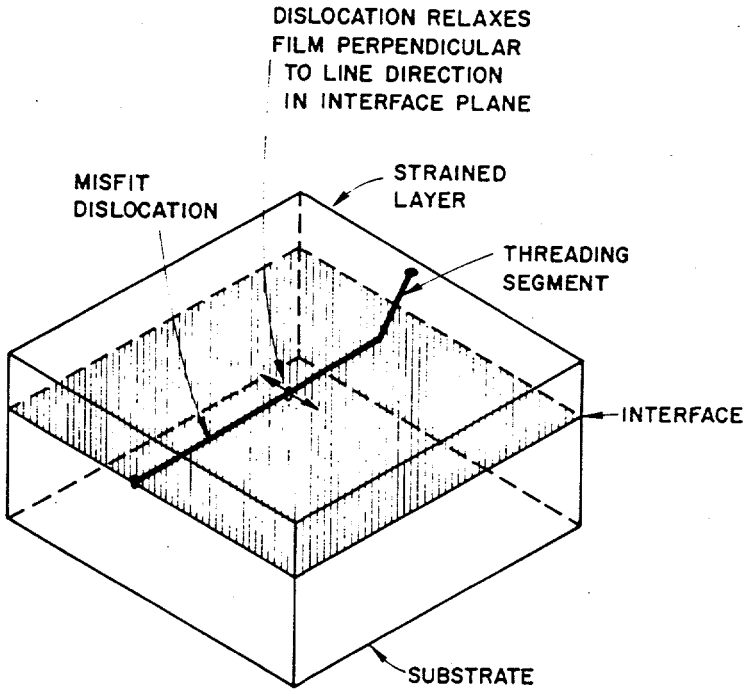

Figure 2.1: A schematic diagram of a misfit dislocation, its glide segment, and the direction of strain relief experienced by the epitaxial layer.

direction. The interatomic distances of epitaxial layer atoms along the dislocation line direction cannot change, no matter what the Burgers vector is. Figure 2.3 illustrates this point. The above argument is valid only for a cubic lattice type substrate with an epitaxial layer with the same structure. Matthews discusses strain relief due to screw dislocations for one special case [MBM76].

As Figure 2.2 suggests, a 60° dislocation is not the most efficient dislocation type, to relieve strain. A pure edge dislocation with the same Burgers vector magnitude would possess twice the strain relief. However, an edge dislocation is not glissile in the zincblende structure. Even so, edge dislocations are found at (or near) III-V strained layer interfaces; Fitzgerald et al. described a mechanism where two 60° dislocations (formed by glide) react, creating an edge dislocation just below the interface [FWP+89]. The nature of the 60° dislocations is discussed in more detail later in this chapter.

2.2.2 Matthews' Glide Force Theory

Matthews and others described the formation of misfit dislocations as a competition between two competing forces, one caused by the relaxation of the strained layer by the dislocations and another by the strain field around the dislocations. Direct consideration of the various energies involved is more transparent and facilitates modification of the theory. Matthews considered energies as well in some publications, but only in a simplified manner. The derivation that follows yields precisely the same critical thickness equation as a force balance approach.

The derivation below is based on isotropic elasticity. Matthews considered the

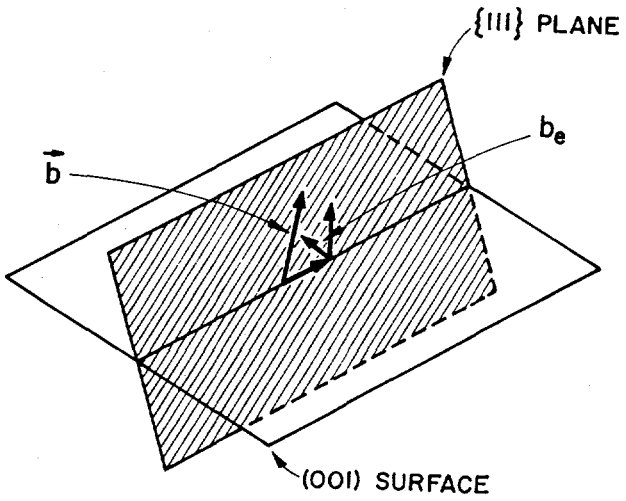

Figure 2.2: A diagram of the components of a 60° misfit dislocation Burgers vector.

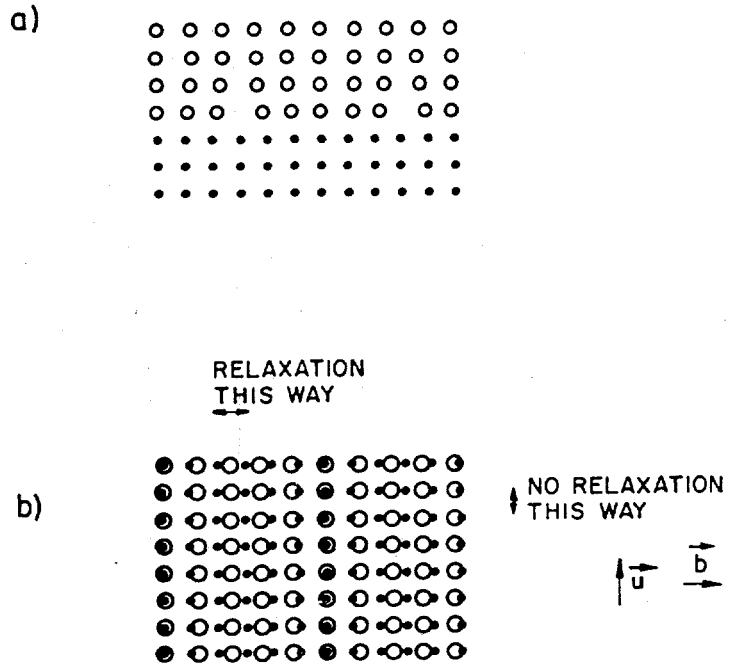

Figure 2.3: A schematic describing the directions of compressive or tensile strain relief experienced by a strained epitaxial layer. The open circles denote atoms in a simple cubic structure epitaxial layer; the solid circles represent substrate atoms. In *a*, two edge misfit dislocations are seen in a cross-sectional view. In *b*, the same two dislocations are seen in plan view. The interatomic spacing is effected only in the direction perpendicular to the dislocation line direction

effects of non-isotropic elastic constants and the different elastic properties of the epitaxial layer and the substrate [Mat75a]. Fitzgerald et al., using anisotropic theory, compared the predicted critical thickness of InGaAs alloys grown on GaAs with the isotropic elasticity calculations [FWP+89]. The differences are not large, considering the probable magnitude of errors due to other approximations used in the development of the model.

The energy necessary to compress a slab of the epitaxial layer of dimensions $L_1 \times L_2$ and with thickness h into an area of $L_1(1 + \epsilon_{11(f)}) \times L_2(1 + \epsilon_{22(f)})$ is calculated in two steps, as illustrated in Figure 2.4. The terms $\epsilon_{11(f)}$ and $\epsilon_{22(f)}$ are the compressive strains in the directions 1 and 2, respectively. In general, work done is

$$W = L_1 L_2 h \sum_i \sum_j \int_{\epsilon_{ij(b)}}^{\epsilon_{ij(f)}} \sigma_{ij} \cdot d\epsilon_{ij} \tag{2.2}$$

where the σ_{ij}'s are the stress tensor components and the subscripts b and f refer to the beginning and final strains, respectively [Nye85]. For an isotropic solid, Nye relates the stress tensor components to the strain components as follows:

$$\epsilon_{11} = 1/Y\,(\sigma_{11} - \nu(\sigma_{22} + \sigma_{33})) \tag{2.3}$$

$$\epsilon_{22} = 1/Y\,(\sigma_{22} - \nu\,(\sigma_{22} + \sigma_{11})) \tag{2.4}$$

$$\epsilon_{33} = 1/Y\,(\sigma_{33} - \nu\,(\sigma_{11} + \sigma_{22})) \tag{2.5}$$

where Y is the Young's modulus and ν is the Poisson's ratio [Nye85]. All shear tensor components of the stress and strain are zero. Since direction 3 of the epitaxial layer is not constrained, $\sigma_{33} = 0$ and the Equations 2.4, 2.5, and 2.5 reduce to

$$\sigma_{11} = \frac{Y}{1 - \nu^2}(\epsilon_{11} + \nu\epsilon_{22}) \tag{2.6}$$

$$\sigma_{22} = \frac{Y}{1-\nu^2}(\epsilon_{22} + \nu\epsilon_{11}). \tag{2.7}$$

The system used in the following description is InGaAs grown on GaAs where the natural epitaxial layer lattice parameter is larger than the substrate. However, the energies derived are valid for any mismatch relationship. In the first step, the unstrained material is squeezed in direction 1 until the length is $L_1(1 + \epsilon_{11(f)})$ is reached, with the direction 2 length, L_2, held constant. The work done to create this configuration, W_1, is

$$\begin{aligned} W_1 &= L_1 L_2 h \int_0^{\epsilon_{11(f)}} \sigma_{11} d\epsilon_{11} \\ &= L_1 L_2 h \frac{1}{2} \frac{Y}{1-\nu^2} \cdot \epsilon_{11(f)}^2. \end{aligned} \tag{2.8}$$

Next, the epitaxial layer is strained in direction 2, holding the direction 1 dimension constant. The work done is

$$\begin{aligned} W_2 &= L_1 L_2 h \int_0^{\epsilon_{22(f)}} \sigma_{22} d\epsilon_{22} \\ &= L_1 L_2 h \frac{Y}{1-\nu^2} \left(\frac{1}{2}\epsilon_{22(f)}^2 + \nu\epsilon_{11(f)}\epsilon_{22(f)} \right). \end{aligned} \tag{2.9}$$

The total lattice mismatch energy, E_{mis}, is the sum of the work terms in Equations 2.8 and 2.9:

$$E_{mis} = \frac{\mu}{1-\nu} \left(\epsilon_{11(f)}^2 + \epsilon_{22(f)}^2 + 2\nu\epsilon_{11(f)}\epsilon_{22(f)} \right) L_1 L_2 h, \tag{2.10}$$

where $\mu = Y/(2(1+\nu))$ is the shear modulus for an isotropic solid [Nye85].

The strains $\epsilon_{11(f)}$ and $\epsilon_{22(f)}$ are based on the average interatomic spacing in the epitaxial layer, as Figure 2.5 illustrates. In distance L there should be, on average, $\rho L b_e / a_{GaAs}$ missing lattice planes in the epitaxial layer, where b_e is defined

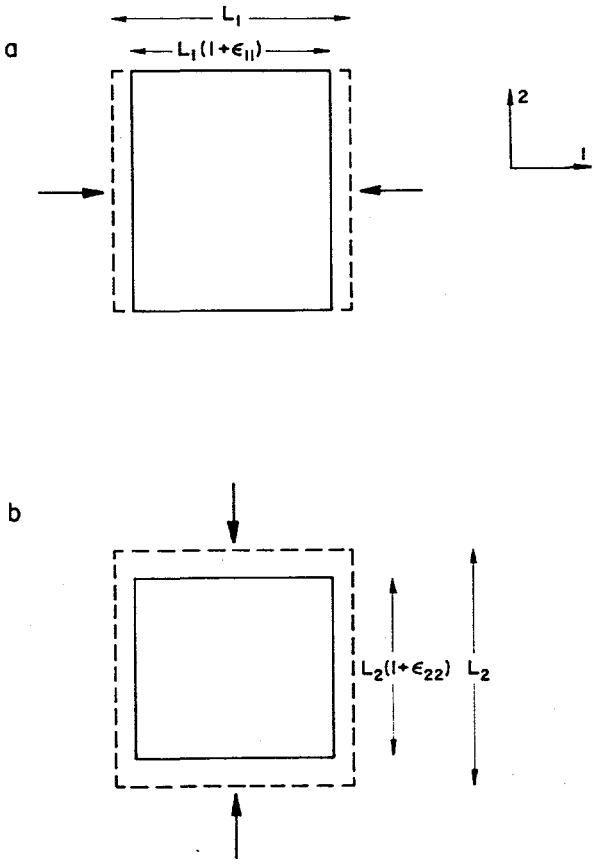

Figure 2.4: The definition of directions and terms used to calculate the elastic strain energy in an epitaxial layer. In *a*, the unstrained layer is compressed in direction 1 while holding the direction 2 dimension constant. In *b*, the action in the two directions is reversed.

in Equation 2.1, ρ is the interface dislocation density in units of length^{-1}, and a_{GaAs} is the substrate lattice parameter. The number of epitaxial layer planes in L is $L/a_{GaAs} - \rho L b_e/a_{GaAs}$. The natural, or unstrained distance between these planes, L_{nat}, should be

$$L_{nat} = a_{GaAs}(1 + qx)(L/a_{GaAs} - \rho L B_e/a_{GaAs}). \tag{2.11}$$

The lattice parameter mismatch between the substrate and the epitaxial layer is determined by the term qx, where q is the Vegard's law slope ($q = (a_{InAs} - a_{GaAs})/a_{GaAs}$ with a_{InAs} and a_{GaAs} as the lattice parameters of those binary materials) and x is the fraction of the InAs in an InGaAs epitaxial layer. The mismatch strains, $\epsilon = (L - L_{nat})/L_{nat}$ for each in-plane direction, are

$$\epsilon_{11(f)} = -qx + \rho_2 b_e \tag{2.12}$$

$$\epsilon_{22(f)} = -qx + \rho_1 b_e. \tag{2.13}$$

where ρ_1 and ρ_2 are the misfit dislocation densities in directions 1 and 2, respectively. The dislocation strain relief term, ρb_e, is the opposite sign of the mismatch term. Note that dislocations lying in direction 1 relieve strain in direction 2 and visa versa.

The energy stored in the epitaxial layer/substrate material due to the strain field of a dislocation has been derived and discussed in several texts [HL82,Nab67,KG70]. For edge and screw dislocations, the strain energies are

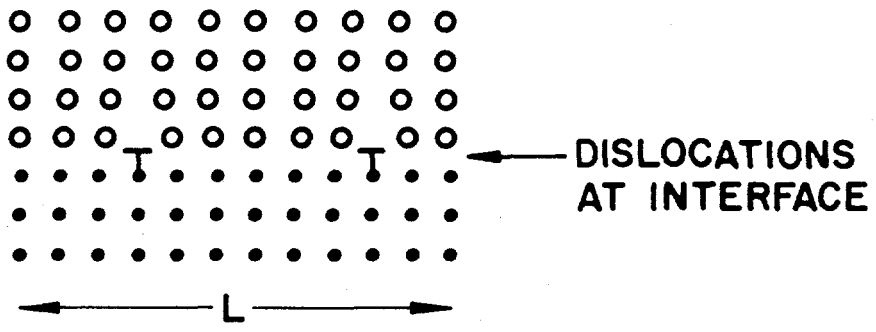

Figure 2.5: The relation between the lattice parameter mismatch, misfit dislocation density, and in-plane epitaxial layer strains. In length L there are $\rho L b_e / a_{GaAs}$ missing lattice planes in the epitaxial layer. To calculate the epitaxial layer strain, the natural length of these remaining planes must be estimated.

$$E_{edge} = \frac{\mu b^2}{4\pi(1-\nu)} \ln\left(\frac{R}{r}\right) L \tag{2.14}$$

$$E_{screw} = \frac{\mu b^2}{4\pi} \ln\left(\frac{R}{r}\right) L \tag{2.15}$$

where L is the dislocation length, and R is the upper cutoff radius of a cylindrical region that determines the limit of the dislocation strain field influence. The term r is the inner cutoff radius, which is chosen so that the energies determined by Equations 2.14 and 2.15 match the actual dislocation strain energy, including the core, where linear elastic theory no longer holds. The inner cutoff radius is defined in terms of the dislocation Burgers vector as $r = b/\alpha$, where α is an empirically determined constant (assumed to be independent of b and dislocation type), taken to be 4.0 for covalently bonded materials [HL82].

For an array of misfit dislocations lying in two perpendicular directions in an $L_1 \times L_2$ slab of material, the overall number of dislocations are $L_1\rho_2 + L_2\rho_1$. Using Equations 2.14 and 2.15, the energy for an array of mixed misfit dislocations is simply:

$$E_{dis} = \frac{\mu b^2}{4\pi}\left(\frac{1-\nu\cos^2\theta}{1-\nu}\right) \ln\left(\frac{R\alpha}{b}\right) L_1 L_2 (\rho_1 + \rho_2), \tag{2.16}$$

where θ is the angle between the Burgers vector and the line direction (60°).

The total strain energy of the system is the sum of Equations 2.10 and 2.16 with one other condition: the upper cutoff radius, R, is assumed to be the epitaxial layer thickness, h [MML70]. Fitzgerald et al. pointed out that at high misfit dislocation densities, half of the average dislocation spacing may be a more appropriate cutoff radius than the thickness (whichever is smaller) [FAA+88]. The total system energy

is then:

$$\begin{aligned} E_{tot} &= \frac{\mu b^2}{4\pi}\left(\frac{1-\nu\cos^2\theta}{1-\nu}\right)\ln\left(\frac{h\alpha}{b}\right)L_1L_2\left(\rho_1+\rho_2\right) \\ &+ \frac{\mu}{1-\nu}L_1L_2h\left(\left(-qx+\rho_2b_e\right)^2\right. \\ &+ \left.\left(-qx+\rho_1b_e\right)^2+\left(-qx+\rho_2b_e\right)\left(-qx+\rho_1b_e\right)\right). \end{aligned} \tag{2.17}$$

This basic equation is an important starting point in derivations described in Chapters 4 and 5.

The critical thickness, the value of h where misfit dislocations are thermodynamically favored to form, can be found by calculating the point where the system free energy decreases (or is stationary) as dislocations are introduced. It is assumed that the entropy and volumetric terms in the free energy are negligable; the free energy is then equal to the internal energy, E_{tot}. A plot of E_{tot} versus misfit dislocation density in Figure 2.6 for various thicknesses illustrates the critical thickness idea. In this example, an epitaxial layer of $In_{0.05}Ga_{0.95}As$ on GaAs is considered. The energy is plotted in dimensionless form of energy per epitaxial layer volume divided by the shear modulus. The dislocation densities ρ_1 and ρ_2 are both assumed to be equal to the x-axis parameter ρ. Below a layer thickness of 35 nm, the system energy increases with increasing dislocation density - preventing their formation. But at about 35 nm and higher, the system energy decreases with increasing density. The critical thickness, in this case 35 nm, is determined by solving for h at the condition that E_{tot} is stationary at $\rho = 0$, or

$$\left.\frac{\partial E_{tot}}{\partial \rho}\right|_{\rho=0} = 0. \tag{2.18}$$

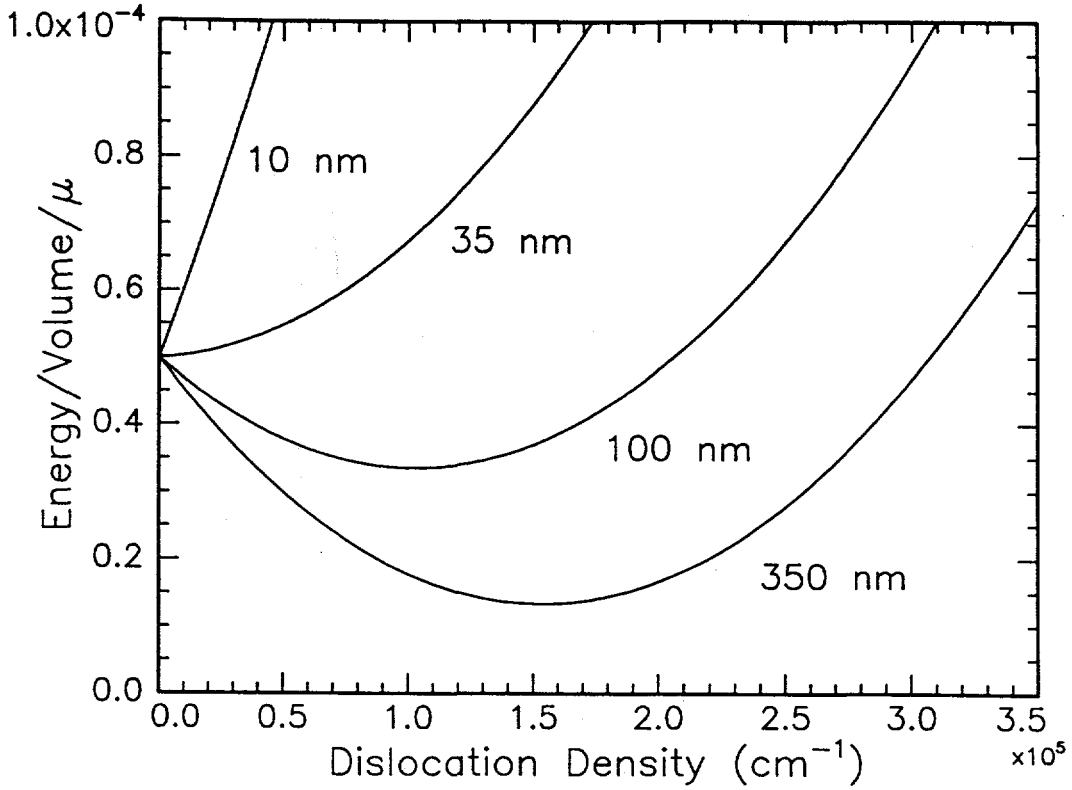

Figure 2.6: A plot of the total system energy per unit volume of epitaxial layer (dimensionless) vs. the misfit dislocation density for four epitaxial layer thicknesses.

Solving for h in Equation 2.18 yields the transcendental critical thickness equation of Matthews et al. [MML70]:

$$h_c = \frac{b}{8\pi q x \sin\theta\cos\phi}\frac{1-\nu\cos^2\theta}{1+\nu}\ln\left(\frac{h_c\alpha}{b}\right). \tag{2.19}$$

A simple program is listed in Appendix C to solve for h_c, using a Newton-Raphson iterative technique.

2.2.3 Limitations of the Theory

One basic problem with Matthews' theory is that the two strain field energies are treated independently. The strains of the components are in effect squared to form two energies. But the strains are not independent or orthogonal; the strain energy should be calculated from the sum of the two strain fields instead. The difference, mathematically, is that Matthews' theory sums the squares of the two strains, while the true energy is the square of the strain field sums.

Other researchers, using the force balance approach, begin with the Peach-Koehler equation to derive the critical thickness relationship. While an equation identical to Equation 2.19 is reached, the force balance method masks the strain field problem described above. In addition, there is a conceptual problem in this approach; a force is assumed to be applied to the threading segment which can induce it to move. However, from a more fundamental standpoint, the driving force generated by the lattice mismatch does not *push* the threading segment, it extends the misfit dislocation (although the end result is the same).

Another disputable assumption is that the epitaxial layer containing misfit dislocations can be described as one averaged pair of in-plane strains in Equations 2.12

and 2.13. The true epitaxial layer strain is much less uniform - especially in epitaxial layers that are less thick than the average dislocation spacing.

Van der Merwe considered the combined strain fields of equally spaced edge dislocations at a strained layer interface. Using a simple model for the interplanar spacing of the epitaxial layer compared to the substrate, he derived relations between the strain field and position. Van der Merwe and Jesser, and Hirth and Feng later expanded on and compared the critical thickness predictions of Matthews and van der Merwe [vdMJ88,HF90]. Both theories were found to agree quite well if a judicious choice is made of the core parameter, α [HF90].

For completeness it should be noted that some experimental observations of the apparent critical thickness of SiGe strained layers showed a different relationship between critical thickness and lattice parameter mismatch than Equation 2.18. This lead People and Bean to propose a different model [PB85]. Although it has been found to fit some data very well, the physical basis of the model has been questioned in the literature; Hu has recently reviewed this model and its assumptions [Hu91].

2.2.4 Comparison with Experiment

Gourley et al. compared the various techniques used to measure the strained layer critical thickness [GFD88]. They noted that the apparent discrepancy between the results of the different analyses was in large part due to the precision of the technique. X-ray diffraction, for instance, is capable of measuring plastic strain relief only for relatively large dislocation densities. Therefore, the layer thickness that first shows signs of strain relief may be many times larger than the thickness where the

first threading segment begins to glide. Other techniques that indirectly measure strain relief, such as photoluminescence (PL) peak shift measurements, also possess this flaw. Electron beam induced current (EBIC), cathodoluminescence (CL), and imaging PL, allow researchers to image individual dislocations by exploiting the electronic properties of these defects. Unlike transmission electron microscopy, the three techniques listed above can be used to scan large areas, so that they are inherently the most sensitive critical thickness test procedures. In fact, Kohama et al. showed that EBIC images of strained SiGe grown on Si possessed some misfit dislocations in layers much thinner than People and Bean found in similar material using x-ray diffraction [KFS88]. People and Bean were in effect basing the predictive success of their model on inappropriate data, if the concept of critical thickness is defined in its strictest sense [PB85,GFD88].

Grundmann et al. using (CL), and Weng, using (PL), determined the critical layer thickness of InGaAs strained layers on GaAs substrates [GCB+89,Wen89]. Both groups found that Matthews' equation (Equation 2.19) predicts the onset of misfit dislocation formation well. Gustafsson et al. studied GaAsP/GaAs strained layers with CL and found Matthews' theory to work well also [GPG+91]. Beernink et al. studied the degradation of InGaAs/GaAs quantum well lasers. They found that devices below or near Matthews' critical thickness were much more reliable than those that exceeded the critical thickness, presumably because the thicker epitaxial layers contain misfit dislocations (with adverse electronic properties) [BYC+89].

2.3 Dislocation Types

2.3.1 Direction Convention

Different crystal direction conventions are found in the literature, causing some confusion when III-V materials are discussed. The convention used throughout this thesis is described in detail below to facilitate descriptions in later chapters.

Figure 2.7 is a schematic diagram of a GaAs wafer and indicates some important directions and planes. The substrate itself is a (001) surface with two perpendicular {110} surfaces on the edges (these are easily cleaved crystal planes as well). In addition, there are two chemically different {111} planes. This fact is the result of the non-centrosymmetric crystal basis of a III-V semiconductor. The convention used here for the basis is as follows: a III-V material such as GaAs consists of two FCC sublattices of cube edge size a, one containing only Ga atoms, starting at $(0,0,0)$ and an As sublattice starting at $(a/4, a/4, a/4)$. The planes (111), $(\bar{1}\bar{1}1)$, $(\bar{1}1\bar{1})$, and $(1\bar{1}\bar{1})$ are known as Ga planes since they can terminate with all Ga atoms at the surface, each with one tetrahedral bond pointing outward and normal to the plane. Similarly, the $(\bar{1}\bar{1}\bar{1})$, $(11\bar{1})$, $(1\bar{1}1)$, and $(\bar{1}11)$ planes are known as As planes.

2.3.2 Wet Etching and Crystal Orientation

Gatos and Lavine described in detail the chemical etching of semiconductor materials in an early review paper [GL65]. One important aspect of etching III-V compounds they discuss is the relative reactivity of Ga and As {111} planes in various etchants. Most etchants attack and remove material much more quickly perpendicular to {111} As planes than Ga ones because of the distribution of bonding electrons. Group III

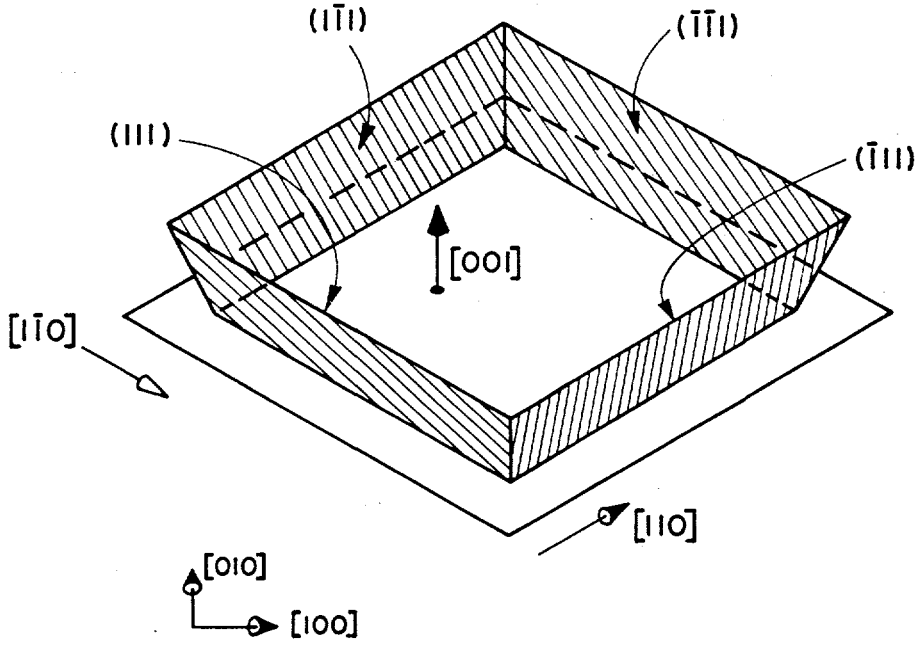

Figure 2.7: Crystallographic directions for a (001) GaAs wafer.

elements such as Ga possess 3 valence electrons, each of which would bond to an As below it when the Ga atoms are situated on an exposed {111} Ga plane. The sp^3 orbital pointing out of the plane is unoccupied, and the reactivity with liquid etchants would be expected to be low. Group V elements (As atoms) on a {111} As plane would possess an orbital with 2 electrons pointing out into an etchant. In this configuration, the As atoms can be oxidized and dissolved without difficulty.

The different chemical reactivities of the Ga and As planes has been exploited to determine the crystal orientation of the substrates. The procedure used throughpout this thesis is described below.

A substrate is patterned with a photoresist mask so that all of the surface is covered except for an array of holes 500 μm in diameter. The patterned wafer is etched for 30 s in a solution of 1:1 by volume HNO_3:H_2O_2 and rinsed in de-ionized water. This etchant has been found to have highly anisotropic etch rates in different crystal directions [Ada82]. Figure 2.8 is an optical photograph of one of the photoresist holes after etching. Note that the the two perpendicular edges do not appear the same; the exposed {111} Ga planes appear as dark regions. Figure 2.9 is a schematic diagram indicating the crystal directions.

2.3.3 Core Structure

The structure of zincblende lattice dislocations has been discussed in detail in several papers [AHLS79,OAZ74,ABB72,DCC89]. The 1979 conference at Hünfeld on Dislocations in Covalent Crystals, with discussions by many leading researchers is particularly instructive [oDiCC79]. The aim of discussion in this subsection is to

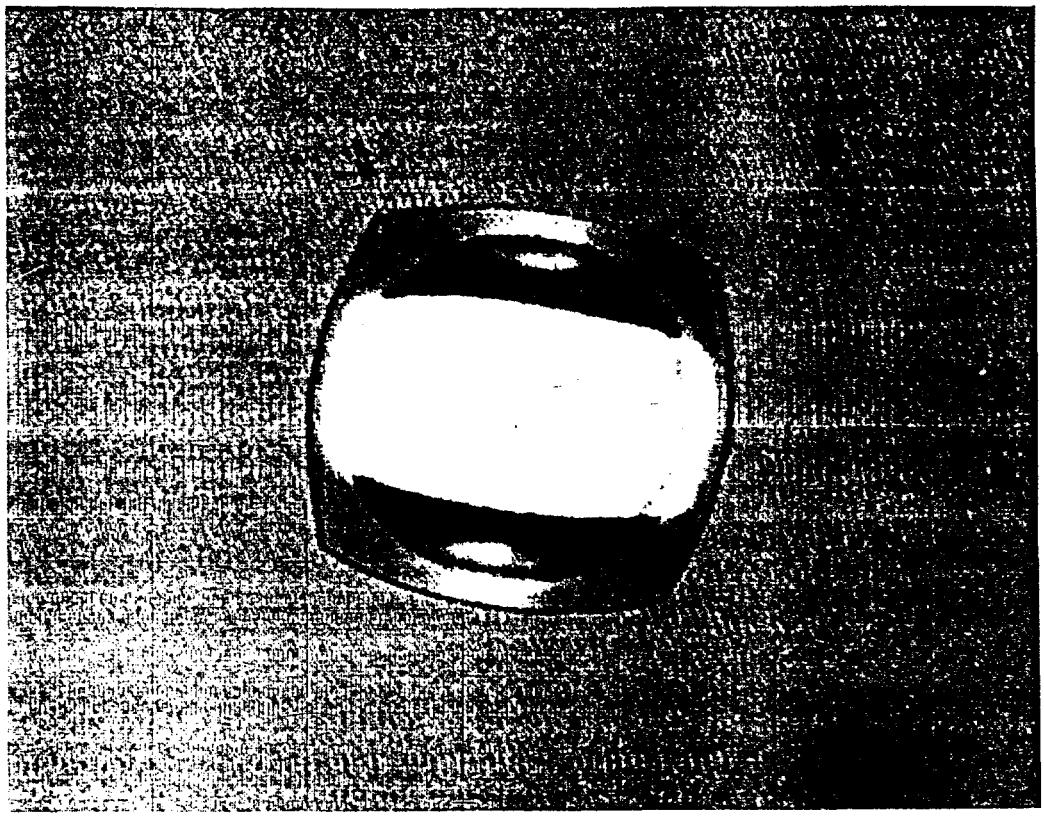

Figure 2.8: A photograph of a photoresist hole exposing the GaAs beneath it after etching in 1:1 HNO_3:H_2O_2.

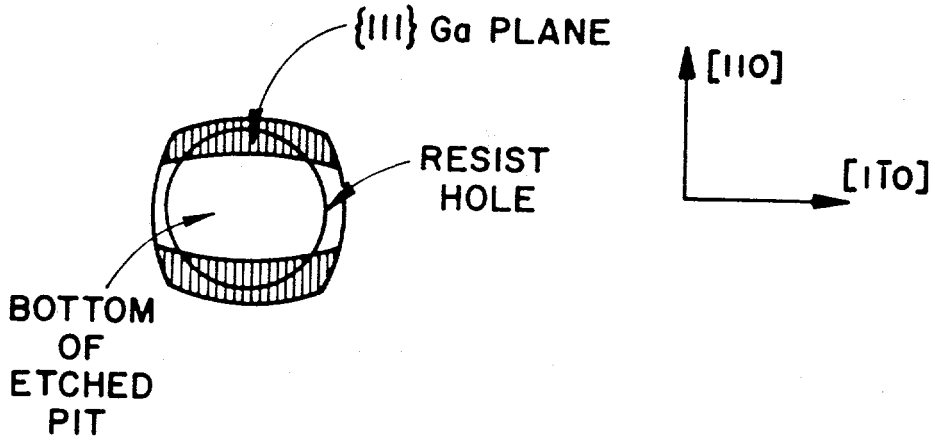

Figure 2.9: A schematic diagram showing the features in Figure 2.8 and the corresponding crystal directions.

simply describe the notation used to represent linear defects in III-V compounds.

Figure 2.10 is a photograph of a ball and stick model of GaAs containing a 60° dislocation. The view is in the $[1\bar{1}0]$ direction. This model is of an undissociated dislocation - it is well established that dislocations in GaAs and related materials dissociate into Shockley partial dislocations when static and most are likely to be so when in motion as well [Ale79]. The dislocation in Figure 2.10 is said to be in the glide set configuration, since the black core atoms possess two highly distorted tetrahedrally coordinated bonds [HL82]. If a row of blue atoms is placed in the dislocation core, the dislocation is said to be in the shuffle set. It is important to note that the strain field far from the dislocation core is unaffected by the core configuration; a glide or shuffle misfit dislocation should relieve the same amount of strain in an epitaxial layer, for instance.

Figures 2.11 and 2.12 are schematics illustrating the four possible core configurations for an undissociated 60° dislocation. Alexander et al. defined the following notation for each of the four: 2.11 *a* is Ga(s) (group III or Ga in a shuffle set configuration), 2.11 *b* is an As(g) (group V glide), 2.12 *a* is an As(s) and 2.12 *b* is a Ga(g) [AHLS79]. Figures 2.11 *a* and *b* are known as α dislocations (differing from each other by only one core atom), while Figures 2.12 *a* and *b* are β dislocations. The terms α and β originally represented a group A shuffle set dislocation and a group B shuffle set dislocation, respectively, for an AB compound such as GaAs. However, the meanings have been expanded to both glide and shuffle set dislocations; α and β now represent only the *sense* of the dislocations in terms of their long range strain fields.

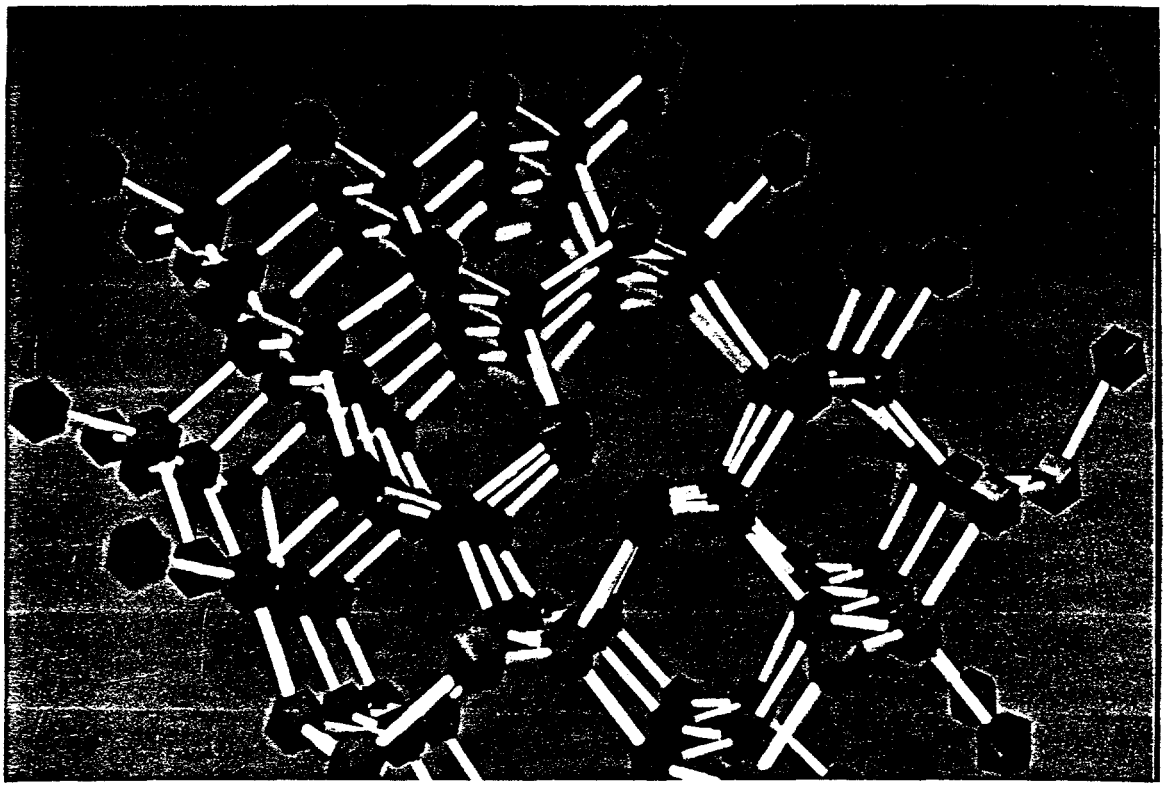

Figure 2.10: A photograph of a ball and stick model of an undissociated, group V glide set, 60° dislocation in a GaAs. The black atoms represent As and the blue represent Ga. The (111) plane normal points to the upper right.

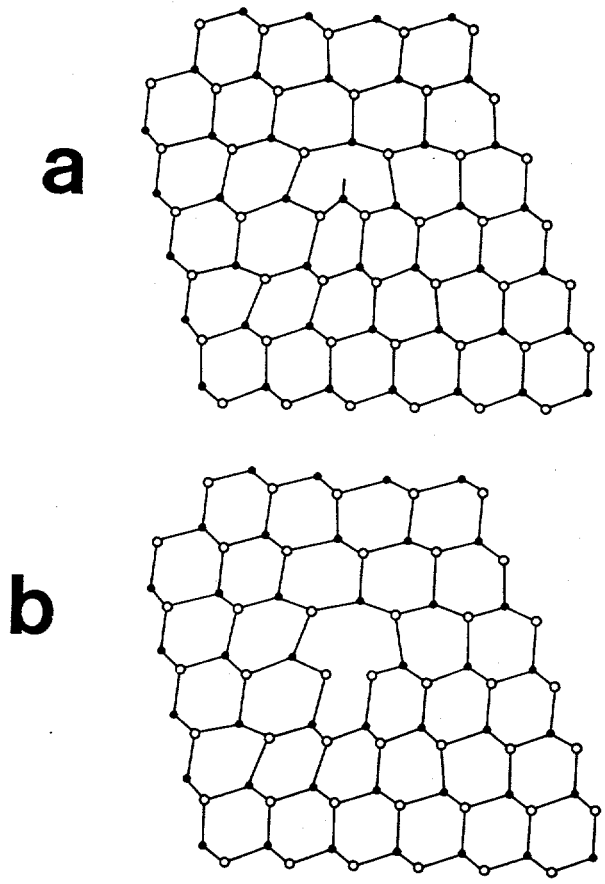

Figure 2.11: Sketches of the two possible core configurations of 60° α dislocations in a III-V material. The open and solid circles represent As and Ga atoms, respectively. Sketch *a* is a shuffle set and *b* is a glide set configuration.

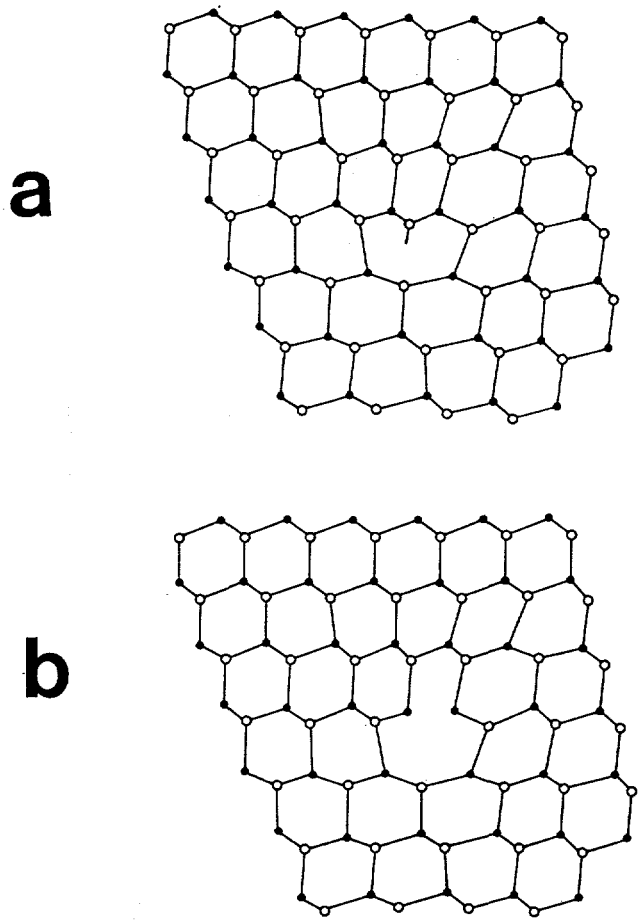

Figure 2.12: Sketches of the two possible core configurations of 60° β dislocations in a III-V material. The open and solid circles represent As and Ga atoms, respectively. Sketch a is a shuffle set and b is a glide set configuration.

Dislocations of the 60° type are glissile; they can move along (111) planes that contain both the line direction, $\vec{u}$, and the Burgers vector, $\vec{b}$ (the notation 60° describes the angle between $\vec{u}$ and $\vec{b}$) [HL82]. A misfit dislocation formed by glide must also have these properties; Figure 2.13 is a ball and stick model of a misfit dislocation lying in a {111} glide plane and at the (001) interface. The arrow corresponds to the position of a missing half-plane in the epitaxial layer. If the epitaxial layer has a larger natural lattice parameter than the substrate (such as InGaAs on GaAs), then the dislocation relieves strain in the layer. Notice that since the half-plane is not perpendicular to the interface, only a portion of the dislocation Burgers vector actually relieves strain (compare the model with Figure 2.2).

2.3.4 Burgers Vectors

Using the line direction and crystal conventions described above, the character of misfit dislocations and their glide segments have been calculated. The signs of the dislocation Burgers vectors are assigned according to the FS/RH Burgers circuit convention described by Hirth and Lothe [HL82]. Tables 2.1 and 2.2 list the possible dislocation Burgers vectors, their core type, glide segment types and glide planes for the defects that relieve strain in the InGaAs on GaAs system. The segment orientation (*forwards* or *backwards*) is described in Figure 2.14 and is used in the discussion in Chapter 3. Note that *forward* oriented segments always have either the same character as the misfit dislocations or are screw dislocations. Only a *backwards* oriented segment can be α type for a β type misfit dislocation (and visa-versa).

One consequence of the zincblende crystal symmetry is that GaAs is unchanged

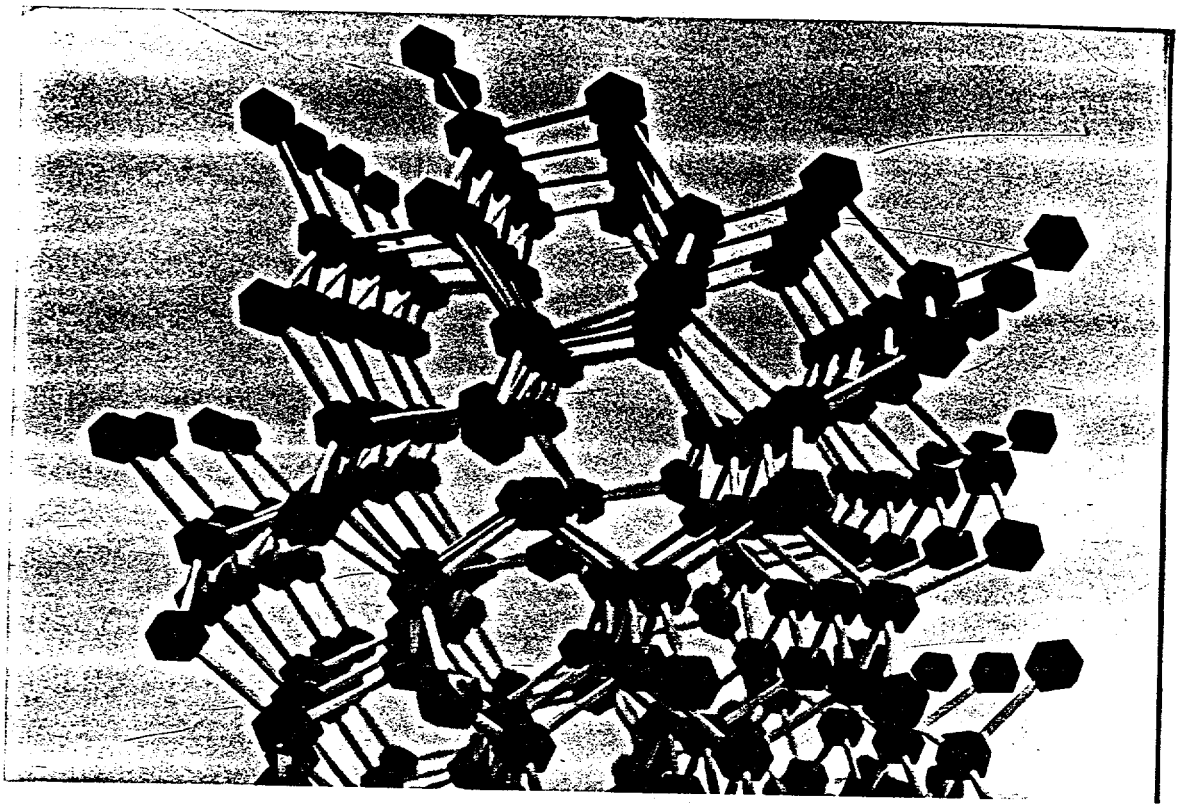

Figure 2.13: A photograph of a ball and stick model of an undissociated, group V glide set, 60° misfit dislocation at an InGaAs/GaAs interface. The black atoms represent As, the blue represent Ga and the green represent an In/Ga mixture. The arrow indicates a missing half plane of atoms in the epitaxial layer side.

Table 2.1: Misfit Dislocations in InGaAs/GaAs with $\vec{u} = [1\bar{1}0]$. All misfit dislocations are α type. Glide planes are Ga type. Segment types are α, β, and screw (s).

$\vec{b}$	$[0\bar{1}1]$	$[\bar{1}01]$	$[\bar{1}0\bar{1}]$	$[0\bar{1}\bar{1}]$
Glide Plane	(111)	(111)	$(\bar{1}\bar{1}1)$	$(\bar{1}\bar{1}1)$
Forward Segment 1	s	α	s	α
Forward Segment 2	α	s	α	s
Backward Segment 2	s	β	s	β
Backward Segment 1	β	s	β	s

Table 2.2: Misfit Dislocations in InGaAs/GaAs with $\vec{u} = [110]$. All misfit dislocations are β type. Glide planes are As type. Segment types are α, β, and screw (s).

$\vec{b}$	$[101]$	$[0\bar{1}1]$	$[0\bar{1}\bar{1}]$	$[0\bar{1}\bar{1}]$
Glide Plane	$(\bar{1}11)$	$(\bar{1}11)$	$(1\bar{1}1)$	$(1\bar{1}1)$
Forward Segment 1	s	β	s	β
Forward Segment 2	β	s	β	s
Backward Segment 2	s	α	s	α
Backward Segment 1	α	s	α	s

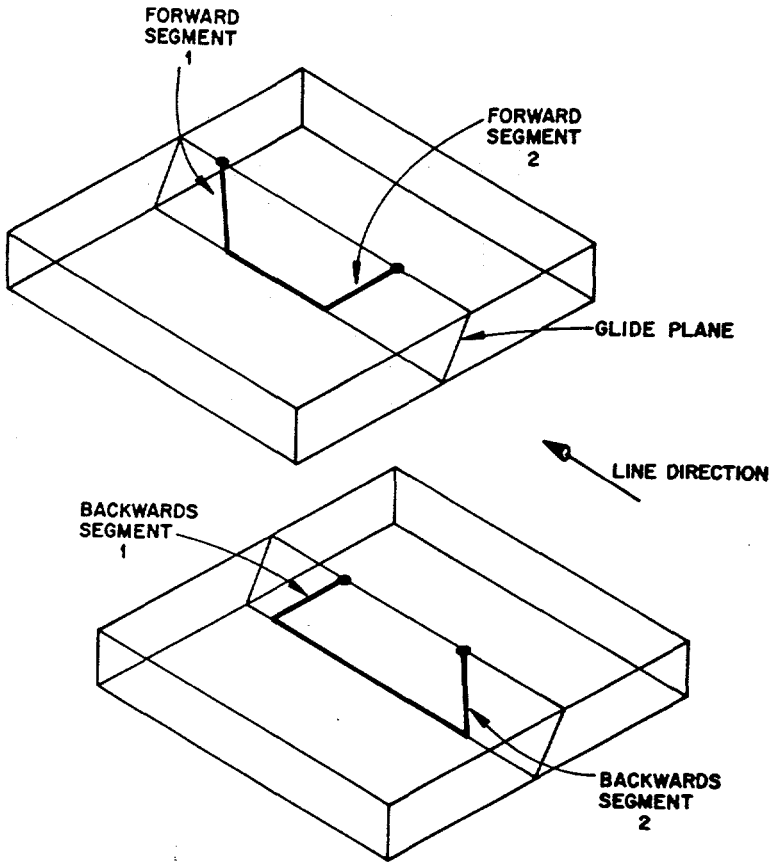

Figure 2.14: Schematic representations of forward and backward glide segments and their glide directions.

under a rotation of 180° around the [001] axis. If a GaAs crystal contains misfit dislocation lying in the (001) plane with a thread segment, then a 180° rotation creates the same crystal and a misfit dislocation with a different (but chemically equivalent) glide plane that lies along the same direction as before. Therefore the misfit dislocation $\vec{b} = [0\bar{1}1]$ with the forward oriented 60° thread segment must have precisely the same properties as the $\vec{b} = [0\bar{1}\bar{1}]$ and its forward 60° glide segment. In later chapters, the nucleation process is dealt with in more detail. One important quantity is the nucleation source density, g_x, defined as the number of nucleation sites on a substrate per unit area that can form a misfit dislocation that lies in the x direction. Because of the symmetry of the crystal and the 1 to 1 equivalence of its misfit dislocations, the fraction of misfit dislocations nucleating on a unit area of surface by a segment gliding in the positive $[1\bar{1}0]$ direction is exactly $0.5g_x$ (the other half must form in the $[\bar{1}10]$ direction). However, there is no correlation between the nucleation source densities in the $[1\bar{1}0]$ and the [110] directions since a 90° crystal rotation is not a symmetry operation.

Although the nucleation rates for misfit dislocations must be identical for both the positive and negative line direction sense, this does not necessarily imply that both types of dislocations exist at the same interface density in the same region. Obstructions, or misfit dislocation length attenuation may prevent some dislocation glide segments from reaching all areas. In Chapter 4 it is predicted that certain trench wall geometries, formed by substrate patterning, can selectively block glide segments (and therefore select only certain Burgers vectors), depending on the their orientations.

What happens if the substrate surface is not precisely parallel to the (001) crystal plane? Since the misfit dislocations must form by glide in a {111} plane, they must remain in that plane. They must also lie at the strained layer/substrate interface. Consequently, misfit dislocations will no longer appear to run in perpendicular arrays as described in a previous subsection. Goodhew et al. recently reported this effect in InGaAs/GaAs strained layers, using transmission electron microscopy [GK90]. To illustrate, Figure 2.15 is a schematic diagram of misfit dislocation line directions in a crystal that is γ degrees off the (001) plane in the [110] direction. The angle, ς, between the misfit dislocations shown in the figure when viewed from the top is

$$\tan \varsigma = \frac{2 \sin \gamma}{\tan \phi} \tag{2.20}$$

where $\phi = 54.736°$ is the angle between the {111} and the (001) planes.

Figure 2.16 is a scanning cathodoluminescence (CL) image of misfit dislocations in an InGaAs/GaAs heterostructure. The dark lines are the misfit dislocations. Note that the misfit dislocations run into each other at an angle of about 7°. Laue camera x-ray diffraction image of the same material, Figure 2.17, shows that the substrate is about 5° off in both the $[1\bar{1}0]$ and [110] directions. Substituting $\gamma = 5°$ into Equation 2.20 gives $\varsigma = 7.0°$, precisely what is found in Figure 2.16. What is interesting about slightly misaligned strained layer heterostructures is that the electronic effects of dislocation reactions can be studied since the normally perpendicular array of dislocations can now interact. More of this will be discussed in the next section.

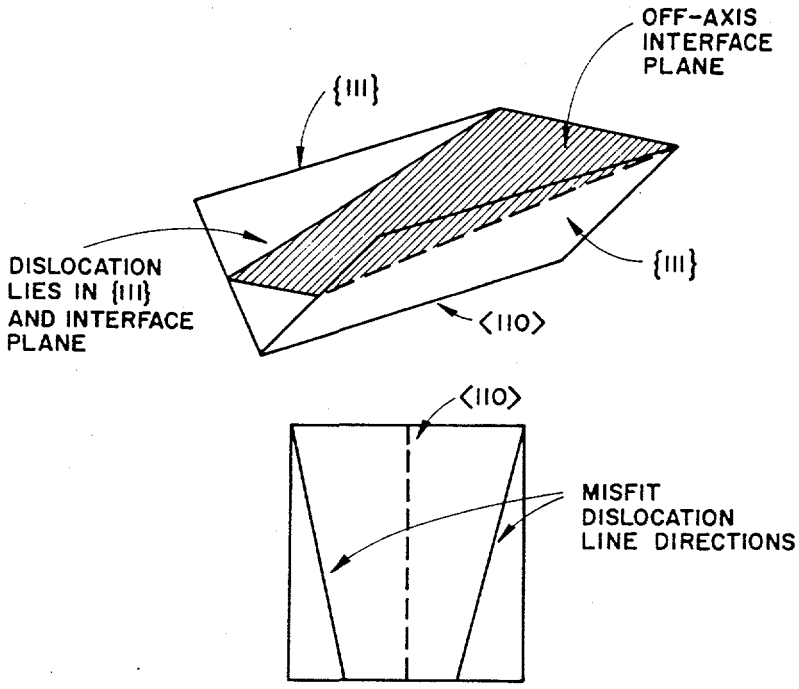

Figure 2.15: A schematic diagram of misfit dislocations in strained material grown on a wafer cut off of the [001] axis. Note that the misfit dislocations on opposing glide planes are no longer parallel.

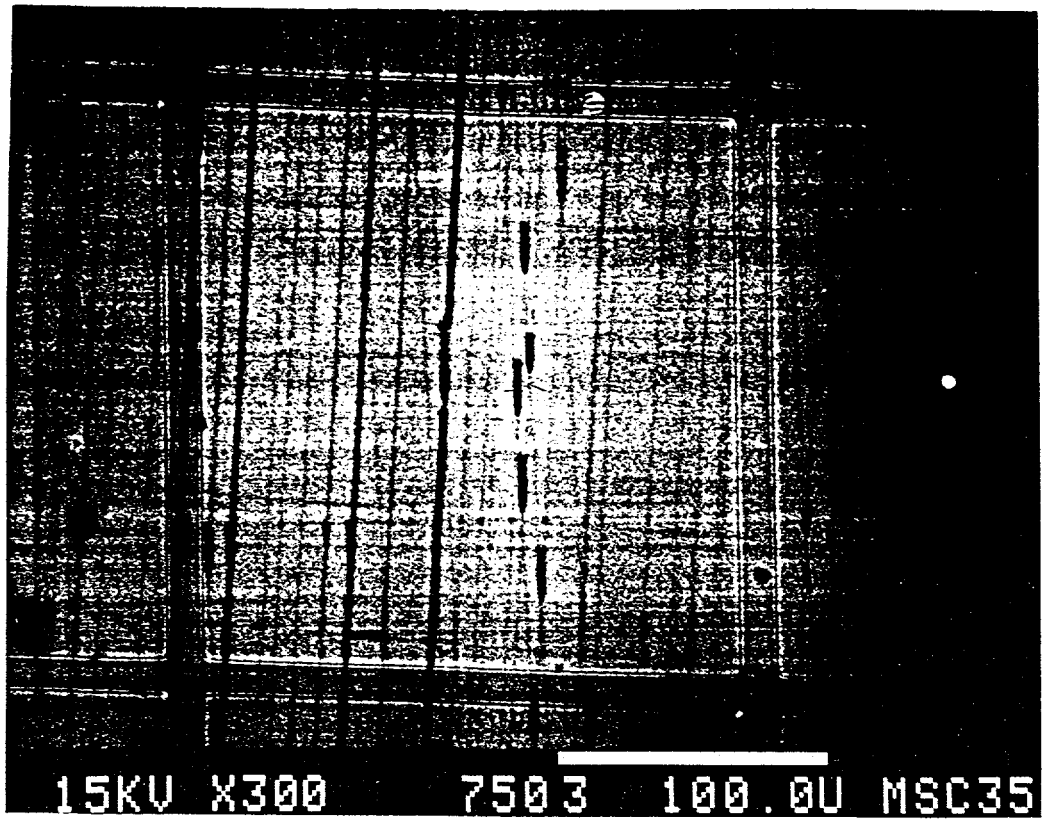

Figure 2.16: A scanning cathodoluminescence image of misfit dislocations in an InGaAs/GaAs heterostructure grown on a substrate cut 5° off the [001] axis in both the [110] and [1$\bar{1}$0] directions. The dark lines are misfit dislocations.

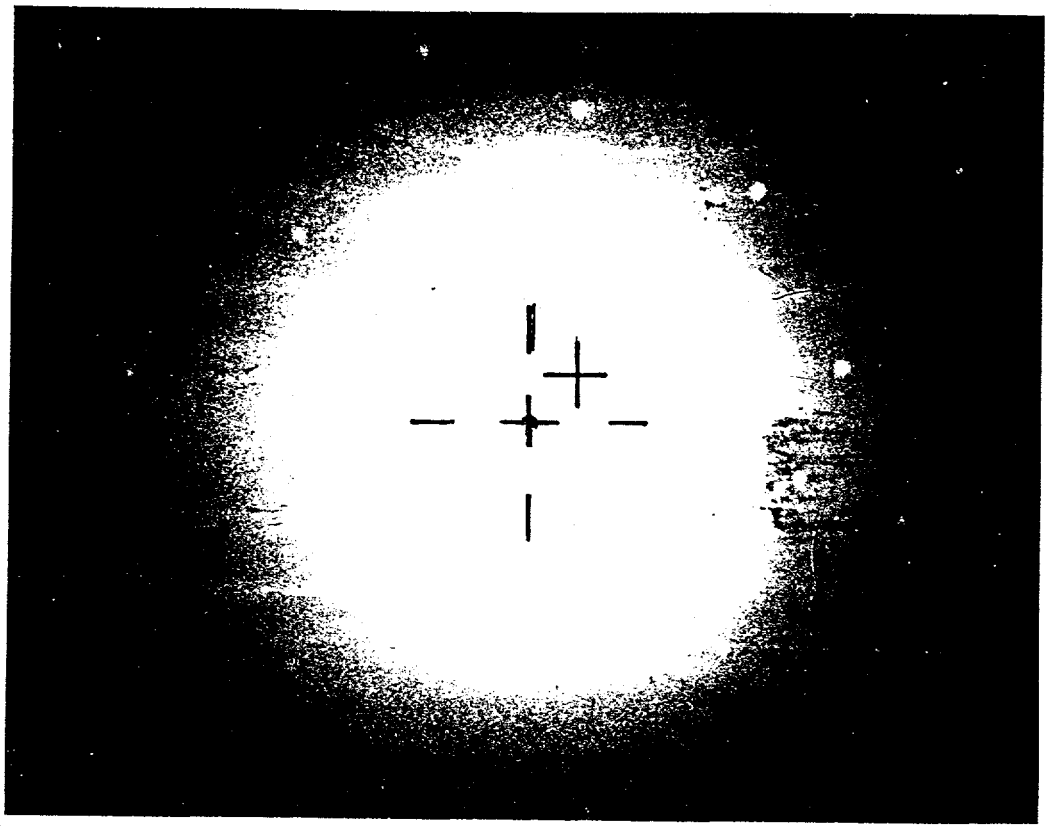

Figure 2.17: A Laue camera x-ray diffraction image of the misaligned substrate in Figure 2.16. The substrate is 5° off in both ⟨110⟩ directions.

2.4 Electrical Activity of Dislocations

2.4.1 Recombination and Deep Level States

The adverse effects that dislocations have on the characteristics of semiconductor devices was described in Chapter 1. To review, dislocations act as electron-hole recombination sites. Devices that operate by minority carrier injection are particularly sensitive to dislocations (Chapter 1). However, from a characterization point of view, the carrier recombination properties of dislocations can be exploited to study these defects.

Electron beam induced current (EBIC) can be used to image dislocations simply by feeding into the SEM signal amplifier the minority carrier current generated by an scanning electron beam. In the vicinity of dislocations, the minority carriers are absorbed and recombine before they have a chance to contribute to the current in a Schottky diode. EBIC has been used to measure misfit dislocation densities in strained SiGe alloys, for instance [Fit88]. Threading dislocation densities have been measured in GaAs grown on Si with this technique as well [OKWO89].

Other techniques such as CL and imaging photoluminescence excite electron-hole pairs by an electron beam or a photon beam in a direct bandgap semiconductor. The variation in the intensity of bandgap radiation emitted by electron-hole recombination is determined (like EBIC) by the local minority carrier density - which in turn is governed by the concentration of recombination centers (radiative and non-radiative). Misfit dislocations appear as dark (low intensity) lines when viewed from top down (hence the term *dark line defects*).

There is evidence that dislocations may sometimes act as *radiative* deep levels. Batstone and Steeds found that carrier recombination in the vicinity of misfit dislocations in ZnSe grown on GaAs substrates created a characteristic emission with a photon energy less than the ZnSe bandgap energy [BS85].

One other important technique has been used to study the properties of dislocation electronic states: deep level transient spectroscopy. This procedure measures the transient response of semiconductor diodes containing deep level trap states and is described in detail in Chapter 8. Previous efforts to study dislocation deep level states has been complicated by the fact that point defects are often induced with dislocations; the point defect deep level signatures tend to mask the dislocation defect state properties. However, as discussed in Chapter 8, patterning combined with strained layer heterojunctions is straightforward method to control the misfit dislocation density without affecting the point defect concentrations.

2.4.2 CL Contrast

In this subsection, the optimum excitation conditions and material parameters (used in the work described in all 6 subsequent chapters) are calculated.

The CL technique is based on electron beam induced excitation of electrons from the valence band to the conduction band of a semiconductor. Thus, the distribution of electrons of the beam in the solid is an important consideration to assess the spacial resolution of the technique. To first order, the high energy scattered electrons that scatter in a solid form a hemispherical or spherical *excitation volume* where most of the beam's energy is dissipated [Rei78, YH90]. The depth of the excitation is

known as the electron penetration range, and it gives the approximate maximum depth that a luminescence signal can be expected to emerge from a direct bandgap semiconductor. Everhart and Hoff established a simple empirical relation between the beam excitation voltage, E_b, in keV, and the electron penetration range, R_e, in μm:

$$R_e = \frac{0.0398}{\rho} E_b^{1.75} \tag{2.21}$$

where ρ is the solid density in g/cm^3 ($\rho = 5.32$ g/cm^3 for GaAs). For GaAs, the expected penetration ranges for 10, 15, and 25 keV beams are 0.4, 0.9, and 2.1 μm, respectively. Since all of the specimens studied by the author consisted of strained layers from 0.2 to 0.7 μm thick, a 15 keV beam is ideal for creating an excitation volume centered at the misfit dislocation depth.

Several theoretical studies are reviewed by Yacobi and Holt and by Holt and Saba concerning the CL contrast expected around a dislocation parallel to the surface of a direct bandgap semiconductor [YH86,HS85]. More recently, Hildebrandt and Hergert developed a simpler model; a series of graphs based on their theory specifically for GaAs indicate that a 15 keV beam gives the best contrast for a dislocation about 0.5 μm below the surface and a minority carrier diffusion length of 1 μm [HH90]. The assumed hole diffusion length is consistent with the experimental results of Grundeman et al., who studied InGaAs/GaAs with time resolved CL [GCB$^+$89].

The material carrier concentration has a profound effect on the overall CL signal intensity. Increasing the donor or acceptor concentration increases the radiative recombination reaction rate under low injection conditions, therefore radiative recombination is enhanced relative to other (non-radiative) recombination processes.

However, at very high doping levels, the impurities can contribute (as complexes, etc.) to the deep level concentrations in the semiconductor material and thus counteract the radiative recombination enhancement. Cocito et al. studied the CL intensity versus donor concentration in Si and Te doped GaAs bulk crystals [CFST86]. They found the optimum carrier concentration to be in the 1 to 5×10^{18} cm^{-3} range. This is consistent with theoretical predictions described by Yacobi and Holt [YH90].

2.4.3 Dislocation Types and CL Contrast

Petroff et al. made an important early study of the correlation between the Burgers vector and CL contrast in misfit dislocations [PLS79]. By simultaeously collecting a CL photon signal and a transmission electron image, they were able to correlate the dislocation structural characteristics with recombination properties in GaAlAsP/GaAs strained layer heterostructures. They found that the more numerous α 60° dislocations had less contrast than the β dislocations. In addition, edge dislocations that form by the reaction of two 60° dislocations were found to have no CL contrast at all - in repeated observations. Petroff and the others concluded that bond reconstruction in the edge dislocations formed dislocation core electron state energies outside the bandgap. The fact that such a defect with a large strain field could exist in the semiconductor without showing up as a recombination center lead the researchers to conclude that impurity gettering was not the cause of the electrical activity in the other dislocations [PLS79].

Fitzgerald et al. studied the recombination activity of misfit dislocations in InGaAs/GaAs heterostructures by comparing high voltage electron microscope images

with scanning CL images (registered to one another by surface defects) [FAA+88]. They found that edge dislocations acted as *more* efficient recombination centers than the 60° dislocations, the opposite of the finding of Petroff and his co-workers.

CL analysis of strained layers grown on off-axis, patterned substrates has been (inadvertently) found to provide a new way to correlate the electronic properties and reactions of misfit dislocations. Figure 2.16 is an example of such material. The off-axis substrate allows misfit dislocations lying on different {111} planes to intersect, as was mentioned in the previous section. In addition, patterning and etching very shallow trenches (about 100 nm deep) into the substrate before growth has been found to limit the interface dislocation density without completely isolating regions of the wafer (see Chapter 5). Consequently, the misfit dislocation density is lower that that of unpatterned material, so that the average defect spacing allows individual dislocations to be imaged, but not so low as to make dislocation reactions improbable.

Figure 2.18 is a close-up of the same region shown in Figure 2.16. Note the very dark *daggers* that form at the intersection of two nearly parallel, less electrically active misfit dislocations aligned approximately along the $[1\bar{1}0]$ direction (labeled A and B in Figure 2.18). Enhanced recombination occurred only in the top half of the intersections in all cases. Similarly, enhanced recombination occurred only on the right hand sides of intersections of nearly parallel [110] dislocations. The intersection of nearly perpendicular dislocations also show enhanced recombination - in some but not all instances. These intersections show up as small black dots in Figure 2.18.

The enhanced recombination daggers are likely to be caused by the formation of

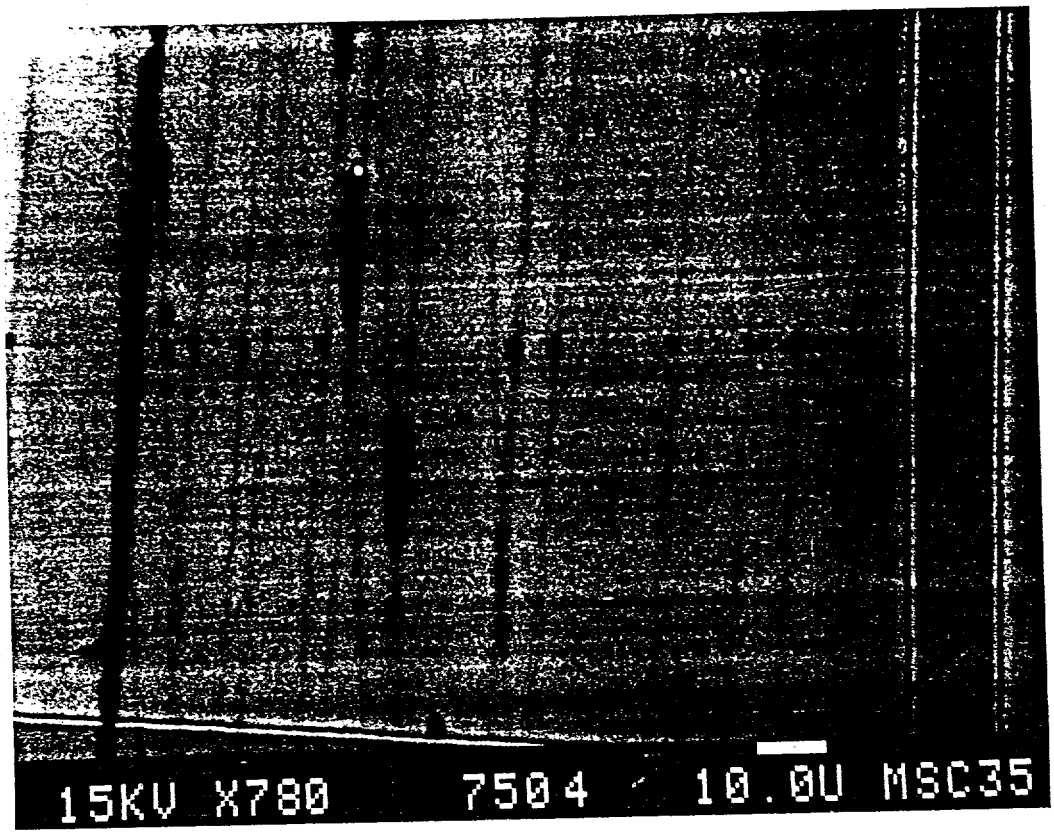

Figure 2.18: A close-up of a portion of Figure 2.16.

edge dislocations by the reaction of two 60° dislocations. This hypothesis is consistent with the results of Fitzgerald et al., who found that edge dislocations appear darker than 60° dislocations in CL images [FAA+88]. Note that an edge dislocation must be the product of two 60° dislocations that lie on opposing {111} glide planes, such as (111) and ($1\bar{1}1$) planes (see Tables 2.1 and 2.2). Figure 2.19 depicts the dislocation reaction schematically. The edge dislocation lies in the substrate side of the interface, not the epitaxial layer side, according to the Laue camera crystal orientation results. The length of the daggers corraborate this result; since the epitaxial layer is 300 nm thick, an edge dislocation oriented about 5° from the interface would reach the surface after travelling $0.3/\sin 5° = 4$ μm. The daggers are on the order of 18 μm long, so the edge dislocation must run in the opposite direction.

Fitzgerald et al. found that edge dislocations formed by misfit dislocation reactions appeared below InGaAs/GaAs interface surfaces (on properly oriented substrates) [FAA+88]. They assumed that a group of closely spaced like-Burgers vector 60° dislocations (generated from the same source) expells one or more members into the substrate because of the repulsion of the non-strain relieving Burgers vector components. Two dislocations expelled from different groups may move in their glide planes until they intersect, forming an edge dislocation. Fitzgerald et al. calculated the expulsion of a dislocation from the interface, induced by groups of dislocations with equal Burgers vectors spaced 25 nm apart. Calculations showed that such groups force some 60° dislocations into the substrate. The reaction between appropriate dislocations expelled from the interface can lead to the formation of edge dislocation segments [FAA+88,Fit88]. However, no closely spaced groups of dislo-

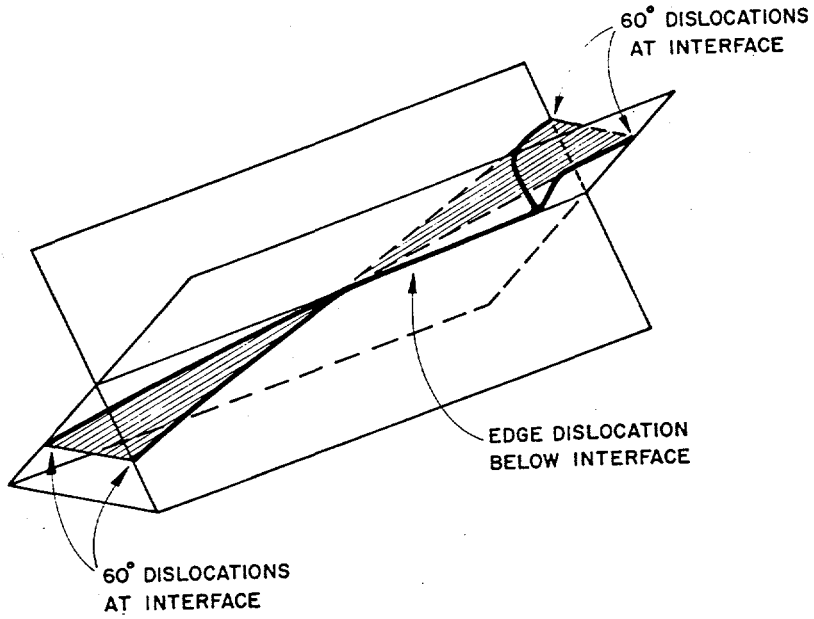

Figure 2.19: A schematic diagram depicting the reaction of two 60° misfit dislocations forming an edge dislocation in material grown on a substrate cut off the [001] axis.

cations are seen in Figure 2.16. The edge dislocations form not by expulsion, but because they are energetically favored over *independent* 60° dislocations.

Whether a dislocation reaction takes place or not is generally determined by Frank's rule,

$$\sum b^2_{product} < \sum b^2_{reactant}, \tag{2.22}$$

which is based on the minimization of the total dislocation strain energy [HL82]. Since an edge dislocation product has a smaller b^2 than the sum of two 60° dislocation b^2's, this reaction would be favored in any case. However, Frank's rule as formulated above does not hold as is because it is based on the strain field energies of dislocations in a single crystal. The energy rules do not apply in the same way at strained layer interfaces. More precisely, the in-plane Burgers vector, b_e, always relieves system strain, while the other Burger's vector components increase the strain, so they should be considered separately. If $\sum b_e$ is unchanged, then Frank's rule for misfit dislocations should be modified to:

$$\sum |\vec{b} - \vec{b_e}|^2_{product} < \sum |\vec{b} - \vec{b_e}|^2_{reactant}. \tag{2.23}$$

It can be seen that the pure edge dislocation contains none of the unnecessary Burgers vector components that are present in the 60° dislocation reactants. Therefore there is a large net energy savings when an edge misfit dislocation assembles. As an edge dislocation forms below the epitaxial layer interface, it begins to strain the substrate lattice and can no longer be considered a misfit dislocation. For epitaxial material and substrate material with similar elastic properties, a dislocation that reaches a depth in the substrate equal to the epitaxial layer thickness must be straining as

much material as it is relaxing. At that point, Frank's rule in its original form may be used to assess whether the dislocation reaction proceeds.

Frank's rule in either form explains why the edge dislocations are so stable for such long lengths (at 18 μm long, the dislocation must extend about 1 μm below the interface) but it does not answer why they form only in the substrate and not in the epitaxial layer.

One final dark line defect type evident in Figure 2.16 is the very dark nearly, vertical lines that are aligned with one set of the 60° dislocations. They are believed to be a closely spaced group of like dislocations. Being so close, they collectively absorb many more minority carriers, leading to the enhanced non-radiative recombination.

Chapter 3

Requirements for the Growth of High Quality, Low Defect Density, InGaAs Strained Epitaxial Layers

3.1 Introduction

Substrate preparation for epitaxial growth on GaAs is an extremely important step that has received relatively little attention in the literature. Many recipes are used, and some reported, but no detailed studies are known to the author. Part of the reason is because a few simple (and successful) principles guide the crystal grower; solvent clean the substrate to remove organic contaminants, wet etch several microns off the substrate surface to remove any crystal damage and other contaminants, and finally remove any native oxides on the substrate by heating it in a reducing atmosphere or vacuum in the growth chamber (many times along with an As source

to prevent surface decomposition).

Unfortunately, patterning complicates this cleaning process because not only must the substrate surface be as clean as before, but the topology must be maintained (or at least controlled) as well. In this chapter some examples of the problems caused by patterned substrate contamination are presented and details of the substrate processing used to create material in subsequent chapters are described.

3.2 Processing Patterned Substrates for Strained Layer Growth

As with unpatterned substrates, the GaAs used throughout this thesis was first solvent cleaned in hot trichloroethylene, acetone, and methanol, followed by a room temperature 2-propanol rinse. After 2 rinses in 17 MΩ de-ionized water (DI), the substrates were etched in 5:1:1 H_2SO_4:H_2O_2:H_2O at 25°C for about 10 minutes to remove about 10 μm of the GaAs and again rinsed repeatedly in DI. At this point, an unpatterned substrate would be ready for loading in an epitaxial growth system. Instead, a 300 nm SiO_2 layer was then deposited to act as an etch mask.

Patterning the substrate through photolithography is accomplished indirectly by first patterning a deposited SiO_2 layer. There are two advantages to using an SiO_2 mask; first, the mask erosion rate is slower and sidewall shape are much more easily controlled during the GaAs etch step with an oxide mask than with photoresist. Second, photoresist is difficult to remove after it is subjected to plasmas and heat. Since the SiO_2 mask is simple to remove in an HF based solution, it is possible to leave the oxide on the substrate until just before growth to prevent contamination

Table 3.1: The Patterning Process.

Step Number	
1	Solvent Clean and Etch 5:1:1 H_2SO_4:H_2O_2:H_2O at 25°C for 10 min.
2	Deposit SiO_2, Technics PECVD, 300 nm typical.
3	Photolithography, HMDS, AZ1400-27 5000RPM 30 s post-bake 100°C 30 min.
4	Mask Etch, RIE 30 sccm of CHF_3, 30 mtorr, 0.15 W/cm^2, 10 min (typical).
5	GaAs etch.

and damage during transport. This is an important consideration, since most of the strained layer material described in this thesis was fabricated and characterized in Ithaca, NY while the growths were done at the University of Florida in Gainesville.

The wafers were solvent cleaned and etched in an O_2 plasma repeatedly during processing to ensure that all organic material is removed prior to epitaxial layer growth. Contamination on the side walls or near the wall edges has been found to cause misfit dislocation nucleation and significantly increase the number of interface defect density. Table 3.1, lists the process sequence used by the author along with some details of the fabrication cleaning and etching steps.

3.2.1 Substrate Etching

Chemically assisted ion beam etching (CAIBE) was employed to etch the GaAs substrates used by Fitzgerald and in early experiments by the author. CAIBE uses an Ar ion beam and a jets of Cl_2 to etch features in GaAs possessing sidewalls that are nearly parallel to the Ar beam, a property of the substrate topology that was originally believed to be necessary for misfit dislocation isolation.

The original CAIBE was built and maintained by Robert Davis of the Cornell Applied Physics and Engineering department. A Technics Plasma GmbH unit was subsequently installed at the National Nanofabrication Facility and was used to create all of the etched substrates described in Chapter 4.

Although satisfactory results were originally obtained with CAIBE, the etch rate varied erratically. Part of the problem was that the CAIBE process etch rate is highly temperature dependent, although it was originally believed to be virtually independent of temperature since the Ar ions were assumed to contribute the energy necessary to break the Ga-As bonds and form chlorinated products [Joh86]. Consequently, minor differences in the contact between wafer and platen strongly affected the final etch depth. Elaborate fixtures were developed by other researchers to control the process - which usually consisted of attaching the wafer backs to the platen with a proprietary thermally conductive paste. This was not a satisfactory solution for substrate patterning since it was found that it was difficult to remove all remnants of the paste later.

Another problem with the CAIBE process became apparent as the machine aged. The stainless steel platen slowly developed an insulating coating that made it difficult

to electrically ground the substrates. As a result, sporadic arcing occurred that damaged the substrate surface.

Because of these problems, the author instead developed an etch process using a reactive ion etcher, also located at the Nanofabrication Facility. The process was based on the work of Scherer et al. and Sonek et al. [SCB87,SB84]. Scherer and co-workers studied the etch characteristics of plasmas composed of BCl_3 and Ar mixtures on GaAs substrates [SCB87]. The compound BCl_3 is used in Si technology as a compound that getters water molecules in a plasma, as well as acts as a source of chlorine. They studied the effects of RF power, pressure and composition on the etch rate and the etched feature characteristics. The etched surfaces and sidewalls were found to be smooth, but the maximum etch rate was so slow that it was larger than, but comparable to the erosion rate of the SiO_2 mask - an unsatisfactory condition.

Sonek et al. studied the RIE characteristics of the BCl_3/Cl_2 mixture on GaAs [SB84]. In this case the etched surfaces were found to be rough, although the etch rate was relatively fast.

A combination of these two gas systems was found to yield smooth etch surfaces, smooth and vertical sidewalls, and an etch rate with a substrate to mask selectivity of 8:1. The addition of small amounts of Cl_2 to the BCl_3/Ar mixture enhances the GaAs etch rate and increases the mask to substrate selectivity without adversely affecting the sidewalls or etched surface smoothness. Table 3.2 lists the RIE process conditions that were found to yield good quality patterned substrates.

To ensure a repeatable etch rate, substrates were etched in 30:1 buffered oxide etch for 30 s to remove any remaining SiO_2 on the exposed GaAs surface. Just before

Table 3.2: RIE GaAs etch conditions.

Ar Flow rate	40	sccm
BCL_3 Flow rate	38	sccm
CL_2 Flow rate	2	sccm
Pressure	25	mtorr
Power	0.55	W/cm^2
Platen Temperature	30	°C
Etch rate	200	nm/min.

RIE, they were etched for 30 s in a 1:10 $HCl:H_2O$ solution, rinsed in DI, blown off and baked at 90°C for 15 min. to ensure that the native oxide was constant across each specimen and also from specimen to specimen. Figure 3.1 is a plot of etch depth vs. time for the conditions listed in Table 3.2. The uniform etch rate, 200 nm/min., was maintained with only small variations for many growth runs over a period of several months. The oxide mask etch rate was only 12 nm/min. Figure 3.2 is a scanning electron microscope cross-section micrograph of a patterned substrate etched about 1 μm deep. Note the nearly vertical walls. Nomarski interference contrast showed that the etched trenches were as smooth as the polished wafer surface.

3.3 Surface Preparation

Based on results from an initial series of experiments, it became evident that the quality of strained epitaxial layers grown by molecular beam epitaxy (MBE) were adversely affected (but not always!) by some form of contamination on the patterned

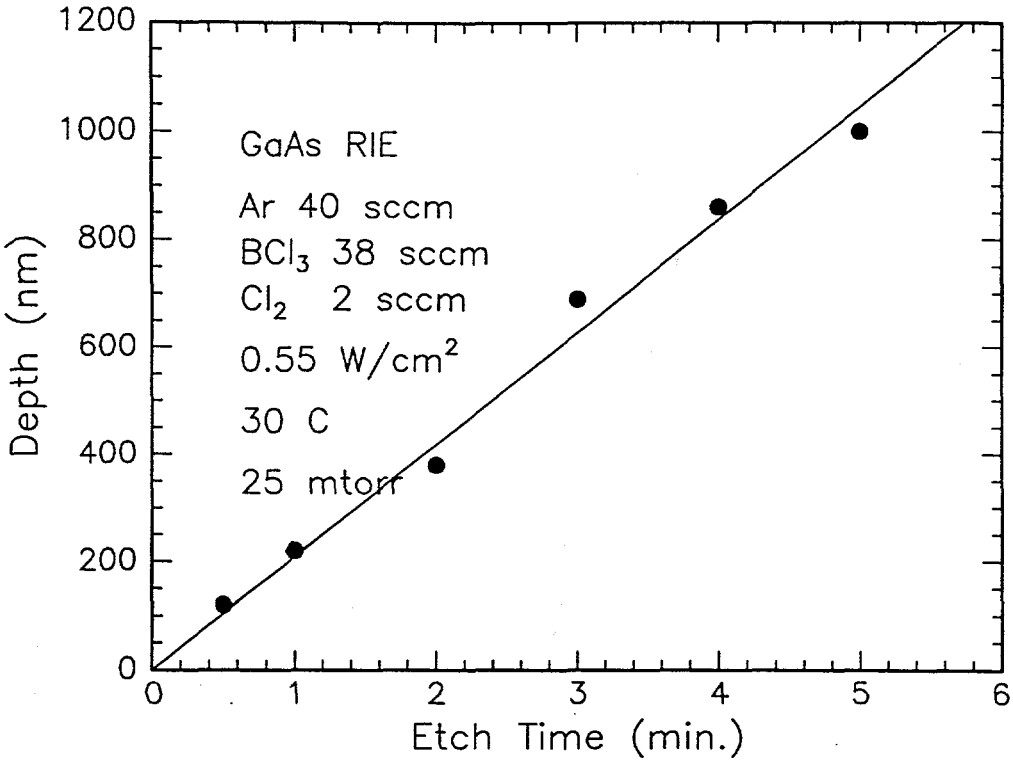

Figure 3.1: A plot of the RIE etch depth in GaAs vs. time.

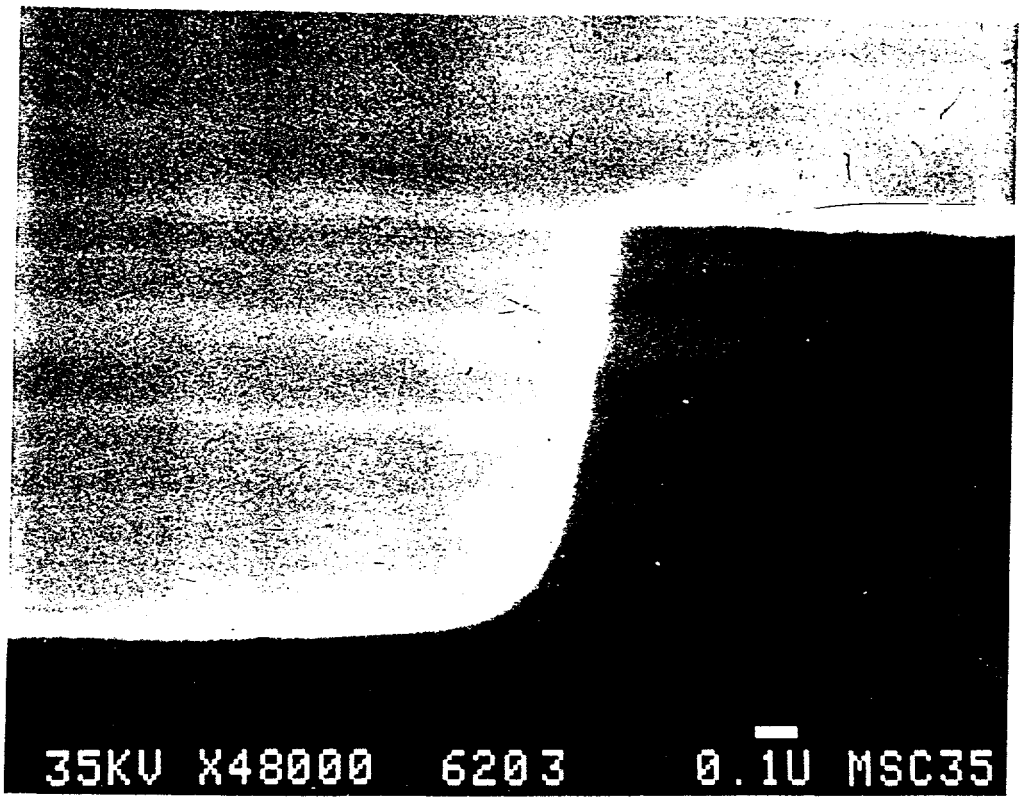

Figure 3.2: A cross-sectional SEM view of an etched trench.

substrates (MBE growths were carried out at Hewlett Packard, see Chapter 4). After solvent cleaning and stripping the oxide mask, these substrates were etched for a short time. The amount of material removed was minimized to ensure that the trench sidewall shapes were not adversely affected (or ion-damaged channels were not removed - described in the next chapter). However, some etching was assumed to be necessary at this point to remove any substrate damage and surface contamination. The following section details the final cleaning process that was developed to create high quality, low defect density, strained epitaxial layers on patterned substrates.

3.3.1 Final Etch

The preparation performed before growth was essentially identical for all specimens; solvent clean, strip oxide mask, and etch the substrate surface. The final etch procedure was the only one that varied to any degree. In the experiments described in Chapter 4 the ion-damaged and etched substrates were etched for 2 s in a dilute NH_3OH, H_2O_2, and H_2O solution just before insertion into the growth chamber. Although several satisfactory specimens were obtained, less than half of the substrates had usable epitaxial layers. Two criteria were used to determine the epitaxial layer quality; the first was surface quality, observed in an optical microscope or SEM. Rough surfaces or non-uniform mesa edges clearly indicated some type of growth problem. The second was cathodoluminescence image quality, both in overall signal intensity and the uniformity of the signal across a mesa surface.

Organo-metallic chemical vapor deposited (OMCVD) strained InGaAs grown at the University of Florida (Chapter 5) proved to frequently yield poor quality material

as well. Initially, no final etch was used; after the HF strip and a DI rinse, the wafers were loaded into the growth chamber. Two of the three wafers were of extremely poor quality, possessing little or no CL direct bandgap emission. However, one wafer was acceptable and its misfit dislocation nucleation properties are discussed in the next section.

Figure 3.3 is a scanning CL image of the surface of an OMCVD wafer with only an HF strip as a final etch. Note the spotty CL signal that hinders dark line defect observation. Figure 3.4 is a CL image of similar material using the NH_3OH, H_2O_2, and H_2O final etch. Note the dark spots centered around each mesa. The etch time was apparently not adequate to remove all of a surface contaminant that was removed more quickly at the mesa edges.

Figure 3.5 is a CL image of a mesa and a 10 μm wide trench. Note that while the mesa epitaxial layer emits a relatively large amount of bandgap radiation (bright region), the trench material is of poor quality. Figure 3.6 is a CL image of spots that resemble water marks. In both of these images, it is believed that the final N_2 blow-off was to blame for these features. Water trapped in the trenches (especially the deeper ones) after the final rinse apparently splattered onto the mesa tops during blow-off.

A series of tests were conducted to improve the yield of the epitaxial layer growths. Patterned samples were etched in various solutions for a range of times and InGaAs test layers were grown by both MBE here at Cornell (by William Schaff of the Electrical Engineering Department) and by OMCVD at the University of Florida. The most successful cleaning process is described below.

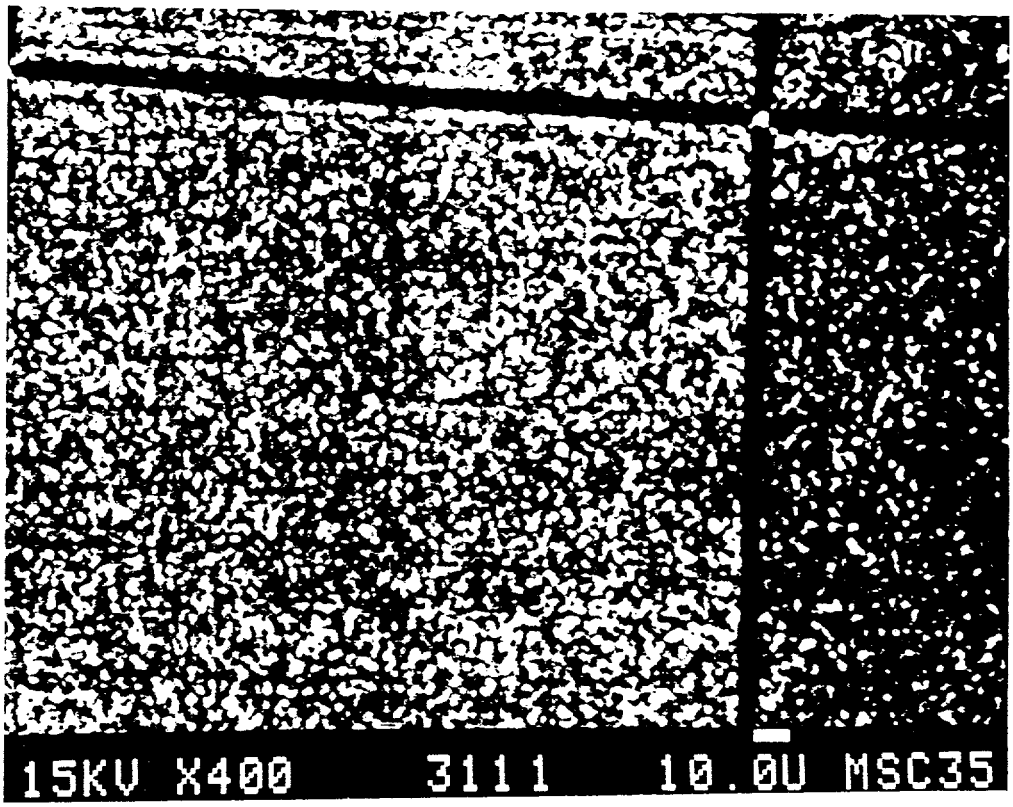

Figure 3.3: A CL image of a poor quality InGaAs strained layer. See text for description.

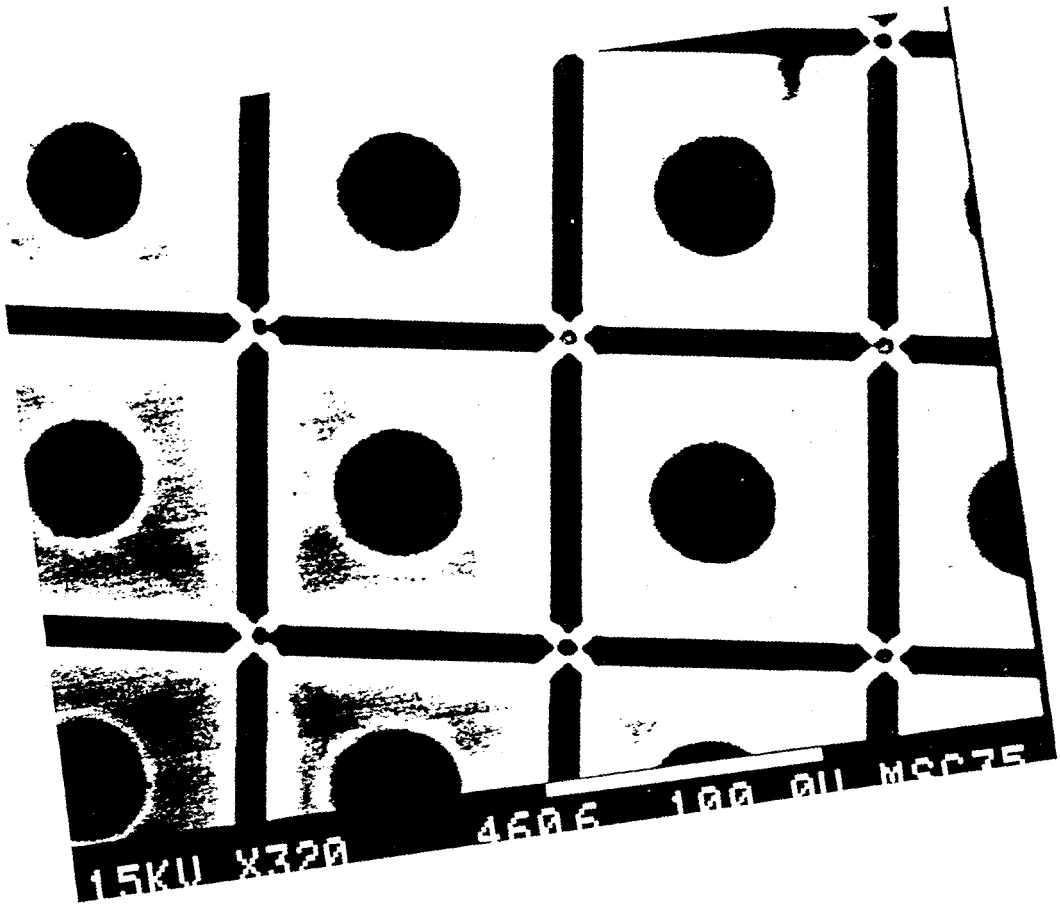

Figure 3.4: A CL image of a poor quality InGaAs strained layer. See text for description.

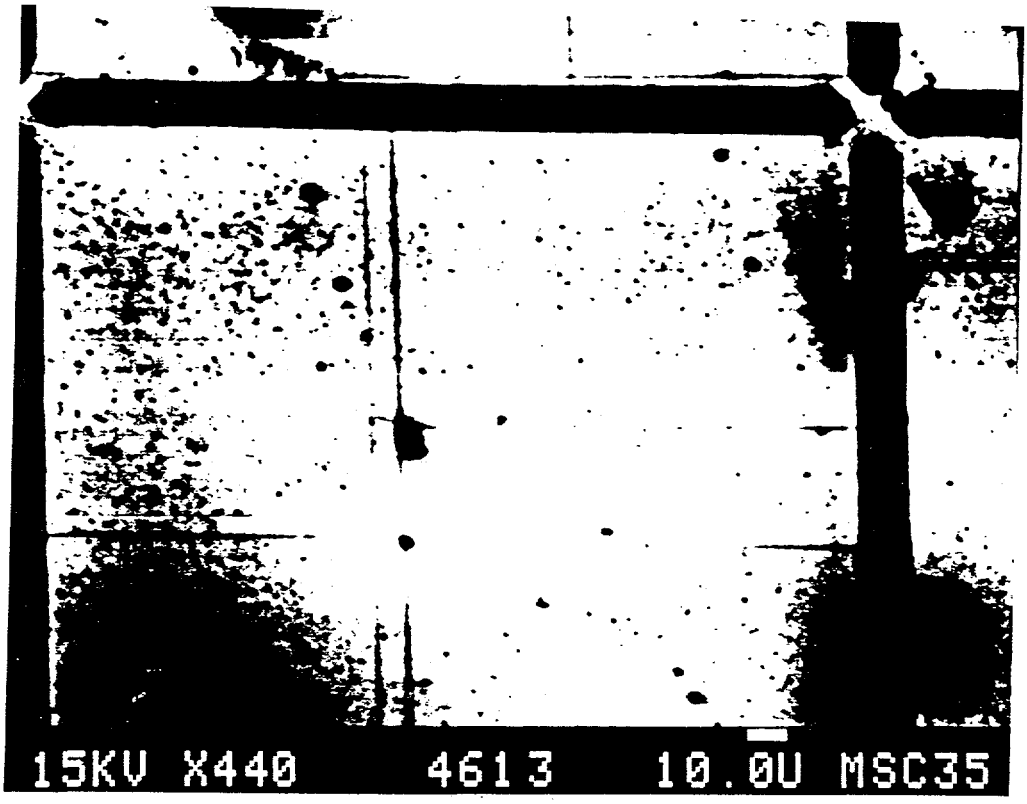

Figure 3.5: A CL image of a poor quality InGaAs strained layer. See text for description.

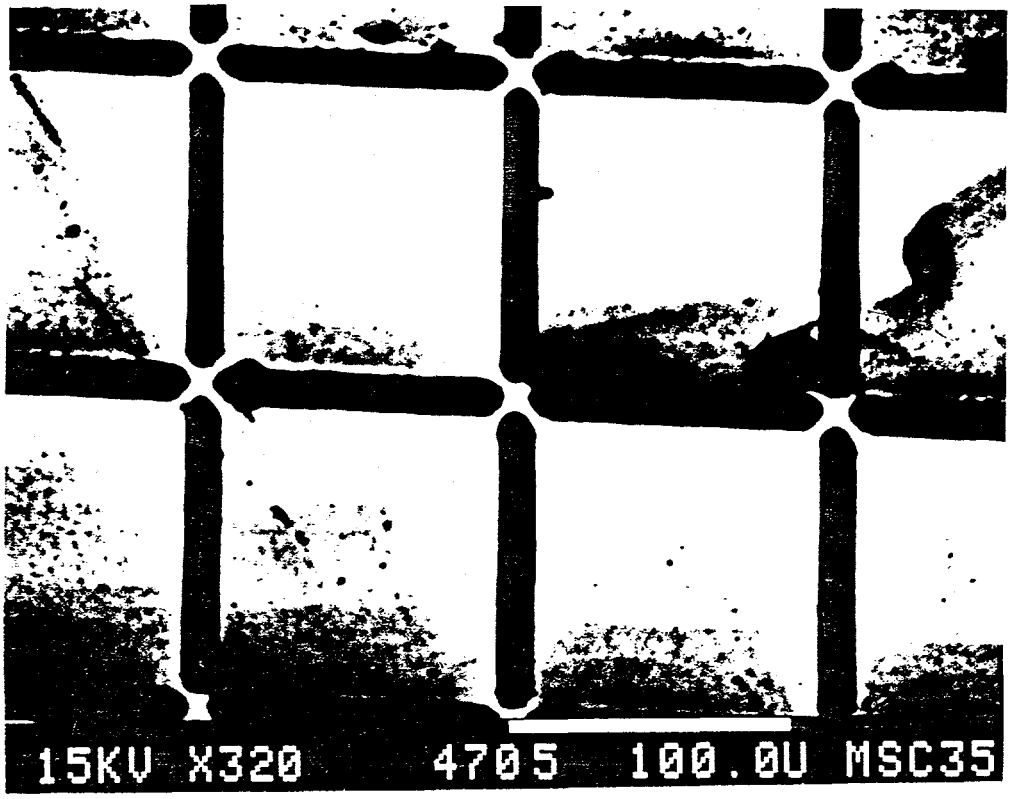

Figure 3.6: A CL image of a poor quality InGaAs strained layer. See text for description.

- Solvent clean with hot trichloroethylene, acetone, and methanol followed by room temperature 2-propanol and two DI rinses (all electronic grade solvents).
- Remove SiO_2 mask in buffered oxide etch (6:1) and rinse twice in DI.
- Etch in concentrated, electronic grade Sulfuric Acid for about 5 minutes to remove any organic contaminants and rinse twice in DI.
- Etch in a solution of 1:1:20 H_2SO_4:H_2O_2:H_2O at 25°C for 30 s to remove about 80 nm of GaAs, rinse twice in DI and blow-off with N_2.

This final etch sequence was used to create all of the material described in Chapters 5, 6, 7, and 8. The most recent series of OMCVD InGaAs growths yielded a better than 75% success rate based on morphology and CL intensity criteria.

3.3.2 Nucleation Source Density and Preparation

Patterned substrate processing not only affected the morphology and radiative efficiency of epitaxial strained layers, but it influenced the dislocation nucleation source density as well. One sample that was only etched in HF as a final clean step, GPW-028, consisted of a GaAs substrate with an etch pit density (EPD) of 5000 cm^{-2} patterned with a series of square mesas separated by 1.2 μm deep trenches and a 350 nm thick $In_{0.035}Ga_{0.965}As$ OMCVD epitaxial layer. Figures 3.7 and 3.8 are CL images of GPW-028. The number of misfit dislocations per cm is clearly much lower in the material isolated into 100 μm squares than the 800 μm squares. As described in Chapter 1, the reduction is an effect of confining the gliding dislocations to small regions.

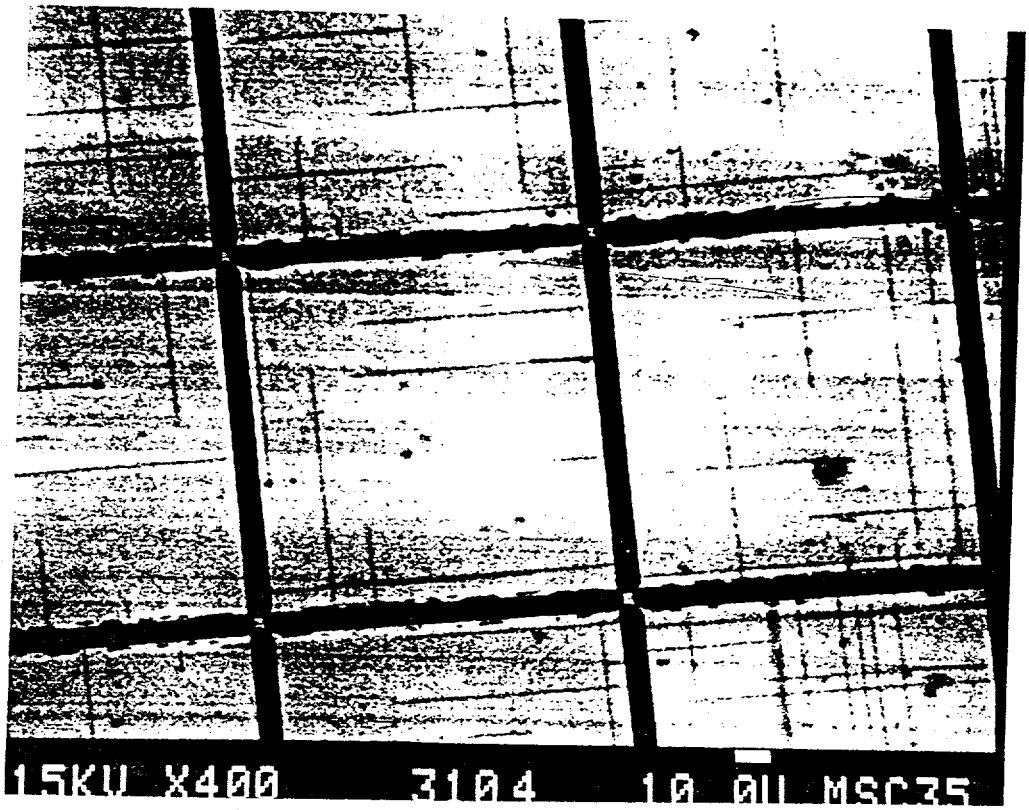

Figure 3.7: A Cl image of a 100 μm wide square mesa on GPW-028.

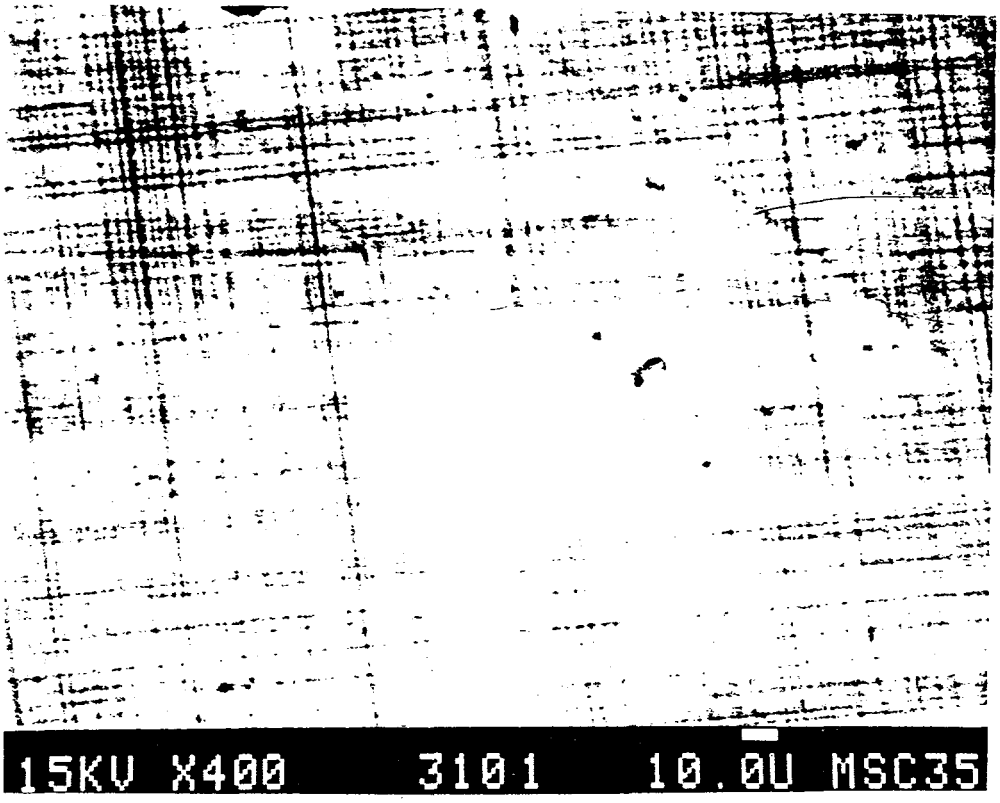

Figure 3.8: A Cl image of an 800 μm wide square mesa on GPW-028.

Figure 3.9 is a plot of how the average misfit dislocation densities change with mesa size for that material. The specimen was of a relatively large size so that it was possible to calculate the average dark line defect density over many squares of each size. For instance, the dislocation densities in 100 μm and 800 μm squares were determined by averaging 60, and 20 mesas, respectively. The error bar shown in the figure corresponds to one standard deviation on each side of the mean. The misfit dislocation nucleation site density (nucleation source density), as defined and described in Chapters 1 and 6, is simply twice the slope of a linear fit of the data in Figure 3.9.

The nucleation source density in the wafer was estimated to be about 50,000 cm^{-2} - 10 times larger than the EPD. Therefore, threading dislocations (assumed to be the same as the EPD) alone cannot account for the observed number of defects. Other defects such as particles on the substrate surface must contribute the majority of nucleation sources.

Figure 3.10 is a CL image of a 200 μm square mesa with 300 nm thick $In_{0.05}Ga_{0.95}As$ subjected to the final clean described in the last section. Although the thickness, strain, and substrate EPD are comparable to GPW-028, it is hard to find any defects at all on the mesas. The nucleation source density is estimated to be below 2500 cm^{-2}. Thus, care in handling and cleaning can significantly affect the misfit dislocation density in strained epitaxial layers grown on patterned substrates.

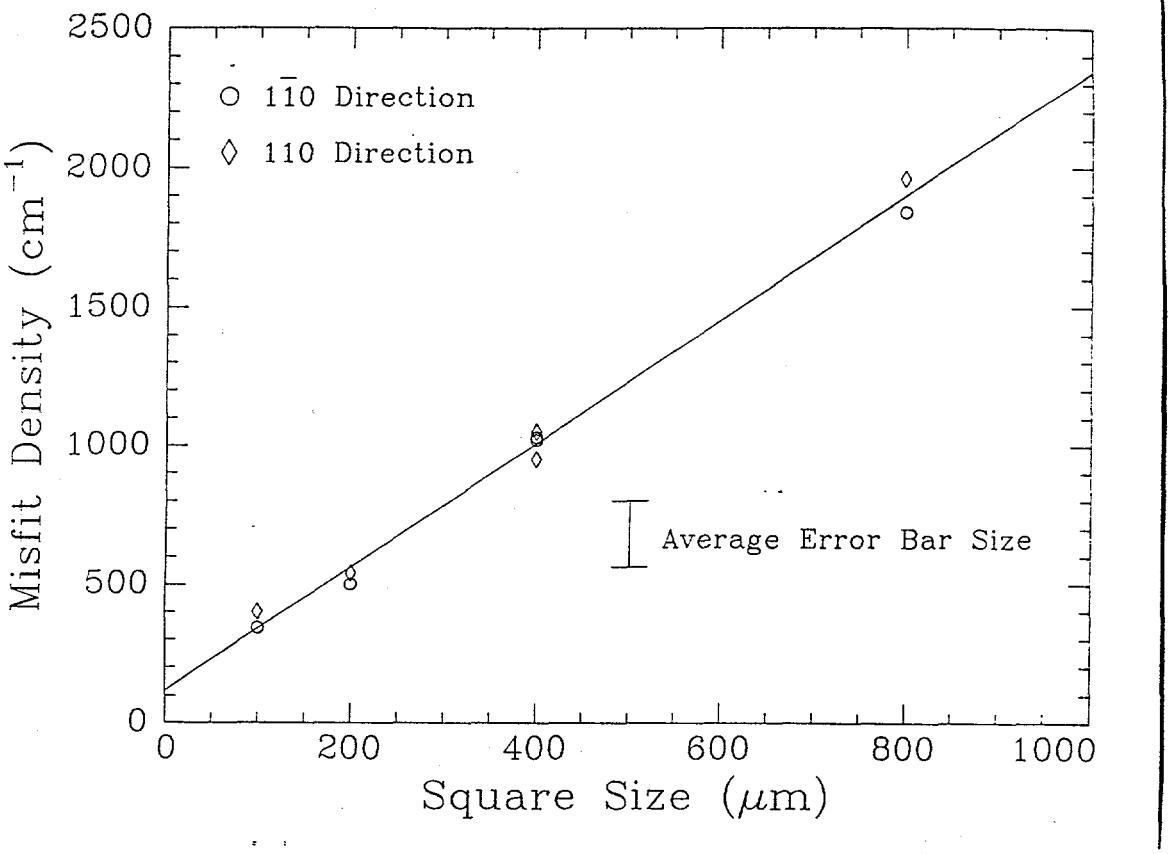

Figure 3.9: A plot of the average misfit dislocation density vs. mesa size for GPW-028. The slope is used to determine the misfit dislocation nucleation site density.

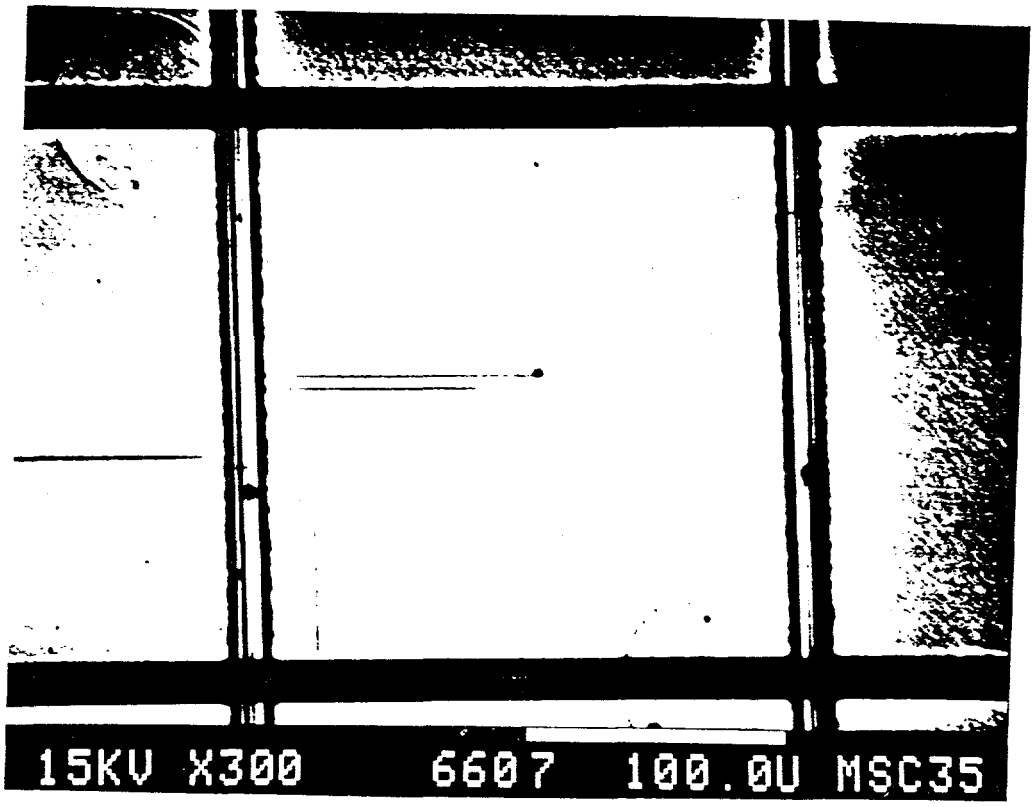

Figure 3.10: A CL image of a strained layer with 200μm square mesas. The final cleaning step is partly responsible for the very low interface defect density.

Chapter 4

The Isolation and Nucleation of Misfit Dislocations in Strained Epitaxial Layers Grown on Patterned, Ion-Damaged GaAs

4.1 Introduction

The technique used by Fitzgerald et al. to control the strained layer misfit dislocation density consisted of selectively etching the substrate surface followed by epitaxial layer growth by MBE [FWP+89]. While successful in suppressing misfit dislocations, the technique had the disadvantage that the resulting wafer surface was no longer planar. Abrupt edges up to 2 μm deep were present which would certainly complicate subsequent device processing. For this reason, it is desirable to block misfit

dislocation glide while maintaining a planar GaAs substrate. The author attempted to do this by isolating regions through selective ion-damage. To investigate this possibility, samples were prepared by ion implanting partially masked GaAs substrates before epitaxial growth.

As described in Chapters 1 and 2, misfit dislocations form in lattice mismatched epitaxial layers when a threading dislocation segment glides and leaves behind a misfit dislocation. The epitaxial material is elastically strained to match the in-plane lattice parameter of the substrate up to the critical thickness, which can be estimated by theories such as Matthews et al.[MML70]. Once the critical thickness is exceeded, misfit dislocations are energetically favored to relieve strain by plastic deformation. On unpatterned wafers, a misfit dislocation threading segment can glide relatively large distances. Blocking this glide by etching or ion-damaging can significantly reduce the local misfit density since the surface topology controls their maximum glide distance.

The basic idea behind selectively ion-damaging a substrate is to create a region of the strained epitaxial layer that is polycrystalline or of such poor crystalline quality that misfit dislocation glide segments cannot pass through it. The resulting material should ideally consist of square regions of high quality epitaxial strained layer with a low interface defect density, each region isolated from each other by narrow channels of damaged epitaxial material. Since the substrate is planar before growth, the wafer should be essentially planar after growth as well.

In addition to techniques such as CL and TEM, which can image misfit dislocations at the interface, the strain relief caused by the misfit dislocations can be mea-

sured by analyzing lattice parameter changes by x-ray diffraction and ion channeling. The properties of films grown at two different temperatures have been characterized by all four techniques.

4.2 Material Preparation

Portions of semi-insulating liquid encapsulated Czochralski (75 mm wafers from Spectrum Technologies) and Si doped horizontal Bridgeman GaAs substrates (from Sumitomo Ltd.), both oriented to within 0.5°C of the (001) surface, were used. The substrates were solvent cleaned in hot trichloroethylene, acetone and methanol, and blown off with compressed N_2, then immediately coated with 300 nm of plasma enhanced chemical vapor deposited (PECVD) SiO_2 in a modified Technics plasma etcher (courtesy of the group led by Dr. Krusius at the Cornell University Electrical Engineering Department). The oxide mask was patterned by standard photolithographic and plasma etching techniques into square regions separated by channels that exposed the substrate. The square edges were aligned along cleaved ⟨110⟩ substrate edges. The square dimensions ranged from 25 to 800 μm on each side. All four corners of each square are attached to the square's neighbors to ensure that the epitaxial layer remained intact during planar transmission electron microscope (TEM) sample preparation. Figure 4.1 is a schematic diagram of a portion of the mask.

The masked substrates were then subjected to a 300 KeV Xe^+ ion implantation at room temperature and 7° off of the [001] wafer axis, using an Accelerators Incorporated ion implanter. Xe was chosen because its large mass ensured that most of

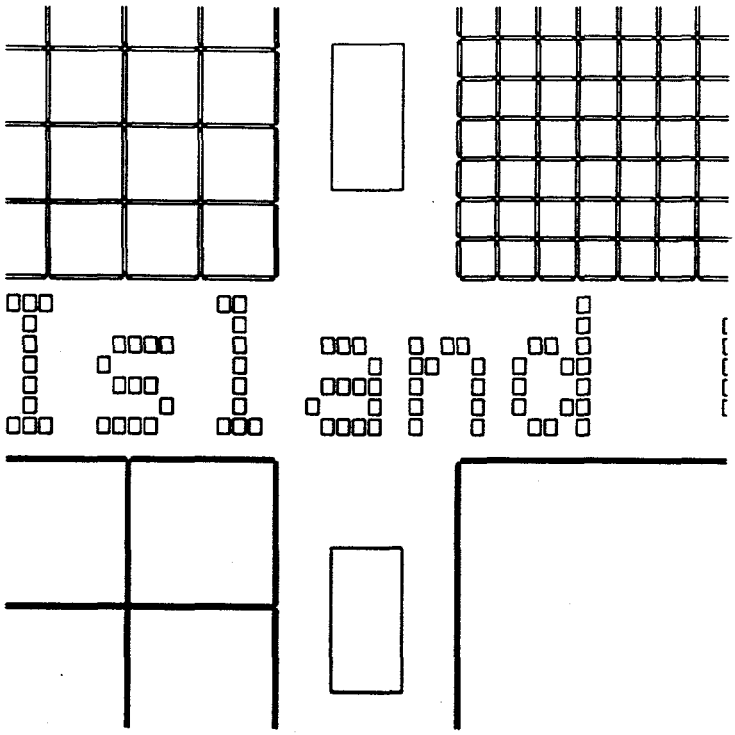

Figure 4.1: A schematic diagram of the photomask used to pattern the substrates.

the crystal damage would extend up to the surface. Other lighter ions would have embedded themselves deeper into the substrate (and penetrated the mask).

The typical dose was 10^{15} cm^{-2}, equivalent to a monolayer of Xe on the GaAs surface. The damage was predicted to be about 100 nm deep, based on a projected range of 69nm and standard deviation of 28nm for Ge according to [GJM75]. Although information on Xe in GaAs was not available, the properties would be essentially the same as those of Xe in Ge (Ge has about the same atomic mass as Ga and As). Virtually no Xe should have penetrated the SiO_2 mask at these conditions (projected range 92 nm with standard deviation of 23 nm). Monte Carlo computer calculations using the program TRIM-88 on a personal computer confirmed these estimates.[1] The material grown on these substrates is called *ion-damaged* material in this chapter for simplicity.

The substrates that were used for what is called *etched* material were masked in the same way as the ion-damaged substrates. They were processed in a Technics Plasma GmbH chemically assisted ion beam etcher at room temperature using Cl_2 gas in an Ar ion beam. Vertical wall trenches were etched about $1\mu m$ deep between the squares. Details of this process are described in Chapter 3.

Just before MBE growth, the SiO_2 masks were stripped in HF, solvent cleaned, and etched for 2 seconds in dilute NH_3OH, H_2O_2, and H_2O. The final etch was kept very short to prevent the loss of the ion-damaged material. At the same time it was felt necessary that at least a small portion of the substrate surface be removed to eliminate any contaminants. The substrates were In bonded and then heated to

[1]Written by James F. Ziegler at IBM Thomas J. Watson Research Center.

645°C for less than 5 minutes under an As_4 flux in the MBE chamber to remove surface oxides. The final cleaning and epitaxial growth were carried out by Alice Fischer-Colbrie at Hewlett Packard Laboratories for the low growth temperatures specimens and by William Schaff of the Electrical Engineering Department and Cornell University for the higher growth temperature samples.

MBE growth was carried out in the two different machines at two conditions: 400°C at a rate of about 1 μm/h (at Hewlett Packard) and at about 500°C at 2μm/h (at Cornell). In all cases, a 350 nm GaAs buffer layer was first grown, followed by a 350 nm layer of $In_{0.05}Ga_{0.95}As$. The epitaxial layer is several times larger than the predicted critical thickness. In addition, both layers were n-doped with Si at 10^{18} cm^{-3} to improve the intensity of the cathodoluminescence signal (Chapter 2).

4.3 Characterization

4.4 Scanning Electronic Microscopy

The cleaved SEM samples were prepared by first coating the epi surface with typically 300 nm of SiO_2 after which the In solder on the back was removed in HCl. They were then cleaved along a 110 direction and stained in a solution of H_2SO_4, H_2O_2, and H_2O at a ratio of 1:1:10 for about 30 seconds. Observations were made with a JEOL JSM35 scanning electron microscope (SEM).

Figure 4.2 *a* is a SEM image of a cleaved and stained cross-section of one of the ion-damaged, 400°C grown samples. Figure 4.2 *b* is a schematic diagram labeling the regions in the image. Note that the ion-damaged channel is easily discerned; the cleaning and high temperatures before and during MBE growth did not anneal out

the implant damage (in accord with the CL images described below). The buffer and InGaAs layers are 150 ± 10 nm and 350 ± 10 nm thick, respectively.

Figure 4.3 is an SEM image of the 400°C wafer surface, taken at an oblique angle to accentuate the surface features. Cigar shaped features in the channels are evident. These bumps on the surface are about 100 nm by 1000 nm and 100 nm high. The epitaxial layer of the squares are much smoother. Cross hatching, caused by the change in growth rates around the strain field of misfit dislocations and commonly seen MBE InGaAs and InGaP ([FWP+89,KCH+88,FJ90]), was not found in these low growth temperature specimens.

4.4.1 Cathodoluminescence

The scanning cathodoluminescence (CL) apparatus is a modified Si photo-detector and amplifiers from GW Electronics, which is fitted to the same electron microscope as used for the SEM analysis [Fit89]. A 15 KeV beam with a current of about 5×10^{-8} A was typically used for excitation.

Figure 4.4 is a CL image of one of the ion-damaged wafers after growth at 400°C. The thin dark lines correspond to misfit dislocations or groups of them at the GaAs/InGaAs interface. The electron/hole pairs created by the electron beam recombine non-radiatively near the dislocation cores which therefore are dark. Regions where direct bandgap recombination is prevalent show up as bright areas. The thick black bars are the ion-damaged regions. One surprising point that is clearly visible in Figure 4.4 is that misfit dislocations form along only the $[1\bar{1}0]$ direction for the most part. Asymmetries in the dislocation densities of the two $\langle 110 \rangle$ type

a

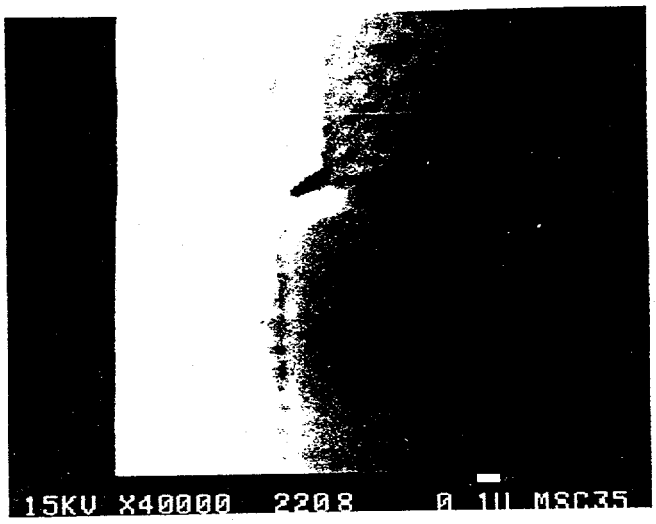

b

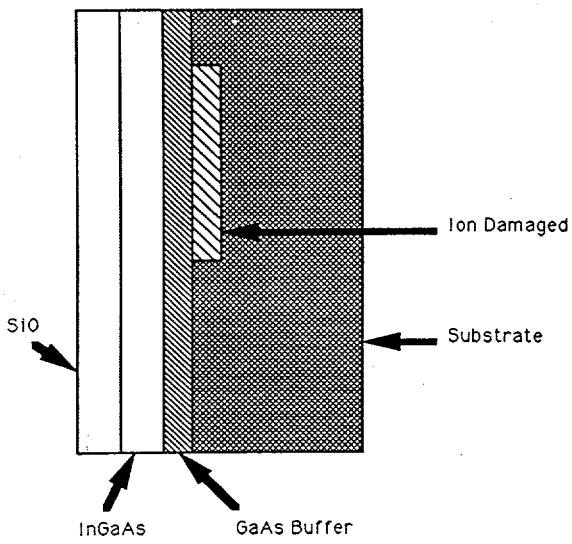

Figure 4.2: a SEM image of the profile of an ion-damaged substrate and epitaxial layer, *a*, and a schematic diagram highlighting the features above, *b*.

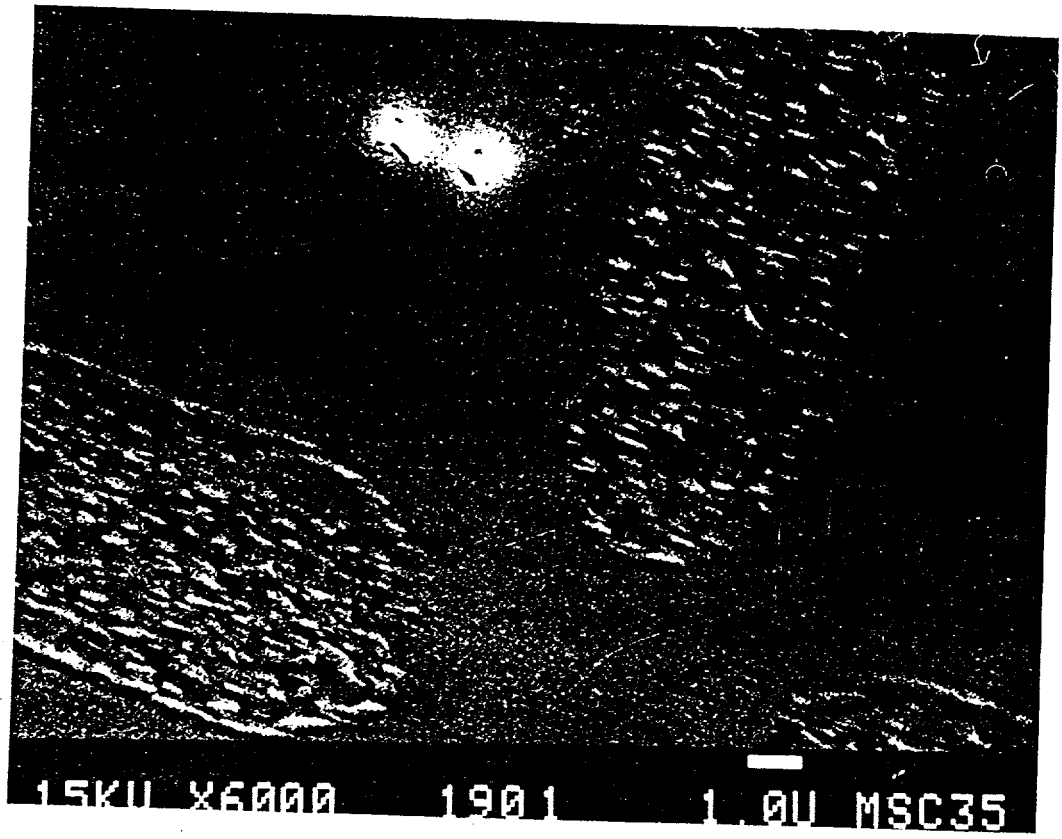

Figure 4.3: A SEM image of the ion-damaged epitaxial layer surface.

directions have been reported before, but not to such an extreme extent [FWP+89, KCH+88]. Interestingly, material grown on etched substrates with the same type of mask also showed similar misfit densities in CL (Figure 4.5). The dark lines run from one channel to another, indicating that the dislocations nucleated at one edge and stopped at the other. Since the CL technique can only resolve separations on the order of 1 to 2 μm, the misfit dislocation density in Figure 4.4 is much larger than 10,000 cm^{-1}.

Figure 4.6 is a CL image that indicates that a large region between isolated squares has even less misfits than the squares themselves; the "isolating" channels appear to nucleate more misfits than would be present in even unpatterned wafers.

Another interesting feature in Figure 4.4 is that there appear to be bright bands along some of the channels. The reason for this is that the SiO_2 mask was slightly misaligned relative to the $\langle 110 \rangle$ cleave direction. Evidently only a few misfits are nucleated at the corners of the channels (pointed to by arrows in Figure 4.4), leading to a region of slightly higher luminescence. The orientation of the channels has a small affect on the misfit density.

Figure 4.7 is a CL image of ion-damaged material grown at 500 °C. There are about 5000 cm^{-1} misfit dislocations in the $[1\bar{1}0]$ direction and about 1500 cm^{-1} in the [110] direction. Figure 4.8 shows a closeup of a channel in this material. Notice that there is some bandgap emission from the damaged region - an indication that regrowth has occurred. Dark lines in Figure 4.8 can evidently pass through the damaged area from one square to the next, implying that the channels are no longer isolating surface regions.

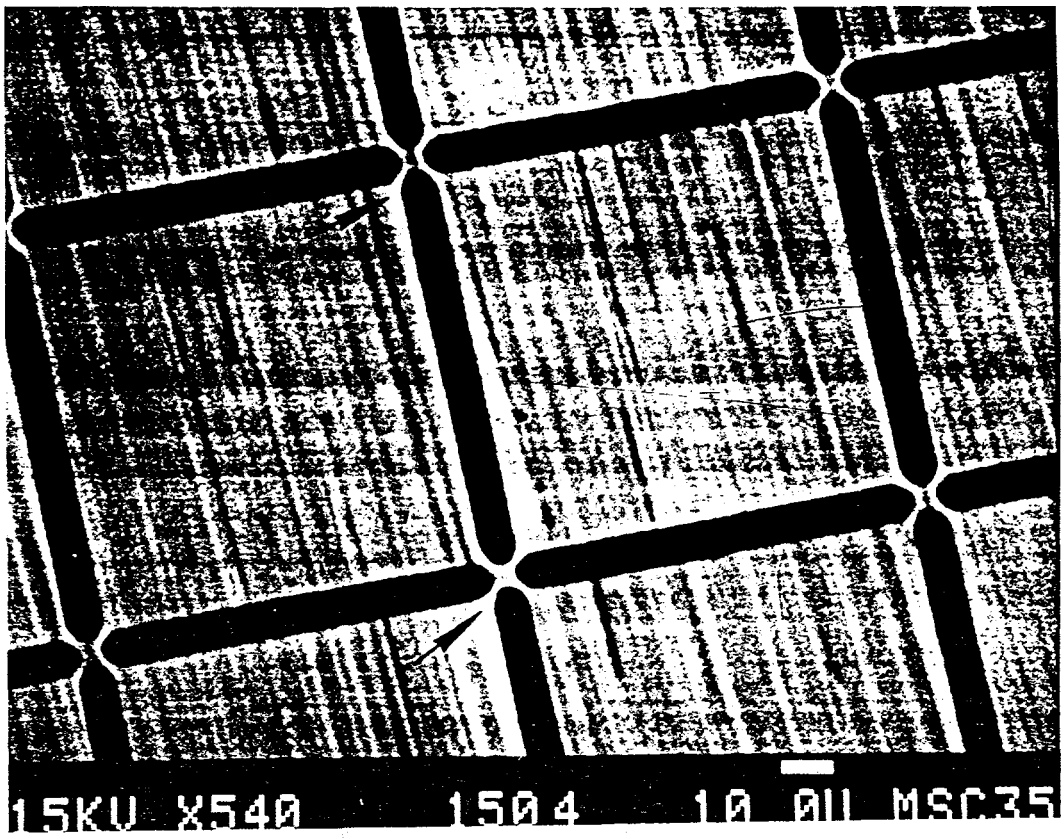

Figure 4.4: A CL image of 400 °C grown InGaAs on an ion-damaged substrate. The black areas are ion-damaged channels. The dark lines are misfit dislocations that have formed in only one direction. The arrows point to regions where the CL signal is greater, indicating that there are few misfit dislocations there.

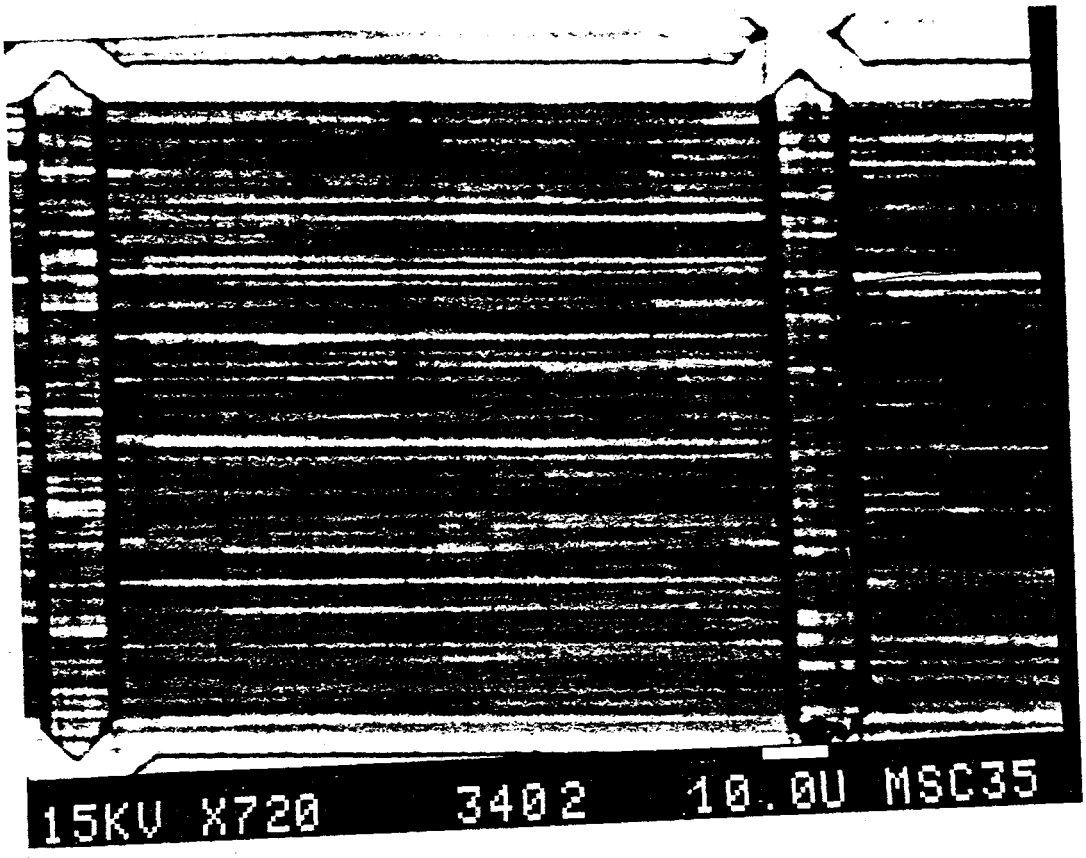

Figure 4.5: A CL image of 400 °C InGaAs on an etched substrate. Again misfits form in one direction.

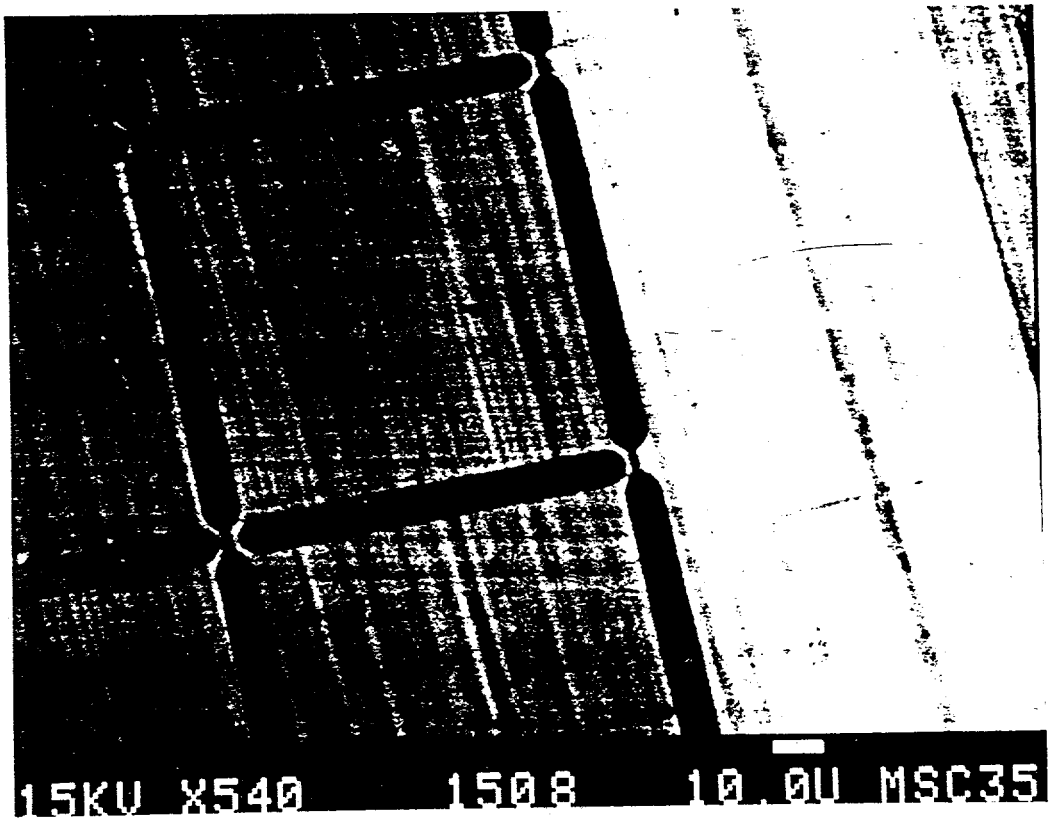

Figure 4.6: A CL image of 400 °C ion-damaged material and an adjacent region on the right that was not patterned at all. The misfit dislocation density appears higher in the damaged portion.

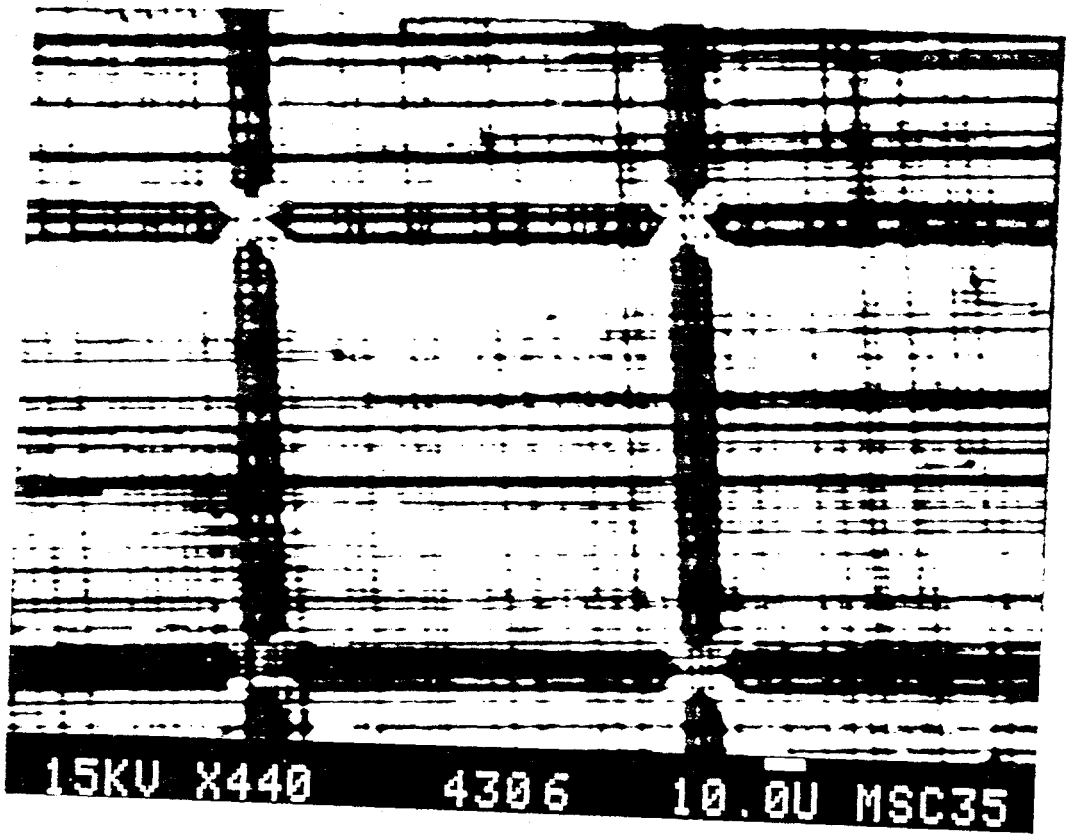

Figure 4.7: A CL image of 500 °C ion-damaged material. The misfit density is relatively low.

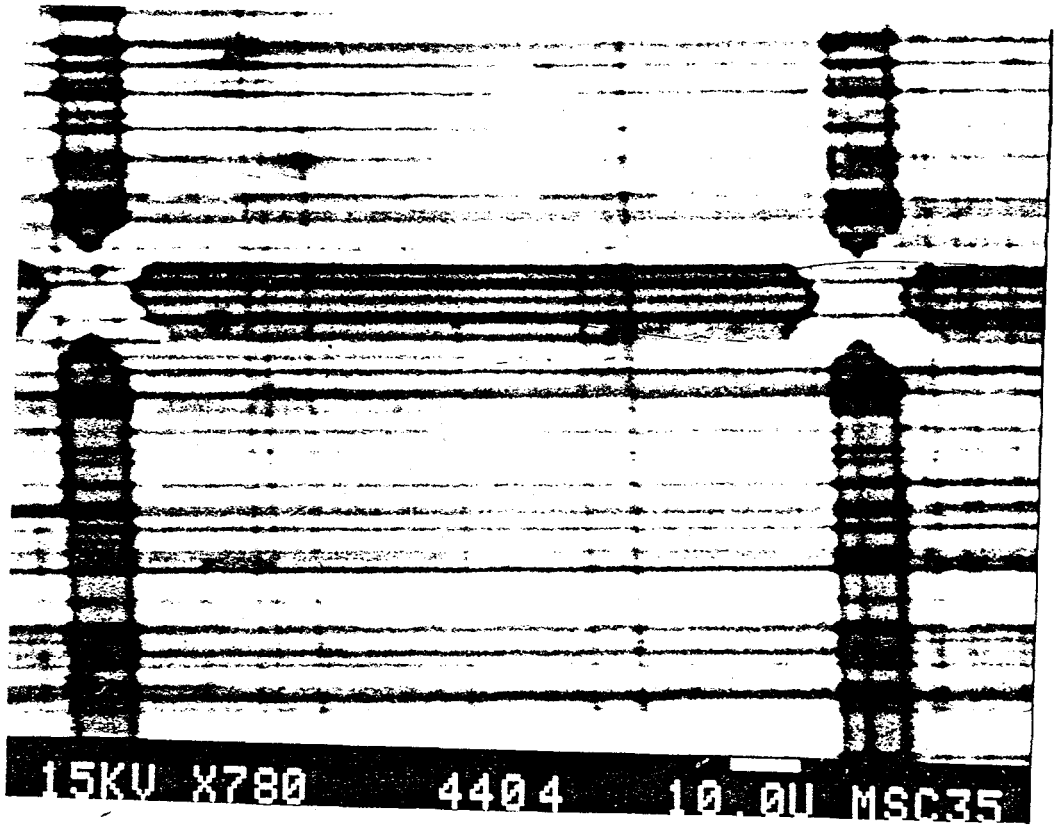

Figure 4.8: A Close up CL image of the material in Figure 4.7. The ion-damaged channel did not prevent misfits from gliding from one square to another.

Figure 4.9 is a CL image of etched material grown under identical conditions. The dislocation densities are about 5000 cm^{-1} in the $[1\bar{1}0]$ direction and about 500 cm^{-1} in the [110] direction for 100 μm squares. Edge nucleation is still prominent but much less so than the 400 °C material.

Figures 4.10 *a* and *b* are CL images of identical regions of an ion-damaged wafer. The image *b* was taken about 1 minute after *a*. Note the darker line defect labeled *A* in Figure 4.10 *a* no longer appears in *b*. The electron beam presumably caused a dislocation reaction to take place. Based on observations of similar material described in Chapter 2, the darker line defect in *a* is an edge dislocation formed by the reaction of two nearby 60°C misfit dislocations, as described by [FAA+88]. The increase in dislocation mobility under electron beam irradiation has been investigated by Maeda et al. [MSIT84]. In the present case the beam apparently facilitated the splitting of a higher contrast sessile edge dislocation back the original glissile 60° dislocations.

4.4.2 Transmission Electron Microscopy

The planar TEM samples were prepared by purely wet chemical means; ion milling was avoided to ensure as little damage as possible was imposed on the strained layer interfaces. The epitaxial side was first coated with PECVD SiO_2 to ensure that the top layer was not scratched or attacked by etchants during processing. The In solder on the back of the MBE wafers was removed in HCl and the backs were polished chemo-mechanically in a 1% Br_2 in methanol solution until the substrate thicknesses reached about 100μm.[2] Part of the SiO_2 mask on the epitaxial side was stripped

[2]The chemo-mechanical polisher was designed and provided by Jack Berry of the Electrical Engineering department and Cornell University.

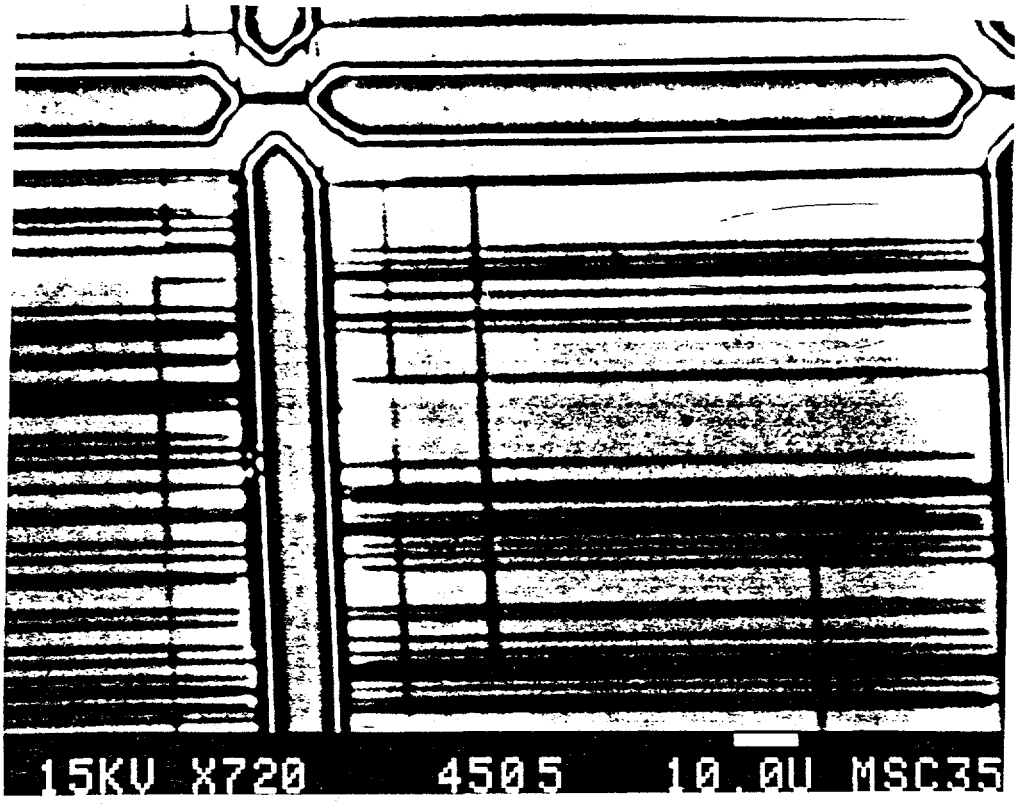

Figure 4.9: A CL image of 500 °C etched material. Some nucleation at the channel edges is evident, but much less than that seen in the material in Figure 4.5.

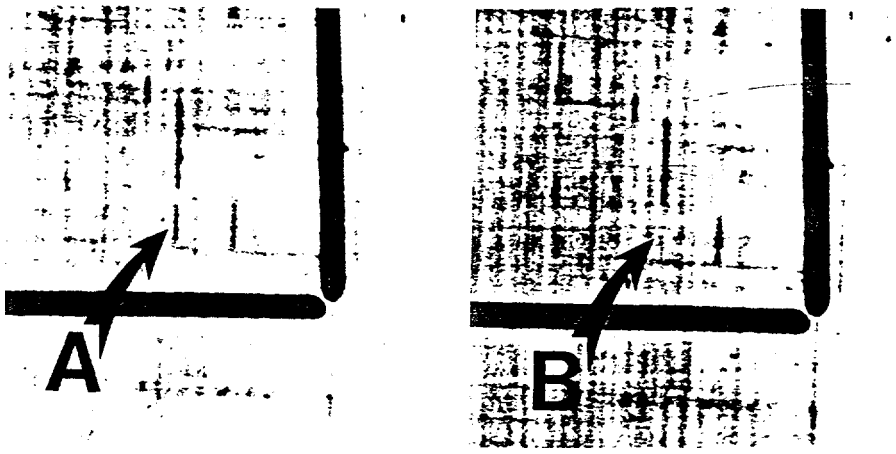

Figure 4.10: A CL image of misfit dislocations in the InGaAs/GaAs interface on patterned, ion-damaged substrates grown at 400°C. In *a*, a darker line defect labeled *A* disappears seconds later in *b*.

and the exposed material was slowly etched with the same solution used in the SEM staining process. The etch was periodically interrupted and the depth relative to the oxide was measured with a Tencor Alpha Step surface profiler until all but about 80 nm of the 350 nm of the InGaAs was left. The sample was then cleaved into 3×3 mm pieces and epoxied to Cu specimen mounts. Further thinning was accomplished by jet etching the substrate side of the specimen in 2% Br_2 in methanol. A simple jet polisher was constructed for the sample preparation as detailed in the appendix. In later work, an etch solution consisting of 100:1 $HCl:H_2O_2$ at 25°C was found to be just as effective and easier to handle than Br_2 in methanol. Observations were made with a JEOL 1200EX microscope.

Figure 4.11 is a planar TEM image of the GaAs/InGaAs interface of the 400°C ion-damaged material. At the bottom is a small portion of one of the implanted channels. It seems to consist of clusters of material and tangles of dislocations at the edge. The TEM of the undamaged region clearly shows what was suspected from the CL information: that the misfit dislocations form overwhelmingly in only one direction ($[1\bar{1}0]$) and they appear to nucleate at one edge of a damaged channel and glide all the way across to another.

The TEM images also show that the damaged regions do indeed stop misfit dislocations from gliding across the wafer interface; this is especially easy to show in the [110] direction since the low density ensures that dislocations running into the edges on either side a channel do not precisely line up by chance. The expected path of a misfit dislocation can be extrapolated from one side of an ion-damaged channel to the other. There were no misfits "re-appearing" on the other side of a channel in

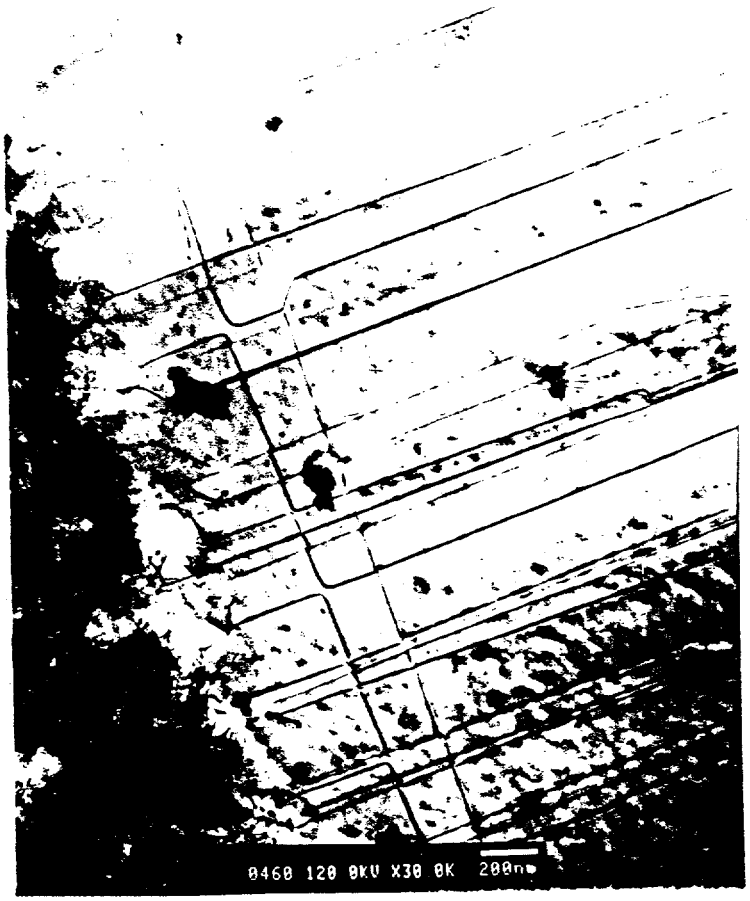

Figure 4.11: A Planar TEM image of misfit dislocations at the InGaAs/GaAs interface of 400 °C material. The region on the left is an ion-damaged channel.

one sample that was studied closely.

The few misfits that did run in the [110] (low density) direction propagated as much as tens of μm's in some cases, indicating that glide of those dislocations was not retarded significantly.

Figure 4.12 presents a TEM view of a channel edge that was oriented so that it did not nucleate misfits. Although the damaged channel material is in intimate contact with undamaged material, no misfit dislocations are formed. For example, dislocations do not glide from the edge and become blocked by some obstruction such as a perpendicular misfit dislocation a short distance away. Triangular planar defects are also present only at these non-nucleating edges.

Selected area diffraction images of the ion-damaged channels reveals that they do consist of single crystal material (Figure 4.13). The diffraction spots are actually closely spaced pairs of spots if Figure 4.13 is closely inspected. One suggested explanation of this phenomena is that these are satellite peaks formed by the modulation of lattice diffraction by small crystallites. The peak spacing is consistent with the small dimension of the cigar shaped features seen in Figure 4.3. In any case, the material that grew in the channel is not amorphous or for that matter polycrystalline (in a strict sense). However, the contrast in the TEM images clearly indicate that many defects are present in the channels.

The dislocation density estimated from TEM for the 400 °C material is about $70,000 \pm 10,000$ cm^{-1} in the [1$\bar{1}$0] direction and much less than 10,000 cm^{-1} in the [110] direction.

An analysis of a representative region was made at near two beam conditions

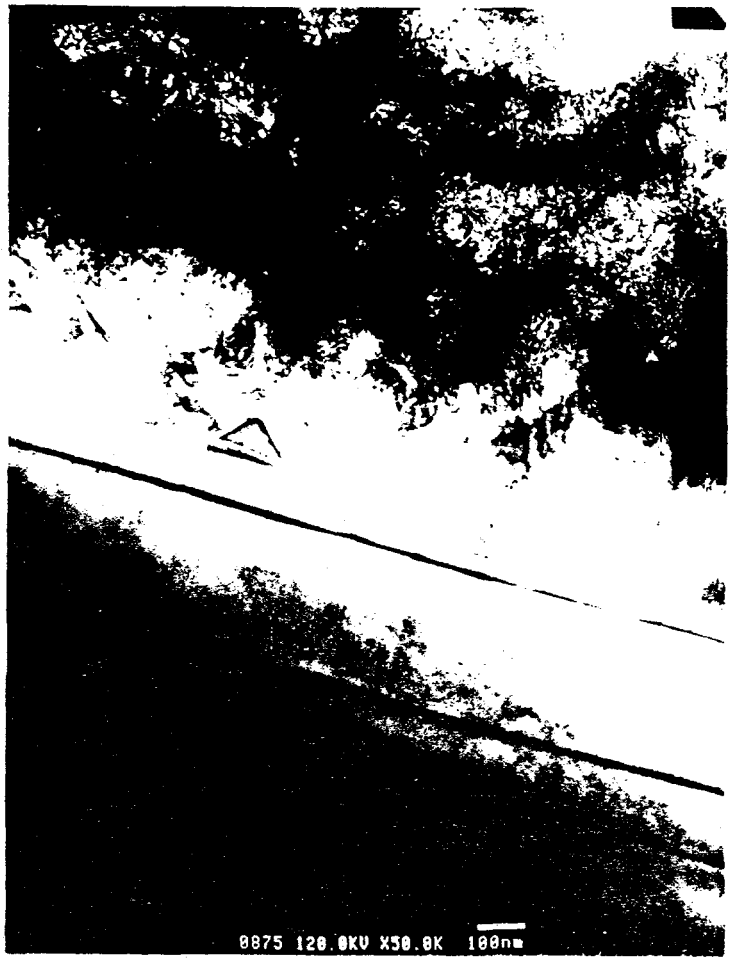

Figure 4.12: A Planar TEM image of the region near a channel that did not nucleate misfit dislocations. The ion-damaged region is on top.

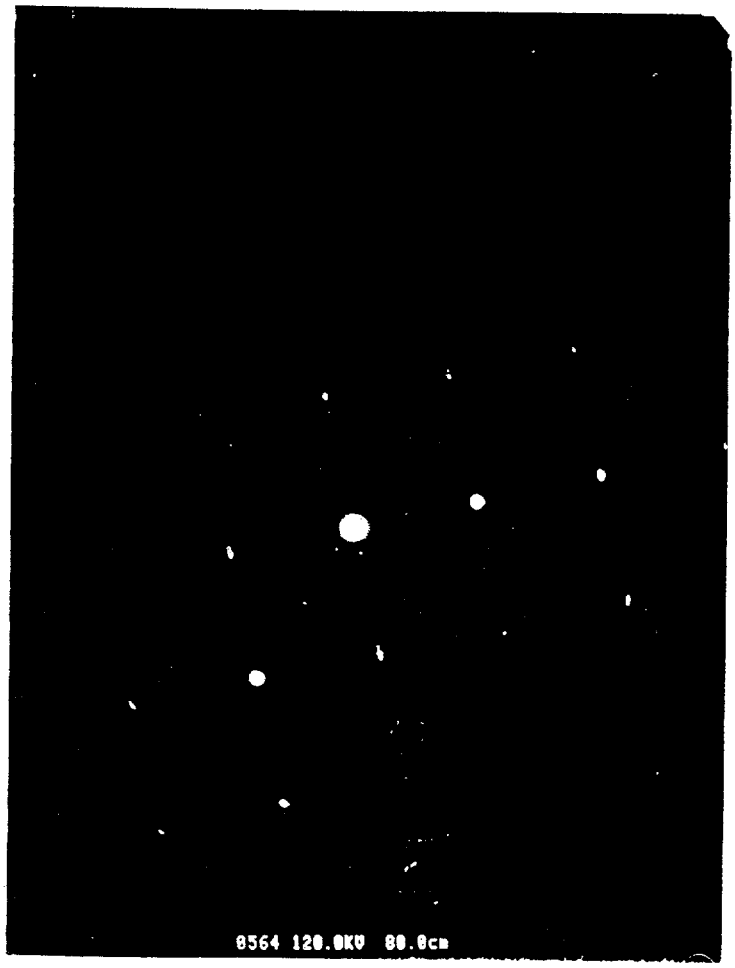

Figure 4.13: A selected area diffraction pattern of material in an ion-damaged channel.

Figure 4.14: TEM image of one region of ion-damaged material at the 220 two-beam condition.

for the 220, $2\bar{2}0$, $\bar{2}42$, $2\bar{4}2$, $4\bar{2}2$, and $\bar{4}22$ Bragg reflections, which should uniquely show loss of contrast for each 110 type Burgers vector (with a line direction, u, of $\langle 1\bar{1}0 \rangle$) since both $\vec{g} \cdot \vec{b}$ and $\vec{g} \cdot \vec{b} \times \vec{u}$ are zero [HHN+65]. Unfortunately, assigning a Burgers vector to a dislocation in GaAs is much more complicated than that; the anisotropy of the elastic constants and the effects of dissociation are factors that make the two conditions above inapplicable [DC87]. Another practical problem was that thickness fringes in the material changed the contrast of the region considerably as the specimen was tilted. It was difficult to simultaneously obtain a suitable two beam condition and ensure that the region of interest was not in a dark fringe (with little contrast).

Figures 4.14 through 4.19 are typical TEM images of one sample region at the six different beam conditions. Three contaminant particles on the left hand side of Figure 4.14 serve as fiduciary marks. It was found that two of these particles rest on opposite sides of the specimen (notice the change in relative positions in Figures 4.14 and 4.18). The sample thickness, simply estimated from this information, was about 100 nm thick.

In spite of the difficulties of the Burger's vector analysis, some conclusions can be drawn from the study. The Burgers vectors of these dislocations are mostly 60° type. In some cases, a particular Burgers vector could not be assigned since contrast was lost in more than one condition or at none of the conditions. An example of one assignment is the dislocation labeled A in Figure 4.14. Note that it is not found in 4.17. Similarly, dislocation B disappears in figure 4.18. The sign of the Burger's vector is determined by assuming that the misfit dislocations would not be there if

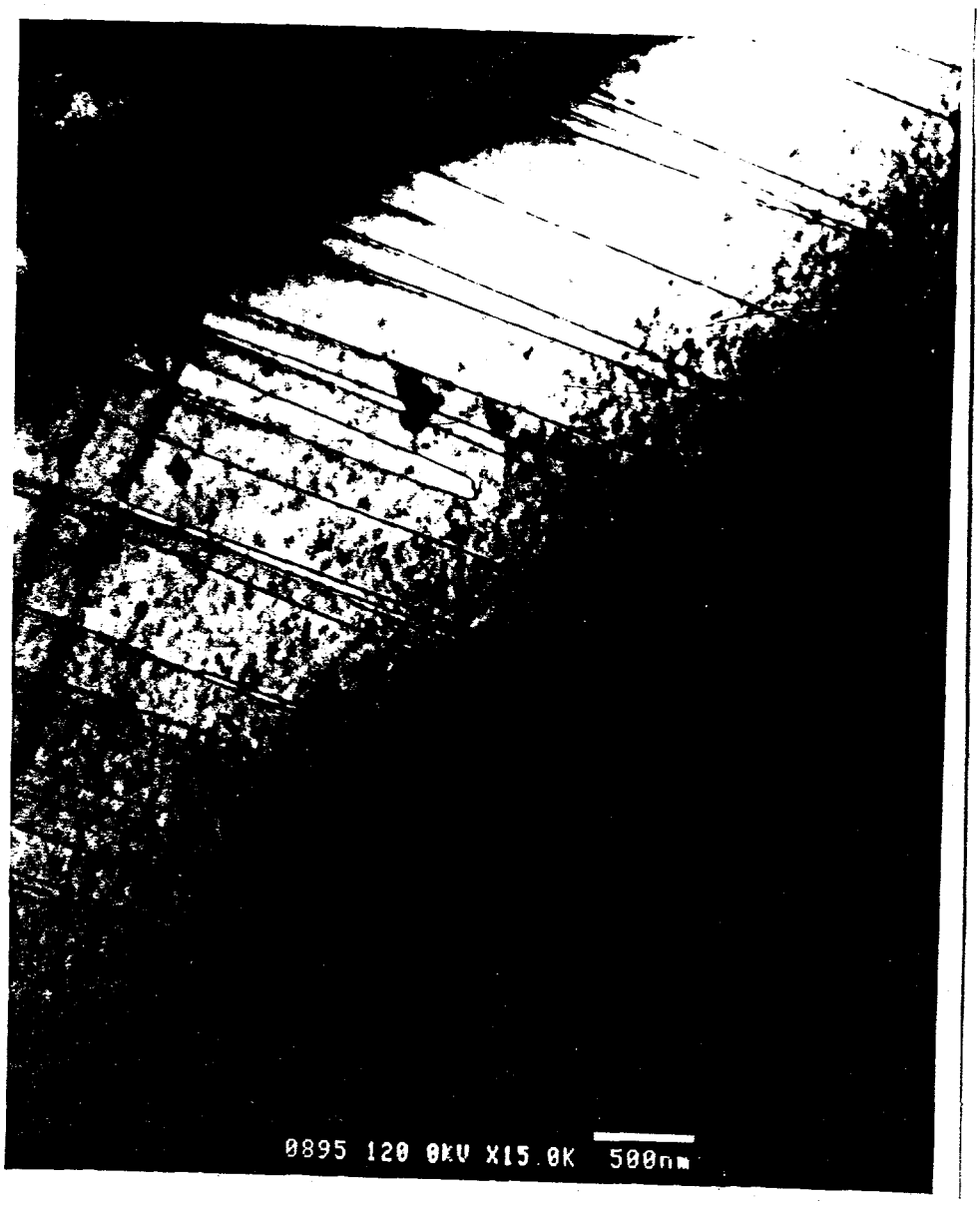

Figure 4.15: TEM image of one region of ion-damaged material at the $2\bar{2}0$ two-beam condition.

Figure 4.16: TEM image of one region of ion-damaged material at the $\bar{2}42$ two-beam condition.

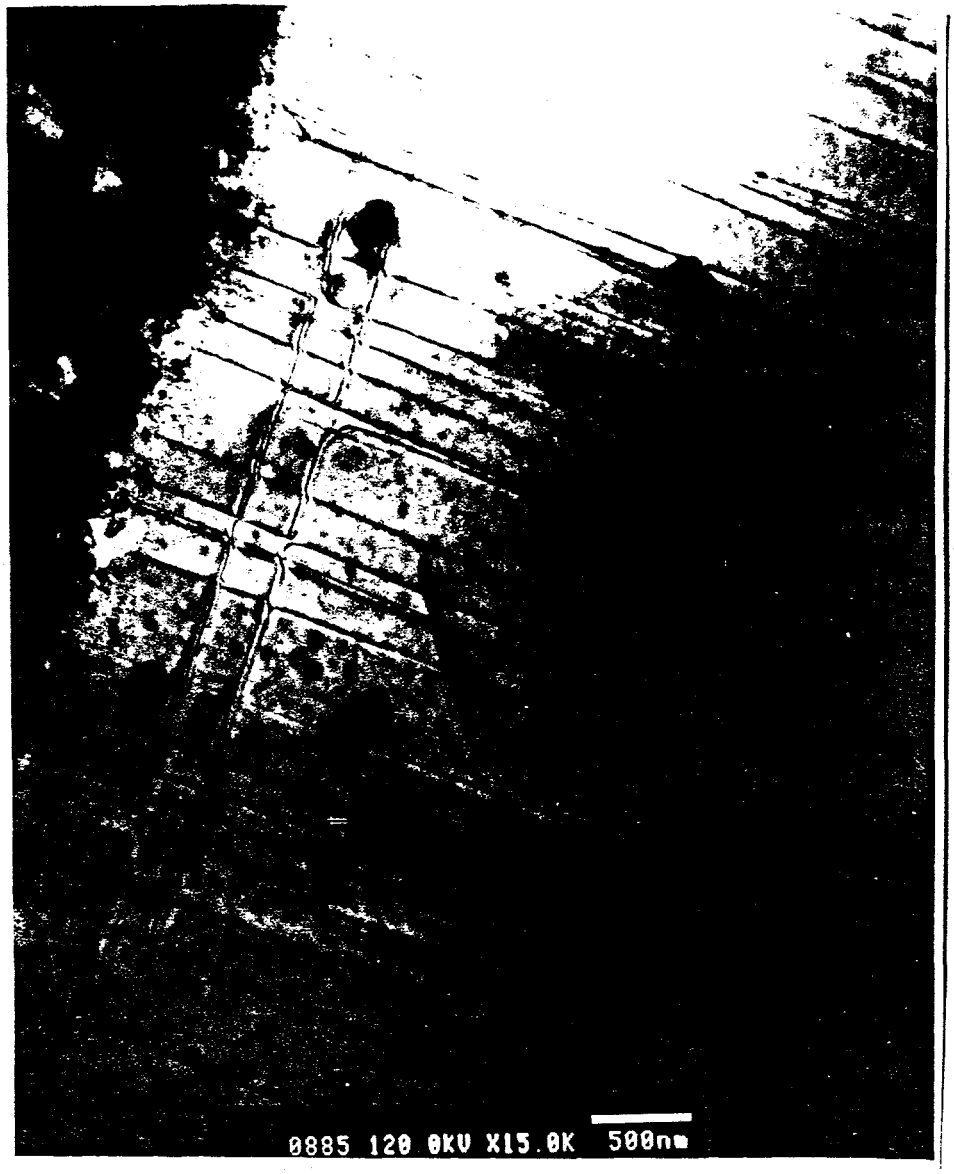

Figure 4.17: TEM image of one region of ion-damaged material at the $2\bar{4}2$ two-beam condition.

Figure 4.18: TEM image of one region of ion-damaged material at the $4\bar{2}2$ two-beam condition.

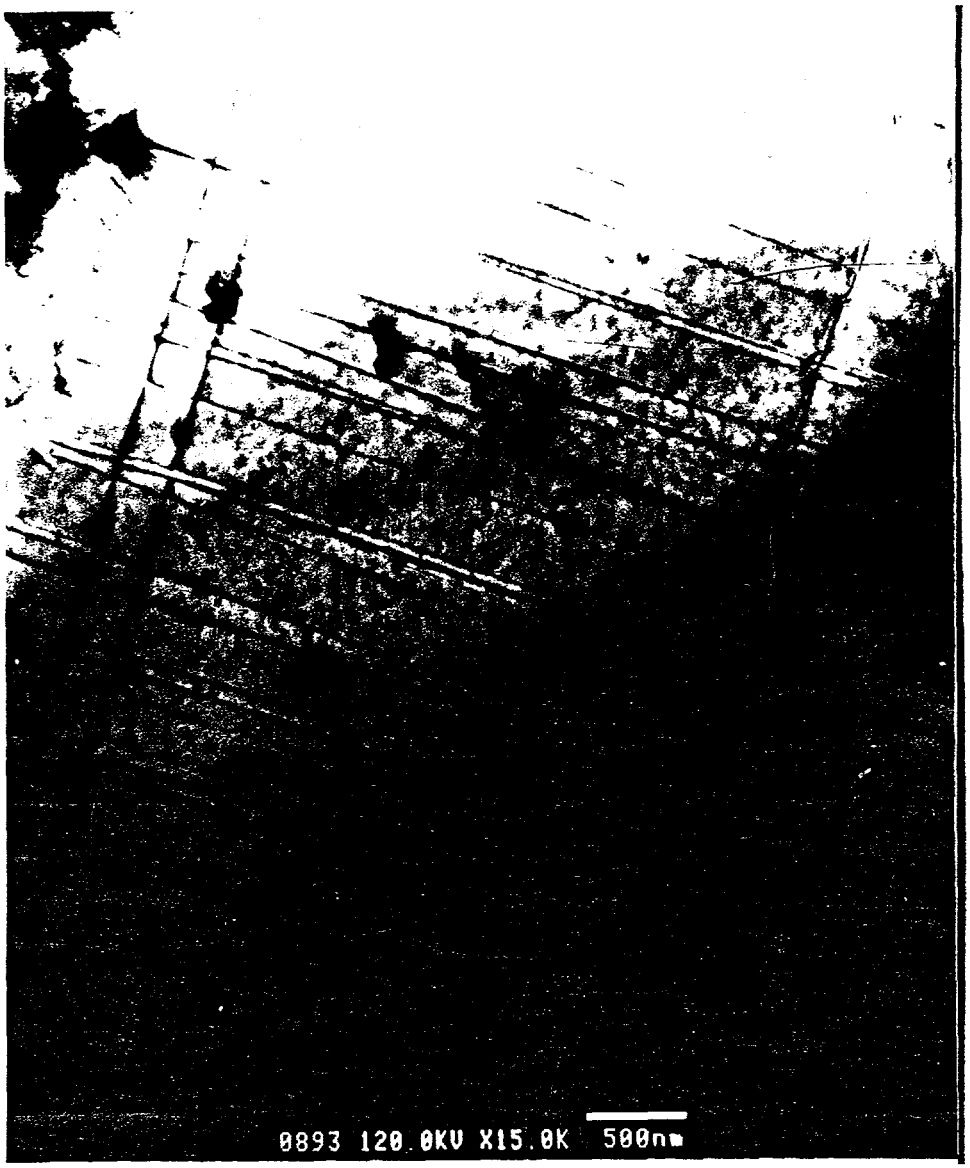

Figure 4.19: TEM image of one region of ion-damaged material at the $\bar{4}22$ two-beam condition.

they did not relieve some epitaxial layer strain. This condition sets the sign of the edge component of the dislocations.

The remaining $\approx 10\%$ dislocations were clearly edge type, in line with the observations of other researchers [FAA+88,KCH+88]. The edge dislocations were particularly simple to assign since they completely lost all contrast at $\vec{g} \cdot \vec{b} = 0$. Dislocation C in Figure 4.14 disappears completely in 4.15, indicating that the Burger's vector is perpendicular to the line direction. Dislocation D also disappears completely in Figure 4.15 and is apparently formed by a reaction between two 60° dislocations above it in Figure 4.14. No screw dislocations were found - as expected since they cannot relieve misfit strain in cubic type lattices. This fact will be discussed later.

4.4.3 X-ray Diffraction

X-ray diffraction rocking curves were obtained from a collimated Cu target tube attached to a precision goniometer.[3] The sample was attached to the goniometer axis with a barrel holder. Asymmetric reflections were obtained by attaching a modified wafer mount that is oriented 35.5° to the normal of the usual wafer surface. The mount was made so that a $\langle 110 \rangle$ cleaved edge of a substrate was aligned parallel to the x-ray plane. The x-rays were detected by a wide angle detector and the x-ray counts were processed through timer/counter circuitry. X-ray count data was taken every 0.01° for 40 seconds.

X-ray diffraction rocking curves for the 004, 224, and $2\bar{2}4$ Bragg conditions for the ion-damaged material grown at 400°C are shown in Figures 4.20, 4.21, and 4.22,

[3]The instrument was made available courtesy of Professor Boris Batterman of the Applied and Engineering Physics department at Cornell University.

respectively. The large pair of peaks in all three correspond to the Cu $K\alpha_1$ and Cu $K\alpha_2$ Bragg reflections of the GaAs substrate. The smaller peak or peaks are the InGaAs Bragg conditions for those x-ray wavelengths. Note that the rocking curves in 4.21 and 4.22 are not the same; the unique strain relief caused by the misfit dislocation asymmetry yields different inter-planar spacings and planar tilts in the different $\langle 110 \rangle$ directions (which influence the 224 reflections). Another important difference is that the peak in Figure 4.22 is much broader than that in Figure 4.21 - indicating that the interplanar spacing and tilt in 4.22 varies more than 4.21.

4.4.4 Rutherford Backscattering and Ion Channeling

Rutherford Backscattering (RBS) and ion channeling were carried out with 3 MeV He^4 ions using the 1.0 and 1.7 Mev accelerators at Cornell University. The thicknesses of the epitaxial layers were 350 ± 20 nm and the compositions were $5 \pm 1\%$ InAs for the samples studied, according to RBS results. The ion-damaged 400°C RBS measured thickness is consistent with the SEM information.

Ion channeling was used to measure the difference between the $\{111\}$ plane tilts of the epitaxial layer and the substrate. The material was patterned and chemically etched so that the surface consisted of 100 μm squares of epitaxial layers and exposed substrate in a checkerboard pattern. Exposing the substrate was necessary to measure the GaAs $\{111\}$ plane tilt angle without beam steering effects caused by the epitaxial overlayer. Simultaneous data collection of both the InGaAs layer and GaAs substrate were made in 0.05° increments during each scan.

Ion channeling measurements of the $\{111\}$ type angles of the substrate and In-

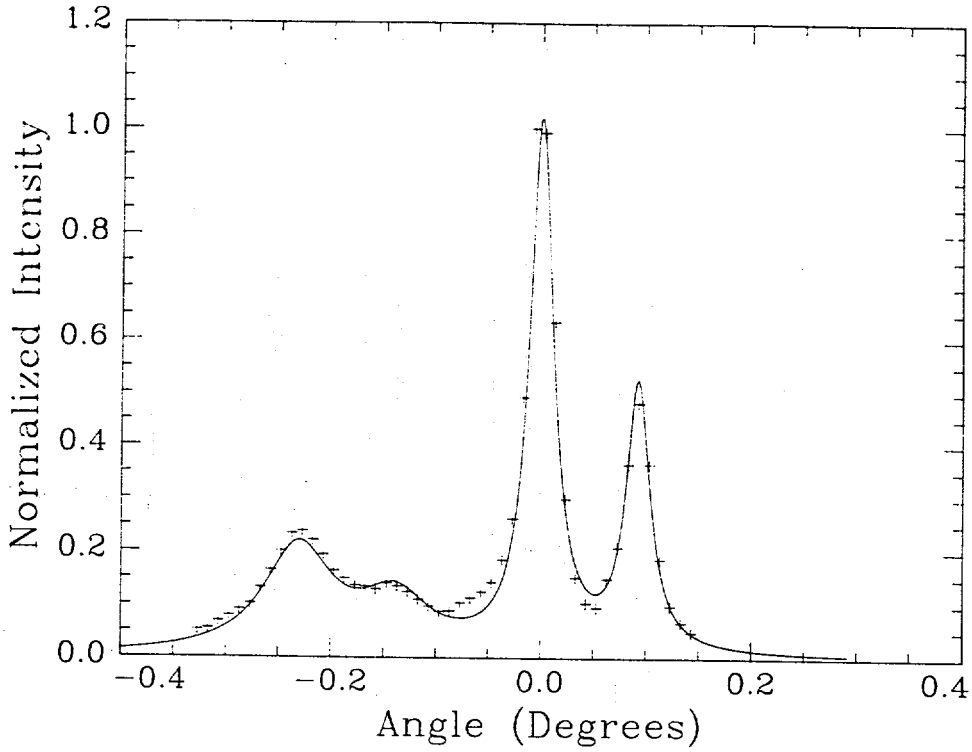

Figure 4.20: X-ray diffraction rocking curve of 400°C ion-damaged material at the 004 reflection. The crosses are actual data points while the solid curve is a fit of the data.

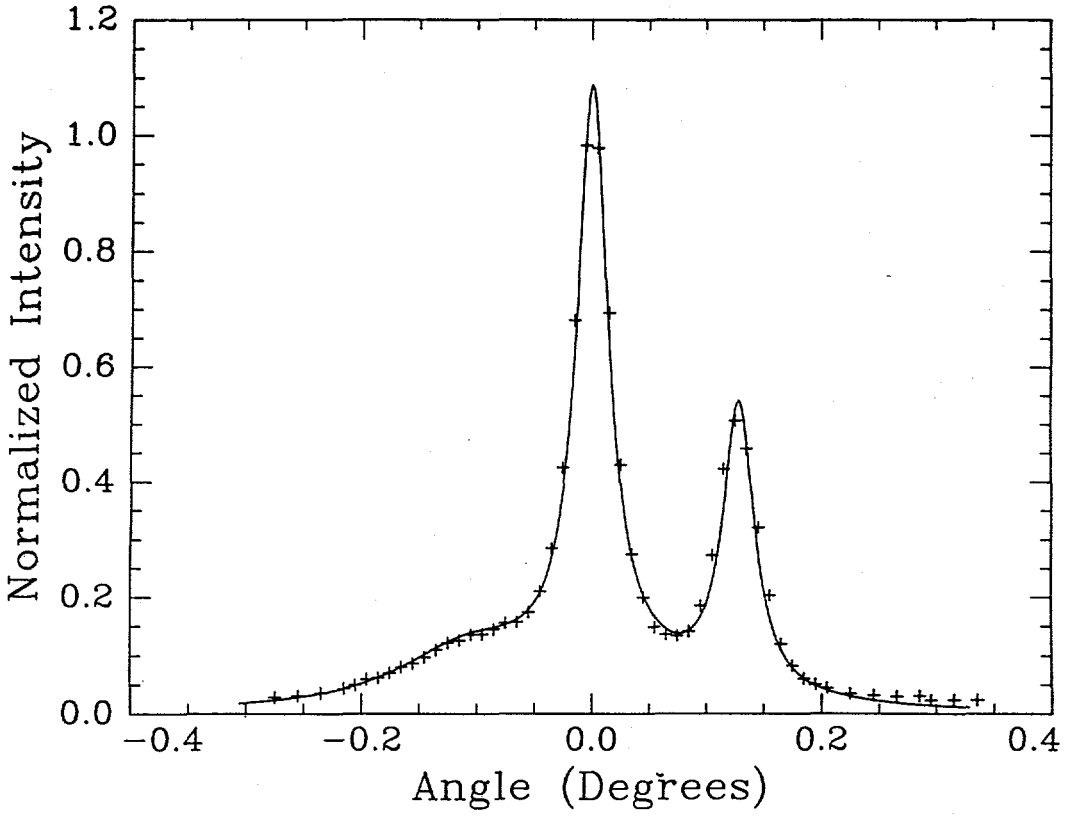

Figure 4.21: X-ray diffraction rocking curves of 400°C ion-damaged material at the $2\bar{2}4$ reflection. The crosses are actual data points while the solid curve is a fit of the data.

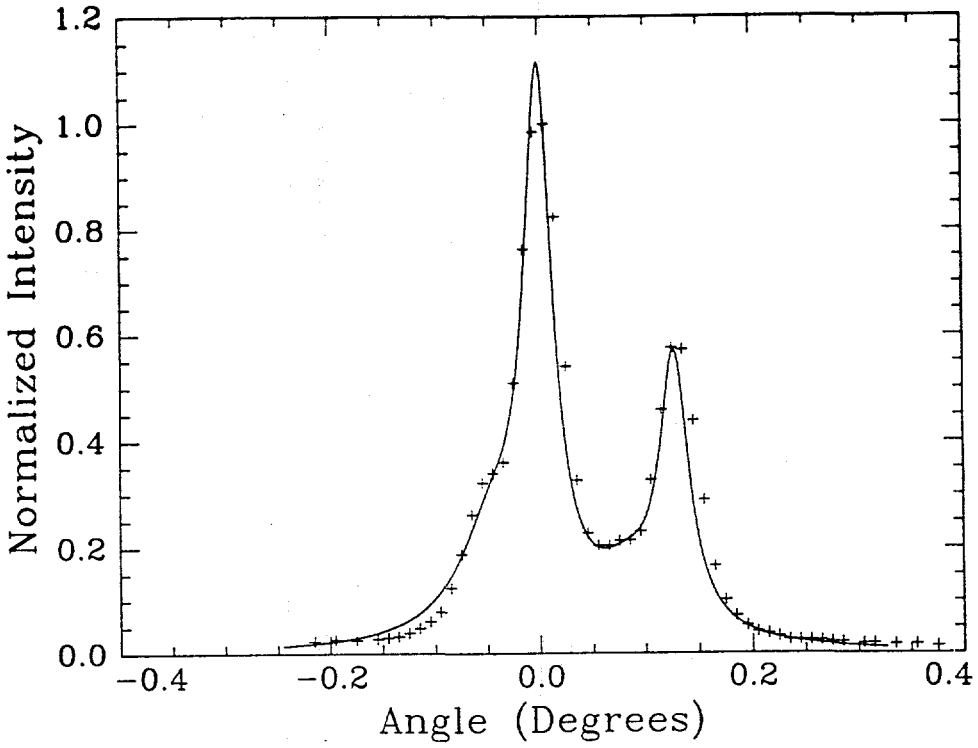

Figure 4.22: X-ray diffraction rocking curves of 400°C ion-damaged material at the 224 reflection. The crosses are actual data points while the solid curve is a fit of the data.

GaAs, although statistically noisy, clearly show different tilts consistent with the x-ray rocking curve data. Figure 4.23 and 4.24 are plots of backscattering intensity versus angle as the 400°C ion-damaged InGaAs is tilted through a {111} planar channel in a direction perpendicular to those planes. The intensities of the epitaxial layer were normalized to make the comparison simpler. The change in angles between the substrate and epitaxial layer are 0.05° for the (111) plane and 0.15° for the $(1\bar{1}1)$ plane. In both cases, the angles of the InGaAs plane normals were farther from [001] than the substrate plane normals.

4.5 Discussion

4.5.1 Epitaxial Layer Strain

Calculations show that the x-ray diffraction data and the TEM dislocation density estimates are consistent. The solid curves drawn in Figure 4.20, 4.21, and 4.22 are the predicted peak positions for a $In_{0.05}Ga_{0.95}As$ layer with 70,000 60° type dislocations per cm lying in the $[1\bar{1}0]$ direction and none in the [110] direction (the results of TEM). The predicted curves were calculated by a program ROCKIT.C, based on the following equations that determine the relative position of the peaks (the program and a derivation of these equations are described in Appendix A):

$$\Delta\theta = \tan\theta\left(Q_1\epsilon_{1\bar{1}0} + Q_2\epsilon_{110} - qx\right) \tag{4.1}$$

$$\Delta\varphi = \cot\varphi\left(\left(Q_1 - \frac{c_{12}}{c_{11}}\right)\epsilon_{1\bar{1}0} + \left(Q_2 - \frac{c_{12}}{c_{11}}\right)\epsilon_{110}\right) \tag{4.2}$$

$$Q_1 = \frac{l^2\left(\frac{2c_{12}}{c_{11}} + 1\right) + 2hk}{2\left(h^2 + k^2 + l^2\right)} - \frac{1}{2} \tag{4.3}$$

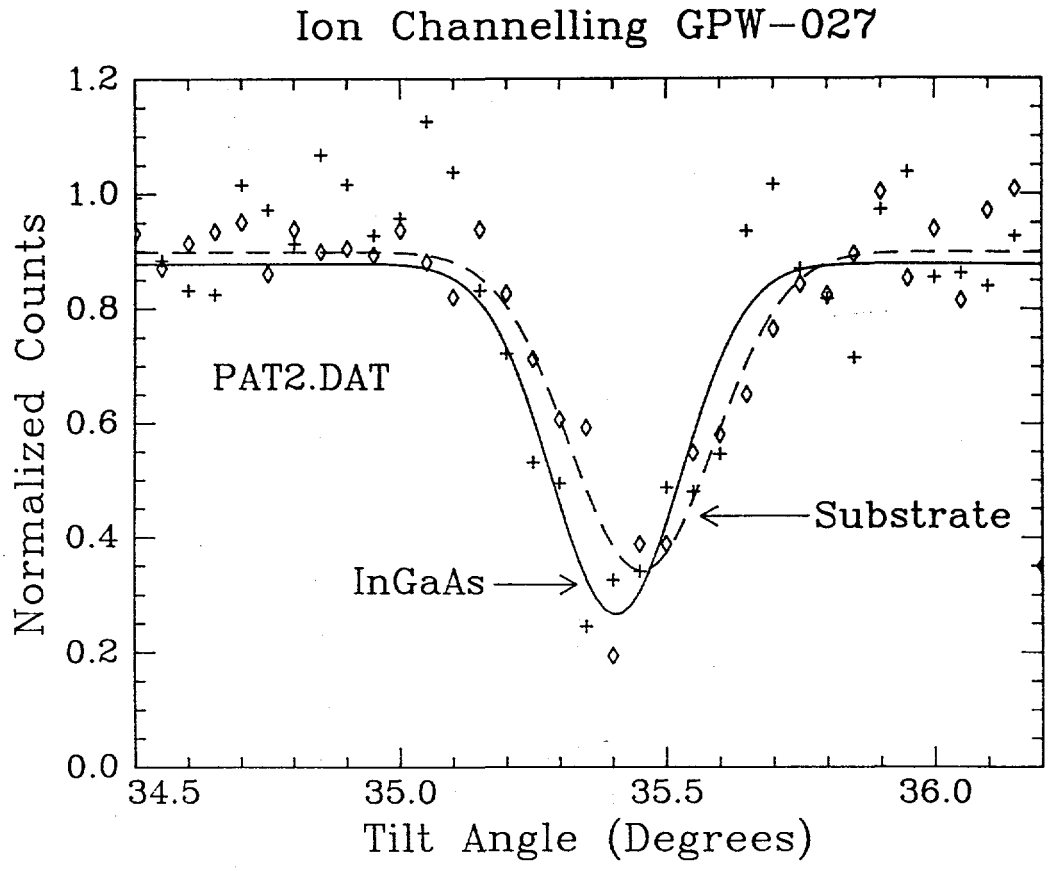

Figure 4.23: Ion channeling plots of backscatter intensity vs. tilt angle for a 400°C ion-damaged substrate in the (111) plane. The solid curve is a fit to the substrate channeling data while the dashed curve is a fit to the strained epitaxial layer.

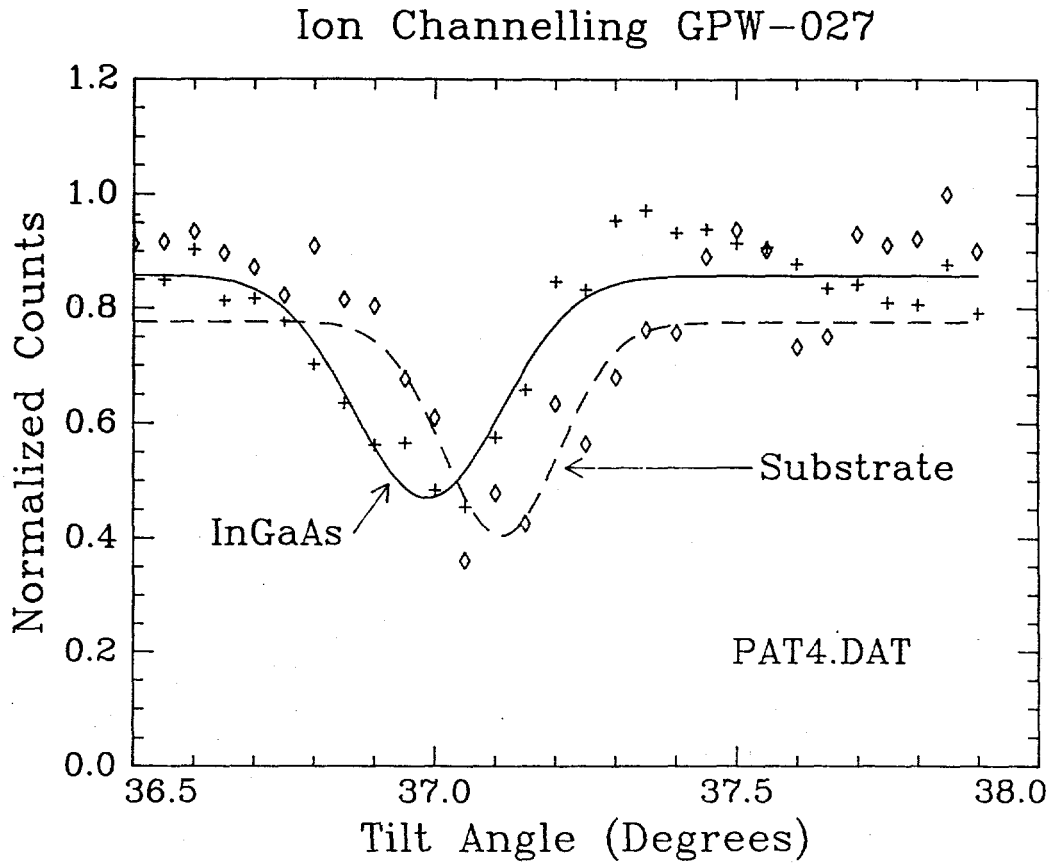

Figure 4.24: Ion channeling plots of backscatter intensity vs. tilt angle for a 400°C ion-damaged substrate in the $(1\bar{1}1)$ plane. The solid curve is a fit to the substrate channeling data while the dashed curve is a fit to the strained epitaxial layer.

$$Q_2 = \frac{l^2\left(\frac{2c_{12}}{c_{11}}+1\right)-2hk}{2\left(h^2+k^2+l^2\right)}-\frac{1}{2} \tag{4.4}$$

where θ is the Bragg angle of the substrate, φ is the tilt of the h,k,l lattice plane relative to the (001) plane, $\Delta\theta$ is the difference between the Bragg angle of the substrate and the strained epitaxial layer, and $\Delta\varphi$ is the difference between the lattice plane tilts of the substrate and strained layer. The terms c_{11} and c_{12} are the elastic compliance coefficients for the epitaxial layers. The in-plane epitaxial layer strains, $\epsilon_{1\bar{1}0}$ and ϵ_{110} are the same strain tensor components described in Chapter 2. As Equations 2.12 and 2.13 imply, only the edge component of the Burgers vector that lies in the interface plane is considered for strain relief.

The x-ray apparatus is configured such that the tilt angle change and the Bragg angle change act in opposite directions. The net difference between the epitaxial layer x-ray peak and the substrate peak is $\Delta\Theta - \Delta\varphi$.

The epitaxial layer and substrate peak heights and widths of the model curves were adjusted freely; they have no theoretical basis, although the $K\alpha_1$ and $K\alpha_2$ heights are kept at a ratio of 2:1 and the angular distances between the two wavelengths are set. The peaks were assumed to be Lorentzian in shape. The close match between the predicted peak positions and the rocking curve data supports the validity of the TEM dislocation density findings.

The ion channeling data also follows the expected trends based on the x-ray and TEM information. The epitaxial layer $(1\bar{1}1)$ plane is $0.15 \pm 0.03°$ closer to the wafer normal than the substrate plane. The predicted value using the RBS composition and TEM misfit densities is 0.17°. The (111) InGaAs plane is more relaxed (only

$0.05 \pm 0.03°$ difference between the planes) since the misfits lying in the $[1\bar{1}0]$ direction relieve stress along the [110] direction. The predicted value is 0.11°.

The x-ray, ion channeling and TEM results all lead to a consistent interpretation of how strain is relieved by misfit dislocations at the InGaAs/GaAs interface as long as it is assumed that only the in-plane edge component of the Burger's vector relieves strain. Kavanaugh et al. have asserted that misfit dislocations that lie in only one direction can relieve strain in both interface $\langle 110 \rangle$ directions [KCH+88]. This cannot occur however, since the compressive or tensile strain tensor component that lies in the line direction of a dislocation is always zero, independent of the Burgers vector. This means that there can be no relief of compressive strain of the material in the line direction. Only by adding a half plane of atoms along the line direction (the edge component) can a dislocation relieve mismatch strain, and only compressive strain in the direction *perpendicular* to the dislocation line. This fact is implied by Matthews et al. development of dislocation glide forces and by the development of the strain tensor components in Chapter 2 [MML70]. This result is only true for cubic lattice substrates and epitaxial layers. Matthews describes an example where pure screw dislocations relieve mismatch in non-cubic crystals [Mat75b].

Figure 4.25 is a sketch of the dislocations shown in TEM images in Figures 4.14 through 4.19 and a best estimate of their Burgers vectors. All four dislocation Burgers vectors must be present in equal quantities so that the screw and out of plane edge components cancel out on average. If this were not so, the epitaxial layer would be tilted or twisted relative to the substrate lattice. Although a very small sample has been examined, the evidence suggests that all four 60° dislocation types

are at least present.

4.5.2 Dislocation Densities

It is interesting to note that although the ion-damaged edges appear to create great numbers of dislocations, especially the 400 °C grown material, the density is not even close to the equilibrium value. In order discuss the misfit densities further it is convenient to develop critical thickness theory on the basis of strain energies as in Chapter 2. The total strain energy (E_{tot}) in the epitaxial layer is assumed to be the sum of the strain energy of each dislocation (E_{dis}) and the mismatch strain energy (E_{mis}). By minimizing E_{tot}, given by Equation 2.17, with respect to misfit dislocation densities, the equilibrium density (ρ_{eq}) can be calculated. For the case in which dislocations form in only the $[1\bar{1}0]$ direction,

$$\rho_{eq} = \frac{qx\,(1+\nu)}{b\sin\theta\cos\phi} - \frac{1-\nu\cos^2\theta}{8\pi h\sin^2\theta\cos^2\phi}\cdot\ln\left(\frac{h\alpha}{b}\right). \tag{4.5}$$

Figure 4.26 is a plot of how the energy per unit volume of epitaxial material (made dimensionless by dividing by the shear modulus μ) varies with misfit density for $In_{0.05}Ga_{0.95}As$ of various thicknesses. Note that the energy vs. dislocation density plot in Figure 2.6 is based on equal densities of misfit dislocations in both perpendicular directions while Figure 4.26 is based on a non-zero misfit dislocation density in only one direction. Also labeled is the actual misfit density found for the 400°C ion-damaged material. Note that there is still a considerable amount of strain energy remaining. The equilibrium misfit dislocation density according to Equation 4.5 is 200,000 cm^{-1} while TEM and x-ray information show that the actual density is 70,000 cm^{-1}.

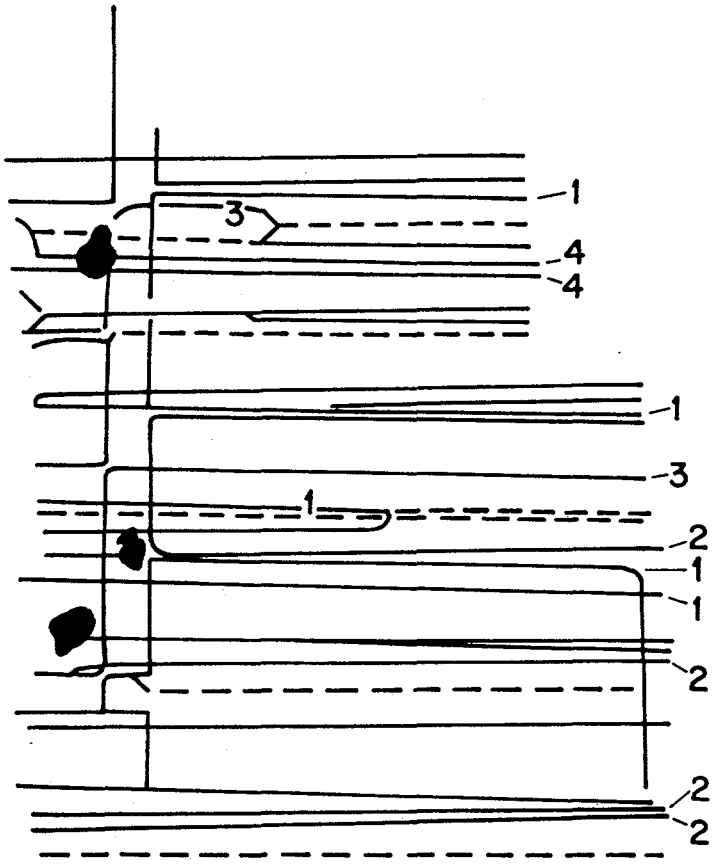

Figure 4.25: A schematic diagram of the dislocations shown in Figures 4.14 through 4.19 and an assignment of several of them. The dashed lines are edge dislocations. Dislocations labeled 1, 2, 3, and 4 have Burgers vectors of $a/2[\bar{1}01]$, $a/2[0\bar{1}1]$, $a/2[\bar{1}0\bar{1}]$, and $a/2[0\bar{1}1]$, respectively.

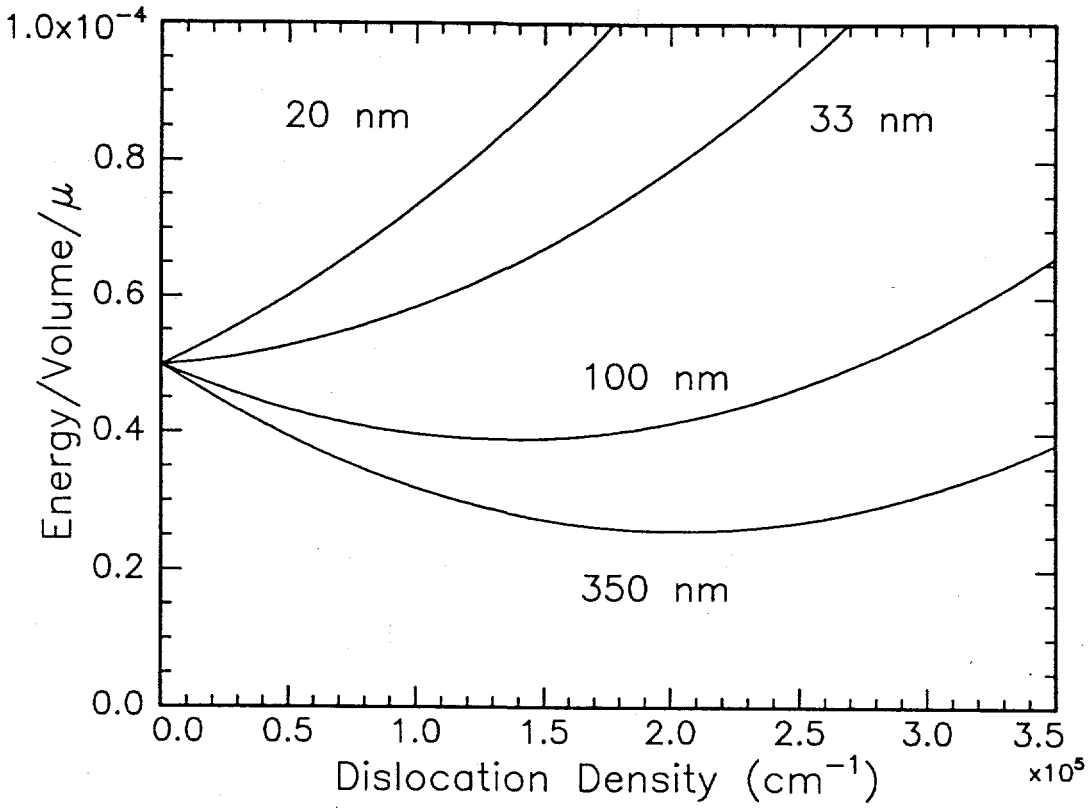

Figure 4.26: A plot of energy per unit volume of strained epitaxial material vs. the misfit dislocation density in the $[1\bar{1}0]$ direction.

Calculations of the interaction energy between adjacent dislocations shows that it is too small to have an important influence on the equilibrium density at the observed average defect spacing. Calculations show that at the average 150 nm spacing, dislocations of the same Burger's vector repel each other by only a small amount compared to the driving force to relieve strain in the epitaxial layer.

One possible reason for the discrepancy between the TEM dislocation density and the estimated equilibrium density that has been studied is frictional forces. These frictional forces act on the gliding dislocation segment as it forms a misfit dislocation in the interface plane. The equation for the total energy, Equation 2.17, in an $L \times L$ epitaxial area with dislocation density ρ, is modified by the frictional term as follows:

$$E_{total} = E_{dis} + E_{mis} + F_{f1} L^2 \rho \tag{4.6}$$

where F_{f1} is a dimensionless constant. The new term is the amount of energy expended per unit length of misfit dislocation threading segment glide. In this case, friction is caused by an interaction that is independent of the length of the threading segment that actually moves in the epitaxial layer. This frictional term also modifies the expected critical thickness since the extra energy cost of misfit formation changes the point where plastic deformation is favored over elastic strain. The new critical thickness is

$$h_{cf1} = \frac{b}{8\pi(qx)} \frac{1 - \nu\cos^2(\theta)}{(1+\nu)\sin(\theta)\cos(\phi)} \ln\left(\frac{\alpha h_{cf1}}{b}\right) + \frac{F_{f1}}{2\mu b q x \sin\theta\cos\phi} \cdot \left(\frac{1-\nu}{1+\nu}\right). \tag{4.7}$$

If, on the other hand, the frictional force is caused by an interaction between point defects and the threading segment as it glides, then the number of point defects encountered and therefore the amount of energy expended is expected to be

proportional to the length of the threading segment and to the length of the dislocation path. As Figure 4.27 shows, the frictional energy is proportional to the area of the region traversed by the threading segment, with a proportionality constant F_{f2} (dimensionless). The critical thickness becomes

$$h_{cf2} = \frac{b}{8\pi}\frac{1-\nu\cos^2\theta}{(1+\nu)\sin\theta\cos\phi}\ln\left(\frac{\alpha h_{cf2}}{b}\right) \times \frac{1}{qx - F_{f2}\left(\frac{1-\nu}{1+\nu}\right)\cdot\frac{1}{2\sin\theta\cos\phi sin\phi}}. \quad (4.8)$$

If the TEM value of ρ is used (70,000 cm^{-1}) and assumed to be the equibrium density, then the critical thickness of $In_{0.05}Ga_{0.95}As$ would change to 220 nm for h_{cf1} and 95 nm for h_{cf2} — both are quite far from the estimate h_c = 35 nm given by Matthew's original equation. Other researchers have shown that Matthews' theory does predict the true critical thickness fairly well for InGaAs [Wen89,GCB+89], so the calculated glide friction effect is not a reasonable explanation for the discrepancy between ρ_{eq} and the actual density.

It must be concluded that if nucleation sources were available, more misfit dislocations would be found at the interface but even the ion-damaged channel edges can not nucleate enough dislocations to reach equilibrium. Other workers have shown that dislocation nucleation is a problem even with InGaAs grown on unpatterned substrates that have been severely furnace annealed [DAC+89]. Chapter 5 describes the effects of thermal annealing of InGaAs on patterned substrates; for some specimens, the dislocation density remained very low even after 850°C heat treatments.

Another interesting feature of the ion-damaged and etched materials is that misfit dislocations form in virtually one direction. The author believes that the asymmetry

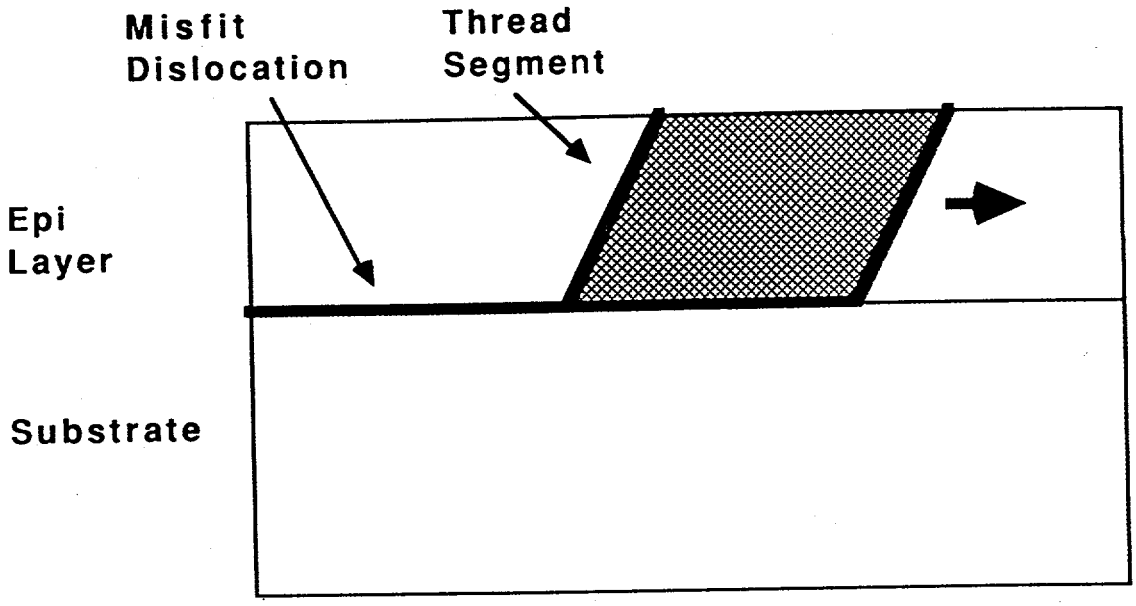

Figure 4.27: Schematic diagram describing one possible form of dislocation glide friction affecting the misfit dislocation glide segments. The grey area denotes region where the glide segment is in contact with a defect atmosphere. The frictional energy is proportional to this area.

in [110] and [1$\bar{1}$0] ρ's is related to the nature of the core structure (α and β type dislocations). In n-type material, Bruno et al. demonstrated that the glide velocity of a β or screw dislocation is orders of magnitude lower than an α type [DCC89]. Since α type dislocations relieve compressed epitaxial layer strain in the [1$\bar{1}$0] direction and β's relieve strain in the [110] direction, different effects caused by kinetics can be expected. If β and screw type dislocation glide is severely inhibited, then segments of these dislocations can be assumed to play no role in strain relief of n-type InGaAs. If so, then dislocation half loops formed at boundaries will only glide if they have both α type gliding segments and if they relieve strain. This is possible in only one direction, as the schematic diagrams in Figures 4.28 through 4.30 demonstrate. The ion-damaged channel edges both had the potential to emit gliding dislocation segments that left a misfit dislocation behind them, but only the channels that created α misfits in the [1$\bar{1}$0] direction were unimpeded by kinetics.

The few misfits that do occur in the low density direction can be formed by α threading dislocations that fold "backwards" to create a β misfit at the interface (see Figures 4.28, 4.29, and 4.30). The creation of β misfit dislocations from α segments does not appear to be considered for single strained layers before, although it is well established in dislocation loops and is implied in multilayer misfit structures [DCC89, Mat75b]. Since the β never moves, only the small α segment controls glide. The small segment that glides backwards should move at velocities similar to those α's that move forward in the perpendicular direction. TEM does indeed show that the few misfits that did form along the 110 moved distances comparable to those in the preferred direction.

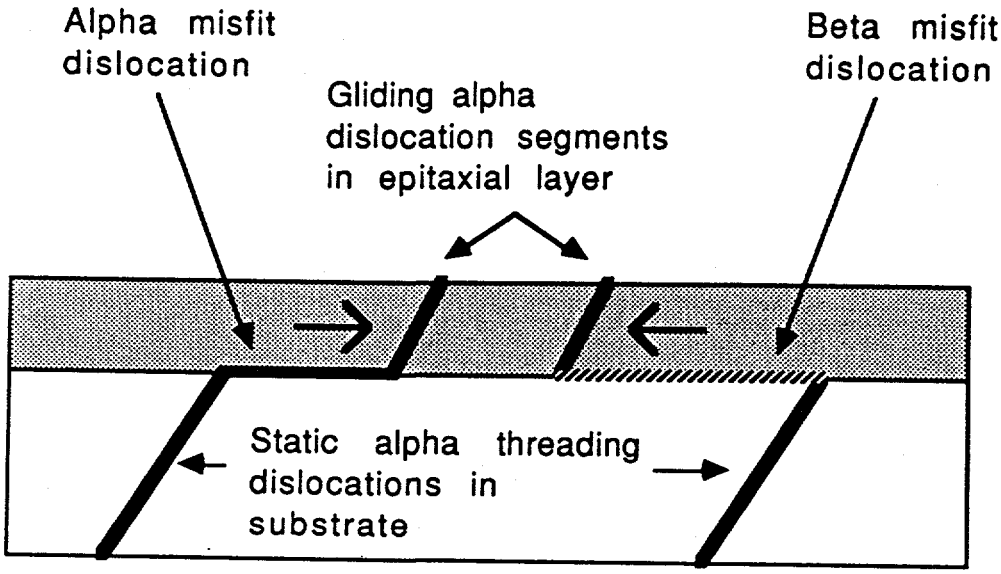

Figure 4.28: A schematic of misfit dislocation formation depicting gliding dislocation segments in a {111} plane. The dislocation on the left describes the meaning of "forward" glide of the small α segment in the epitaxial layer. The misfit dislocation formed is α type. The dislocation segment on the right glides "backwards" and must form a β dislocation.

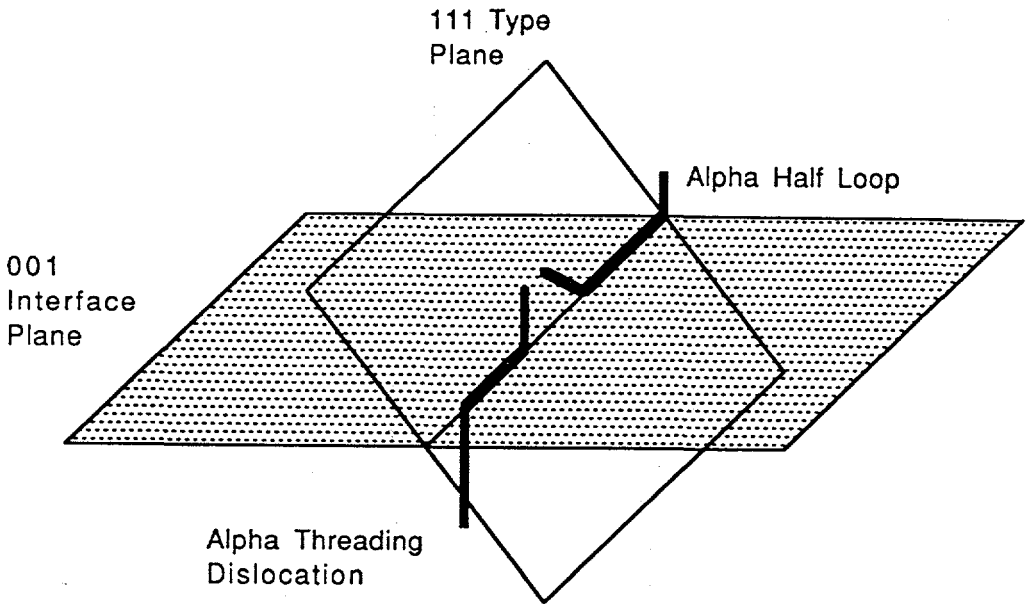

Figure 4.29: A schematic of misfit dislocation formation depicting how α threading dislocations and α segment half loops formed at the edges of ion-damaged channels can glide at the interface and form misfit dislocations in the $[1\bar{1}0]$ direction.

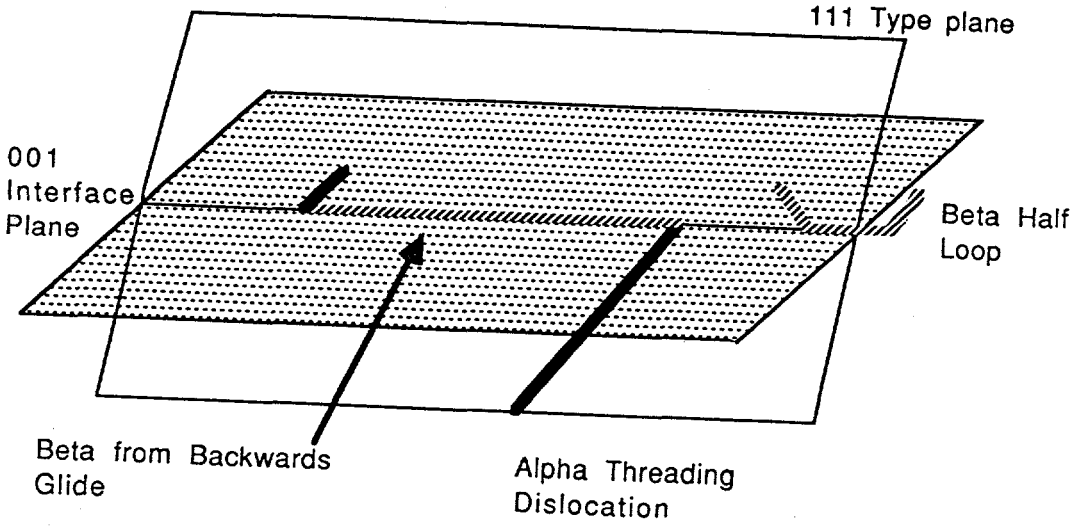

Figure 4.30: A schematic of misfit dislocation formation that shows an immobile β or screw segment half loop on the right. The few misfit dislocations that are observed in this direction can form by "backwards" glide of an α threading segment.

Another important point is the fact that the growth temperature has a strong influence on misfit nucleation, as can be seen from the comparison of CL images of 400°C and 500°C etched materials. It is clear that as the growth temperature is increased, the number of dislocations that nucleate decreases. As a matter of fact, etched material of comparable composition and thickness described by Fitzgerald et al. grown at 550°C on patterned substrates showed no signs of edge nucleation [FWP+89]. The reason for the change in nucleation ability with temperature may be connected with the geometry of the epitaxial growth at the edges of the etched trenches and is the subject of further study (See Chapter 6).

The growth temperature strongly influences the misfit densities of ion-damaged material as well. CL images plainly show that the 500°C material has many less misfit dislocations than the 400°C material. Unfortunately, higher temperatures also remove the misfit blocking ability of the ion-damaged channels.

Chapter 5

The Effect of Patterned Substrate Trench Depth on Misfit Dislocation Density

5.1 Introduction

As described in Chapter 2, misfit dislocations form either by glide of threading dislocations already existing in the substrate, or by surface defects that initiate the formation of dislocation loops which glide along the interface. Once formed, these misfit dislocations may have long mean-free paths in the interface. As outlined in Chapter 1, Fitzgerald et al. showed that by etching 2 μm deep gaps into a GaAs substrate before epitaxial growth of lattice mismatched InGaAs (at a thickness several times larger than the critical thickness) the misfit dislocation density (MDD) can be significantly reduced [FWP+89]. Etching the trenches in the substrate cre-

ated a discontinuous epitaxial layer, thus stopping misfit dislocations from gliding to adjacent areas (effectively reducing their mean-free path).

The drawback of the technique is that the resulting wafer is no longer planar, complicating device processing. The ion damage technique described in the previous chapter was one attempt to to create a planar barrier by selectively ion damaging a GaAs substrate prior to strained layer growth. Although the misfit dislocations were indeed stopped by the ion damaged *channels*, these channels acted as copious nucleation sources as well, defeating the original purpose.

In this chapter we investigate how the depth of these isolating trenches affects the average misfit dislocation density at the InGaAs/GaAs interface and determine the minimum depth necessary to stop dislocation glide in low pressure organo-metallic chemical vapor deposited (OMCVD) material.

5.2 Preparation and Characterization

GaAs substrates (Sumitimo), Si doped, with nominal etch pit densities below 5×10^3 cm^{-2} were used in this study. The wafers were degreased and etched in 5:1:1 H_2SO_4:H_2O_2:H_2O to remove about 10 μm of material. A 200 nm plasma enhanced chemical vapor deposited SiO_x layer was immediately grown on it to be used as an etch mask. Channels were opened up in the oxide by standard photolithographic techniques and the exposed GaAs was etched by a reactive ion etching (RIE). The etching conditions used are outlined in Chapter 3 and follow the basic recipe described by Scherer et al. with the addition of Cl_2 to the gas mixture to increase the etch rate and selectivity [SCB87]. These conditions were found to yield smooth

and nearly vertical sidewalls. Portions of the wafers were cleaved off and etched to various depths, varying from 100 to 1000 nm. The resulting wafer surface consisted of 200×200 μm^2 squares separated by trenches 10 μm wide.

As described in Chapter 3, contamination control is believed to be a critical factor in strained layer growth on patterned substrates. Special care was taken so that a complete series of specimens would be processed under nearly identical conditions.

Epitaxial growth was carried out in a Japan Oxygen reactor. A GaAs buffer layer and an InGaAs strained layer were grown, each S doped to about $5 \times 10^{18} cm^{-3}$. The InAs fraction was varied from 4 to 8%. The buffer layer was grown at two thicknesses, 100 and 300 nm. The InGaAs layer was grown at 300 and 600 nm. Tables 5.1 and 5.2 list the range of etch depths, In content and layer thicknesses used in this study.

The InGaAs layer cross sections were imaged by cleaving and staining the wafers and observing them in a scanning electron microscope (SEM). Because of the high doping level of the epitaxial layers and the low In content, staining the samples by wet etching techniques was not consistently effective. Instead, the selectivity of InGaAs to GaAs in Cl_2 based plasmas was exploited. Cooper et al. have shown that InGaAs can act as a stop etch layer in a $SiCl_4$ plasma because of the $InCl_3$ etch product has an extremely low vapor pressure at room temperature [CSM89]. Chlorine gas was used in the present case, since it was a readily available Cl source.

The specimens were coated with a thin (50 nm) silicon dioxide layer to protect the epitaxial layer during preparation. The wafer backs were chemo-mechanically polished using the apparatus described in Chapter 4, to a thickness of about 200 μm, since it was found to improve the quality of the cleaved edges, especially near the

Table 5.1: List of patterned InGaAs/GaAs specimens prepared for the trench depth study.

Sample ID	In Fraction (x)	Thickness (nm)	Depth (nm)	Comments
1-A	0.04	300	150	300 nm buffer
1-B	0.04	300	230	
1-C	0.04	300	280	
1-D	0.04	300	330	
2-E	0.04	300	460	
2-F	0.04	300	500	
2-G	0.04	300	570	
2-H	0.04	300	620	
3-A	0.04	600	150	
3-B	0.04	600	230	
3-C	0.04	600	280	
3-D	0.04	600	330	
4-E	0.04	600	460	
4-F	0.04	600	500	
4-G	0.04	600	570	
4-H	0.04	600	620	

Table 5.2: List of patterned InGaAs/GaAs specimens prepared for the trench depth study.

Sample ID	In Fraction (x)	Thickness (nm)	Depth (nm)	Comments
10-A	0.08	300	100	150 nm buffer
10-B	0.08	300	135	
10-C	0.08	300	225	
10-D	0.08	300	300	
10-E	0.08	300	420	
10-F	0.08	300	530	
10-G	0.08	300	565	
10-H	0.08	300	590	

Table 5.3: RIE etch conditions to reveal InGaAs epitaxial layer cross-sectional profiles.

BCl_3 Flow rate	30	sccm
Cl_2 Flow rate	10	sccm
Pressure	30	mtorr
Power	30	Watts
Platen Temperature	30	°C
Etch time	30	s

trenches. The specimens were cleaved along both ⟨110⟩ directions. The sections were held cleaved side up in an Al fixture especially made for these tests. The dimensions of the fixture are important, since it is necessary to ensure that the cleaved surfaces are not too far above the platen. The specimens were etched by RIE for 30 s using the conditions listed in Table 5.3. The oxide mask was removed before SEM observation.

Misfit dislocations were imaged using scanning cathodoluminescence (CL), as described in the previous three chapters.

5.3 Results

5.3.1 Dislocation Densities for 300 nm Thick $In_{0.04}Ga_{0.96}As$

The MDD's of $In_{0.04}Ga_{0.96}As$, 300 nm thick, grown on unpatterned GaAs were about 5000 cm^{-1} each in the $[1\bar{1}0]$ and the [110] directions. Figure 5.1 is a CL image of the dark line defects in the unpatterned material. The same layer grown on GaAs with trenches as shallow as 150 nm shows a much lower MDD - a factor of 15 times less

for dislocations lying in the [110] direction.

Chapter 2 describes the two different 60° misfit dislocation core types, designated as α and β, that lie in the two perpendicular $\langle 110 \rangle$ line directions. The asymmetry in the MDD among these two types has been described throughout this thesis; the more numerous α dislocations lie in the $[1\bar{1}0]$ direction while β's lie in the [110] direction. In the OMCVD material, $[1\bar{1}0]$ and [110] oriented misfit dislocations have comparable densities in unpatterned material but the ratio between the two changes dramatically at a trench depth of 150 nm. For deeper trenches ($>$ 500 nm), the MDD in the two directions is again about the same. Shallow trenches apparently act as more effective barriers to β dislocations than to α dislocations.

Figure 5.2 shows how the average MDD varies with trench depth for the 300 nm thick, 4% In, strained layer. As the trench depth increases, the MDD decreases dramatically. At depths greater than about 400 nm, the MDD is essentially zero (less than one misfit dislocation per 200 μm square). Note that even at depths considerably smaller than the epitaxial layer thickness itself, the MDD is significantly reduced.

CL images show three isolation regimes, depending on the depth of the isolation trenches. In regime I, where the trench depths range from 0 to about 250 nm, misfit dislocations are only partially blocked by the trenches. Figure 5.3 is a CL image of a typical regime I wafer with 150 nm deep trenches. Many α dislocations simply glide from square to square, following the contour of the trenches. Most (but not all) β dislocations are blocked, however. At trench depths between 300 nm and 500 nm, regime II, virtually all misfit dislocations are stopped by the trenches, but the

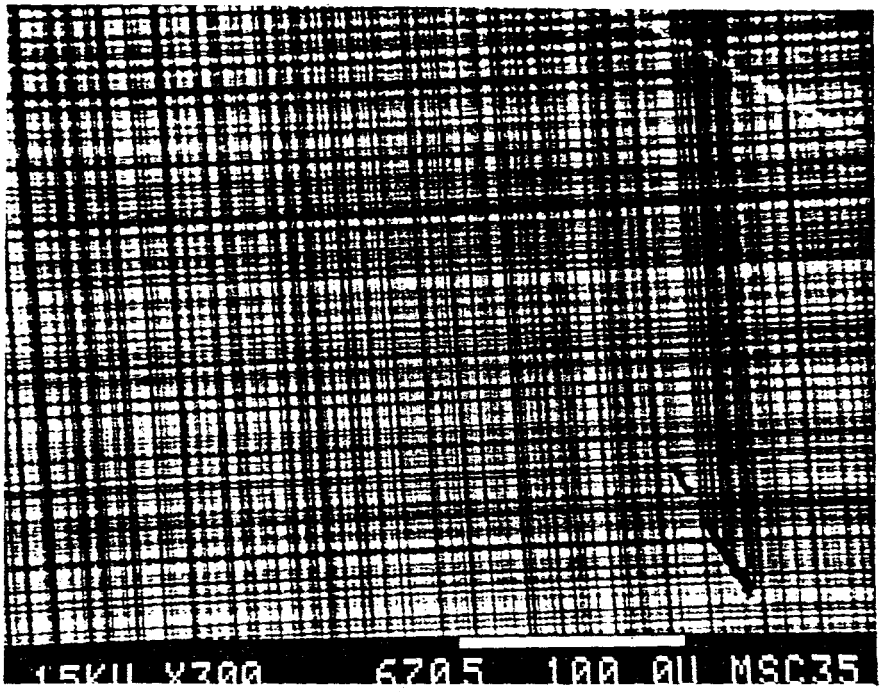

Figure 5.1: A CL image of misfit dislocations at an unpatterned substrate/epitaxial layer interface.

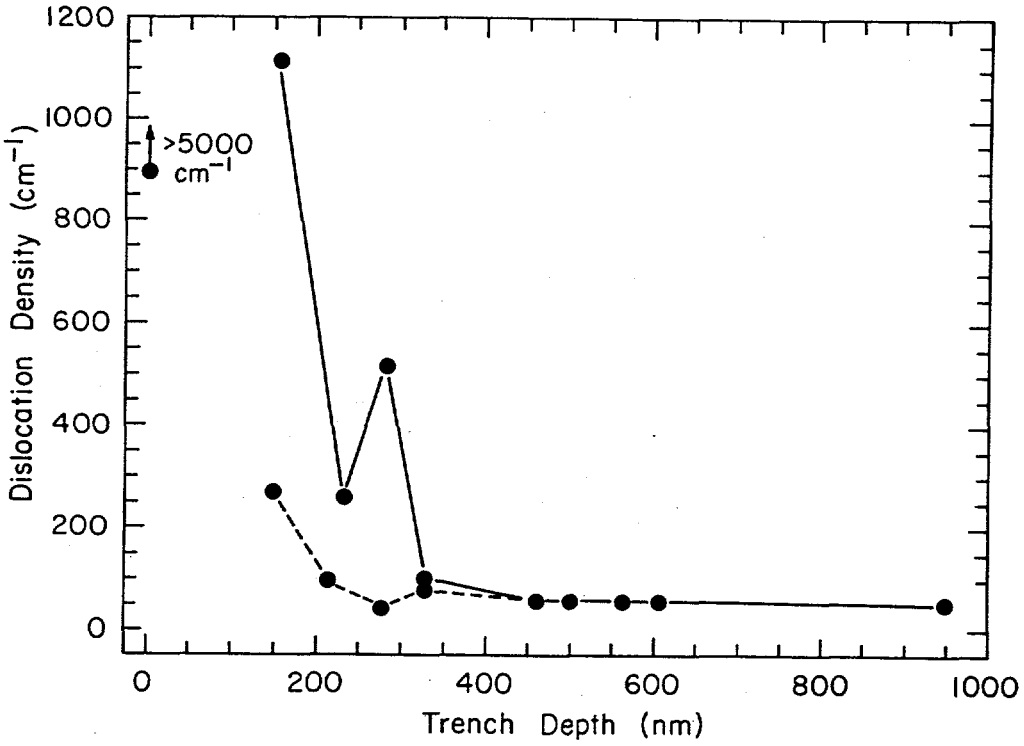

Figure 5.2: A plot of misfit dislocation density vs. trench depth for $In_{0.04}Ga_{0.96}As$, 300 nm thick, on GaAs patterned with 200 μm square mesas. The solid line refers to α dislocations and the dashed line corresponds to β dislocations.

dislocations are able to glide down a trench wall and stop at the far side. Figure 5.4 is a CL image of material with 400 nm deep trenches. The dislocations apparently nucleate from the dark spots on the mesa surface, possibly foreign particles that adhered to the substrate before epitaxial growth. The dark line defects appear to glide down the mesa walls and stop at the far side of the 10 μm wide trenches. In specimens with trenches etched to depths greater than 500 nm, regime III, misfit dislocations stop at the top of the trench edge. Figure 5.5 is a CL image of a regime III sample, showing two misfit dislocations that nucleated elsewhere on the mesa surface stop on the top of the mesa edge. The conditions for the three observed regimes are shown schematically in Figure 5.6.

Figure 5.3 indicates that the transition from regime I to II does not occur at the same depth for both α and β dislocations. In Figure 5.3, most α dislocations, such as the one labeled A glide across the trenches while the β dislocation, labeled B, stops at the bottom of a trench. The relative dislocation densities in Figure 5.2 reflect the fact that total isolation occurs along the β direction at shallower trenches than the α direction.

5.3.2 Dislocation Densities for 600 nm Thick $In_{0.04}Ga_{0.96}As$

Figure 5.7 is a plot of MDD vs. trench depth for the 600 nm thick, 4% In, material. As before, the MDD drops off dramatically with trench depth, even for trenches that are smaller than the layer thickness itself. The isolation depth appears to be slightly larger for the 600 nm layer compared to the 300 nm layer, as expected since the thicker material contains twice the strain energy. Both regime I and regime II

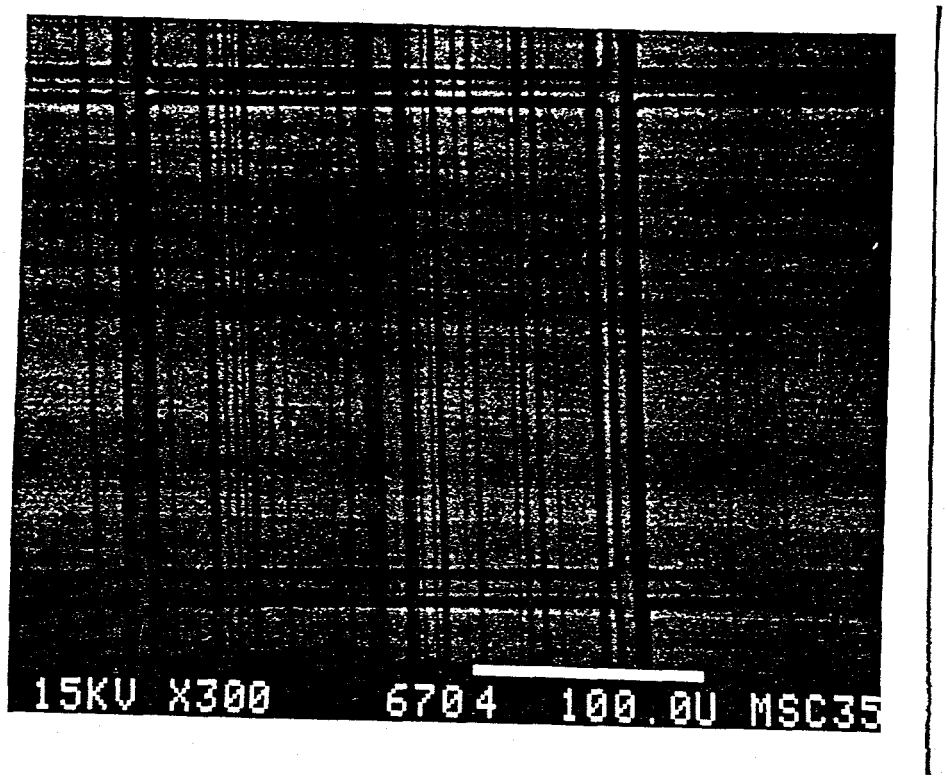

Figure 5.3: A CL image of misfit dislocations in regime I material. The more numerous dark line defects are α misfit dislocations, many of which pass from mesa to mesa unimpeded. Only a few β misfit dislocations are visible.

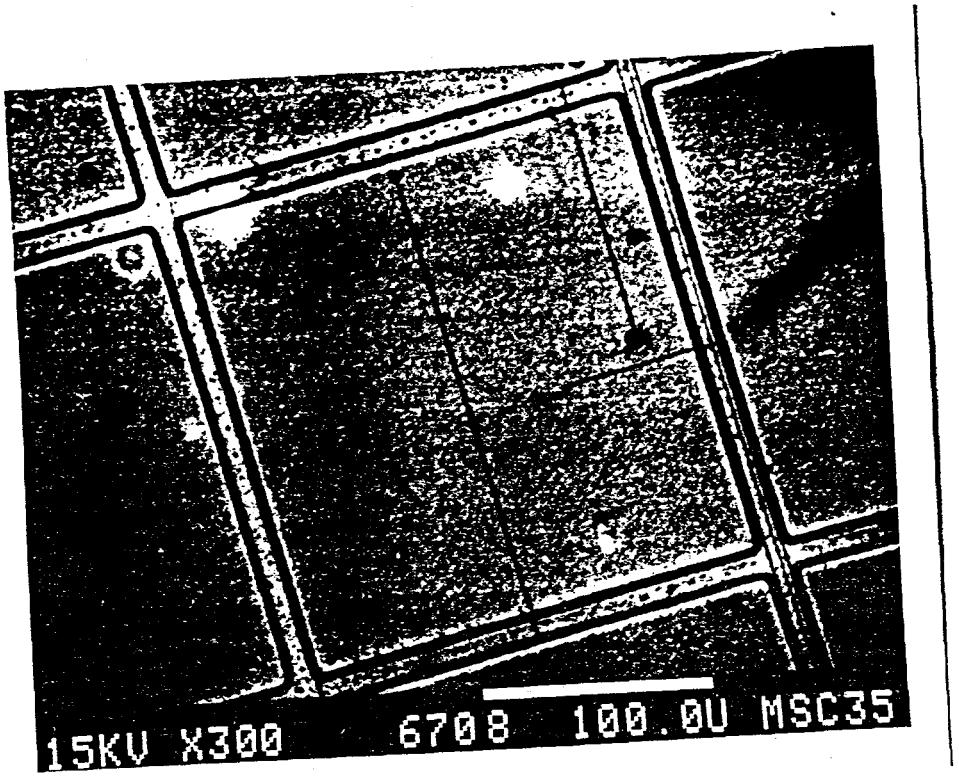

Figure 5.4: A CL image of misfit dislocations in regime II material. The misfit dislocations nucleate at the dark spots and stop at the bottom of the 10 μm wide trenches.

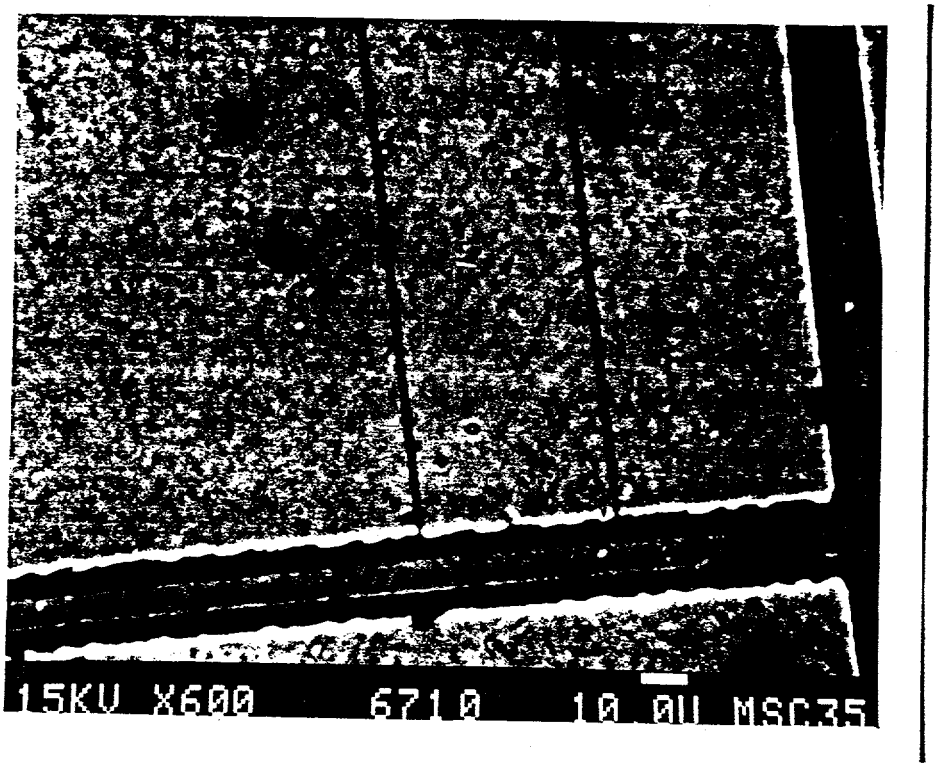

Figure 5.5: A CL image of misfit dislocations in regime III material. The misfit dislocations stop at the top of the mesas.

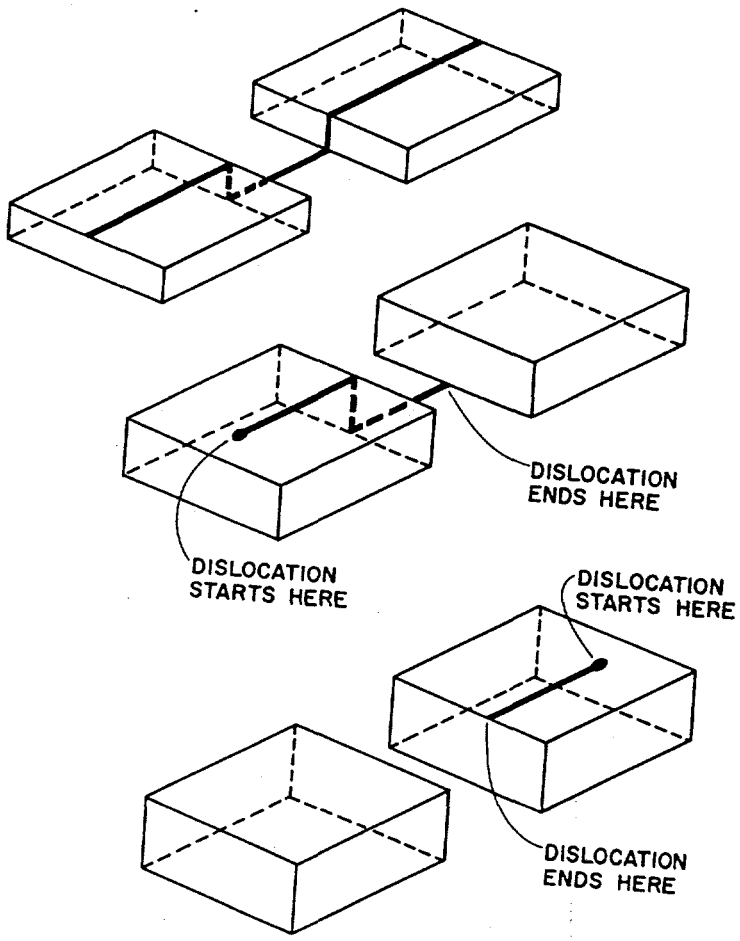

Figure 5.6: A schematic diagram illustrating the three isolation regimes described in the text. Regimes I, II and III are represented by *a*, *b*, and *c*, respectively.

type behavior are observed in this material as well. However, there is no evidence of regime III isolation of α dislocations for depths up to 650 nm.

Figure 5.8 is a CL image of misfit dislocations in the 600 nm thick film with a 570 nm deep trench. Regime II behavior of the misfit dislocations is evident in both line directions. In Figure 5.9 however, where the trenches were etched 620 nm deep, the β dislocations appear to stop at the top of the mesas (regime III).

5.3.3 Dislocation Densities for 300 nm Thick $In_{0.08}Ga_{0.92}As$

Unlike the material containing 4% In, the higher content 8% In material did not show an obvious decrease in MDD with increasing trench depth. The larger lattice parameter mismatch in this system apparently activated nucleation sources not seen in the previously described films. Figure 5.10 is a CL image of misfit dislocations in 300 nm thick $In_{0.08}Ga_{0.92}As$ grown on GaAs substrates with 550 nm deep trenches separating the mesas. The α MDD (vertical direction) is substantial, but these dislocations are clearly blocked by the trenches with regime III-like behavior. There were no indications of regime II trench depths; the specimens made an abrupt transition from regime I to regime III with increasing trench depth.

5.3.4 Layer Profiles

In Chapter 3 it was shown that vertical sidewalls could be produced by RIE (Figure 3.2). An important issue of epitaxial growth on patterned substrates is whether these vertical sidewalls are maintained in the preparation of the substrates after RIE. An experiment was performed determine this; several specimens were processed and one was removed after each etch step just before growth. After the etch in a so-

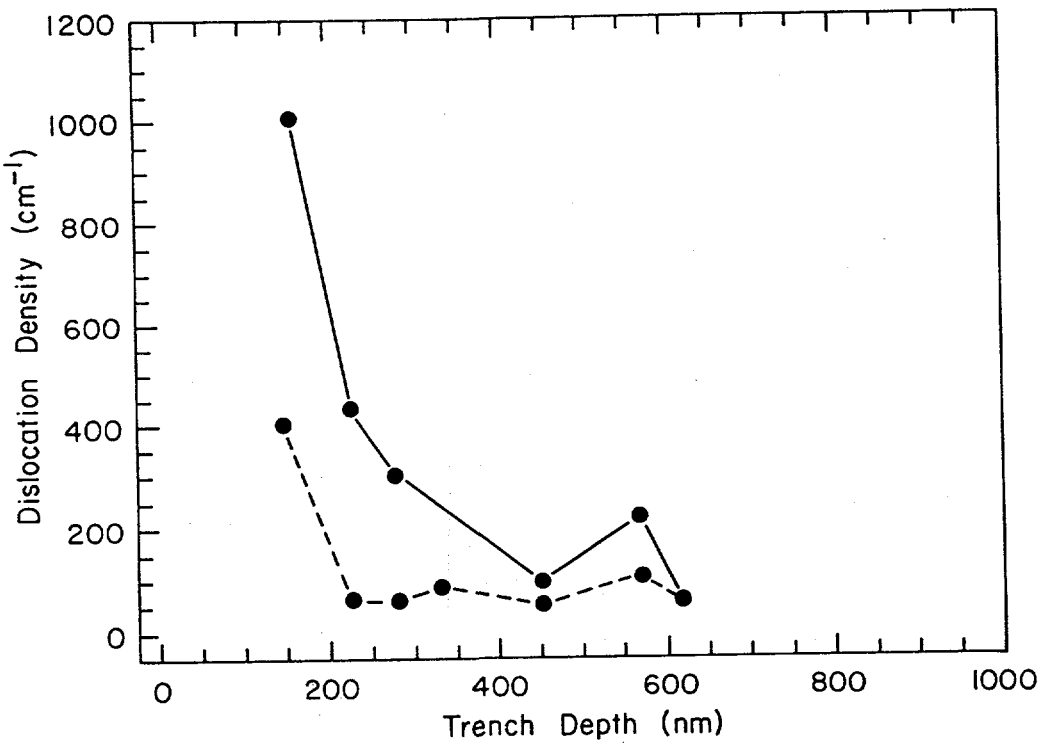

Figure 5.7: A plot of misfit dislocation density vs. trench depth for $In_{0.04}Ga_{0.96}As$, 600 nm thick, on GaAs patterned with 200 μm square mesas. The solid line refers to α dislocations and the dashed line corresponds to β dislocations.

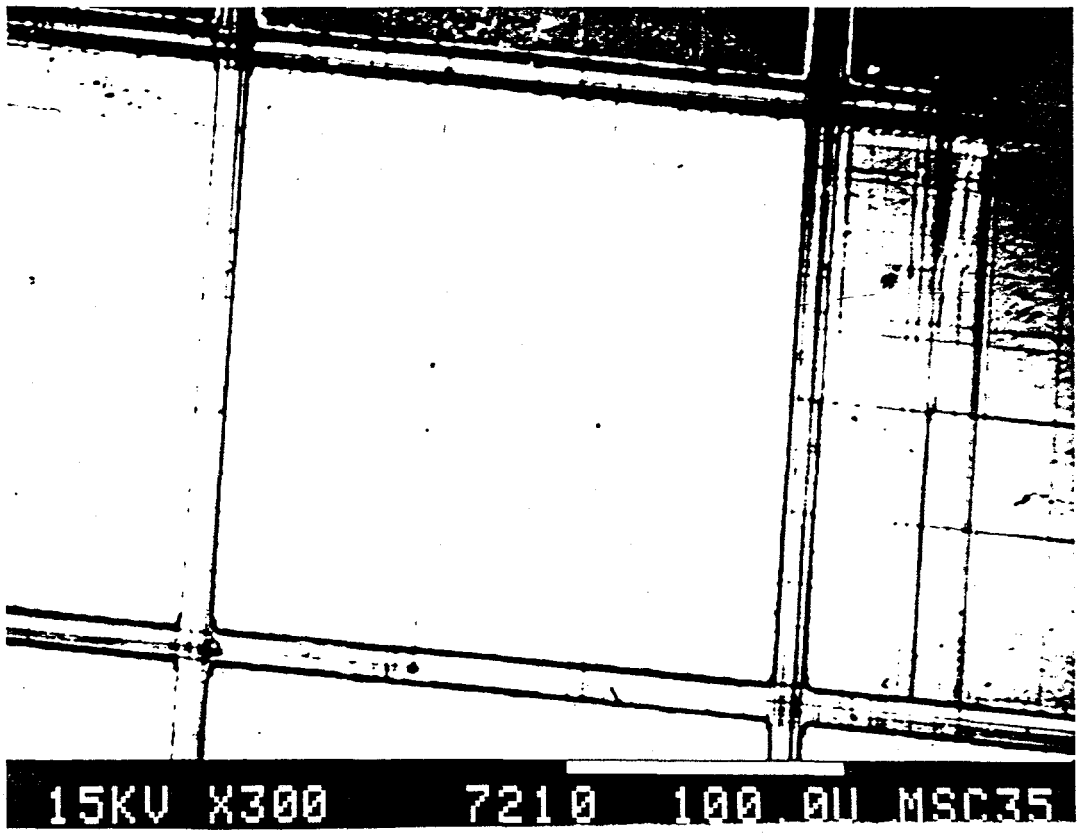

Figure 5.8: A CL image of misfit dislocations in 600 nm thick, 570 nm deep, regime II material. The misfit dislocations stop at the bottom of the trenches.

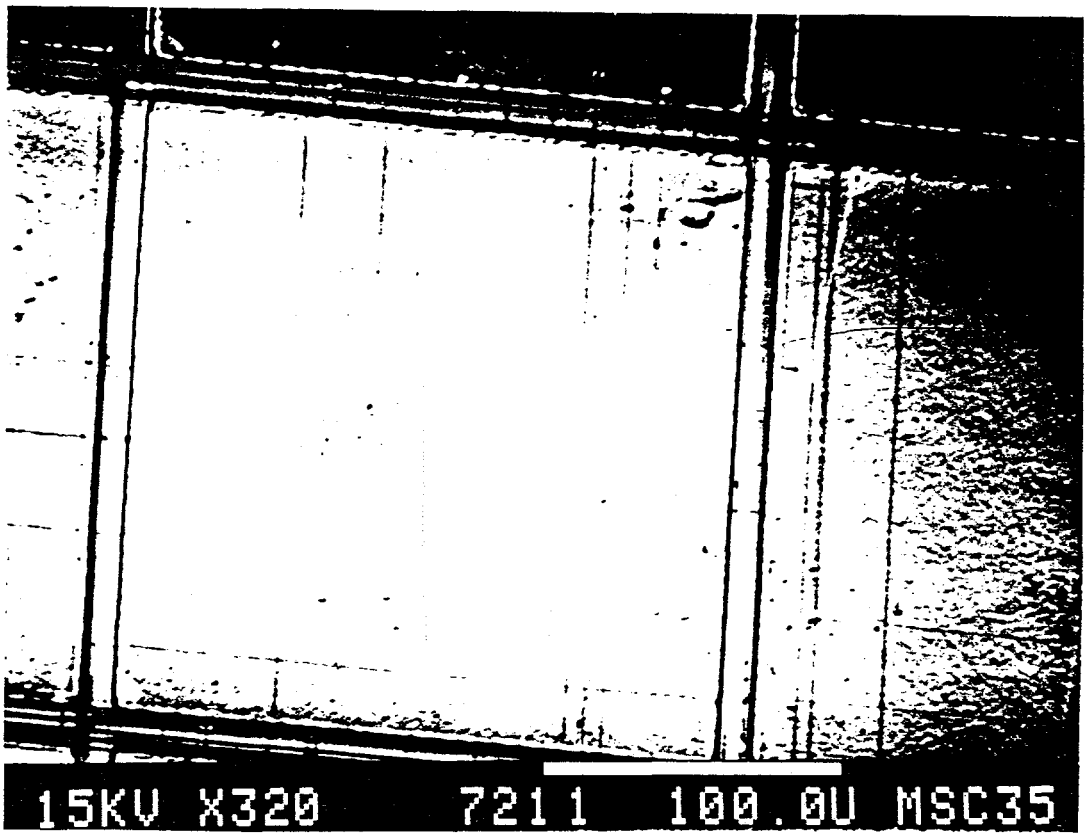

Figure 5.9: A CL image of misfit dislocations in 600 nm thick, 620 nm deep material. The α misfit dislocations stop at the bottom of the trenches (regime II), but the β misfit dislocations stop at the top (regime III).

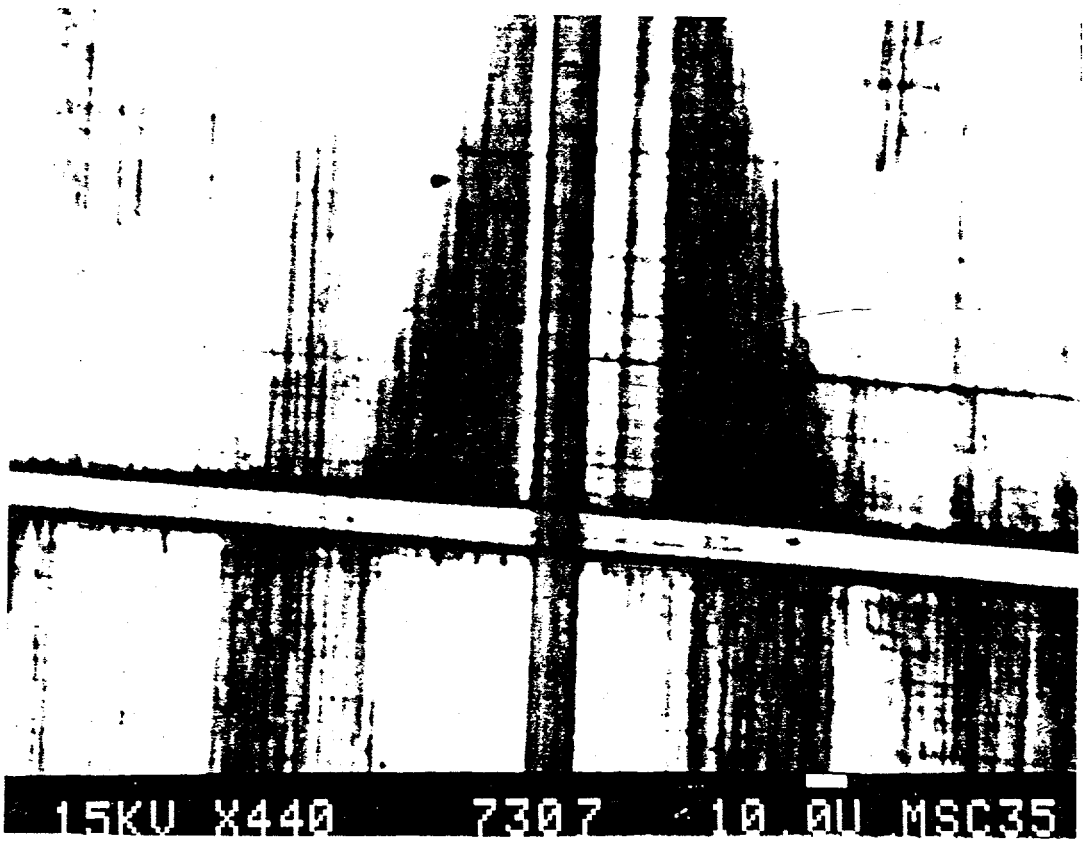

Figure 5.10: A CL image of misfit dislocations in 600 nm thick $In_{0.08}Ga_{0.92}As$ grown on patterned GaAs with 550 nm deep trenches. The α misfit dislocations (vertical dark lines) stop at the top of the mesas (regime III).

lution of 1:1:20 H_2SO_4:H_2O_2:H_2O at 25°C for 30 s, a very small change is seen in the sidewall slope. One specimen was cleaned and etched as before, and in addition it was loaded into the OMCVD reactor and heated to 640°C for several minutes in H_2. The time, a relatively large change was found in the trench wall orientation. Figure 5.11 is a cross-sectional view of the specimen. The trench wall changed from a slope of about 90° to about 70°. Although it is surprising that the surface atoms can rearrange themselves at the OMCVD bake temperature, this phenomena has been describe by Williams et al. as well, who grew AlGaAs on patterned GaAs substrates for laser diode fabrication, and by Hersee et al., who studied the growth of GaAs/AlGaAs on GaAs etched with v-grooves [WHJM91,HBB86].

After growth, the side walls are far from vertical. Figures 5.12, 5.13, and 5.14 are typical stained, cross-sectional profiles of trenches with 300 nm thick $In_{0.04}Ga_{0.96}As$ and 300 nm thick GaAs buffer layers for each of the three regimes. In Figure 5.12, at a trench depth of about 150 nm and looking in the [110] direction, the sidewall is oriented about 30° from the (001) surface. The bright layer is the InGaAs. Figure 5.13 is a regime II type trench 300 nm deep in material of the same composition and thickness. In this case the InGaAs surface is at an angle of 45°. Finally, Figure 5.14 is a cross-section of a regime III material. The epitaxial layer in this case appears to *pinch-off* at the trench wall. In all three cases, the InGaAs layer is continuously connected on the wafer surface. The trench walls are no longer vertical; the combination of wet etching, baking, and growing the GaAs buffer layer has changed the walls into troughs with sloped sidewalls. Table 5.4 lists the trench depths and wall angles for various samples.

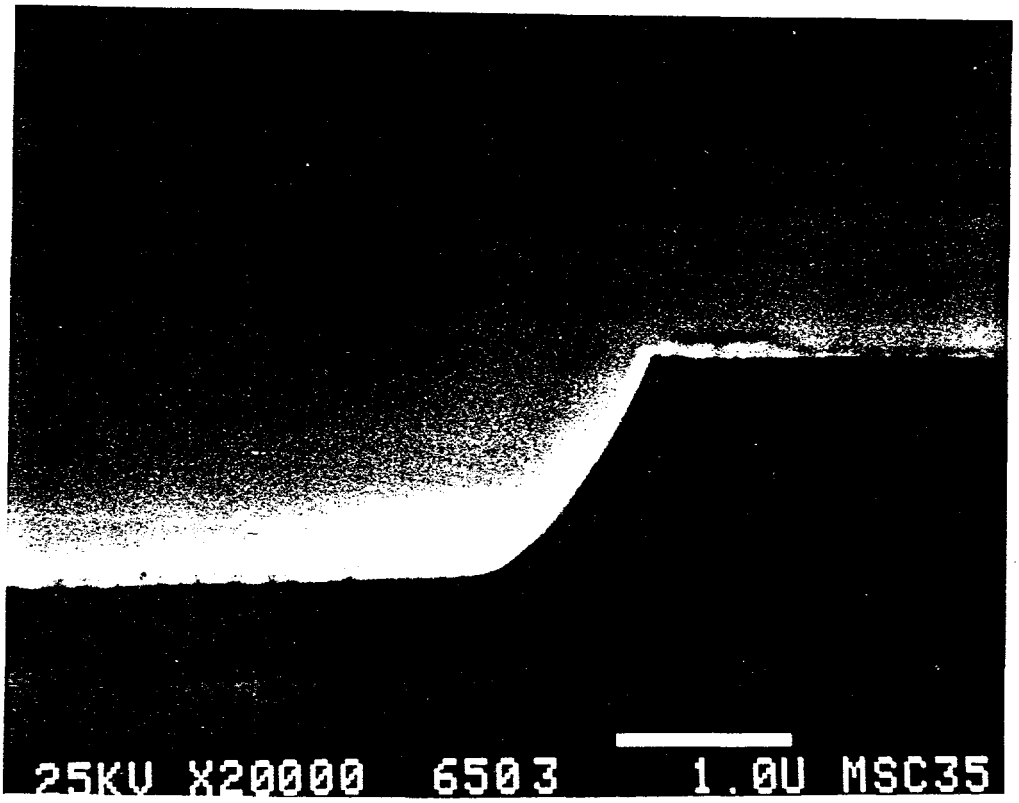

Figure 5.11: A cross-sectional SEM view of a trench wall after baking the sample in a H_2 atmosphere in the OMCVD reactor.

Table 5.4: Trench Depth and Wall Angles.

Sample ID	Trench Depth (nm)	Wall Angle (°)	Regime	Comments
1-B	230	25	I	300 nm thick $In_{0.04}Ga_{0.96}As$ blocking $[1\bar{1}0]$ (α) dislocations
1-D	330	42	II	same as above
2-G	570	55	III	same as above, pinch-off
4-F	500	50	II	600 nm thick $In_{0.04}Ga_{0.96}As$ blocking $[1\bar{1}0]$ (α) dislocations
4-F	500	35/55	II	same as above, but blocking β dislocation glide. Two wall slopes.

In some cases the profiles can be much different in the two perpendicular $\langle 110 \rangle$ directions. A regime II, 600 nm thick strained layer listed in Table 5.4 has two distinct wall angles, and, as Figures 5.9, 5.2, and 5.7 suggest, the transition from regime I to II and from II to III occur at different trench depths.

Cross-sectional profiles of one sample of 600 nm thick $In_{0.04}Ga_{0.96}As$ material possesses two different profiles in the two $\langle 110 \rangle$ directions as can be seen in Table 5.4. The consequence of this will be discussed below.

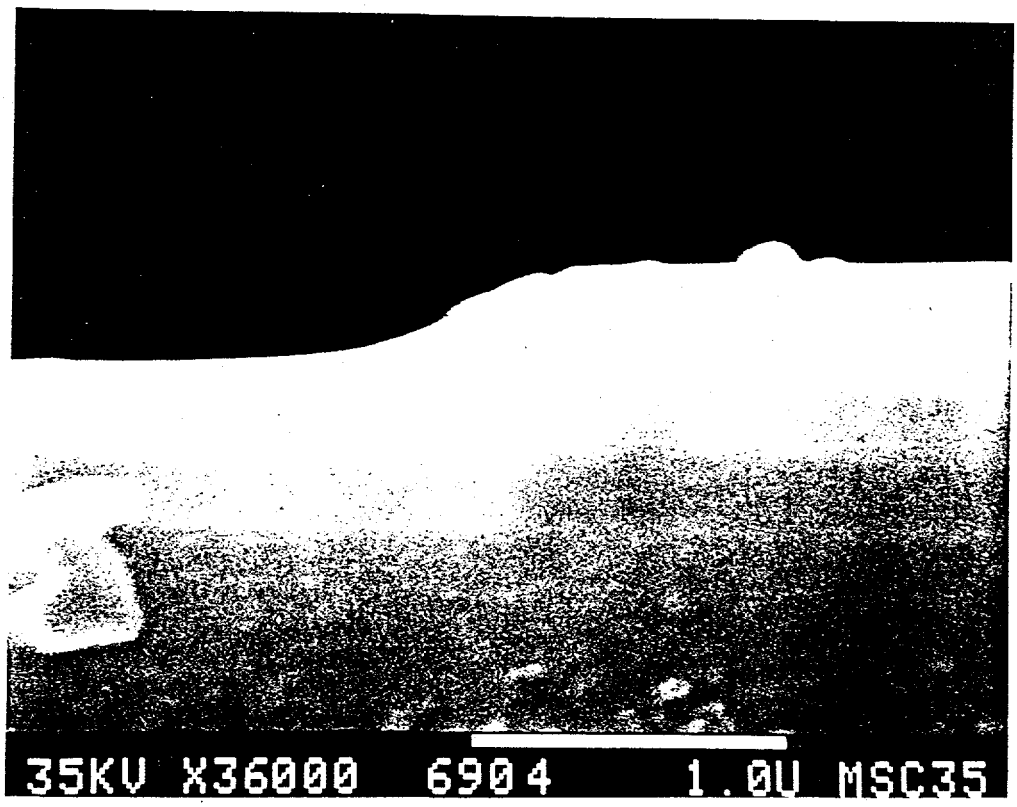

Figure 5.12: A stained cross-sectional SEM profile of a regime I trench. The bright region is the InGaAs epitaxial layer.

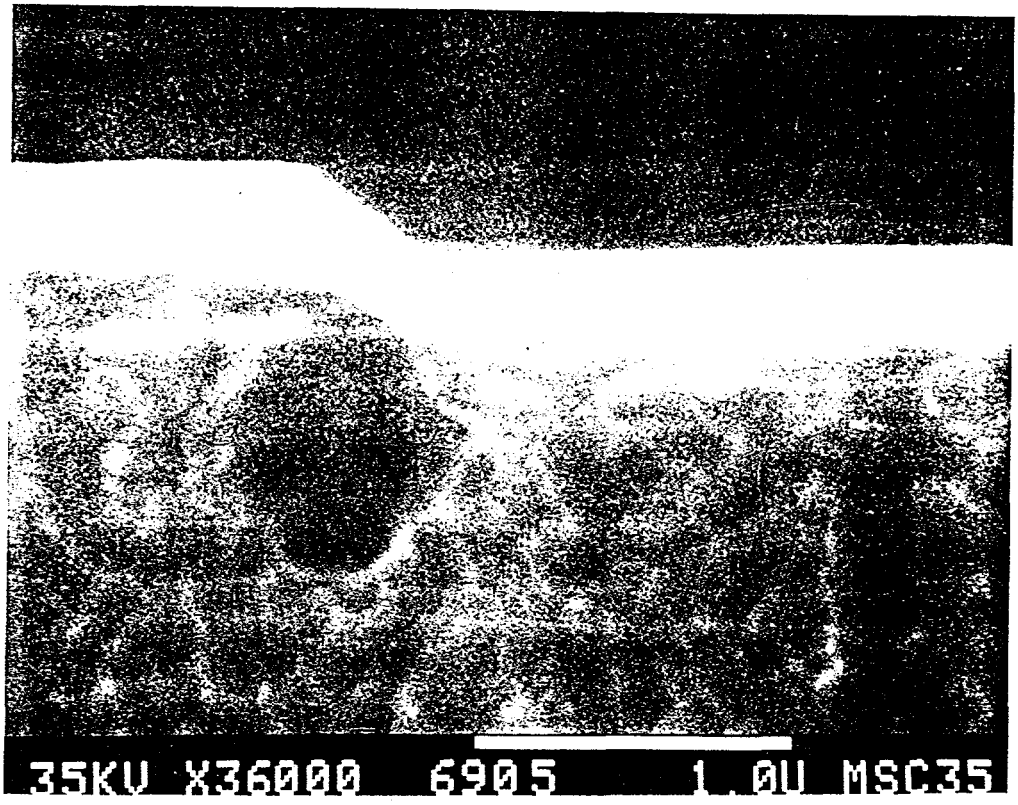

Figure 5.13: A stained cross-sectional SEM profile of a regime II trench. Although the trench wall slope is sharper than regime I profiles, it is qualitatively similar in appearance.

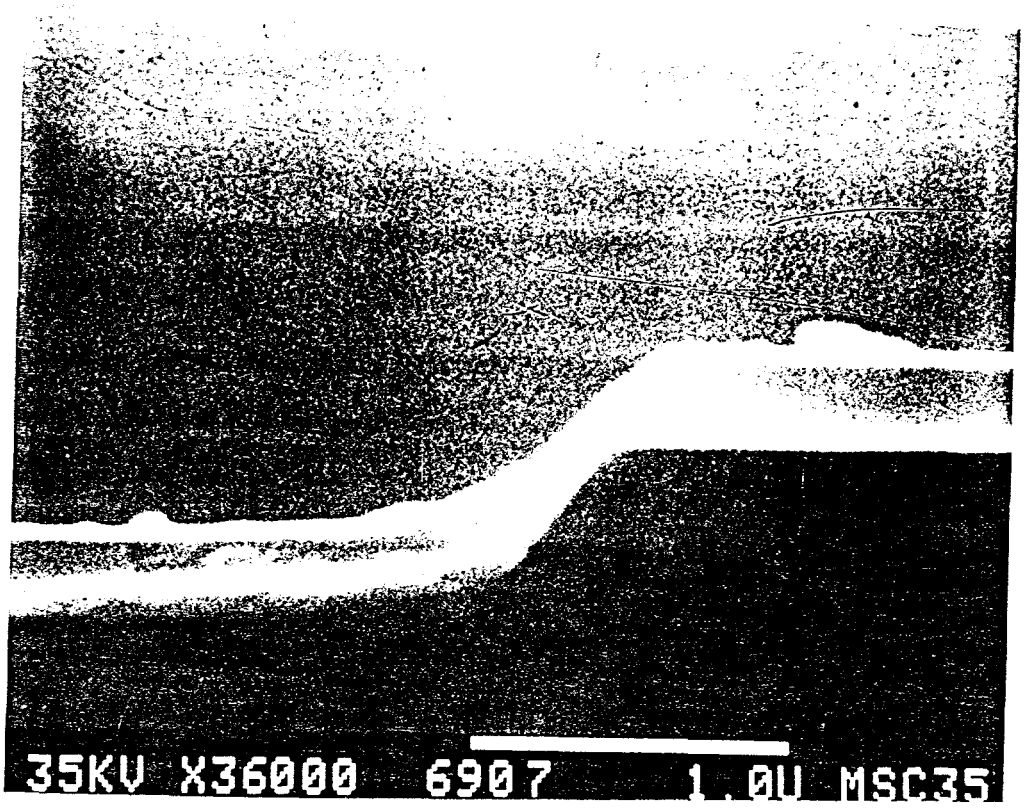

Figure 5.14: A stained cross-sectional SEM profile of a regime III trench. The epitaxial layer appears to pinch-off at the trench wall, inhibiting dislocation motion.

5.4 Discussion - Three Regimes

There is nothing different, from a geometric point of view, between the profiles of the 300 nm thick $In_{0.04}Ga_{0.96}As$ trenches in regimes I and II except for depths and wall angles (Figure 5.12 and 5.13). Yet there appears to be a *critical depth* where trenches begin to fully block the glide of these dislocations. It is surprising, at first glance, that on the one hand misfit dislocations can be blocked by trenches even in continuous epitaxial layers, and on the other hand, there is so little difference between trenches that block dislocations and those that don't.

In regime III, the epitaxial layer is barely continuous, and seems to *pinch off* at the trench walls (Figure 5.14). This pinching-off explains why misfit dislocations cannot glide down into the trenches in regime III material. The epitaxial layer is so thin at the edge that this region is below or close to the critical thickness. The 600 nm thick material showed no pinching-off at any trench depth studied, which explains why no regime III behavior was seen in this material.

Although the cross-sectional profiles of regime I and II type trenches are qualitatively the same, the misfit dislocation thread segment glide properties are quite different. It should be noted that the strain tensor components of the material near and at the trench walls differ from those of the mesas; strain relief at the mesa edge allows the strained epitaxial layer expand in the direction perpendicular to the mesa edge. But mesa edge strain relief cannot explain why misfit dislocations are isolated in regime II material since the misfit dislocation thread segments appear to have no trouble moving down a trench wall into the trench from a mesa in regime II. Only the

movement back up is impeded. Since the strain field felt by the interface segments of the misfit dislocations is equivalent whether they move *up* or *down* a trench wall, the orientation of the threading segments, which do break the up/down symmetry, must be considered.

Figure 5.15 describes what is believed to be happening qualitatively. A forward oriented threading segment has no problem passing down a trench wall in regime II (point 1 to 2), but when it reaches the far side of the trench, it must extend upward to the free surface (point 3 to 4). The threading segment extension will add energy to the system with little gain in strain relief. The threading segment length actually shrinks as it glides down into a trench - this difference between segment sizes when moving up and down a trench wall leads to the unique dislocation isolation effect.

In the following section, a simple model is developed to account for the above observations, based on Matthew's theory (Chapter 2) and the threading segment extension idea.

The fact that pre-growth processing also affects profiles has already been mentioned and the characteristics of OMCVD epitaxial layer wall configurations on patterned substrates has been investigated by several other researchers as well [WHJM91, HBB86,HBG+86,OO89,YMY+87,KSK+86,KTM86]. Hersee et al. found that growth conditions such as temperature and V/III ratio can change the predominant growth facets on patterned substrates. In addition, there can be significant differences between the [110] and [$\bar{1}$10] profiles [HBB86]. Yuasa et al. found that as the epitaxial layer increases in thickness relative to trench depth, the wall angle decreases significantly, in agreement with the data described in the previous section and with

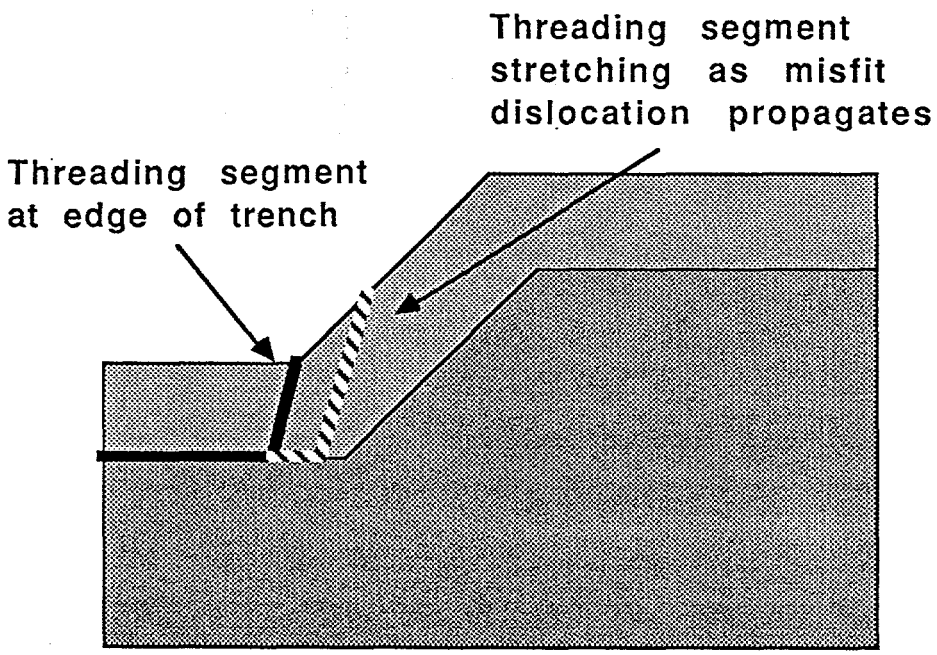

Figure 5.15: A schematic of dislocation glide in regimes I and II.

intuition. OMCVD tends to *flatten out* any non-uniformities on the (001) oriented substrates. Kamon et al. on the other hand found that {111} walls in wet etched trenches were preserved during epitaxial layer growth. However, their material was very different since the substrates were covered with SiN_x except in the trenches, so that growth was arrested on the mesa tops [KSK+86,KTM86].

Another interesting point; Figure 5.2 suggests that the critical depth is much smaller for β dislocations than for α dislocations. The [110] (β) direction MDD drops off to less than 200 cm^{-1} at a trench depth of only 150 nm while a depth of about 300 nm is needed to fully block [1$\bar{1}$0] dislocations. The reason is believed to be linked to the slightly different sidewall profiles in the two directions. Much larger profile differences were found in the 600 nm thick material, which explains the phenomena in Figure 5.9.

5.5 Analysis of Dislocation Glide over Patterned Substrates

To include the effects of the threading segments, Equation 2.17 must be modified. In addition to strain energy terms describing epitaxial layer relaxation via misfit dislocation extension, a threading segment extension term must be added. This new term will be developed in the following subsections.

5.5.1 Derivation of Strain Energy

The model is based on the geometry illustrated in Figure 5.15 which also shows the coordinate system. The starting point of the misfit dislocation is shown as the solid line, with the top of the threading segment just meeting the edge of the trench wall.

As the threading segment glides (the dashed line), the misfit dislocation extends a distance ξ and relaxes the shaded epitaxial layer volume. The segment is assumed to maintain its orientation and extend up to the free surface. The energy required to extend the thread segment is calculated using Equations 2.14 and 2.15 for dislocations in isotropic media. The inner cut-off radius is the same as the one used in Chapter 2, namely b/α. The upper cut-off radius is a bit more complicated to calculate, since the threading segment is not parallel to the free surface (remember that the cut-off radius in Chapter 2 was determined by the distance between the misfit dislocation core and the surface, h).

It is assumed that the volume of epitaxial layer material that is relaxed is of constant height h, which is only true for part of the travel distance, ξ. However, the most important portion of the extension occurs for very small ξ, where h is constant.

To calculate the length of the extended threading segment and the distance between it and the free surface, we will use a geometric description based on miller indices for a cubic lattice. This leads to a simple notation for the GaAs system, but the arguments are not limited to cubic crystals. The misfit dislocation line segment lying in the $[h_L k_L l_L]$ direction is defined as the set of points

$$\begin{pmatrix} \frac{h_L}{l_L} z + X_L \\ \frac{k_L}{l_L} z + Y_L \\ z \end{pmatrix}, \tag{5.1}$$

where X_L and Y_L are the coordinates for a point on the line when $z = 0$. Figure 5.16 illustrates the directions and coordinates used. The plane $z = 0$ is the surface of the epitaxial layer at the bottom of the trench. The index l_L is assumed to be non-zero;

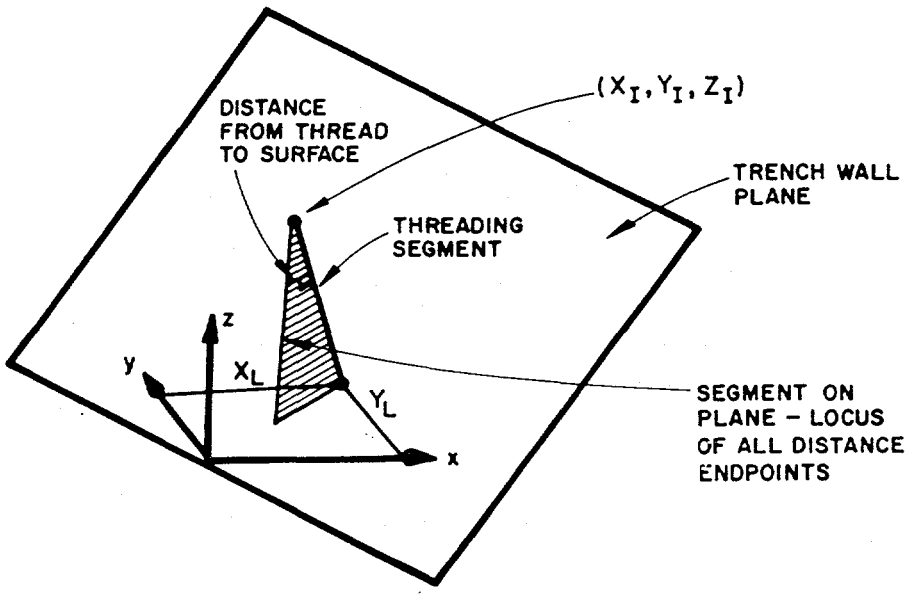

Figure 5.16: A diagram showing the coordinate system used to develop a quantitative description of regime II behavior.

if not, the equation above and the arguments that follow can be changed simply by forming a permutation of x, y, and z so that one non-zero index is in the denominator of Equation 5.1.

The set of points contained in a plane $(h_P k_P l_P)$ that passes through the point (0,0,0) is calculated simply by generalizing the relationship between two perpendicular lines in a plane (slopes of m and $1/m$). This plane represents the epitaxial layer surface of the trench wall. The points are

$$\begin{pmatrix} -\frac{l_P}{h_P}z - \frac{k_P}{h_P}y \\ y \\ z \end{pmatrix}. \tag{5.2}$$

Note the two degrees of freedom, y and z.

Figure 5.17 illustrates the same plane and thread segment viewed from a different orientation. From this direction, the important angles and the minimum distance between the line and the plane (perpendicular to the line) can be simply described. The angle between the segment and the plane normal, ω', and its complement, ω, are simply calculated by taking the dot product of the plane normal $[h_P k_P l_P]$ and the segment $[h_L k_L l_L]$:

$$\begin{aligned} \sin\omega &= \cos\omega' \\ &= \frac{h_P h_L + k_P k_L + l_P l_L}{\sqrt{h_P^2 + k_P^2 + l_P^2}\sqrt{h_P^2 + k_P^2 + l_P^2}}. \end{aligned} \tag{5.3}$$

The distance from the segment to the surface, R, is related to the length from the segment/plane intersection, L, by

$$R = L\tan\omega. \tag{5.4}$$

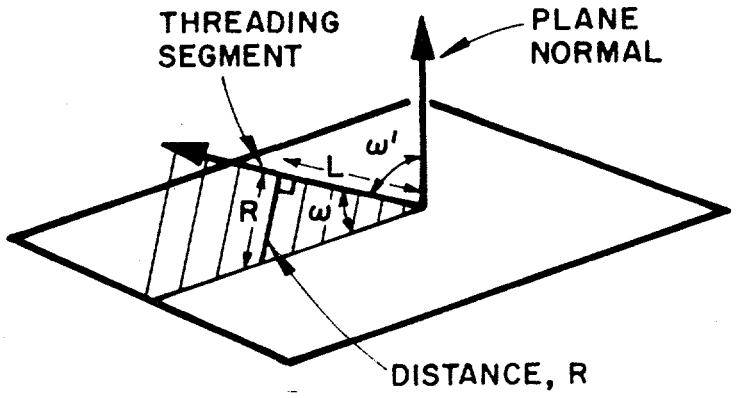

Figure 5.17: A misfit dislocation glide segment intersecting a trench wall viewed from a different orientation.

What is the extent of L? The plane and segment intersect at $L = 0$ (L_{min}) by definition. The point of intersection, (X_I, Y_I, Z_I), is found by equating the coordinates in Equations 5.1 and 5.2, yielding:

$$\begin{aligned} X_I &= \frac{h_L}{l_L} Z_I + X_L \\ Y_I &= \frac{k_L}{l_L} Z_I + Y_L \\ Z_I &= -\frac{\frac{k_P}{h_P} Y_L + X_L}{\frac{h_L}{l_L} + \frac{l_P}{h_P} + \frac{k_P k_L}{h_P l_L}}. \end{aligned} \tag{5.5}$$

The maximum extent of L, L_{max}, occurs at the intersection of the segment and the plane representing the flat surface at the bottom of trench, at $(X_L, Y_L, 0)$. Calculating the distance between (X_I, Y_I, Z_I) and $(X_L, Y_L, 0)$ yields:

$$L_{max} = \left| \frac{k_P Y_L + h_P X_L}{\sin\omega \sqrt{h_P^2 + k_P^2 + l_P^2}} \right|. \tag{5.6}$$

The strain energy caused by the extended threading segment is simply calculated by integrating the energy per unit length of dislocation line with respect to L, using Equation 2.16. The energy is

$$E_{seg} = \int_0^{L_{max}} \frac{\mu b^2}{4\pi} \left(\frac{1 - \nu \cos^2\theta}{1 - \nu} \right) \ln\left(\frac{R\alpha}{b} \right) dL, \tag{5.7}$$

where R is related to L by Equation 5.4 and the upper integration limit is found in Equation 5.6.

Equation 5.7 is now applied to a specific case, a misfit dislocation with a line direction [110], and with a threading segment oriented in the [101] direction, approaching a trench wall with a surface $(\bar{1}\bar{1}\ell)$ (and trench angle $\gamma = \arctan(\sqrt{2}/\ell)$). Figure 2.7 may assist the reader in visualizing the geometry. The parameter ξ represents the extension of the misfit dislocation length along the [110] direction. The

position of the threading segment relative to the edge of the trench wall is defined by the coordinates $X_L = \xi/\sqrt{2}$ and $Y_L = \xi/\sqrt{2}$. Equation 5.7 simply reduces to:

$$E_{seg} = \frac{\mu b^2}{4\pi}\left(\frac{1-\nu\cos^2\theta}{1-\nu}\right)\frac{2\xi}{\ell-1}\left(\ln\left(\frac{2\alpha\xi}{b\sqrt{(\ell+1)^2+2}}\right)-1\right). \quad (5.8)$$

Equation 5.8 (and Equation 5.10) now can be added to Equation 2.17 to form the basis of the misfit dislocation driving force theory at the edge of trench walls. One more simplification is done; the misfit dislocation density is assumed to be negligible in the y direction and so low in the x direction that only terms first order in ρ_x are retained. The total energy change of an epitaxial layer/substrate system per dislocation as a misfit dislocation extends by amount ξ is:

$$E_{tot} = E_{mis} + E_{dis} + E_{seg} \quad (5.9)$$

$$E_{tot} = \frac{\mu b^2}{4\pi}\left(\frac{1-\nu\cos^2\theta}{1-\nu}\right)\ln\left(\frac{h\alpha}{b}\right)\xi - 2\mu\frac{1+\nu}{1-\nu}hqxb_e\xi + \frac{\mu b^2}{4\pi}\left(\frac{1-\nu\cos^2\theta}{1-\nu}\right)\frac{2\xi}{\ell-1}\left(\ln\left(\frac{2\alpha\xi}{b\sqrt{(\ell+1)^2+2}}\right)-1\right). \quad (5.10)$$

Also of interest is the "force" applied to the treading segment as it attempts to glide up the trench wall. The force is defined as the derivative of E_{tot} with respect to the travel distance, ξ. Then:

$$\frac{\partial E_{tot}}{\partial \xi} = \frac{\mu b^2}{4\pi}\left(\frac{1-\nu\cos^2\theta}{1-\nu}\right)\ln\left(\frac{h\alpha}{b}\right) - 2\mu\frac{1+\nu}{1-\nu}hqxb_e + \frac{\mu b^2}{4\pi}\left(\frac{1-\nu\cos^2\theta}{1-\nu}\right)\frac{2}{\ell-1}\ln\left(\frac{2\alpha\xi}{b\sqrt{(\ell+1)^2+2}}\right). \quad (5.11)$$

Equations 5.10 and 5.11 must be modified, however, for one important reason. Referring to Figure 5.15, as a misfit dislocation threading segment glides up a wall, it extends until it reaches the mesa top surface, where its length then becomes constant.

The volume element of material considered in the segment energy calculation must be a truncated cone after the top is reached. The energy in Equation 5.10 is too large after that point, since it considers the segment to extend indefinitely. In the particular case treated here, the segment reaches to the top of the mesa at $\xi = D(\ell-1)/\sqrt{2}$, where D is the trench depth. After this point, the following term is added to E_{tot}:

$$- \frac{\mu b^2}{4\pi}\left(\frac{1-\nu\cos^2\theta}{1-\nu}\right)\left(\frac{2\xi}{\ell-1}-\sqrt{2}D\right) \times \left(\ln\left(\frac{\alpha(\ell-1)}{b\sqrt{(\ell+1)^2+2}}\cdot\left(\frac{2\xi}{\ell-1}-\sqrt{2}D\right)\right)-1\right). \quad (5.12)$$

The driving force equation likewise must be modified for $\xi > D(\ell-1)/\sqrt{2}$ by adding the following term:

$$- \frac{\mu b^2}{4\pi}\left(\frac{1-\nu\cos^2\theta}{1-\nu}\right)\frac{2}{\ell-1} \times \ln\left(\frac{\alpha(\ell-1)}{b\sqrt{(\ell+1)^2+2}}\cdot\left(\frac{2\xi}{\ell-1}-\sqrt{2}D\right)\right). \quad (5.13)$$

5.5.2 Calculation Results

Figure 5.18 is a plot of how the system energy per dislocation changes as the segment travels distance ξ for various trench wall angles, using Equations 5.10 and 5.12. In this example, the epitaxial layer is assumed to be 300 nm thick $In_{0.04}Ga_{0.96}As$ covering a 300 nm deep trench (these are the approximate parameters at the transition from regime I to regime II). As the trench wall approaches 54.536° ($\ell = 1$), a

very large energy barrier appears; only for wall angles below about 45° is the system energy per dislocation monotonically decreasing. The wall angle is clearly an important parameter in determining misfit dislocation isolation in continuous layers. The reason is simple; the slope of the trench wall determines how fast the threading glide segment increases in length relative to the misfit dislocation extension, ξ. With steep slopes, the thread segment extends quickly, costing the system energy that it cannot retrieve in strain relief as quickly. At shallower angles (below 45°), the thread segment grows slowly enough so that the net strain relief is always larger. Note that at $\xi = 100$ nm all of the curves are below $E_{tot} = 0$, so that the net free energy of the system decreases with dislocation motion, but the considerable energy barrier for high wall angles prevents motion at realistic temperatures.

Figure 5.19 is a plot of the driving force (Equations 5.11 and 5.13) for the same system. Note that the values are greater than zero at some portions of the curves at high wall angles. The curves drop abruptly and approach negative values at $\xi = D(\ell - 1)/\sqrt{2}$. This fact allows for a simple criterion to determine the *critical wall angle*, the angle which separates regime I and regime II behavior; if the driving force is non-positive for all $0 < \xi < D(\ell - 1)/\sqrt{2}$, then the trenches cannot block dislocation glide. If it is positive at any ξ in the range above, the system is in regime II. Larger values of ξ need not be considered. More specifically, the critical angle, γ_{crit}, occurs at

$$\left.\frac{\partial E_{tot}}{\partial \xi}\right|_{\xi = D(\ell-1)/\sqrt{2}} = 0. \tag{5.14}$$

The program LSOLVE.C in Appendix C calculates the critical angle based on Equation 5.14 for a given h, D, and x.

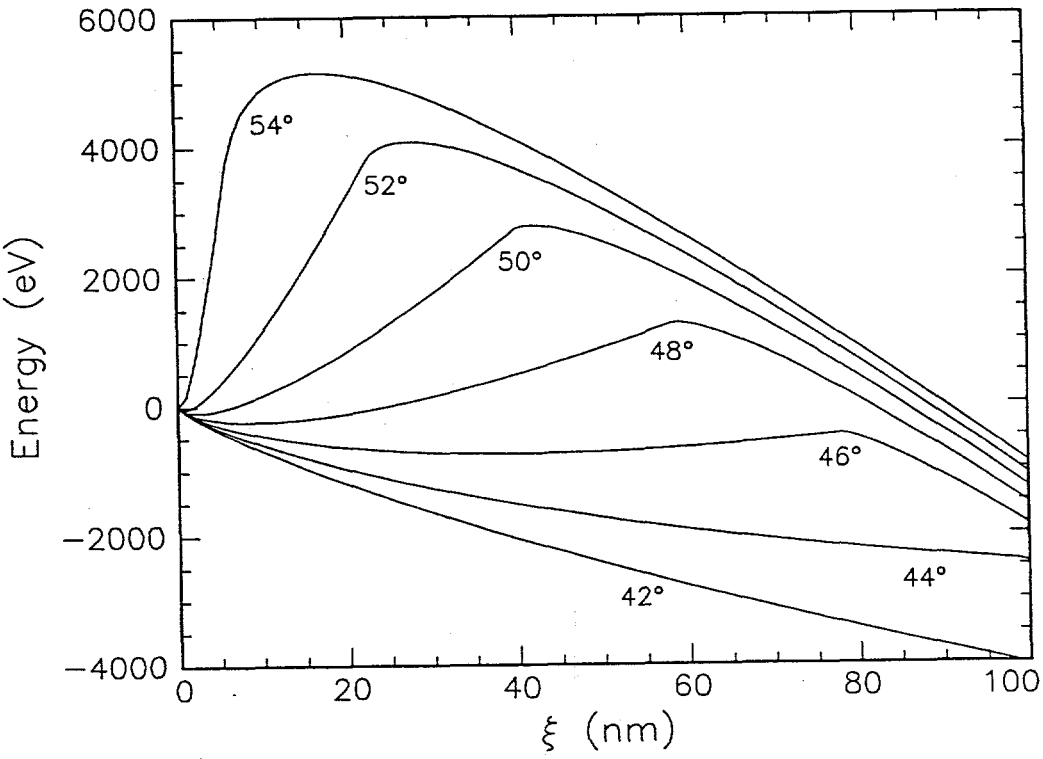

Figure 5.18: A plot of the system energy per misfit dislocation vs. the extension of the misfit dislocations, ξ, for various trench wall angles. The epitaxial layer is 300 nm thick $In_{0.04}Ga_{0.96}As$ grown on a substrate with 300 nm deep trenches.

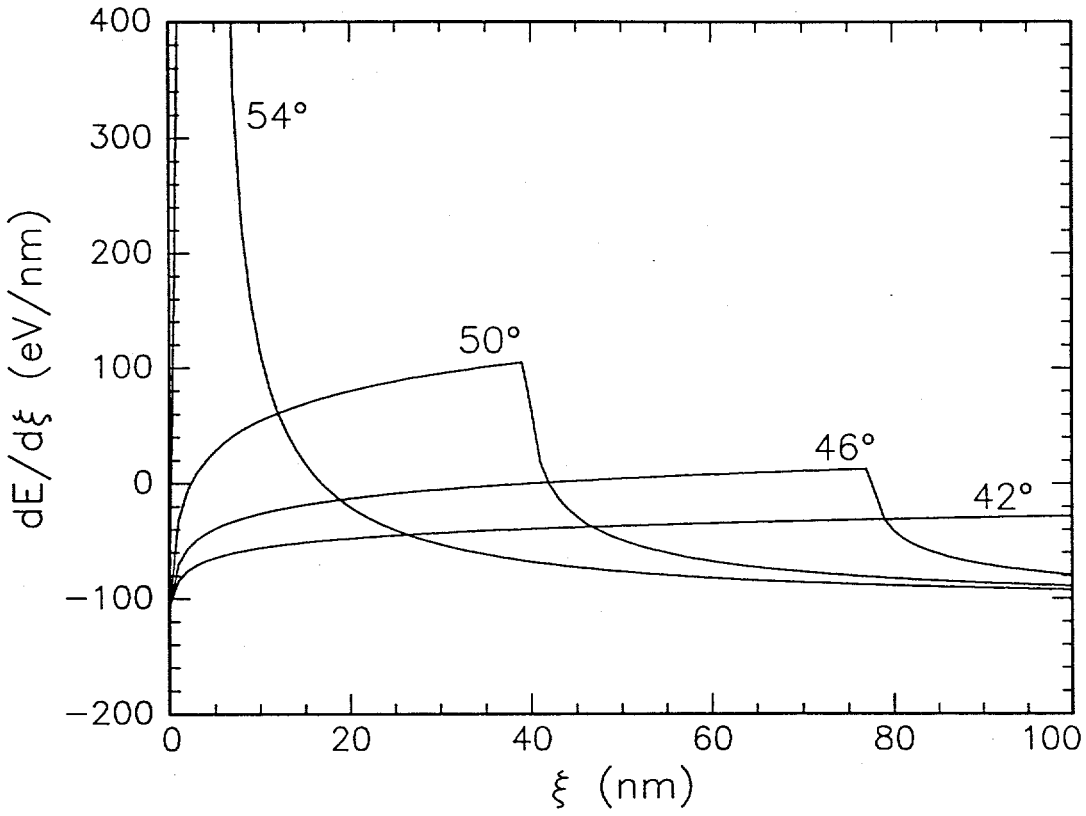

Figure 5.19: A plot of the driving force vs. ξ for the same material in Figure 5.18.

Figure 5.20 is a plot of γ_{crit} versus trench depth for three epitaxial layers: 300 nm $In_{0.04}Ga_{0.96}As$, 600 nm $In_{0.04}Ga_{0.96}As$, and 300 nm $In_{0.08}Ga_{0.92}As$. Notice that the critical wall angle is insensitive to the trench depth. This is a surprising and an important result; the trench depth can be reduced to very small values without affecting the capability to block misfit dislocation thread segment glide. It is possible to create low defect strained epitaxial layers on nearly planar substrates. The important factor is the orientation of the trench walls. If growth and processing conditions can be optimized to create {111} trench walls, essentially any reasonable trench depth is adequate.

If, according to the results of the above analysis, the trench depth D is unimportant, why does it clearly control the transition from regime I to II, as Figures 5.2 and 5.7 indicate? The reason is because D (and h) determines the resulting trench wall angle for the specimens in this study. Shallow trenches created low angle epitaxial layer trench walls, and the steepness of the walls increased with D (see Table 5.4).

5.5.3 Comparison with Trench Profiles

The theory described above does qualitatively explain many of the features of the specimens studied. The 300 nm thick $In_{0.04}Ga_{0.96}As$ material follows the predicted relationship between the trench wall angles and the regime characteristics. The regime I trench angle in Table 5.4, 35°, is below $\gamma_{crit} \approx 45°$ and the regime II wall angle is about 45° in the α misfit dislocation direction.

The transition from regime I to II occurred at larger trench depths for the 600 nm thick $In_{0.04}Ga_{0.96}As$ (Figure 5.7) compared to the 300 nm thick material because, as

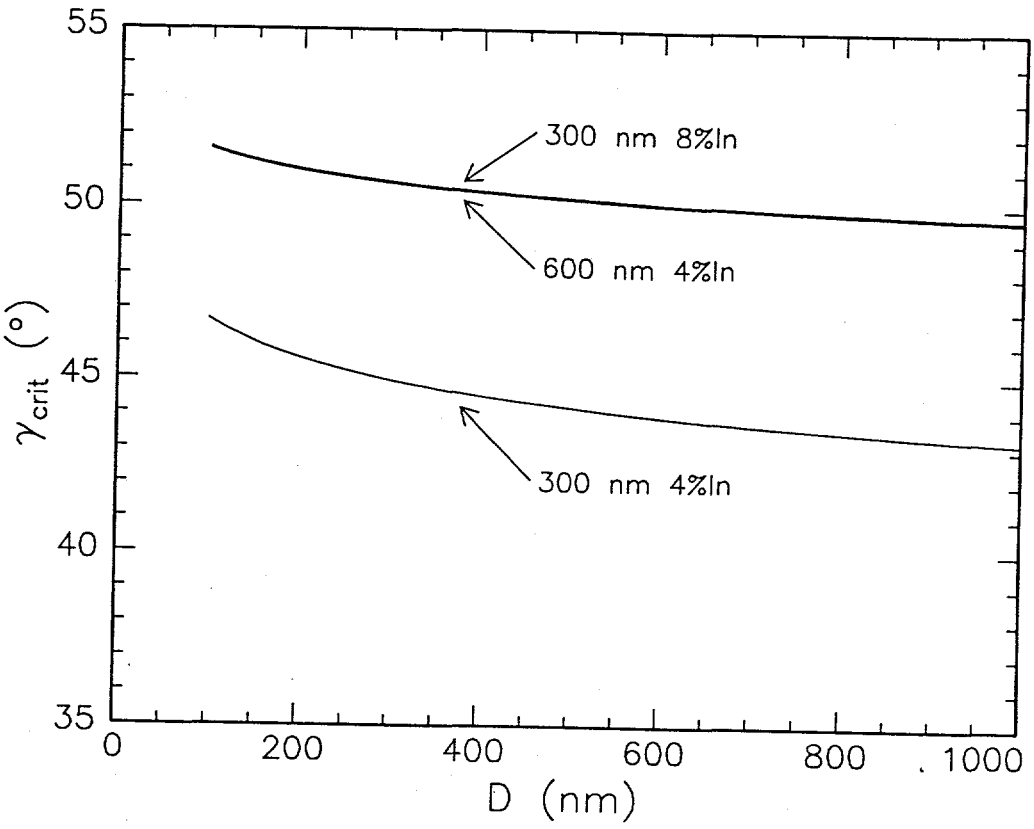

Figure 5.20: A plot of the critical wall angle, γ_{crit}, vs. trench depth, D. The critical angle is essentially independent of D so that it is possible to block misfit dislocation motion with very shallow trenches if a large wall angle can be maintained.

Figure 5.20 indicates, a steeper trench is necessary to block dislocation glide in the thicker layer specimens.

Finally, the 300 nm $In_{0.08}Ga_{0.92}As$ material never exhibited regime II blocking. The large trench angle necessary for the onset of regime II occurs at depths approaching layer pinch-off. Therefore, regime II behavior is not expected to occur in material of this thickness and composition (the transition is directly from I to III).

5.5.4 Trench Wall Orientation

The specimens and model examples described above consisted misfit dislocations that approached trench walls in a sense *head-on*. It was not necessary to consider what glide planes the misfit dislocation glide segments were in as they reach a trench since the essential characteristics are identical. However, what if a trench wall is constructed so that it is no longer a plane of the form (11ℓ)?

A trench wall/misfit dislocation configuration with interesting properties is illustrated in Figure 5.21. A mesa may be fabricated with an edge along the [100] direction by photolithography. After etching and growth, the edge becomes a (01ℓ) wall. The two misfit dislocation glide segments moving in the $[1\bar{1}0]$ direction in Figure 5.21 experience two different environments as they approach the wall. For a wall angle of about 45°, the $[0\bar{1}1]$ oriented segment must immediately stretch to the mesa top as the misfit dislocation extends at the wall. In contrast, the [101] oriented segment stretches gradually.

These observations are put on a quantitative basis using the theory developed in this section with the geometry of Figure 5.21. As an example, a 300 nm thick

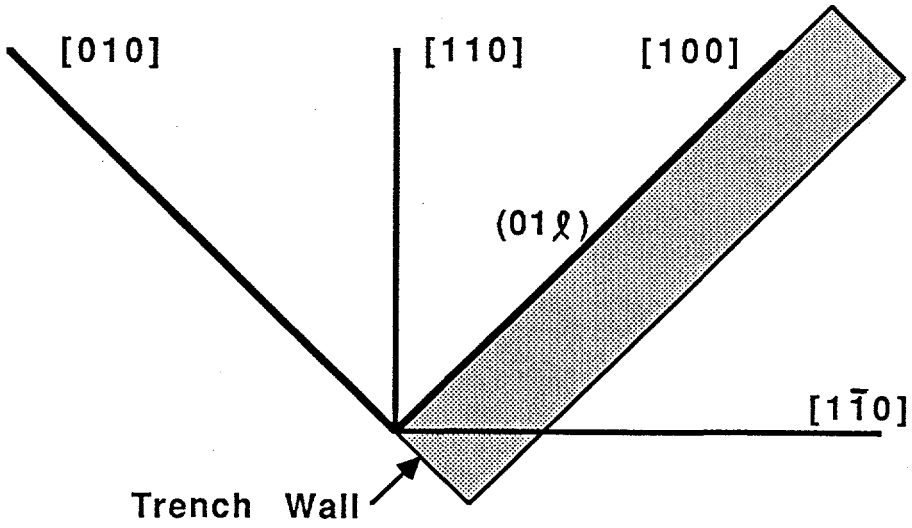

Figure 5.21: A plan view schematic of a trench wall oriented along the [001] direction. Misfit dislocations moving in the [1$\bar{1}$0] direction with forward directed glide segments on two different glide planes are shown as well. The trench can block one of them while allowing the other to continue.

$In_{0.04}Ga_{0.96}As$ is assumed to be grown over a 300 nm deep trench etched along the [100] direction. After etching and growth, the trench wall is assumed to be at an angle of 40° measured from the wafer surface. Figure 5.22 is a plot of the system energy with respect to misfit dislocation extension, ξ, similar to Figure 5.18. A $[1\bar{1}0]$ misfit dislocation with a [101] glide segment is unimpeded by the wall, since the system (free) energy drops as the misfit dislocation extension progresses. However, the $[0\bar{1}1]$ segment experiences a large energy barrier. Consequently, such a trench only partially blocks misfit dislocation motion.

It is possible to exploit the threading segment orientation selectivity to *filter* misfit dislocations of only one Burgers vector. Figure 5.23 illustrates a structure that can be used to study this filtering. Ion-damaging is used to nucleate misfit dislocations in only one direction ($[1\bar{1}0]$, for example), while growth temperature and/or doping type and concentration my be used to allow only α threading segment motion (preventing screw dislocation threading segment glide). Patterning and etching along the $\langle 110 \rangle$ directions will minimize misfit dislocation formation from sources other than the ion-damaged channel. Finally, a trench oriented along the [100] direction selects misfit dislocations in one particular glide plane. Consulting Table 2.1, Figure 2.7, and Figure 5.21, the only threading segment type that can reach the top of the mesa in Figure 5.23 must possess a Burgers vector of $b = [0\bar{1}\bar{1}]$.

Characterization techniques such as x-ray diffraction, ion-channeling, and TEM could be used to confirm that filtering has occurred. It is possible that the unique crystal strain in the epitaxial layer located on the filter mesas may possess interesting electronic and piezoelectric properties.

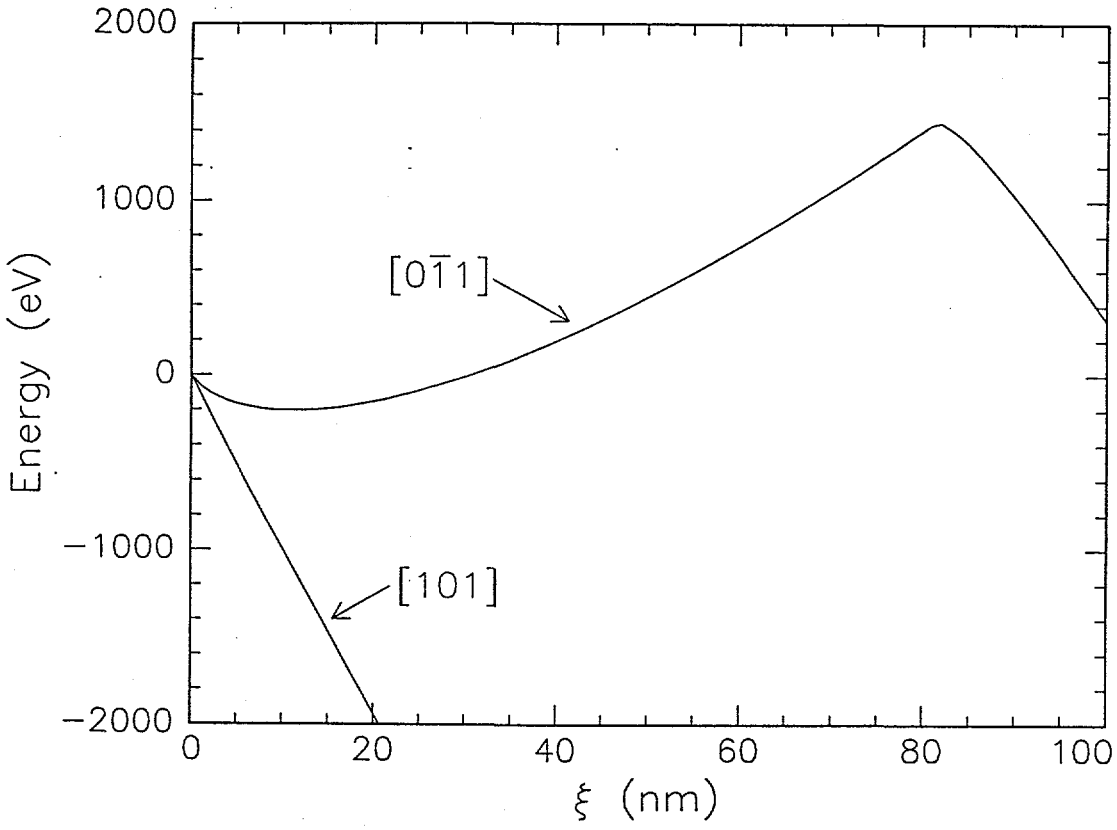

Figure 5.22: A plot of the system energy per misfit dislocation vs. the extension of the misfit dislocations, ξ. The epitaxial layer is 300 nm thick $In_{0.04}Ga_{0.96}As$ grown on a substrate with 300 nm deep trenches. The trench wall is a (01ℓ) plane. The indices refer to the two different glide segment line directions shown in Figure 5.21.

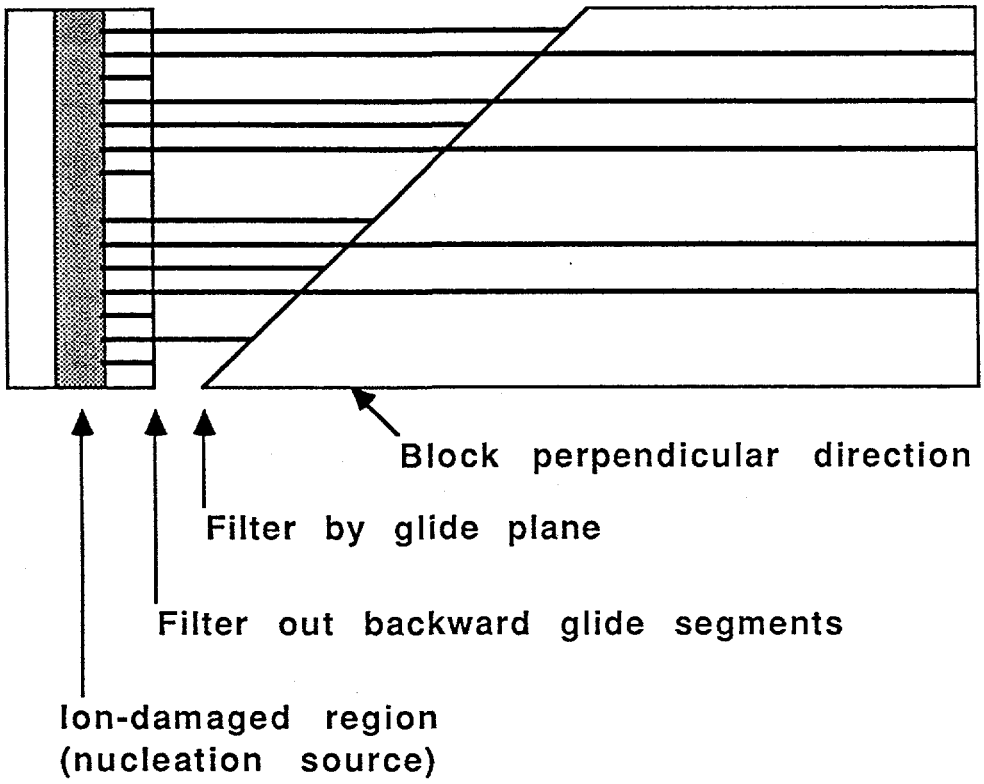

Figure 5.23: A plan view schematic of a Burger's vector filter structure.

5.6 Conclusions

To summarize, the misfit dislocation density in strained, continuous, OMCVD InGaAs layers can be significantly reduced by patterning and etching the GaAs substrate before growth. The etch depth needed to isolate misfit dislocations in $In_{0.04}Ga_{0.96}As$ is about 250 nm for a 300 nm thick epitaxial layer and 450 nm for a 600 nm thick layer. Isolation occurs at a trench depth of about 500 nm for 300 nm thick $In_{0.08}Ga_{0.92}As$. Three isolation regimes are seen, depending on the etch depth. In regime I, the shallowest depths, some dislocations can glide across the trenches, reaching adjacent islands. In regime II, dislocations are stopped, but are blocked only after gliding down into the trenches where they come to rest at the far side. In regime III, dislocations stop at the edge of the mesas because the strained epitaxial layer thins down below the critical thickness at the trench wall, preventing the misfit gliding segment from getting through. However, epitaxial layer discontinuity, or near discontinuity at large trench depths is not necessary to prevent the glide of misfit dislocations. Continuous layers in regime II material can stop virtually all of the dislocations from crossing from one isolated region to another.

Chapter 6

The Thermal Stability of Lattice Mismatched InGaAs Grown on Patterned GaAs

6.1 Introduction

In the last chapter, we showed that it is not necessary to create discontinuities in the strained epitaxial layer to isolate misfit dislocations. Trenches shallower than the epitaxial layer thickness itself were found to stop misfit dislocation glide segments at the mesa edges, even though the strained layer conformally covers the substrate. Three misfit dislocation isolation regimes were found, depending on the trench depth and level of epitaxial layer strain. The shallowest trenches (regime I) did not stop all misfit dislocation glide. The deepest trenches (regime III) stopped misfit dislocation threading segments at the top edge of the mesas, where the epitaxial layer thins,

thus, reducing the driving force for glide.

Regime II trenches, at depths between the other two regimes, completely stopped misfit dislocations by allowing threading segments to glide from mesas down into the trenches but prevented them from gliding back up the trench walls to adjacent mesas. The shape of the trench wall and the local strain field around it does not cause isolation since a segment, driven by the epitaxial layer strain, can make its way down a trench wall.

The dislocation densities in InGaAs grown by MBE on patterned GaAs substrates was discussed in Chapters 3 and 4. The misfit dislocation density of MBE grown InGaAs is generally higher than that of OMVPE grown layers of similar compositions and thicknesses.

In this chapter we investigate the thermal stability of the reduced dislocation densities on patterned GaAs substrates. One reason for the interest in high temperature stability is practical; if strained layers can be grown many times their critical thickness with very few interface defects, how robust is this material when subjected to device processing steps? Another point of interest is related to the unique way misfit dislocations are isolated in regime II OMCVD material. Can threading segments that stop at the bottom of trenches be induced to glide back up?

6.2 Experimental

Three types of strained InGaAs samples were studied and are described in Table 6.1. The substrate preparation is described in Chapter 4. The patterned GaAs substrates consisted of 200 μm by 200 μm square mesas separated by 10 μm wide trenches etched

Table 6.1: Specimens used in the annealing study.

Sample	In Composition and Thickness	Trench Depth	Comments
MBE-4	5%, 300 nm	1.0 μm	MBE grown,annealed at 600,700, 800, and 850°C.
9-G	4%, 300 nm	0.60 μm	Regime III OMCVD, annealed at 600, 700, 800, and 850°C.
9-E	4%, 300 nm	0.40 μm	Regime II OMCVD, annealed at 600, 700, 800, and 850°C.
4-H	4%, 300 nm	0.70 μm	Regime III OMCVD, edge etched before annealing at 800°C.
1-D	4%, 300 nm	0.35 μm	Regime II OMCVD, for comparison with other regime II sample, 9-E.

to depths shown in the table. Just before growth, the substrates were degreased, etched in HF, and in etched again in a dilute solution of H_2SO_4, H_2O_2, and water. The final etch removed about 80 nm of GaAs.

The sample grown by molecular beam epitaxy (MBE) consisted of a 300 nm GaAs buffer layer followed by a 300 nm $In_{0.05}Ga_{0.95}As$ layer, both n typed doped at 1×10^{18} cm^{-3} with Si. The growth was carried out at 520°C. The OMCVD samples consisted of a 300 nm GaAs buffer layer and a 300 nm $In_{0.04}Ga_{0.96}As$ layer, both Sulfur (n type) doped at 5×10^{18} cm^{-3} and both grown at 620°C. The samples were doped to these carrier concentrations to enhance the cathodoluminescence (CL) intensity,

as described in Chapter 2. The thicknesses and compositions were determined by Rutherford backscattering. Thickness measurements were confirmed by cleaving, staining, and imaging the cross-sections by scanning electron microscopy.

The samples were annealed in an AG Associates rapid thermal annealer for various times in an Ar atmosphere on a Si substrate. The samples were *capped* with a GaAs substrate to minimize thermal decomposition at elevated temperatures.

The misfit dislocations were measured by counting dark line defects at the GaAs/InGaAs interface by scanning cathodoluminescence. Figure 6.1 is an example of a typical CL image of the MBE grown sample. A square mesa can be seen, surrounded by 10 μm wide trenches. Each dark line corresponds to a misfit dislocation or a closely spaced group of dislocations (spaced less than 2 μm apart). When multiple dislocations occur in a closely spaced group, it can be inferred by the dark line contrast. As the density increases, it becomes difficult to precisely assign a dislocation count, as can be seen in Figure 6.2 (the same region as Figure 6.1 is shown after a 700°C, 180 second anneal). Based on the 2 μm minimum separation needed to resolve misfit dislocations, the maximum dislocation density that can be measured by this technique is about 5000 cm^{-1}.

Figures 6.1 and 6.2 show examples of the effectiveness of the isolation technique in suppressing dislocation propagation. Misfit dislocations on the central mesa are stopped before they reach adjacent regions. The misfit dislocation density of a 300 nm thick $In_{0.04}Ga_{0.96}As$ layer grown on an unpatterned substrate is 5000 cm^{-1} or more.

For very low dislocation densities, up to 30 mesas were sketched to calculate an

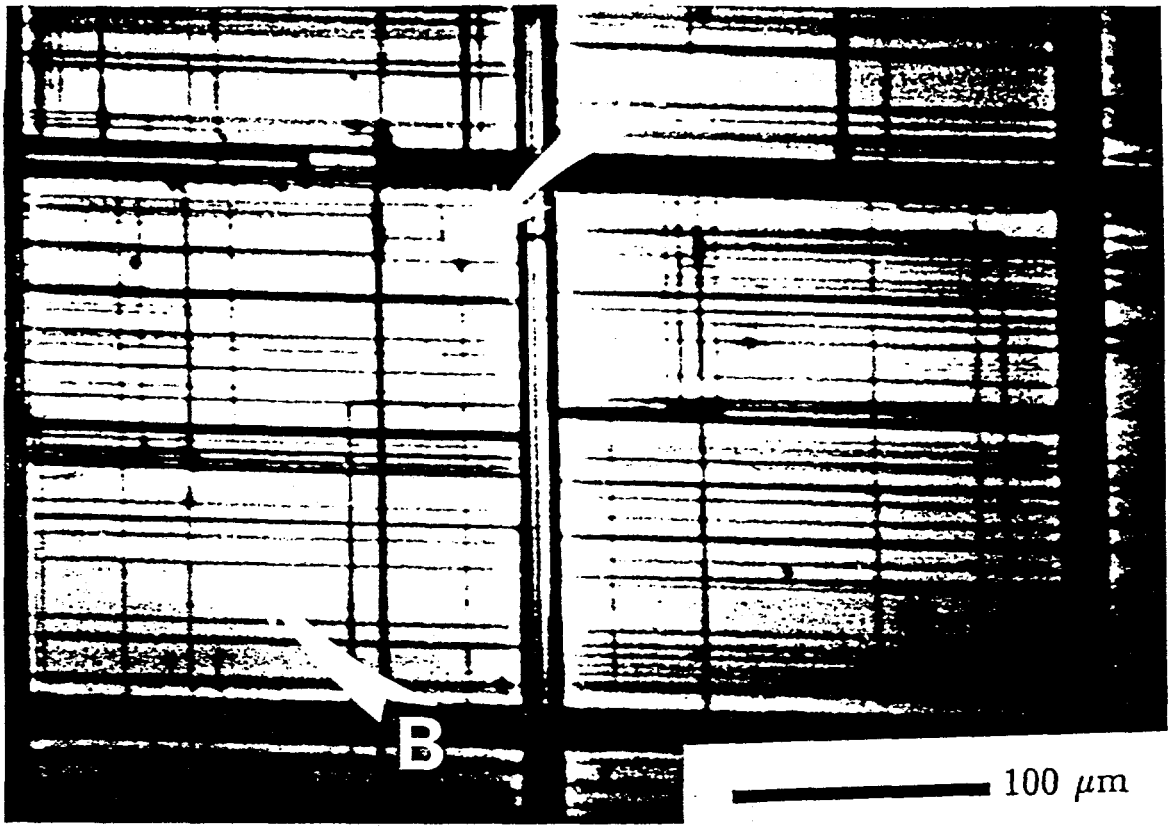

Figure 6.1: A CL image of misfit dislocations (dark lines) in strained $In_{0.05}Ga_{0.95}As$, 300 nm thick, grown by MBE on a patterned GaAs substrate. The pattern consists of 200 μm $\times$ 200 μm square mesas separated by 10 μm wide trenches, 1.0 μm deep. Misfit dislocations are formed in two ways: label *A* refers to a surface defect on the mesa (a dark spot) that nucleated a misfit dislocation below it. Label *B* refers to a horizontal misfit dislocation that appears to nucleate from one mesa edge and stop at the edge on the far side.

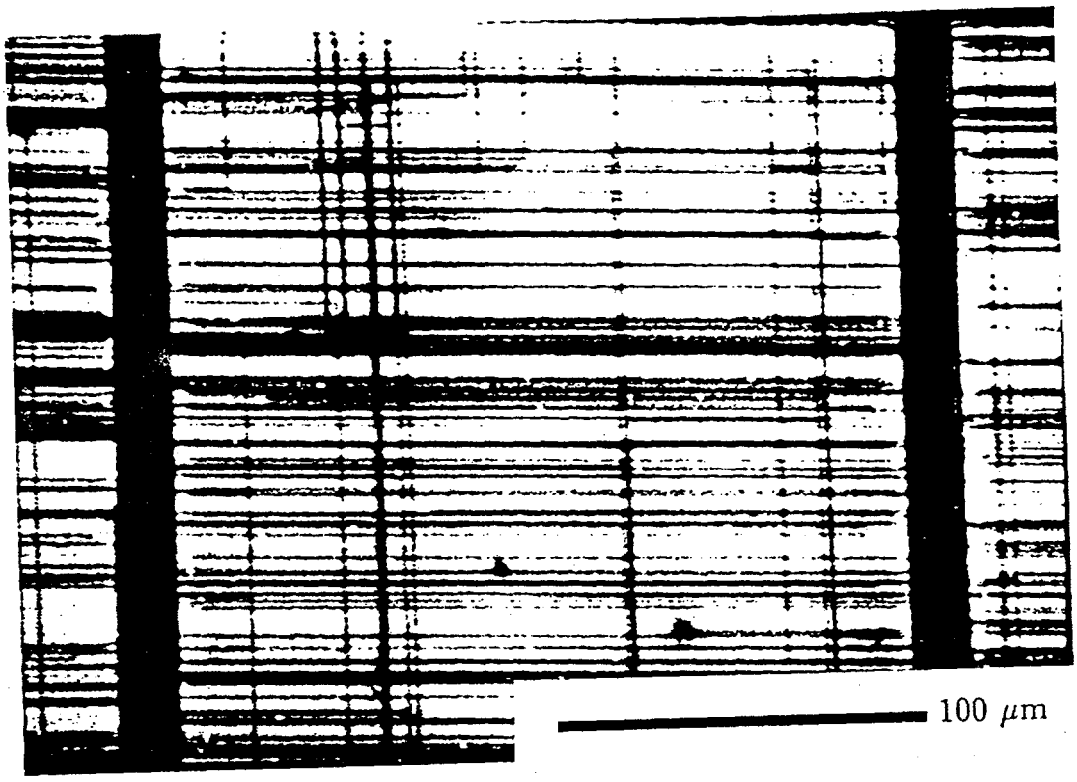

Figure 6.2: A CL image of the same mesa on the right in Figure 6.1 after annealing at 700°C for 180 s. A large number of edge nucleated misfit dislocations form, but essentially in only one direction (horizontal).

average misfit density. For higher densities, photos were taken of the CL images for later counting (usually averages of at least 8 squares). Identical regions were observed before and after annealing so that the nucleation of individual misfit dislocations could be tracked. Scanning a sample region with the CL electron beam before annealing did not affect the average dislocation density. The orientation of the dislocations in the substrate plane were found by wet etching, as described in Chapter 2.

To study the influence of the topology of the mesa edges on misfit nucleation properties, some samples were patterned with a photoresist mask of 160 μm by 160 μm squares registered to the mesa squares (known as *edge etched* material). The samples were then etched in a 100:1 solution of HCl and H_2O_2 for 60 s (approximately 1 μm deep) to remove the epitaxial layer edges that were formed during growth. The etchant is nearly isotropic, creating quarter round profiles at mesa edges in both of the $\langle 110 \rangle$ directions [Sha81].

6.3 Results and Discussion

6.3.1 The Effects of Anneal Time and Temperature

Essentially no change occurred in the average misfit dislocation density for any of the specimens studied after subjecting them to 600°C anneals for times up to 360 s. Since the epitaxial layers were grown at comparable temperatures (520°C for MBE and 620°C for OMCVD), any misfit dislocation nucleation sites active at these temperatures would already have been active during growth.

Two types of misfit dislocation nucleation sources appear in the as grown MBE

material, as is indicated in Figure 6.1. The feature labeled A is a nucleation source that is apparently a defect on the mesa surface. A particle adhering to the wafer before or during growth may create a large degree of local strain which in turn forms a misfit dislocation and its glide segment.

Other misfit dislocations, such as the one labeled B in Figure 6.1, extend from one mesa edge to another. Glide segments appear to nucleate at one of the edges and travel across the GaAs/InGaAs interface before being stopped at the far side.

The fact that foreign particles or threading dislocations are not the only nucleation sources on patterned substrates has been noticed before. Watson et al. studied the nucleation of misfit dislocations from the mesa edges and ion damaged regions [WTA+90]. It was found that pattern orientation and MBE growth conditions strongly influenced the nucleation rate of misfit dislocations in InGaAs (see Chapter 4).

Another aspect of the material in Figure 6.1 is the asymmetry in misfit dislocation density in the two perpendicular directions. The more numerous defects are α dislocations; the larger density of α dislocations compared to β dislocations in InGaAs and similar materials has been reported by other researchers [FWP+89,KCH+88, WTA+90].

It is interesting to note, however, that the asymmetry does not appear to be caused by the particle defect nucleation sources but by edge nucleation. After subjecting the same sample to a 700°C anneal for 180 sec, many more misfit dislocations form in essentially only the α direction (Figure 6.2). These new dislocations all appear to be edge nucleated types.

Figure 6.3 is a plot of the average misfit dislocation density versus annealing time at 700°C for the three categories of strained layer material. The asymmetry in the α and β densities is clearly seen in the MBE material. The edge nucleation mechanism is active for only one misfit dislocation core type.

After annealing the OMCVD grown samples at 700°C the new dislocations formed were mostly edge nucleated. A small α/β asymmetry is seen in the OMCVD regime II specimen, but the difference is much less pronounced than in the MBE material. Only a few new misfit dislocations formed in the regime III OMCVD sample. After 180 s of annealing, the α misfit dislocation the density was as large as 4000 cm^{-1} for the MBE material compared to only about 100 cm^{-1} for the regime III OMCVD sample.

It is surprising that the OMCVD regime II and III samples, which were processed and grown at the same time (they were separated only at the trench etch step), differed markedly in their misfit nucleation properties. The larger misfit density of the regime II sample is not due to "breaking the barrier" created by the trenches. No evidence was found of misfit dislocations gliding down one trench wall and up the other side. Mesa isolation remains active at 700°C for the regime II material, but why are edge nucleation sites more active in it than regime III material? A possible explanation is related to the topology of the epitaxial layers covering the mesas and trenches. As discussed in Chapter 5, it was found that the epitaxial layer thins out at the edges of deeper (regime III) trenches. If nucleation of misfit dislocations occurs at a section near the edge where the strained layer is below or near the critical thickness, then there is no local driving force pushing the loop toward the mesa center. Regime

II material, on the other hand, consists of a relatively thick epitaxial layer at the trench sidewall. If misfit dislocations form at an edge, there exists sufficient driving force to push their glide segments along.

One very important feature in Figure 6.3 is that the misfit dislocation density saturates with annealing time. Both the MBE and the OMCVD regime II specimens show a limit to the number of misfit dislocations that form. For all three of the materials, the final dislocation density is much lower than the equilibrium density predicted by Matthews' theory (1.1×10^5 cm^{-1} in each direction for a 300 nm $In_{0.04}Ga_{0.96}As$ layer using the methods of Chapters 2 and 4). Although new misfit dislocation nucleation sources appear, the number is insufficient to relax the strained layer. Drigo et al. studied the relaxation of InGaAs on unpatterned GaAs subjected to anneals at a comparable temperature and found that limited nucleation of misfit dislocations also prevented the full relaxation of that material as well [DAC+89].

Figure 6.4 is a plot of the misfit dislocation density as a function of time for an 800°C anneal. Error bars corresponding to plus or minus one standard deviation from the average misfit dislocation density are also shown. At this temperature, the asymmetry between the α and β misfit densities in the MBE sample disappears. The MBE misfit dislocation densities was beyond the measurement capability of the CL technique (greater than 5000 cm^{-1}) after 90 sec. As was observed at the lower anneal temperature, misfit dislocations appear to nucleate at MBE mesa edges - but this time misfit dislocation nucleation sources were also activated at edges that produce β dislocation cores and overwhelmed the as-grown misfit asymmetry.

Very little difference was found between the dislocation densities observed in the

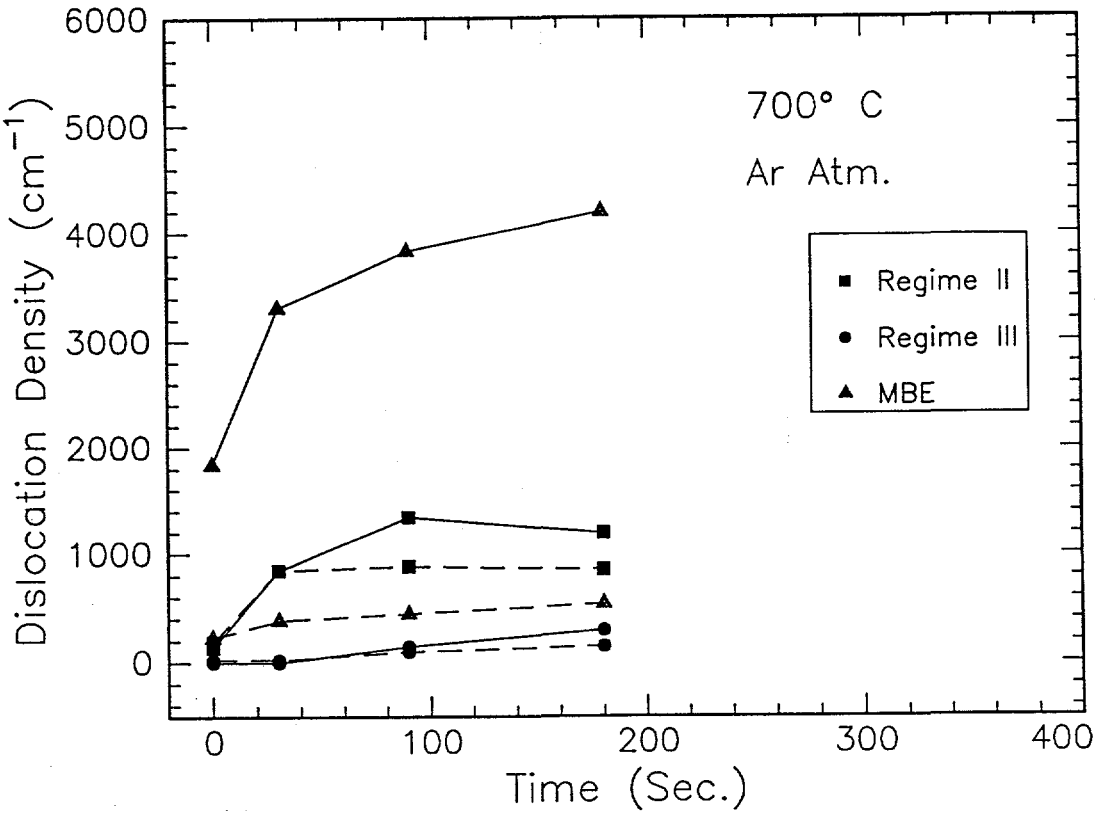

Figure 6.3: A plot of dislocation density as a function of anneal time at 700°C. The squares are the regime II OMCVD material, the circles are the regime III OMCVD material and the triangles are the MBE material. The solid lines connect data points corresponding to dislocations that lie in the $[1\bar{1}0]$ direction (α dislocations) and the dashed lines correspond to those in the [110] direction (β dislocations).

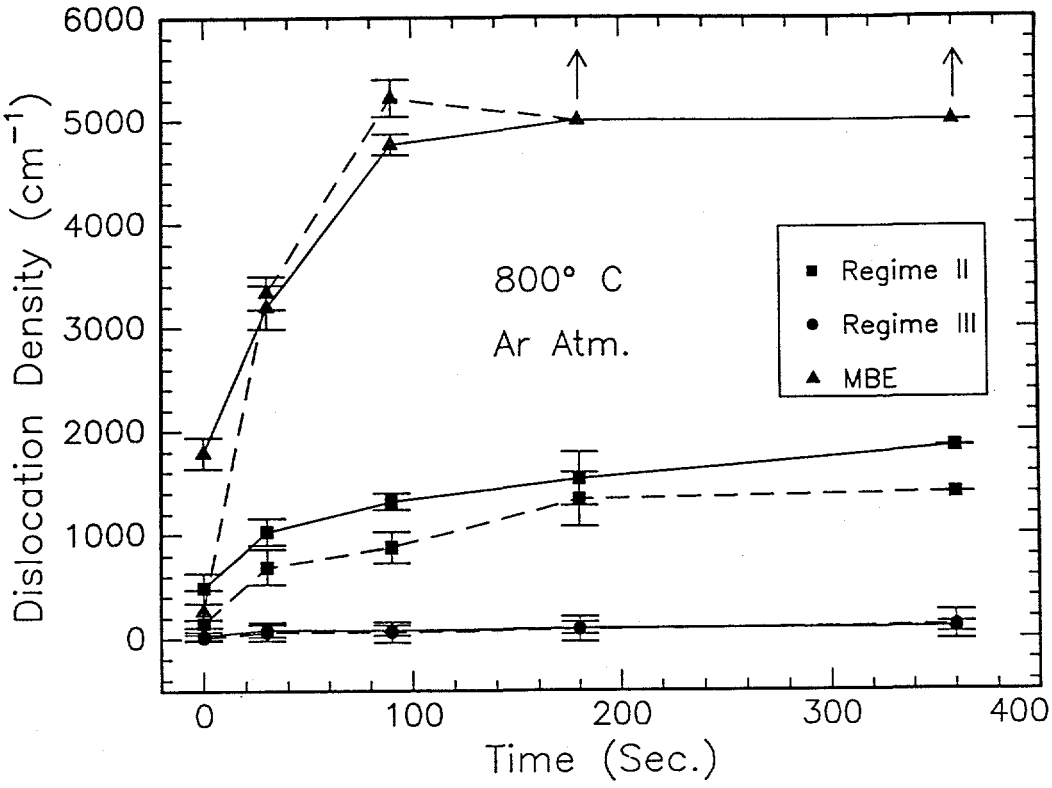

Figure 6.4: A plot of dislocation density as a function of anneal time at 800°C. The squares are the regime II OMCVD material, the circles are the regime III OMCVD material and the triangles are the MBE material. The solid lines connect data points corresponding to dislocations that lie in the $[1\bar{1}0]$ direction (α dislocations) and the dashed lines correspond to those in the [110] direction (β dislocations). Error bars corresponding to plus or minus one standard deviation from the mean misfit dislocation density are included.

OMCVD films annealed at 700 and 800°C. No new nucleation sources are activated at the higher anneal temperature, other than those that form at the lower temperature.

No conclusive evidence was found that showed misfit dislocations crossing trenches in most regime II samples. An exception is illustrated in Figure 6.5, a CL image of one regime II sample that exhibited unique characteristics when annealed at 800°C for 30 s. The new misfit dislocations that formed were found to react with surface contaminants and cross-slip. The dislocation labeled AB in Figure 6.5 appears to glide up one one trench wall at A and down another trench wall at B (or visa-versa).

Figure 6.6 again shows the misfit dislocation density as a function of time with an anneal temperature of 850°C, the highest one studied. The misfit dislocation density in the MBE material grows to greater than 5000 cm^{-1} at less than 15 s while the OMCVD samples are much more stable. Again, the misfit dislocation density saturates with time in the OMCVD samples, but at this temperature the final density is much higher than that found at the lower anneal temperatures. A larger number of nucleation sources are activated than that found in the lower temperature heat treatments of the OMCVD materials. The saturation densities of the regime II and III specimens are closer at this temperature, suggesting a new nucleation mechanism that they both share is active.

6.3.2 The Effect of Surface Topology

The most notable difference between the MBE grown samples and the OMCVD material is the cross-sectional profile of the epitaxial layers. The MBE grown InGaAs

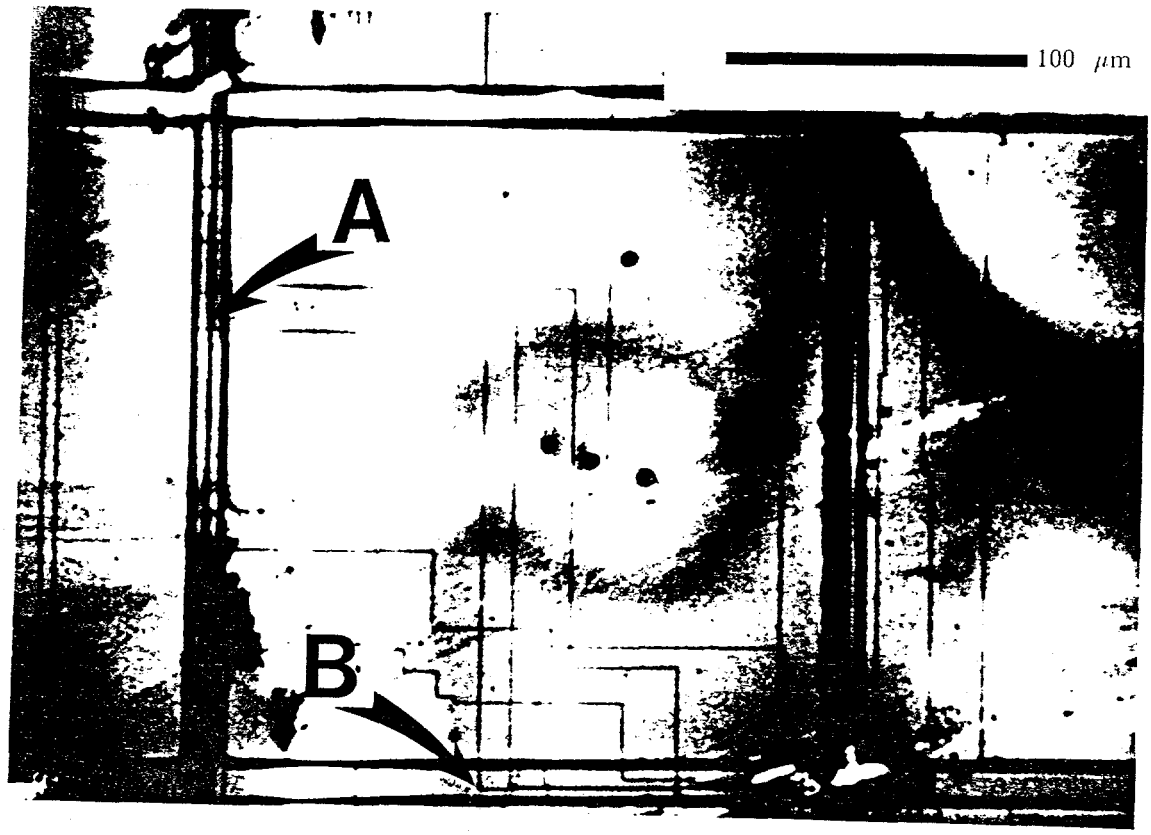

Figure 6.5: A CL image of misfit dislocations that glide and cross-slip in a regime II OMCVD specimen after annealing at 800°C for 30 s. One misfit dislocation can be traced from the trench at the label "A", across the mesa and to the bottom of the trench at label "B". Regime II dislocation isolation no longer appears to hold.

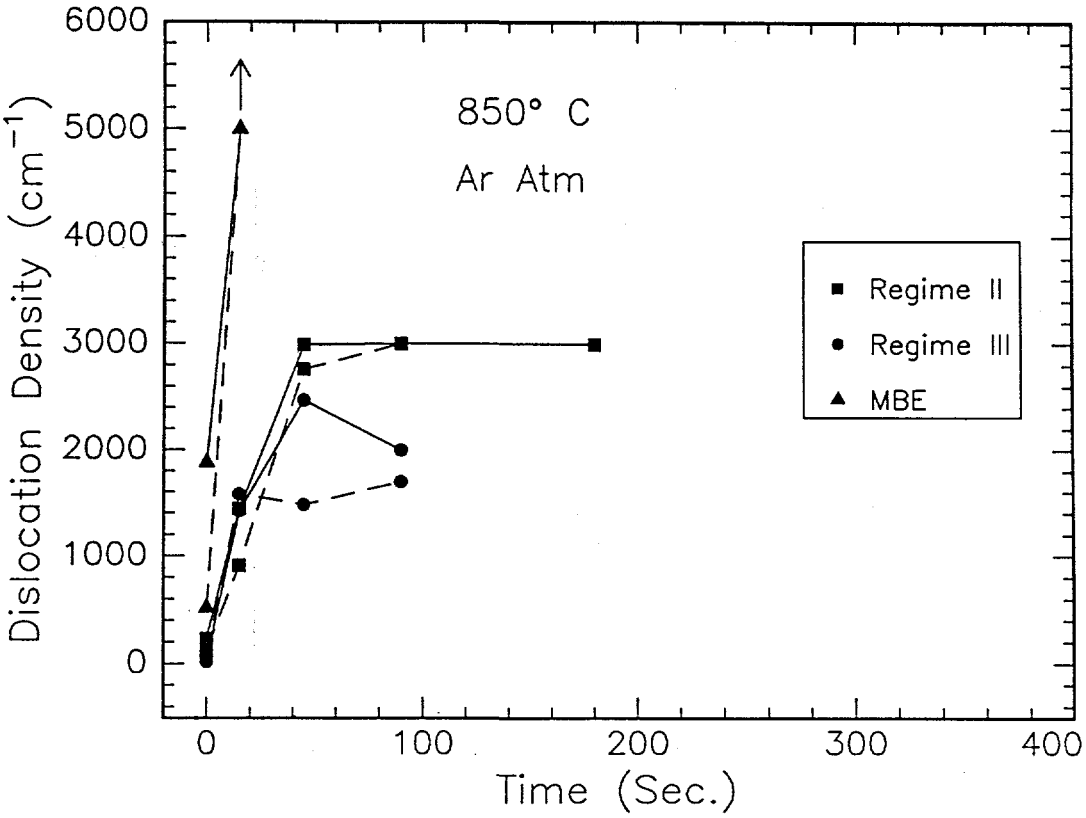

Figure 6.6: A plot of dislocation density as a function of anneal time at 850 °C. The squares are the regime II OMCVD material, the circles are the regime III OMCVD material and the triangles are the MBE material. The solid lines connect data points corresponding to dislocations that lie in the $[1\bar{1}0]$ direction (α dislocations) and the dashed lines correspond to those in the [110] direction (β dislocations).

ends abruptly at the mesa edge and creates an exposed InGaAs/GaAs interface, while the OMCVD material forms a continuous layer over the substrate surface. It seems reasonable to expect that the larger nucleation density of the MBE material at the edge during annealing is caused by the exposed interface.

A Regime III OMCVD sample was *edge etched* to expose the InGaAs/GaAs interface in this material as well. The sample was subjected to an anneal at 800°C for 30 sec. - conditions that lead to a large difference in misfit dislocation densities between MBE and OMCVD material. However, the dark line defect density found in this material after the anneal averaged about 300 cm^{-1} - between regime II and regime III misfit dislocation densities at those conditions - and much less than the MBE density (see Figure 6.7). The sample topology is therefore not the controlling factor in misfit dislocation edge nucleation in the MBE material.

The nucleation properties of the OMCVD and MBE films must differ because of characteristics inherent in the material, such as point defect density. One important characteristic that sets the two types of material apart is the n-type dopant used in the epitaxial growth. The Sulfur (OMCVD) or Silicon (MBE) impurities are present in concentrations exceeding 1×10^{18} cm^{-3} and can be expected to play some role in the formation and propagation of other defects in InGaAs. At these concentrations, the dopants are the most abundant impurities in the crystals and should overwhelm the effects of vacancy concentration differences, for instance. We speculate that the particular dopant may also be responsible for the difference between the α and β misfit dislocation nucleation density in MBE material. Another important fact that differentiates the two growth techniques is that OMCVD growth operates closer to

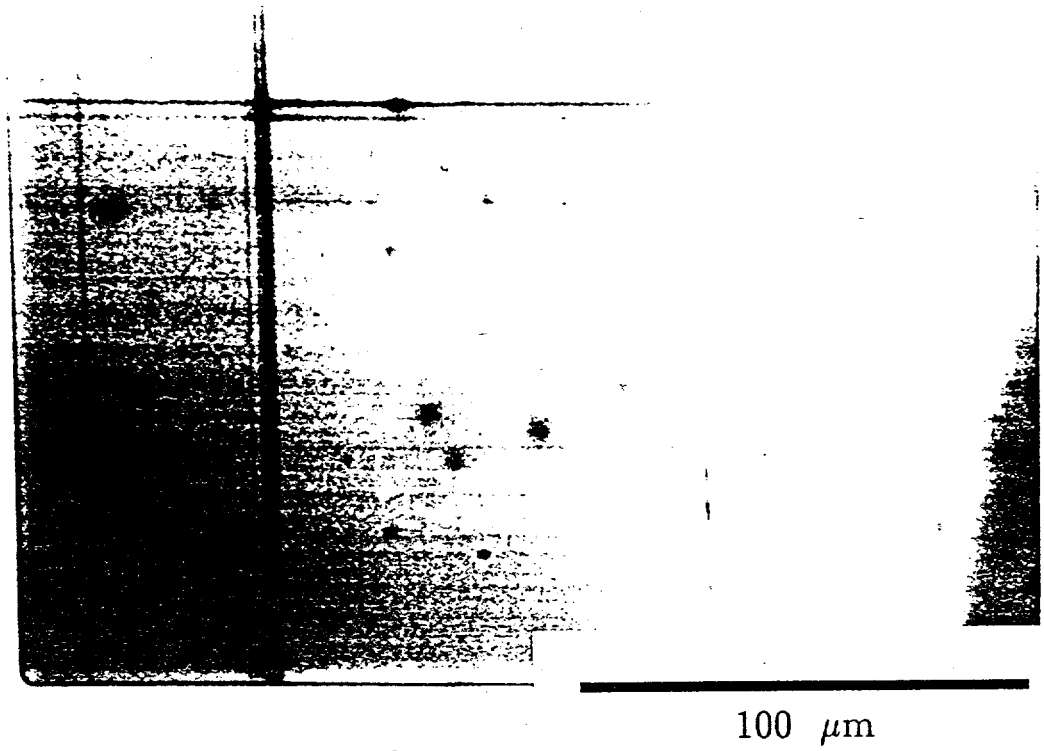

Figure 6.7: A CL image of misfit dislocations in a regime III OMCVD sample after annealing at 800°C for 30 s. Before annealing, the sample was patterned and etched to remove the as-grown trench wall profiles and expose the epitaxial layer/substrate interface (edge etching). A low misfit dislocation density is found even after edge etching, indicating that the surface topology does not control the edge nucleated misfit dislocations in MBE material, which has a similar profile.

thermodynamic equilibrium than does MBE. Hence there are fewer avenues available to suppress temporary concentration or stoichiometry deviations during MBE growth relative to OMCVD. These deviations may contribute to the higher density of nucleation sites in MBE material.

6.4 Conclusions

Annealing strained epitaxial layers grown on patterned substrates induces new misfit dislocations to form by the apparent nucleation of half-loops that glide along the interface, leaving a strain relieving dislocation behind. These dislocations nucleate for the most part only at edges created by the patterning and etching before epitaxial growth.

OMCVD InGaAs epitaxial layers grown on patterned GaAs substrates possess a very small misfit dislocation density, and even after severe annealing for up to 300 s at 800°C the defect density is less than 1500 cm^{-1}. Though their density increases with annealing, the misfit dislocation density remains well below the density found in unpatterned substrates. The MBE grown epitaxial layers are much less stable; misfit dislocations nucleate in much greater numbers in MBE material at all of the temperatures studied.

The misfit dislocation nucleation properties of OMCVD grown material is found to depend on the trench depth. Films deposited on patterned substrates with deeper trenches (greater than 0.5 μm) are more stable, apparently because a thinning of the epitaxial layer occurs at the edges of these trenches. A thinner layer means less strain energy is available in the region where the misfit dislocations apparently

nucleate. Furthermore, if the layer thickness locally falls below the critical thickness, the propagation of misfit dislocations is inhibited.

The reason that MBE material is less stable than OMCVD grown samples is not epitaxial layer topology. OMCVD material that was etched to expose the InGaAs/GaAs interface (and thereby "mimic" an MBE grown profile) is no less stable than unetched material. The different dopants used in the two growth processes or the difference in concentrations of other defects may cause the different nucleation properties of these materials.

Chapter 7

Misfit Dislocations in ZnSe Strained Epitaxial Layers Grown on Patterned GaAs

7.1 Introduction

ZnSe epitaxial layers on GaAs are not only of important technological interest; this material system is ideally suited as a model system of mildly mismatched epitaxial layers as well. ZnSe has a large, direct bandgap, facilitating CL characterization. The lattice parameter of ZnSe at 300 K is 0.56683 nm, about 0.27% larger than that of GaAs [KP87]. However, a new twist is added; the epitaxial layer is a II-VI semiconductor, grown on a III-V substrate.

ZnSe on GaAs is of interest because the II-VI compound luminesces in the visible region - allowing one to create blue LED's or lasers on GaAs substrates. Blue LED's

and lasers have been demonstrated in MBE grown material, however problems with the electrical and optical properties - some caused by defects at the heterojunction interface - have so far limited their performance [RBS+90,HCDP90].

One problem that has so far limited the practical application of these devices is the inability to create low resistivity p type ohmic contacts in ZnSe. One solution has been to use the GaAs as a p contact [HCDP90]. This requires a good quality epitaxial layer interface with a defect density as low as possible. Thus, patterning is of interest. Haase et al. found that in addition to a voltage drop across the interface due to (possibly) misfit dislocations, the valence band offset of 1.3 ev must be overcome [HCDP90]. The devices had large turn-on voltages of about 15 V. The resistance of the contacts and heterojunction defect level are expected to seriously degrade the performance of LEDs over time and probably preclude the operation of lasers (devices that are very sensitive to non-radiative defects and temperature).

Ren et al. succeeded in creating working ZnSe LEDs on GaAs with a p type contact on the ZnSe [RBS+90]. The MBE grown devices had large turn-on voltages, presumably (in part) due to the low p-type doping level in the vicinity of the contact.

As with InGaAs on GaAs or GeSi on Si, the linear interface defect density can be reduced by patterning before epitaxial growth. The unique interaction between misfit dislocations and other interface defects in OMVPE ZnSe allows one to explore the nature of misfit dislocation propagation on patterned substrates.

s ap

7.2 ZnSe Growth

Patterned and etched substrates of GaAs were prepared as described in Chapter 4. The photomask pattern is shown in Figure 4.1. The OMVPE epitaxial growth was carried out at the University of Florida in a system capable of supplying H_2S, H_2Se, and organometallics of Zn, S and Se, as well as N_2 dopants and AsH_3. Figure 7.1 is a schematic of the system, courtesy of Balu Pathangey at the Microfabritech facility at the University of Florida.

Table 6.1 lists the growth conditions for each of the samples tested. They were prepared using the substrate cleaning techniques described in Chapter 3. Initial tests were conducted at a growth temperature of 350°C since the previous ZnSe specimens were found to have good luminescence properties (on unpatterned substrates). This is also a typical MBE growth temperature [PCMS87].

Figure 7.2 is a typical CL image of this material, reminiscent of the poor quality InGaAs described in Chapter 4. The epitaxial layer was about 500 nm thick - exceeding the estimated critical thickness by about a factor of 10. In spite of the thick strained layer, no dark line defects were seen.

However, there was CL contrast at the ZnSe/GaAs interface. Figures 7.3, 7.4, and 7.5 are images recorded at three different electron excitation energies. As described in Chapter 2, changing the beam energy changes the position of the excitation volume in the sample, so that rudimentary depth profiling can be conducted. The CL images in Figure 7.3 and 7.4, at 10 KeV and 15 KeV, respectively and at the same beam currents show a pair of bright rings emanating from the corners of two etched

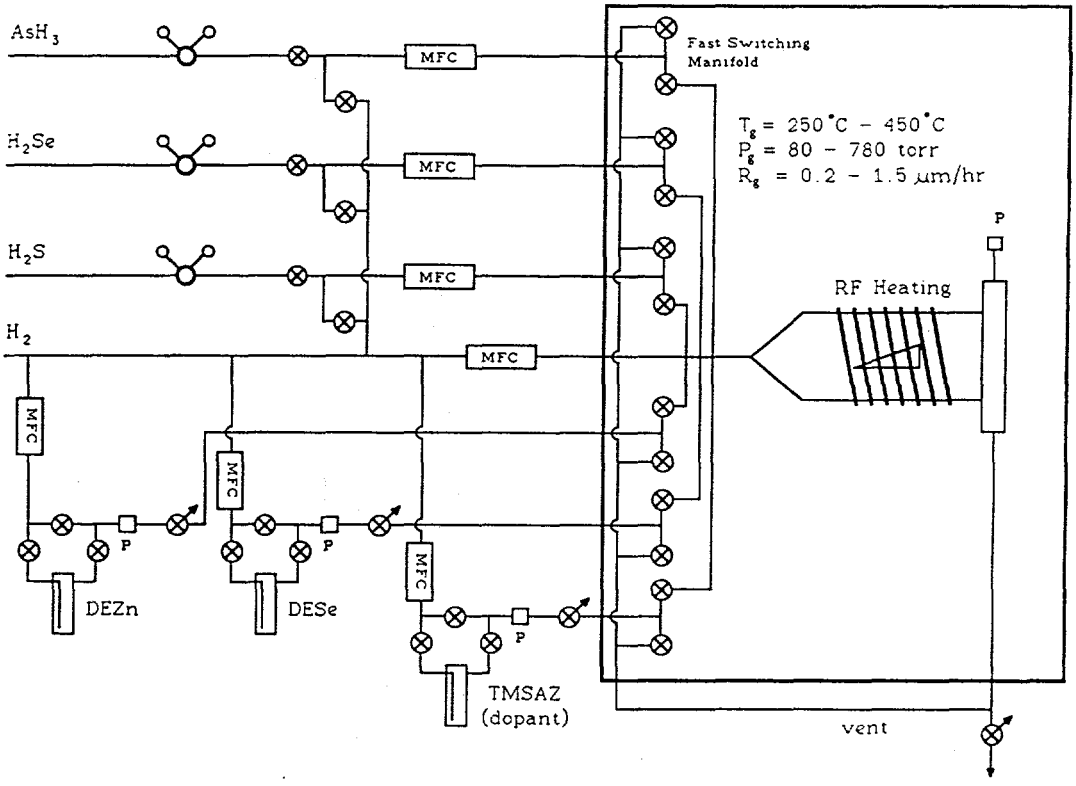

Schematic of ZnS_xSe_{1-x} MOCVD system and typical operating conditions.

Figure 7.1: A schematic diagram of the University of Florida OMVPE reactor.

s ap

Table 7.1: Growth Characteristics of OMVPE ZnSe on GaAs.

Sample ID	Growth Temperature (°C)	Comments
GPW-094, GPW-095	350	"Grainy" CL interface contrast, epi layer completely relaxed (x-ray diffraction), no AsH_3 surface clean, low pressure growth.
GPW-102	350	Some linear defects seen in CL - but not in [110] directions, AsH_3 surface clean at 550°C, low pressure growth. TEM dislocation density 10^8 cm^{-2}.
GPW-103	420	Many linear defects seen in CL - but not in [110] directions, AsH_3 surface clean at 550°C, high pressure growth.
GPW-108	440	Linear defects seen in CL - look like β misfit dislocations, AsH_3 surface clean at 550°C, high pressure growth.

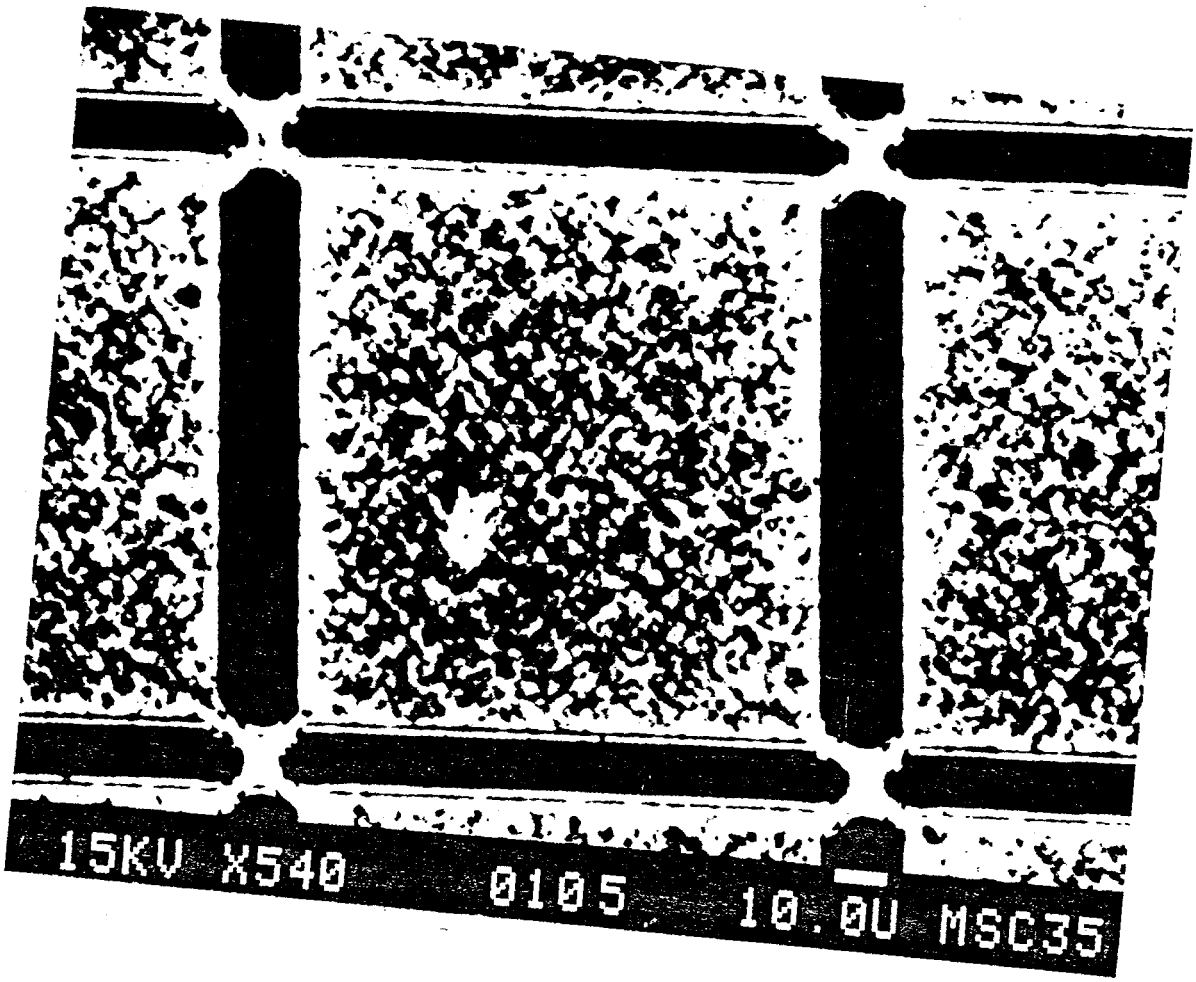

Figure 7.2: A CL image of ZnSe on GaAs with poor interface quality.

wells. The rings are most likely caused by small droplets of water that that were not removed in the final N_2 blow-off just before growth and subsequently slowly evaporated, leaving residual dissolved solids on the GaAs surface (or protecting the surface from contamination). Since no liquids contacted the samples after growth, the rings cannot be on the ZnSe surface and it must be concluded that the contrast is caused by the distribution of electrically active impurities at the ZnSe/GaAs interface.

Although the images in Figures 7.3 and 7.4 are similar, there is much more contrast at the higher electron energy. The reason for lower contrast for a shallower excitation volume is probably because non-radiative surface recombination dominates. At 15 KeV, the interface recombination properties become more important. At 25 KeV, Figure 7.5, the bright rings are no longer apparent, but a dark *comet-shaped* feature is prominent on the right hand side. At this voltage, most of the electron-hole pairs are generated deep within the GaAs below the epitaxial layer. Since ZnSe is transparent to the GaAs direct bandgap emission, much of the luminescence originates from the substrate. Consequently, the comet is a non-radiative defect in the GaAs.

The x-ray diffraction rocking curve of sample GPW-102 was measured on a Phillips MPD1880/HR diffractometer at the University of Florida in Gainesville, FL. The (004) reflection showed that the ZnSe epitaxial layer was completely relaxed - indicating that some extended defects of some form must be relieving lattice mismatch strain. Cross-sectional TEM (observed at the University of Florida) showed that there were indeed many dislocations at the interface; so many, in fact, that they formed a tangled bundle at the ZnSe/GaAs interface. The threading dislocation

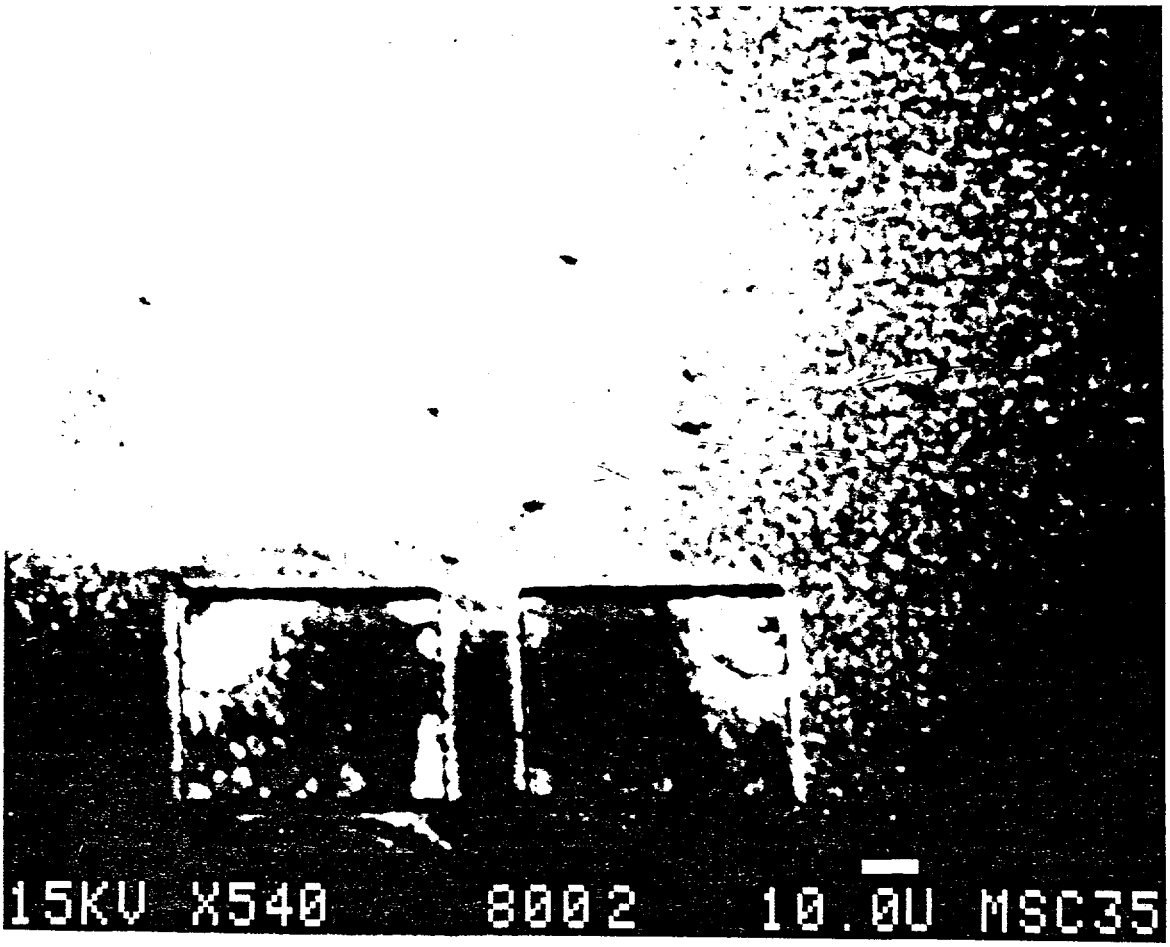

Figure 7.3: CL images of ZnSe grown on patterned GaAs at 350°C. The electron beam excitation voltage is 10 KeV.

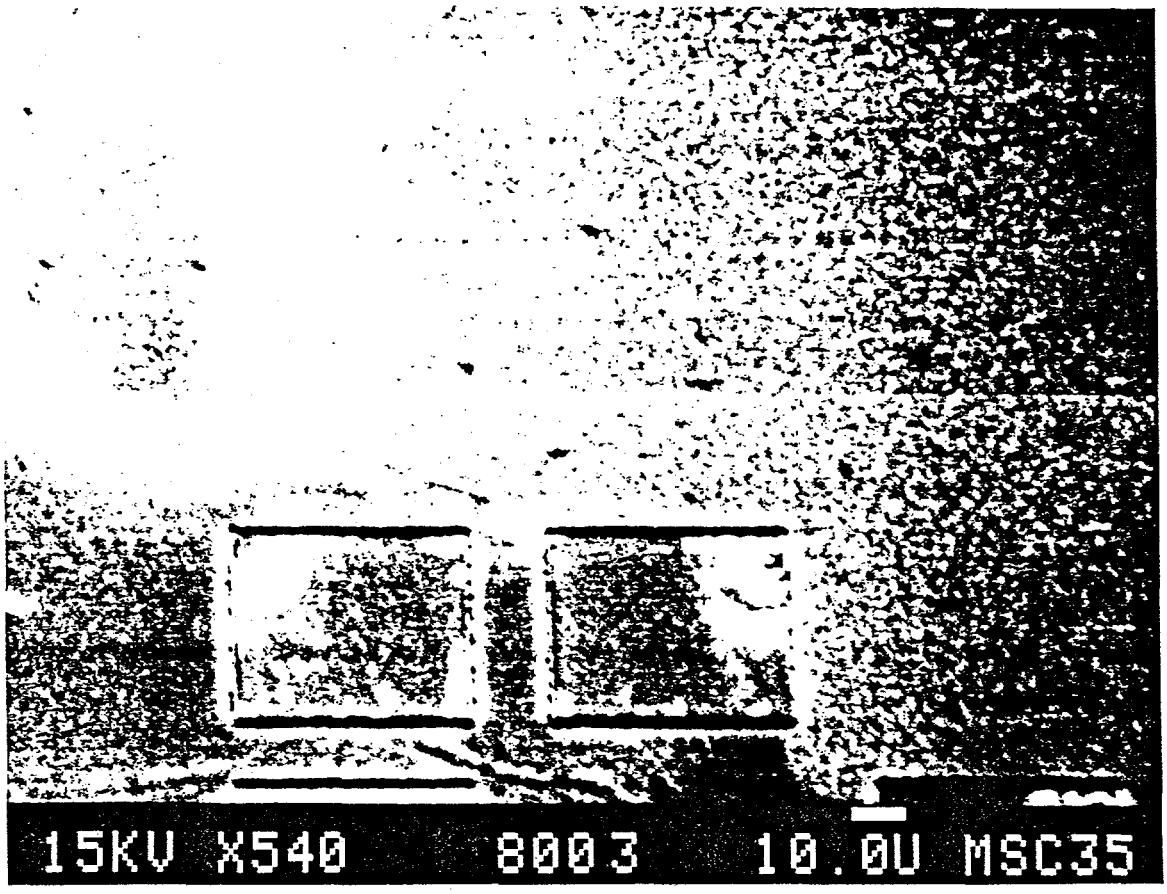

Figure 7.4: A CL image of ZnSe grown on patterned GaAs at 350°C. The electron beam excitation voltage is 15 KeV in the same region as Figure 7.3.

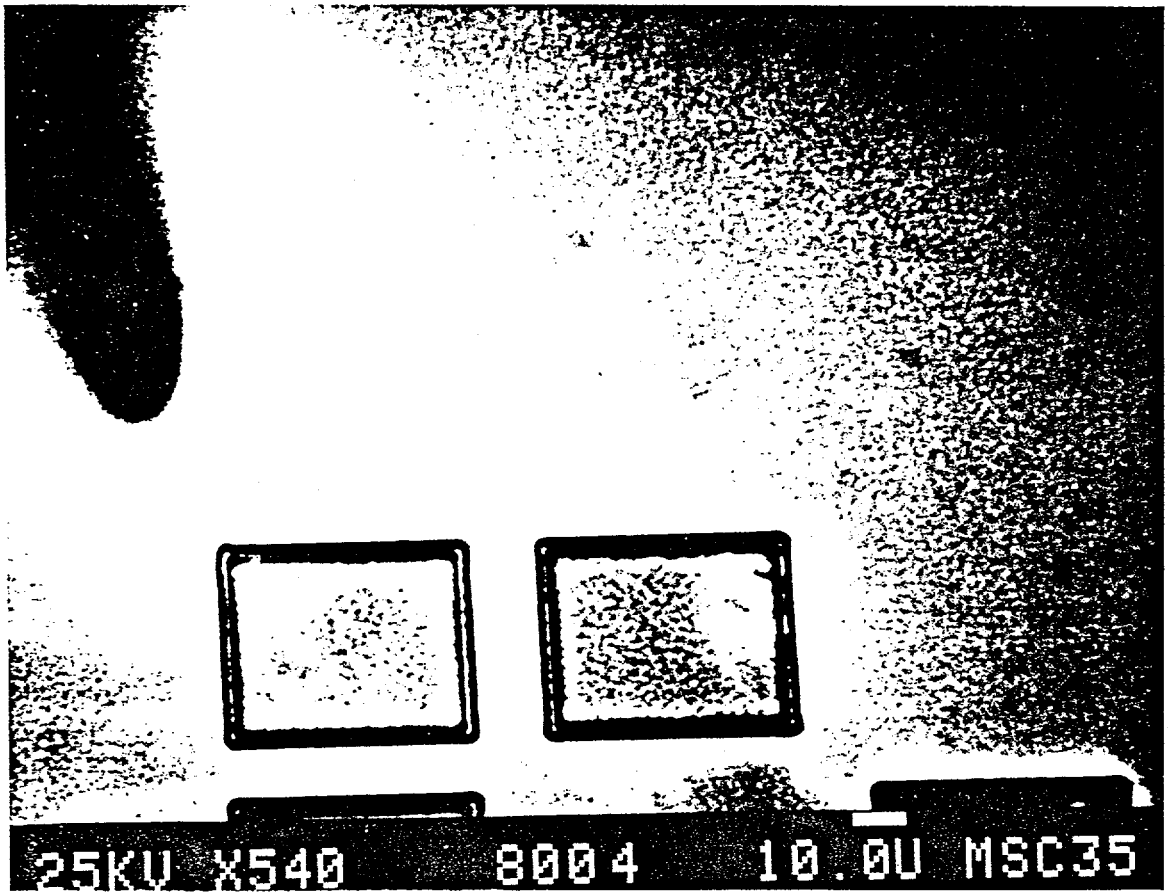

Figure 7.5: A CL image of ZnSe grown on patterned GaAs at 350°C. The electron beam excitation voltage is 25 KeV in the same regions as Figures 7.3 and 7.4.

density in the epitaxial layer was found to be about 2×10^8 cm^{-2}, measured by planar TEM (by the author, at Cornell, using the techniques described in Chapter 4). Thus, many more thread segments were present than were necessary to relieve strain if those dislocations were allowed to glide a distance as small as 30 μm and form misfit dislocations. No misfit dislocations were observed however.

Both the texture of the CL contrast at the interface and the high dislocation density indicate that the samples GPW-094 and GPW-095 were grown on poorly prepared substrates; if, for instance, even a small fraction of the GaAs was covered with a thin native oxide, it could interfere with growth and act as a misfit dislocation nucleation source. The author believes that this is indeed what happened with those samples. Again (as in Chapter 3), the final preparation of the substrate surface was found to be critical for good growth. Since the GaAs specimens were not heated to about 650°C, the thin native could not be removed after the sample was loaded into the reactor. The samples that followed, GPW-103 and GPW-108, were treated in the growth chamber by heating them to 550°C for several minutes in H_2 and AsH_3 to ensure that any native oxide was removed. There was also strong evidence that an air leak existed during the earlier growths. The system pressure was therefore increased to minimize the leak. Unfortunately, the high pressure growths had poor thickness uniformity, so that only regions of the wafers that were immediately adjacent to one another could be meaningfully compared.

Sample GPW-108, grown at 440°C, was found to have surface corrugations (using interference contrast in an optical microscope) that suggested the presense of misfit dislocations. Dark line defects were found that did resemble the familiar misfit dislo-

cations of the InGaAs/GaAs system. Figure 7.6 through 7.9 are CL images of dark line defects in regions of 100, 200, 400 and 800μm sized square mesas, respectively. Note the dark vertical lines in each of the photos. Chemical etching, as described in Chapter 2, revealed that these dislocations lie in the [110] direction, so that they must be β type dislocations if they relieve strain in the epitaxial layer.

Figure 7.10 is a plot of the measured misfit dislocation density versus mesa size for GPW-108. For reference, the data for InGaAs is also shown (the triangles). One curve shows the misfit dislocation density estimated from the surface corrugations (the squares). The dark line defect density is represented by the circles. Note that although the optical and CL measurements follow the same trends, the surface corrugation method significantly underestimates the defect density.

Although the dislocation density of both ZnSe and InGaAs increase monotonically with mesa size, the relationship is certainly not linear for ZnSe/GaAs, as Figure 7.10 shows. Patterning has less influence at larger mesa dimensions, implying that the misfit dislocation lengths are no longer limited solely by the mesa dimensions, but by some other factor as well.

7.3 Discussion

One surprising fact is that the dark line defects seen in the CL images of Figures 7.6 through 7.9 must correspond to β type misfit dislocations if they are to relieve stain in the ZnSe layer. α dislocations are absent. In contrast, if any preference is found in misfit dislocation core type in InGaAs layers, it is always α dislocations that are more numerous.

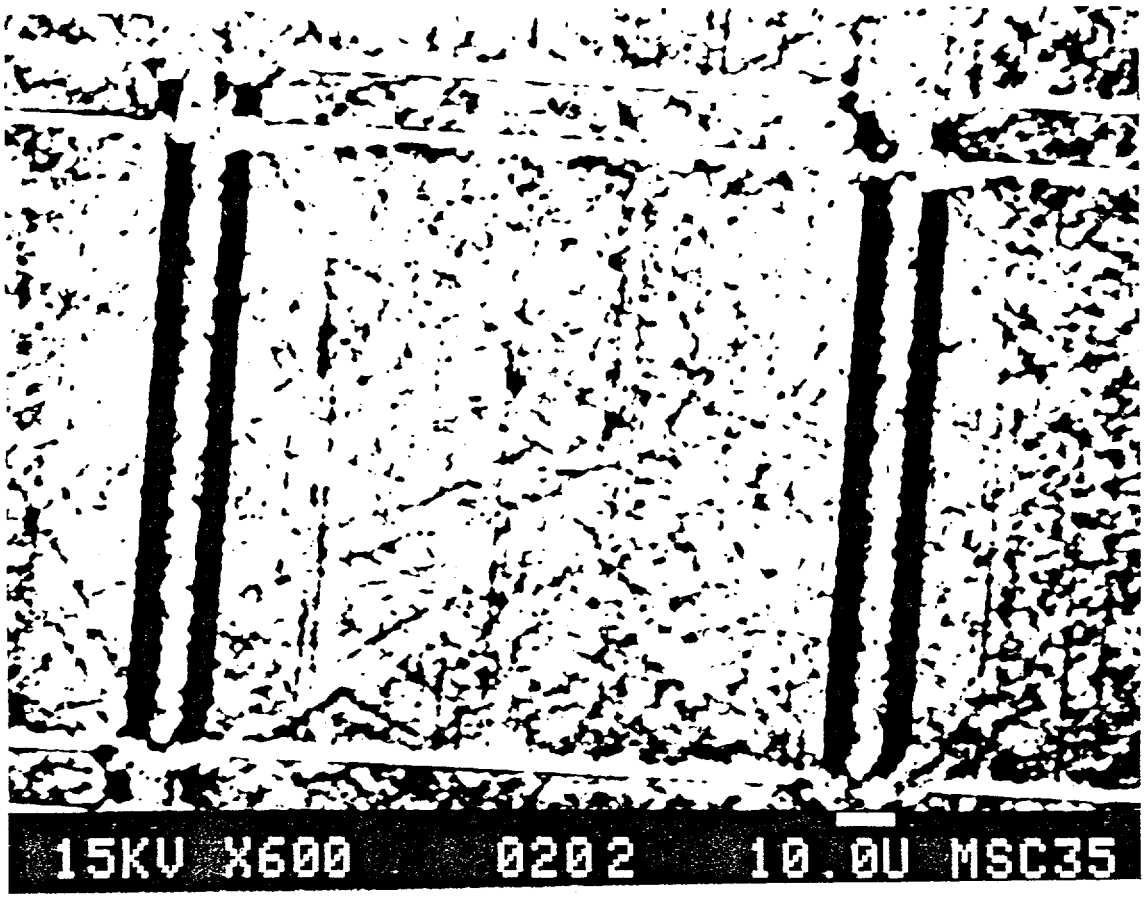

Figure 7.6: CL images of ZnSe grown on patterned GaAs at 440°C. The vertical dark-lines are β misfit dislocations. The mesa size is 100 μm.

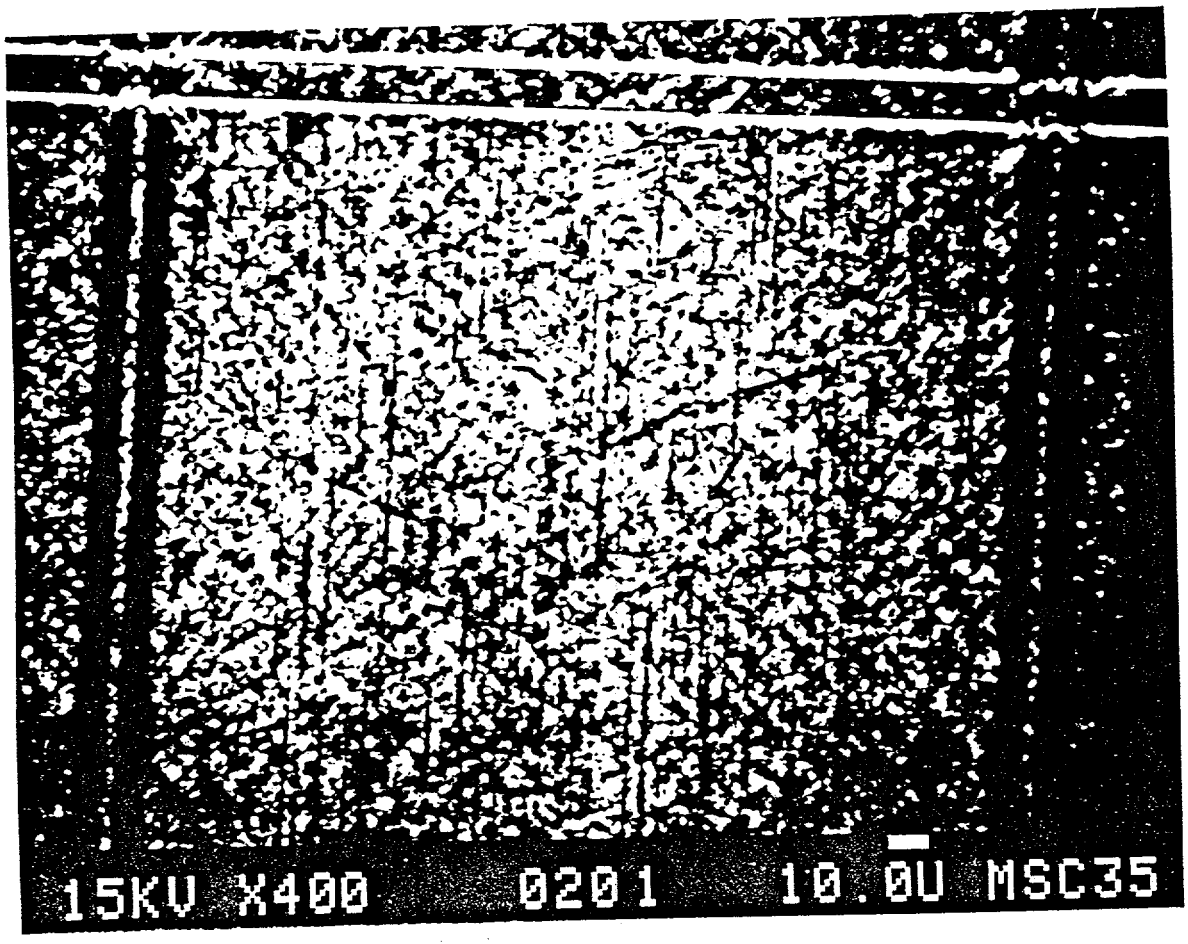

Figure 7.7: CL images of ZnSe grown on patterned GaAs at 440°C. The vertical dark-lines are β misfit dislocations. The mesa size is 200 μm.

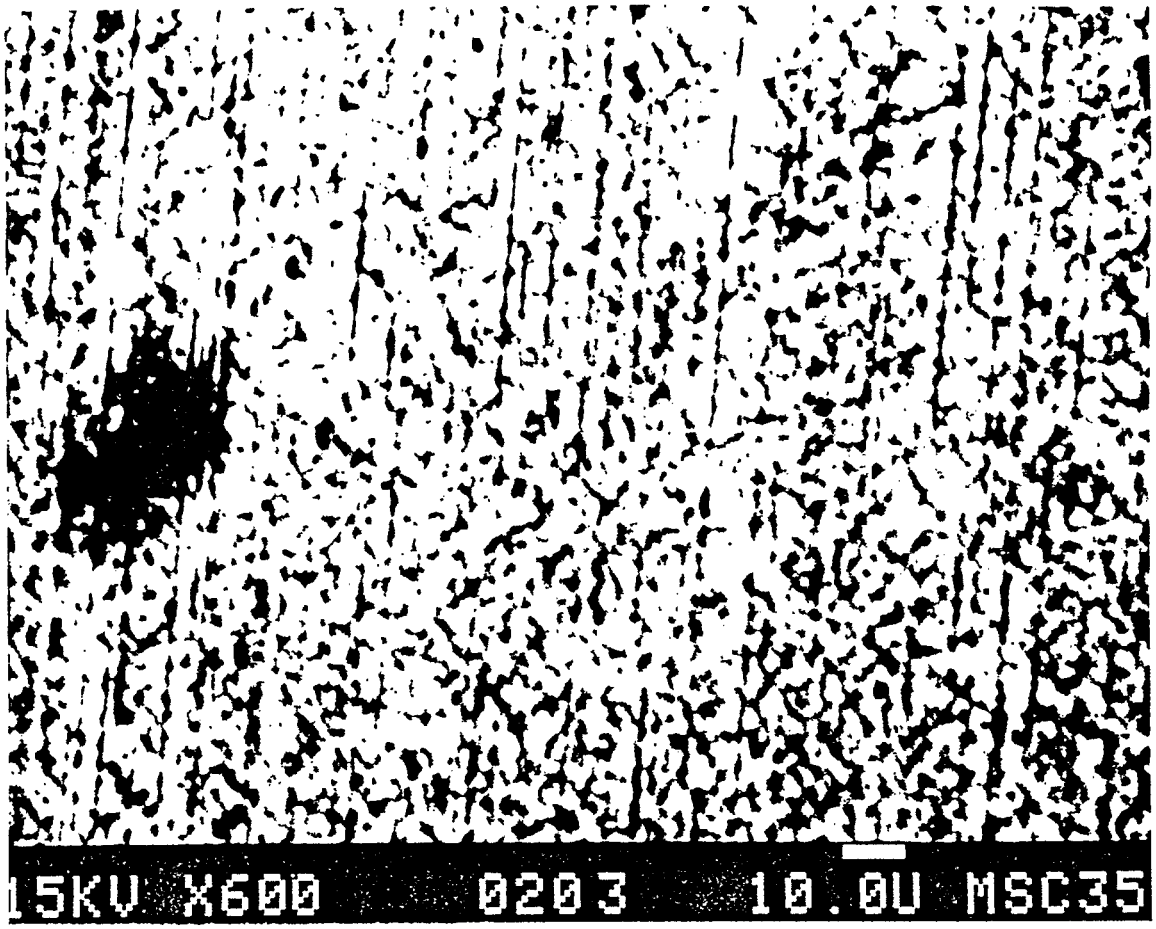

Figure 7.8: CL images of ZnSe grown on patterned GaAs at 440°C. The vertical dark-lines are β misfit dislocations. The mesa size is 400 μm.

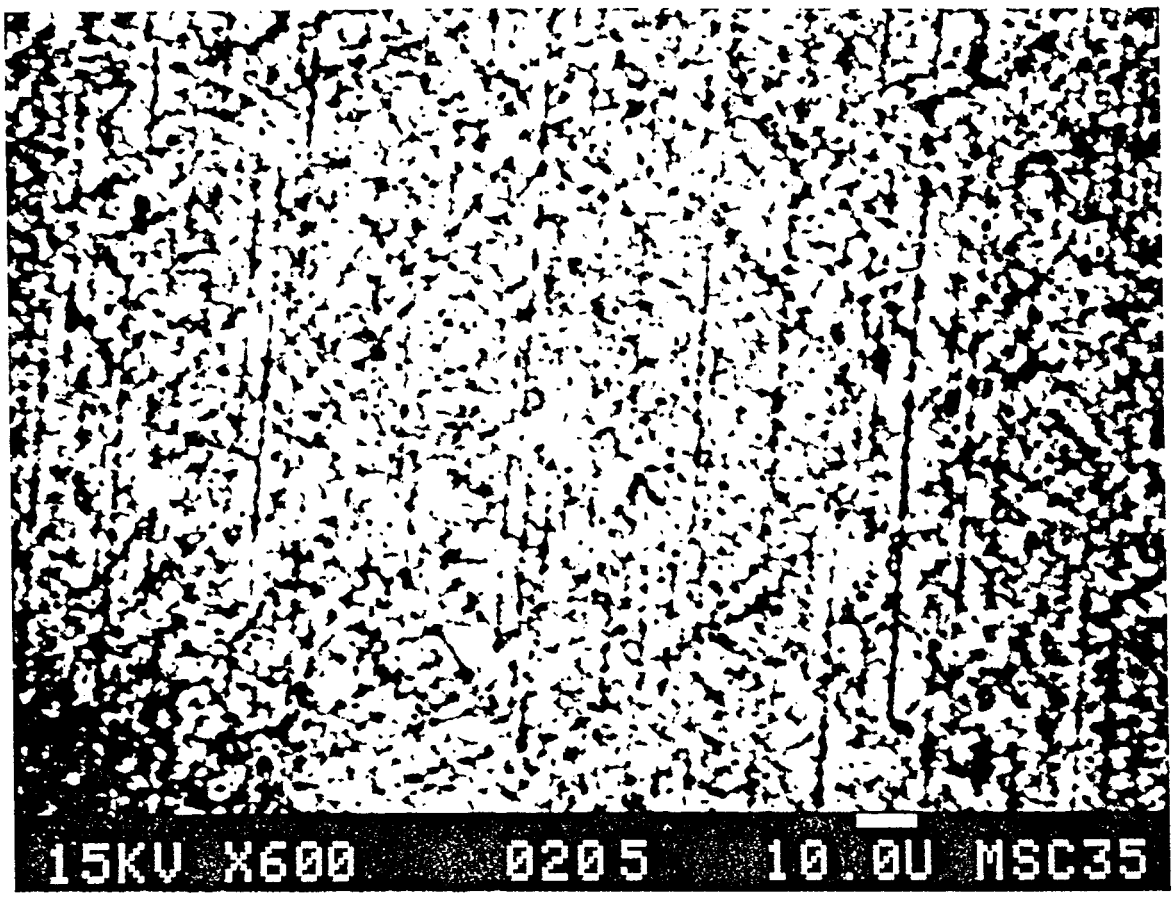

Figure 7.9: CL images of ZnSe grown on patterned GaAs at 440°C. The vertical dark-lines are β misfit dislocations. The mesa size is 800 μm.

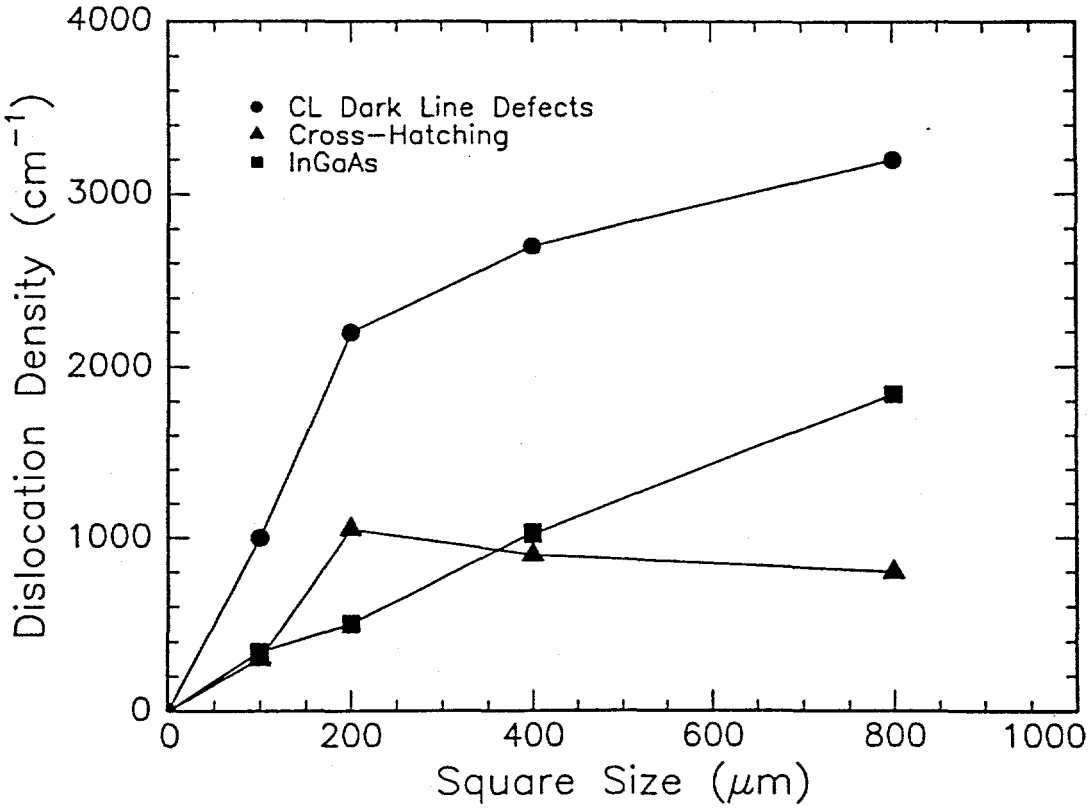

Figure 7.10: A plot of misfit dislocation density vs. mesa square size, for ZnSe measured by CL (circles) and interference contrast (squares). Data for InGaAs (triangles) are shown for comparison.

The character of the misfit dislocation itself is not particularly important as far as propagation is concerned; it is the threading segments that actually glide. Since the threading segments lie completely in the ZnSe, it is probable that the relationship between core type, Fermi level, and mobility is much different than that of segments III-V materials. Note that if a dislocation threading segment is α in a III-V layer, it must also be α in ZnSe, since net surface charge considerations require that the Ga sublattice be replaced by a Zn sublattice and the As sublattice replaced by a Se one (even this configuration has interface charge problems, see Farrell et al. [FTdM+91]). As with III-V crystals and any A-B zincblende type structure, an α defect is defined as a dislocation with an A(s) or B(g) core. If it were possible to switch the A and B sublattices, then a β dislocation threading through GaAs would become α in ZnSe simply because of the switch in sublattice occupation and may simply explain how an α threading segment creates *only* a β misfit dislocation. Therefore a threading segment must maintain its core character - meaning that the β misfit dislocations and forward threading segments (as described in Chapter 2) in the ZnSe/GaAs must glide more easily than α's.

The fact that the interface dislocation density varies sublinearly with square dimension is a new observation in patterning. The saturation of the ZnSe misfit dislocation density at large mesa sizes indicates that the mesa dimensions are not the only factors that attenuate the misfit dislocation path length. Note that many electrically active defects can be seen in Figure 7.6 besides the misfit dislocations. If they impede the motion of the threading segments, then the average misfit dislocation length (and the average density) is a function of both mesa dimension and the glide

obstacle density. Matthews et al. first described the effects of misfit dislocation density in terms of the areal density of misfit dislocation nucleation sources from the substrate [MML70]. Fitzgerald et al. extended this argument to patterned substrates and described qualitatively how impediments to dislocation motion would affect the defect density [FWP+89]. Below, these ideas are put on a more general footing so that the trends seen in Figure 7.10 can be described quantitatively.

Figure 7.11 is a diagram that describes how the misfit dislocation density, ρ_y, is calculated from the misfit dislocation nucleation source density (in the y direction), g_y, and the probability that the misfit dislocation generated is longer than a length y, $f(y)$. Based on Figure 7.11, the misfit dislocation density is measured by counting the number of dislocations that cross the line $y = 0$. The probability that the small area $dxdy$ will contribute a misfit dislocation to the density count is

$$0.5 g_y f(y) dx dy. \tag{7.1}$$

The misfit dislocation density is found by integrating equation 7.1 over the complete area of interest (from the mesa edges in the y direction and any length of x) and dividing by the length in the x direction, giving units of length^{-1}:

$$\rho_y = \frac{1}{x_2 - x_1} \int_{x_1}^{x_2} \int_{y_1(x)}^{y_2(x)} 0.5 g_y f(y) dx dy. \tag{7.2}$$

In the case where the mesas are squares with edges oriented in the same direction as the misfit dislocations, the mesa limits, y_1 and y_2, are independent of x. The upper limit can be represented as ζL_s and the lower limit $(1 - \zeta)L_s$, where L_s is the mesa square size and ζ is a dimensionless parameter varying from 0 to 1, then Equation 7.2

simplifies to:

$$\rho_y = \int_{\zeta L_s}^{(1-\zeta)L_s} 0.5 g_y f(y) dy. \tag{7.3}$$

What is the form of $f(y)$? If it is assumed that the defects that impede misfit dislocation propagation are uniformly distributed, then there is a constant probability that one particular dislocation will be stopped at each increment of length as it glides. This situation is identical to photon absorption in solids; the probability that a misfit dislocation can stretch out a length y or longer is $e^{-K|y|}$, precisely the same form as the probability that an x-ray will be absorbed in a solid of thickness y with absorption coefficient K. Inserting $f(y) = e^{-K|y|}$ in to Equation 7.3:

$$\rho_y = \frac{0.5 g_y}{K} \left(2 - e^{-K\zeta L_s} - e^{-K(1-\zeta)L_s}\right). \tag{7.4}$$

Figure 7.12 is a plot of the ZnSe misfit dislocation density data versus mesa size with the solid curve representing a non-linear least squares fit of the data to Equation 7.4. The coefficient ζ was chosen to be 0.5, which corresponds to the misfit dislocation density measured at the center of the square mesas. The nucleation density, $g_{[110]}$, is $3.0 \pm 0.5 \times 10^5$ cm^{-2} and the attenuation coefficient, K, is $9.2 \pm 1.9 \times 10^1$ cm^{-1}. The reciprocal of K is the average length of a misfit dislocation, about 110 μm in this case. The fit certainly follows the trend of the data, although other functions $f(y)$ may also fit the data reasonably well (such as a step function or a Gaussian).

It is unlikely that the trend seen in Figure 7.12 is caused by a mechanism other than misfit dislocation length attenuation since there is one other feature of Equation 7.4 that corroborates the theory. In Figure 7.13 we plot the expected change

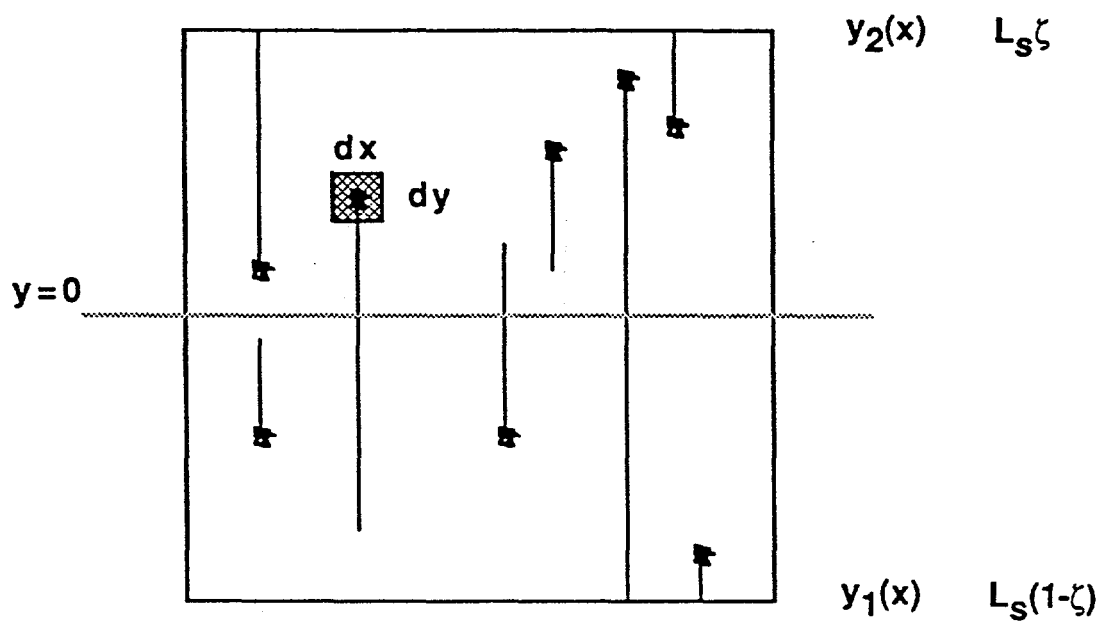

Figure 7.11: A schematic diagram of the method used to estimate the misfit dislocation density at the line $y = 0$.

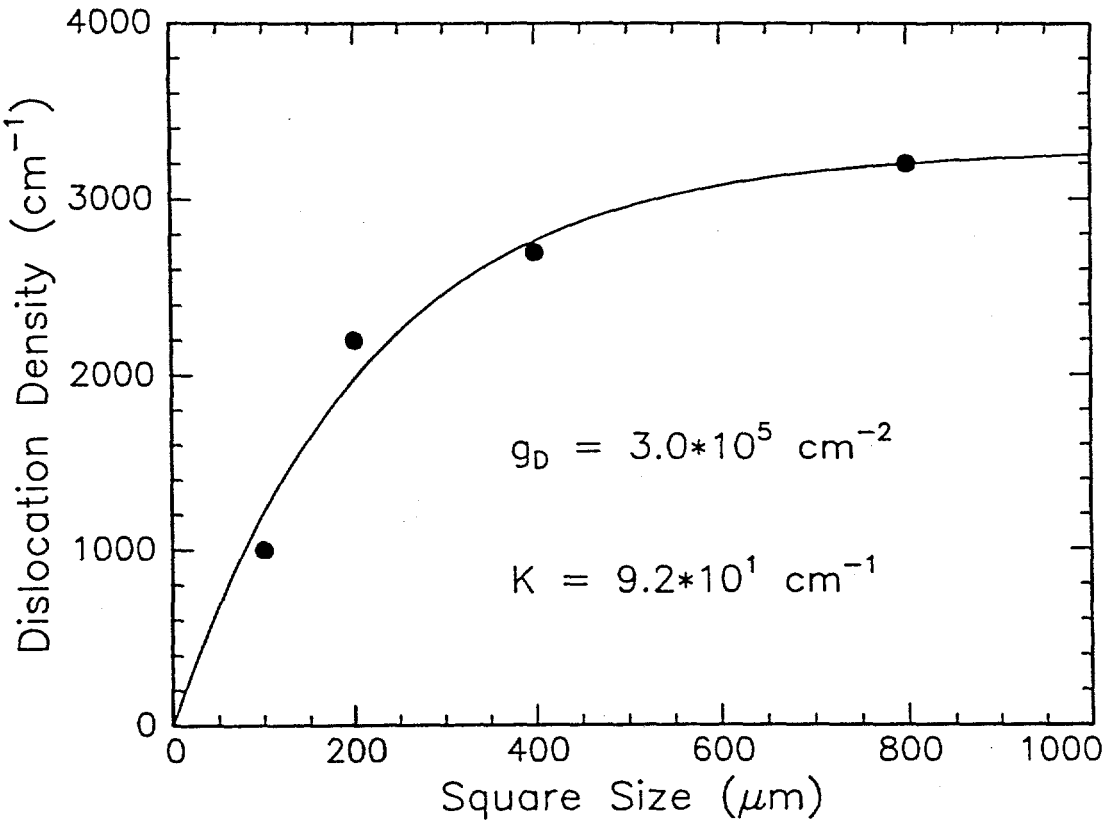

Figure 7.12: A plot the [110] misfit dislocation density vs. mesa size. The solid curve represents a least-squares fit of the data to Equation 7.4.

in misfit dislocation density with ζ, the normalized distance form the mesa edge. The parameters $g_{[110]}$ and K are those found by the least-squares fit in Figure 7.12. Inspection shows that for 100 μm mesas it does not matter where the misfit dislocation density is measured; $\rho_{[110]}$ is essentially independent of ζ, as should be expected since the average misfit dislocation length comfortable exceeds the mesa size. Only when $L_s >> \frac{1}{K}$, such as for the 800 μm mesas, is ζ important. Note that for the largest mesas, the misfit dislocation density can differ by as much as a factor two, depending on where ρ is measured (Figure 7.13). The characteristic misfit dislocation propagation length defines an *effective* mesa size on the order of $2K$ (one K on each side of the measurement line). If measured at the mesa edge, only half of the effective size can be considered, since the rest of the misfit dislocations are blocked by the trench at the edge. Therefore the effective mesa size changes from $2K$ near $\zeta = 0.5$ to K near $\zeta = 0$ and the density scales accordingly. If such a change in ρ is measured, then misfit dislocation attenuation must be active.

Recent CL work by William Edwards at Cornell University on the same wafer, GPW-108, at least qualitatively supports this attenuation model. He measured the misfit dislocation density of two mesas 800 μm and 200 μm long at various positions and found that there was a significant difference between the density measured at a mesa edge and near the center for the larger mesa. The dislocation density changed very little with position for the smaller squares, however. Figure 7.14 is a plot of his data along with the curves predicted by Equation 7.4 for the two mesa sizes. The parameter K was taken to be 9.2×10^1 cm^{-1} as before, but $g_{[110]}$ was set at slightly smaller value of 2.5×10^5 cm^{-2}. The region that Edwards studied was in a

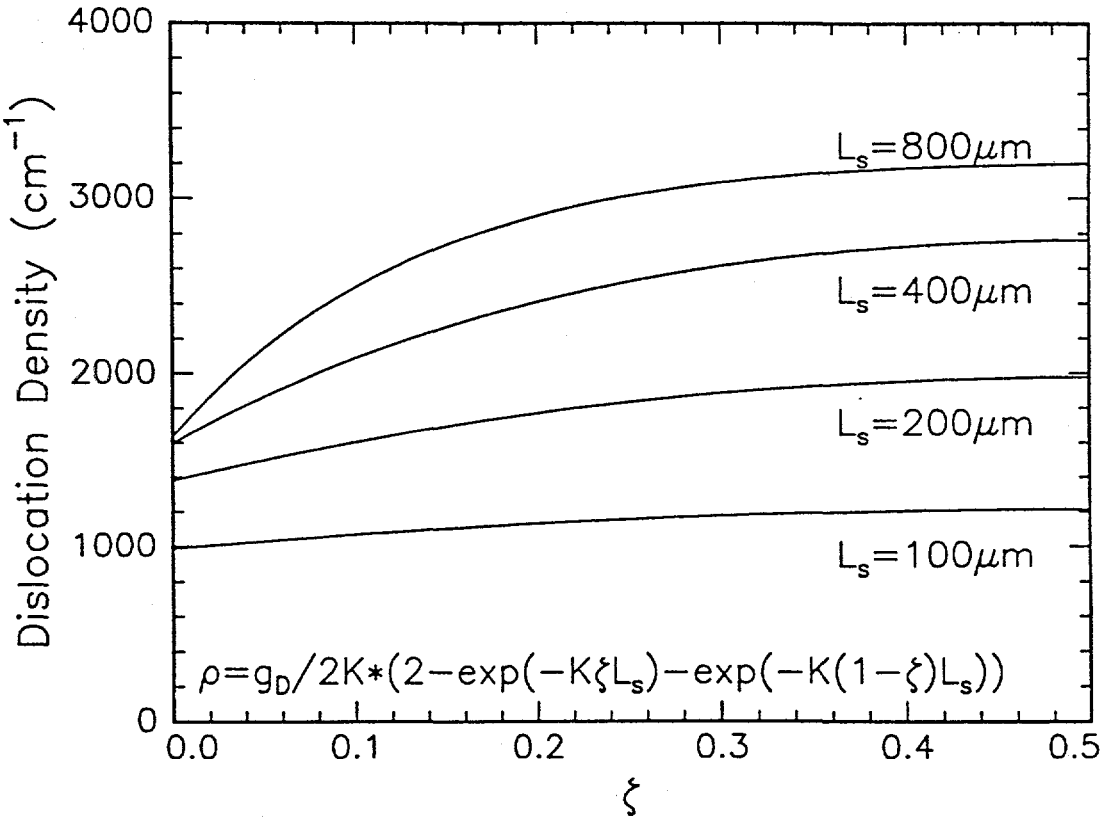

Figure 7.13: A plot of the theoretical misfit dislocation density as a function of the distance from the mesa edge (ζ).

different region of the specimen than that used by this author to collect the data in Figure 7.12, so some parameter changes should be expected (remember that there was a relatively large thickness gradient due to the growth conditions). Although the measured misfit dislocation change is not as pronounced as predicted for the 800 μm mesa, the data does appear to be consistent with the model.

Figure 7.14: The measured misfit dislocation density vs. ζ of William Edwards. The circles are for the 800 μm mesa and the triangles are for the 200 μm mesa. The solid curve is the predicted trend for an 800 μm mesa and the dashed line for a 200 μm mesa.

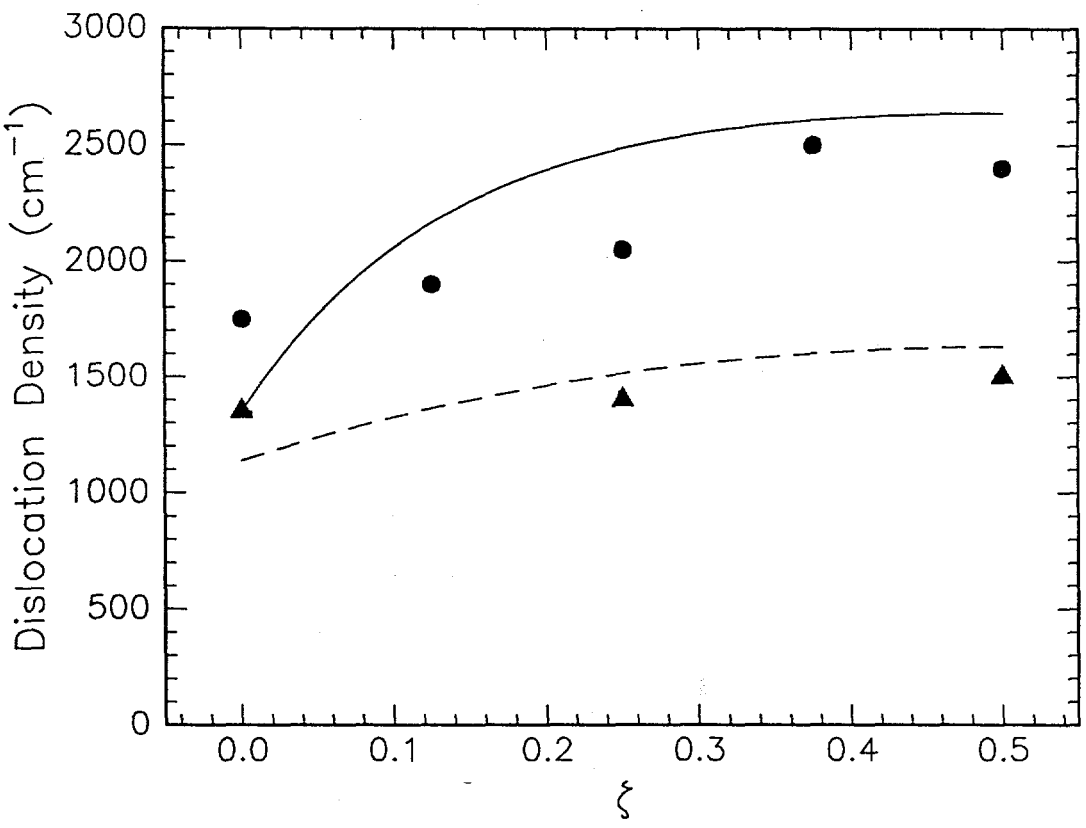
3000
2500
2000
1500
1000
500
0
Dislocation Density (cm^{-1})
0.0
0.1
0.2
0.3
0.4
0.5
ζ

Chapter 8

The Measurement of Deep Level States Caused by Misfit Dislocations in InGaAs/GaAs Grown on Patterned GaAs Substrates

8.1 Introduction

8.1.1 Electrical Activity of Dislocations

The presence of a dislocation in a crystal lattice destroys the translational symmetry, and in the case of semiconductors, this local symmetry breakdown leads to the formation of localized energy states which may reside in the bandgap. Such states act as traps and recombination sites and thus influence device performance. Dislocations are associated with the degradation of light emitting diodes and lasers and

when they are located at lattice mismatched heterojunctions they can adversely affect the operation of other devices as well [AAS+88]. Read was the first to describe in detail the basic properties expected of dislocations introduced into semiconductor crystals and then applied these arguments to the interpretation of electrical properties in plastically deformed Ge [Rea54]. However, associating the dislocation cores with specific electron energy states within semiconductor bandgaps has proved to be a difficult task.

The effect of plastic deformation of semiconductors on trap concentrations measured by deep level transient spectroscopy (DLTS) has been studied by several groups. For example, Skowronski et al. studied the effect of plastic strain in GaAs on the EL2 point defect trap concentration [SLM+87]. Patel and Kimmerling studied the DLTS spectra of plastically deformed Si [PK79]. They found that annealing was required to remove the large concentrations of point defects so that the effects attributed to dislocations could be measured. Wosinski plastically deformed GaAs and found a DLTS peak with an intensity that varied with the estimated dislocation density [Wos89]. Zozime and Schroter plastically formed dislocations in InP by indentation and were able to select the dislocation core type by changing the orientation of their diode contacts over the dislocations [ZS90]. Unfortunately, plastic deformation generates electrically active point defects in addition to dislocations. Because the concentration of several defect types tends to increase with strain, it is difficult to draw unambiguous conclusions on the activity of dislocations from the DLTS spectra.

Petroff et al. noted that dislocations can be formed in semiconductors without

changing point defects densities (and the necessity of severe anneals) by growing lattice mismatched mismatched heterostructures [PLS79]. Misfit dislocations form to relieve some of the strain in the epitaxial layer when it is thicker than the critical thickness. Petroff and his co-workers studied the *clean* misfit dislocations in liquid phase epitaxially grown GaAlAsP by cathodoluminescence (CL) and electron beam induced current. Dislocations appeared as dark lines in these images because of the enhanced nonradiative recombination at the dislocation cores. They found that 60° dislocations with different core structures did have slightly different contrast.

Several studies have been made of defect states in lattice mismatched epitaxial InGaAs and InGaAsP layers [AAS+88,BDBJ86,JLSM87,IHI88,STII81]. The misfit dislocation density can be controlled to some extent by varying the lattice mismatch; however, both the overall strain in the epitaxial layer and the alloy composition change as well [STII81].

8.1.2 Control of Dislocation Density

The evidence obtained so far paints an unclear picture of just how dislocations act electronically. The basic problem is that the dislocation density must be varied from sample to sample in a controlled way without inducing other side effects such as changing the point defect concentration or the composition of the material. If an electrical property can be shown to vary linearly with dislocation density and all other side effects held constant, then this property can be attributed to the dislocations or their immediate environment with confidence. Patterning substrates before epitaxial growth of strained layers allows us to accomplish this objective.

To review, misfit dislocations may form only if two conditions are met. First, the epitaxial layer thickness must exceed the critical thickness - the point where the relief in strain energy in the epitaxial layer, caused by the misfit dislocation, just exceeds the energy due to the strain field around the dislocation [MML70]. The second condition is that nucleation sites are available to form the dislocation threading segments that glide and leave behind a misfit dislocation [FWP+89]. These dislocations nucleate from threading dislocations in the substrate or from other defects on the substrate surface when the lattice parameter mismatch is 1% or less. Only at high degrees of mismatch can the second condition be relaxed; loop nucleation may spontaneously occur at high strains which forms a dislocation at the mismatched interface [MB74].

As described in detail in Chapter 1, Fitzgerald et al. have shown that the density of misfit dislocations in mildly strained layers grown by molecular beam epitaxy (MBE) can be controlled simply by limiting the path length of the misfit dislocations [FWP+89]. By patterning and etching mesas onto GaAs substrates before stained layer epitaxial growth, misfit dislocation threading segments, which form and glide during growth, are blocked from passing from one mesa to an adjacent one. Varying the size of the isolated region changes the misfit dislocation density (the number of dislocations lying in the interface and crossing a line per unit length). The shape and orientation of the region also controls the type of misfit dislocation formed, as is described below.

8.1.3 α and β Dislocations

Chapter 2 describes the chemical and structural differences α and β 60° dislocations in III-V semiconductors. The core type notation and line directions are restated here. Using the notation of Alexander et al. for GaAs, an As core glide set dislocation (As(g)) or a Ga shuffle set core (Ga(s)) are known as α's, while Ga(g) or As(s) are $\beta's$ [AHLS79]. An α misfit dislocation and a β misfit dislocation lying in the same {111} glide plane will have the opposite Burgers vector edge component; one would relieve strain and the other enhance it. If the two were oriented perpendicular to the original direction they would reverse their role. Thus, misfit dislocations running in the $[1\bar{1}0]$ direction would be α type and those in the [110] direction would be β for epitaxial layers such as InGaAs, where the lattice parameter is larger than the GaAs substrate. Furthermore, since the Burgers vectors of α and β dislocations differ only in sign, they possess identical strain fields outside the immediate core regions.

Because these two dislocation types possess different core structures, different electronic properties are to be expected. By controlling the geometry of the patterns, α and β types could be studied separately and their relative number simply controlled. This paper describes a series of devices that were used to measure the electrical properties of misfit dislocations at InGaAs/GaAs interfaces.

8.2 The DLTS Technique

8.2.1 Trap Kinetics

Deep level transient spectroscopy is an elegant yet simple technique that can yield important information about electronic defects in semiconductors. The basic idea is to abruptly change the Fermi level (or pseudo Fermi level) in a region of the material of interest. Since the Fermi level determines the occupation level of electron states in the crystal, deep levels in that region may change their charge state. When the system returns to its original state, the traps do so as well, but at a slower rate than the Fermi level (assuming the traps have only a negligible effect on the Fermi level itself). Quantities such as current or capacitance, measured after the Fermi level returns to its original state, therefore vary with time in a way that depends on the trap concentration and characteristics.

Figure 8.1 is a band diagram of an n-type semiconductor with a deep level electron trap state in the bandgap. By the definition of electron trap, we assume that the deep level is much more likely to absorb an electron from the conduction band than it is to absorb a hole from the valence band ([Lan74, Joh86]). With this assumption, a simple kinetic model can be developed. The more general case is treated in [Sch90] by simply using the conservation of charge and some basic assumptions about the transition probabilities of the electrons in the trap states. If the Fermi level of the region of interest is at its filling position (diagram a in Figure 8.1) for a long time, the electron traps will be essentially filled, assuming the trap energy level is below the Fermi energy. When the trap energy, E_T, is raised

above the Fermi energy, E_F, at time $t = 0$ (as in Figure 8.1 *b*), the trap emits electrons to the conduction band at E_C such that the occupied trap concentration at time t is

$$n_T(t) = N_T e^{-t/\tau_e}, \tag{8.1}$$

where emission time constant is

$$\frac{1}{\tau_e} = \frac{g_T}{\sigma v_{th} N_C} e^{-\frac{E_C - E_T}{kT}}. \tag{8.2}$$

The coefficient g_T is the degeneracy factor of the trap, σ is the electron capture cross-section, v_{th} is the electron thermal velocity, N_C is the effective density of states in the conduction band, k is the Boltzmann constant, T is the temperature, and N_T is the trap concentration in the region. (More precisely, the electron free energy and not the trap energy should appear in the exponent in Equation 8.2, but this fact is ignored in the present argument. It is still valid to define the properties of a trap with some characteristic energy that enters the above equation as $E_C - E_T$ [Joh86].)

In the above case the trap acts as a donor that emits electrons into the conduction band when the energy levels are adjusted relative the Fermi energy. In this state the effective donor concentration is

$$N_{D\ eff} = N_D + N_T \left(1 - e^{-t/\tau_e}\right). \tag{8.3}$$

This is the basic time dependent characteristic of the material that DLTS measures.

Another important time dependent quantity is the capture time constant, τ_c. If the traps act independently, then the number of traps that are filled with electrons when the system is in its filling state for time t_{fill} is

$$N_{T\ filled} = N_T \left(1 - e^{-t_{fill}/\tau_c}\right). \tag{8.4}$$

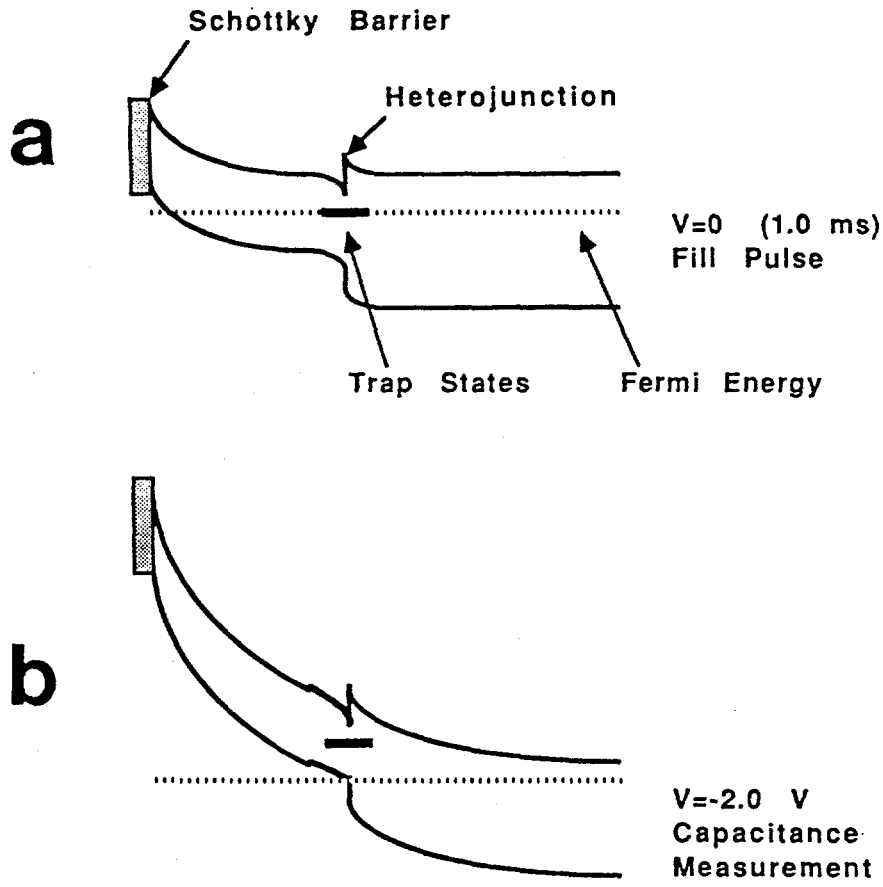

Figure 8.1: Band diagrams of an electron trap in a semiconductor in the filling state, *a*, and when the energy levels are raised relative to the Fermi energy, *b* (the measurement state).

Using the assumption above, the capture time constant is

$$\tau_c \frac{1}{\sigma v_{th} n}, \tag{8.5}$$

where n, the carrier concentration, is essentially N_D.

Equations 8.4 and 8.5 are based on the assumption that the capture probability rate of one trap site is independent of the status of its neighbors. In the case of traps located at the core of a dislocation, these sites are arranged in a linear array separated by about 0.4 nm from each other. The Coulombic repulsion between other electrons in the immediate vicinity cannot be ignored. Read first depicted how dislocation core trap sites are occupied with a simple dangling bond model[Rea54]. The fraction of filled sites determined the overall electron energy needed by an electron to fill one more site. The additional energy was calculated by considering the Coulomb repulsion of the electrons and the attraction of the depletion region around the dislocation. The electrostatic energy, E_s, was found to be

$$E_s = \frac{2q^2 f}{4\pi\varepsilon\varepsilon_0 c}\left(\frac{3}{2}\ln\left(\frac{f}{c\pi^{1/3}N_D^{1/3}}\right) - \left(\frac{1}{2} + \ln(2)\right)\right) \tag{8.6}$$

where c is the spacing between dangling bond sites, f is the fraction of filled trap sites. For the minimum system free energy, the equilibrium value of f must satisfy

$$E_F - E_T = \frac{q^2}{4\pi\varepsilon\varepsilon_0} f\left(3\ln\left(f/f_c\right) - 0.232\right) \tag{8.7}$$

where q is the absolute charge of one electron, ε_0 is the dielectric constant of vacuum, ε is the dimensionless ratio of dielectric constants, and $f_c = c\sqrt[3]{\pi N_D}$. The Fermi energy, E_F, is determined by the shallow donor concentration.

Labusch and Schroter ([LS80]) modified Read's approach by considering the singly occupied orbitals making up the core as both potential acceptors or donors. In addition, they also modified the electrostatic energy terms. The fraction of occupied sites (besides the already half-occupied orbitals) must satisfy:

$$E_F - E_T = \frac{q^2 f}{2\pi\varepsilon\varepsilon_0 c} \ln(f\lambda/c) \tag{8.8}$$

$$\lambda = \sqrt{\varepsilon\varepsilon_0 kT/q^2 N_D} \tag{8.9}$$

where λ is the Debye length. Like equation 8.7, f must be solved for iteratively.

Unlike non-interacting point defects, dislocation trap sites will never be completely filled no matter how long the region of interest is held at a certain Fermi level position. Note that for long times, Equation 8.4 predicts that the measured point defect trap concentration approaches the actual concentration. But by knowing f, the maximum concentration of active dislocation trap sites can be calculated.

Figielski ([Fig78]) and Wosinski ([Wos89]) estimated the capture kinetics of dislocation core trap states, based on the form of Equation 8.6. Since the natural logarithm term in Equation 8.6 varies slowly with f, the electrostatic energy may be represented by $E_S \propto f$. The electrostatic energy controls the position of the conduction band relative to the Fermi energy (Figure 8.1) and therefore controls the local free carrier concentration. This means that f determines n locally. In addition, the rate at which carriers are captured is a function of n, as can be seen in Equation 8.5. Wosinski showed that Equation 8.4 must be modified, and the concentration of filled dislocation trap sites depends on time as

$$N_T \propto \ln\left(t_{fill}\right). \tag{8.10}$$

8.2.2 Measuring the Transient Behavior

In its simplest form, DLTS measures the transient differential capacitance of a reverse biased diode whose depletion region is changed (along with the Fermi level in that region) by varying the bias. In the discussion that follows, the device under test is assumed to be an n-type Schottky diode with one majority carrier (electron) deep level trap. The differential capacitance, C, which is the change in accumulated charge in the diode that occurs when a small voltage change is applied, is, according to [Sze81],

$$C = \sqrt{\frac{q\varepsilon\varepsilon_0 N_{D\ eff}}{2\,(V_R + \phi_B)}}, \tag{8.11}$$

where V_R is the absolute value of the applied reverse bias potential, and ϕ_B is the (positive) natural barrier height of the Schottky diode. In typical operation, traps are allowed to fill by setting the diode bias to zero for some time t_{fill}. The diode is then reverse biased to V_R and the capacitance is measured as a function of time. Since the effective donor concentration changes with time (Equation 8.3), the capacitance does as well.

When N_T is very small compared to N_D, the trap concentration may be simply calculated from the values of the diode capacitance, $C(t)$, at $t = 0$ and $t = \infty$ using Equation 8.3 and a Taylor's series expansion of Equation 8.11:

$$\Delta C/C = \frac{C(\infty) - C(0)}{C(0)} = \frac{N_T}{2N_D}. \tag{8.12}$$

Equation 8.12 is only valid if both N_D and N_T are constant throughout the sampled region. If, as in the case of misfit dislocations, defect states are concentrated at one depth in the semiconductor, Equations 8.11 and 8.12 must be modified.

Figure 8.2 illustrates the system geometry. Poisson's equation has been solved for this case using the depletion approximation and a sheet of traps at a depth x_I from the metal/semiconductor surface. The integration yields a DLTS signal

$$\Delta C/C = \frac{N_t x_I}{N_D W^2}, \tag{8.13}$$

where the subscript I represents the strained layer heterojunction interface and W is the depletion width at the reverse bias applied to the diode during the capacitance transient measurement. Effects caused by the heterojunction band offsets are ignored and it assumed that the trap concentration inside the depletion region is negligible compared to the donor concentration.

8.2.3 Spectrum Collection

Lang first recognized that the capacitance change of a diode according to Equation 8.11 can be monitored by simply measuring and comparing it at two points in time [Lan74]. A diode fabricated with the material of interest is attached to a cryostat so that the device temperature can be controlled. As the temperature rises, the emission time constant of traps in the material decrease (Equation 8.2). The difference between the two capacitance measurements reaches a maximum at one temperature, creating a peak in a plot of the signal difference versus diode temperature - this is the DLTS spectrum. The measurement times, which may be selected by the investigator, determine the emission time constant, τ_e, at the DLTS signal peak maximum (or minimum). A series of such scans with different measurement times may be used to generate an Arhenieus-like plot based on Equation 8.2. Since v_{th} and N_C together depend on temperature as T^2, the ordinate is $1/(\tau_e T^2)$.

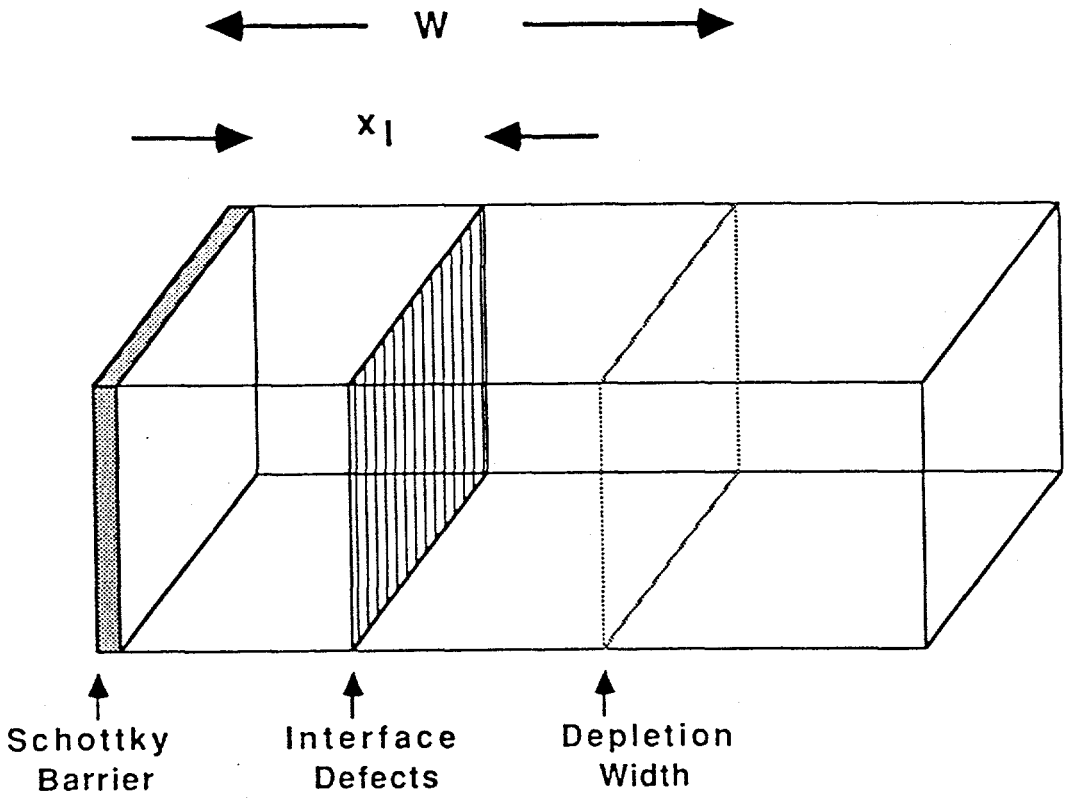

Figure 8.2: A schematic of a Schottky barrier diode containing interface trap states a distance x_I from the contact. The depletion width is represented by W.

The abscissa is $1/T$. The slope of the points for one trap should be constant and proportional to the trap energy measured from the conduction band.

The instrument used in this study, a Sula Technologies unit, measures and averages the capacitance transient in two time intervals instead of at two points in time. The advantage of this strategy is that the signal to noise ratio can be increased while only slightly complicating the mathematics involved in deriving the emission time constant. The signal is averaged over many measurement periods as well to further reduce spectrum noise.

8.3 Experimental

8.3.1 Device Fabrication

A (001) Crystal Specialties GaAs substrate with a nominal etch pit density of 5000 cm^{-1}, and Si doped at 10^{18} cm^{-3}, was patterned as described in Chapter 3. The photolithography mask, shown schematically in Figure 8.3, consists of a series of rectangles all 200 μm wide and 2000, 1500, 1000, or 500 μm long. The mask was aligned to a cleaved [110] GaAs edge so that the rectangles lie in either the [110] or [1$\bar{1}$0] directions. After patterning, the GaAs substrate was exposed everywhere except for the portion protected by the SiO_2 rectangles.

The wafer was then reactive ion etched as in Chapter 3. Etching for 300 s created a series of rectangular mesas about 0.9 μm high on the substrate surface. After a final clean, the substrate was loaded into a Japan Oxygen Corporation OMVPE reactor and heated to 640°C in an AsH_3 atmosphere for about 10 minutes. A 300 nm GaAs buffer layer and a 250 nm $In_{0.06}Ga_{0.94}As$ lattice mismatched epitaxial layer

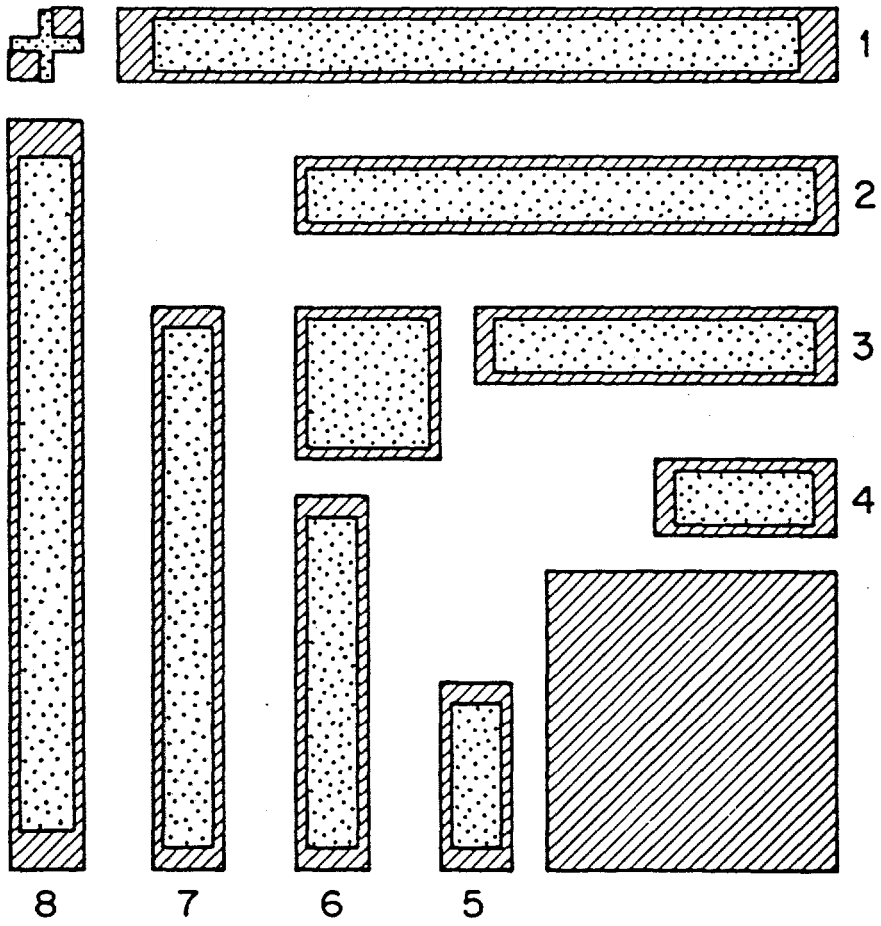

Figure 8.3: Plan view schematic of the misfit dislocation DLTS mesas and diodes.

were grown on the substrate, both S doped at 7×10^{16} cm^{-3}.

Schottky diodes were then prepared on the mesas. The top surface was coated with 80 nm of plasma enhanced chemical vapor deposited SiN_x to protect the surface and to facilitate lift-off. The back of the wafer was cleaned and an ohmic Au/Ge alloyed contact was formed by evaporation and rapid thermal annealing at 400°C. Using photolithography, plasma etching, electron beam evaporation, and lift-off, Ti/Pt/Au Schottky contacts were formed onto the epitaxial layers that, just prior to contact evaporation, were cleaned with 1:1:20 H_2SO_2:H_2O_2:H_2O at 25°C for 15 s (removing about 100 nm of InGaAs). A cross-sectional view of the final device is shown schematically in Figure 8.4.

8.3.2 DLTS Characterization

Data from the Sula Technologies instrument mentioned above was acquired by an AST 286 microcomputer. The Sula DLTS apparatus consists of a circuit to periodically change the bias of the diode under test, a fast response capacitance meter and two correlators that measure the capacitance signal change. The specimen is attached to a Au coated sapphire disk with Ag paint so that both good thermal and electrical contacts are made to the back surface. The Schottky diode on top of the fixture is electrically connected through a probe. The probe and specimen mount are described in more detail in the appendix. The specimen is placed in a liquid N_2 cryostat, and its temperature is set and monitored by a resistive heater wire and two Pt resistance thermometers all attached to a Lakeshore cryogenic controller. The program, DLTS2.C, operating on the microcomputer, controls the Lakeshore

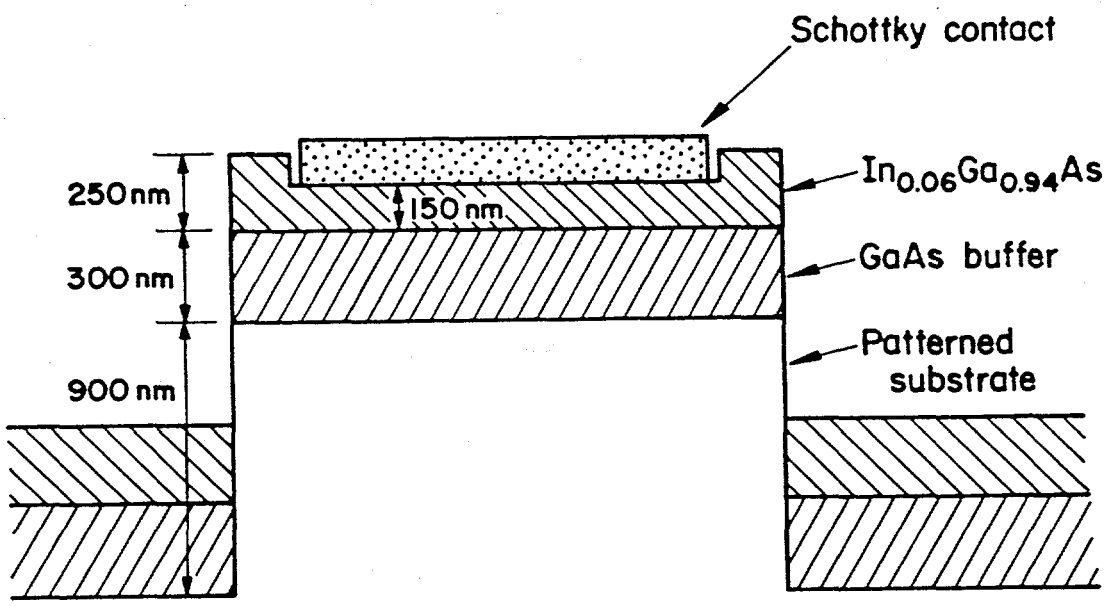

Figure 8.4: Cross-sectional schematic of the structures used to study misfit dislocations by DLTS.

instrument through an IEEE-488 standard interface and records the correlator data through a Data Translation A/D converter board. More information and a program listing may be found in the appendix.

The capacitance transient was measured at -2.0 V bias and the filling pulse was set at 0.0 V for all of the scans presented here. Except for the capture rate tests, the filling pulse time, t_{fill}, was set at 1×10^{-3} s for all experiments described below.

8.3.3 Other Characterization

The strained layer composition and thickness were determined by Rutherford backscattering spectrometry (RBS). Capacitance-voltage (CV) profiles of the Schottky diodes were taken to determine the epitaxial layer doping level and the interface carrier characteristics.

The misfit dislocation density was measured by counting the dark line defect density in scanning CL images. The photon signal was detected with a Si photo diode from GW electronics, installed in a JEOL JSM35 scanning electron microscope. Typical excitation conditions were 15 kV at 0.5×10^{-7} A (Chapter 2).

The crystal orientation was determined by etching an exposed portion of GaAs on the substrate back as described in Chapter 2. In the InGaAs/GaAs system, α misfit dislocations must lie in the $[1\bar{1}0]$ direction, in one of the above Ga glide planes on (001) oriented wafer. Similarly, β misfit dislocations must lie in the [110] direction.

One set of 8 rectangular diodes were cleaved off after DLTS analysis to determine the misfit dislocation density under the contacts. The specimen was simply etched

for about 120 s in HF with ultrasonic agitation to remove the Ti metallization. After contact removal, the dislocation densities were determined from CL images.

8.4 Results

8.4.1 Dislocation Densities

RBS analysis indicated that the InGaAs layer was 250 nm thick and contained 6 atomic percent InAs, in line with previously established growth calibrations. At this composition the thickness is more than 8 times larger than the critical thickness (29 nm) [MML70].

Etching revealed that the $[1\bar{1}0]$ direction points along the long side of the rectangles 5 through 8 as labeled in Figure 8.3. The α type misfit dislocation density is expected to increase from rectangle 5 to 8 as the rectangle length increases. Rectangles 4 through 1 should contain increasing amounts of β dislocations.

The average misfit dislocation density in rectangles oriented along the $[1\bar{1}0]$ (α) direction, ρ_α, is plotted against the appropriate rectangle length in Figure 8.5. The average density of each rectangle size was calculated from images of at least 5 regions. In addition to the data from the rectangles 5 to 8, which vary in length, the α dislocation density of rectangles 1 through 4 is plotted as well, all of which are 200 μm long in the α direction. Figure 3 shows that the data follow a linear relationship to a reasonable degree, as expected. The slope, obtained by least squares analysis fit with the intercept constrained to zero, is $2.8 \pm 0.3 \times 10^3$ cm^{-2}. The correlation coefficient, r, is 0.929 for the 8 points, indicating that the probability is very small that the trend seen is due to random fluctuations.

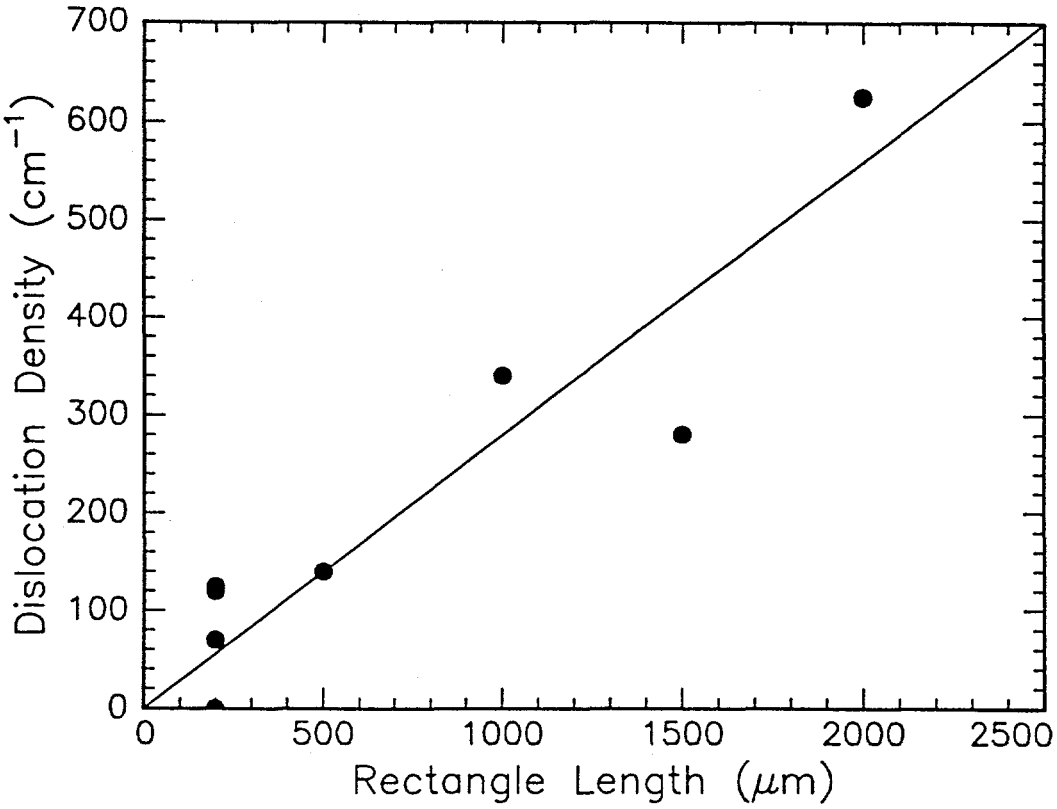

Figure 8.5: A plot of α misfit dislocation density vs. rectangle size.

Similarly, the β misfit dislocation density, ρ_β, versus rectangle size is plotted in Figure 4. The slope found in this case is $8.3 \pm 0.9 \times 10^2$ cm^{-2} ($r = 0.922$), about one third of the α dislocation density slope. Different α and β dislocation densities have been observed (at about the same ratio) in MBE grown InGaAs on patterned GaAs [FWP+89].

8.4.2 Electronic Effects

CV curves of two perpendicular rectangular diodes (1 and 8) are shown in Figure 8.7. Although dislocation densities, dislocation types, and majority carrier trap DLTS spectra differ significantly, the CV profiles are virtually identical. The carrier concentration in the epitaxial layer is about 7×10^{16} cm^{-3}. The net carrier concentration drops off to a minimum at about 230 nm from the contact, which is relatively far from the location of the heterojunction (150 nm, estimated by RBS and etch depth measurements). This is in qualitative agreement with the the CV results and model of Kroemer and co-workers [KCHE80] who studied the characteristics of AlGaAs/GaAs n-n heterojunctions. However, a rise in the carrier concentration caused by electron accumulation on the InGaAs side is not seen. Presumably, some carriers do accumulate on the low bandgap material side, but the region is within the natural depletion width of the Schottky diode and cannot be probed.

In contrast to the identical CV profiles, the DLTS spectra of two of the same two diodes were found to be much different (Figure 6); note that the peak labeled *BC* is significantly larger in the diode type 8. In each of the 4 complete sets of diodes tested, the type 8 *BC* peak was always larger (in one case 10 times larger)

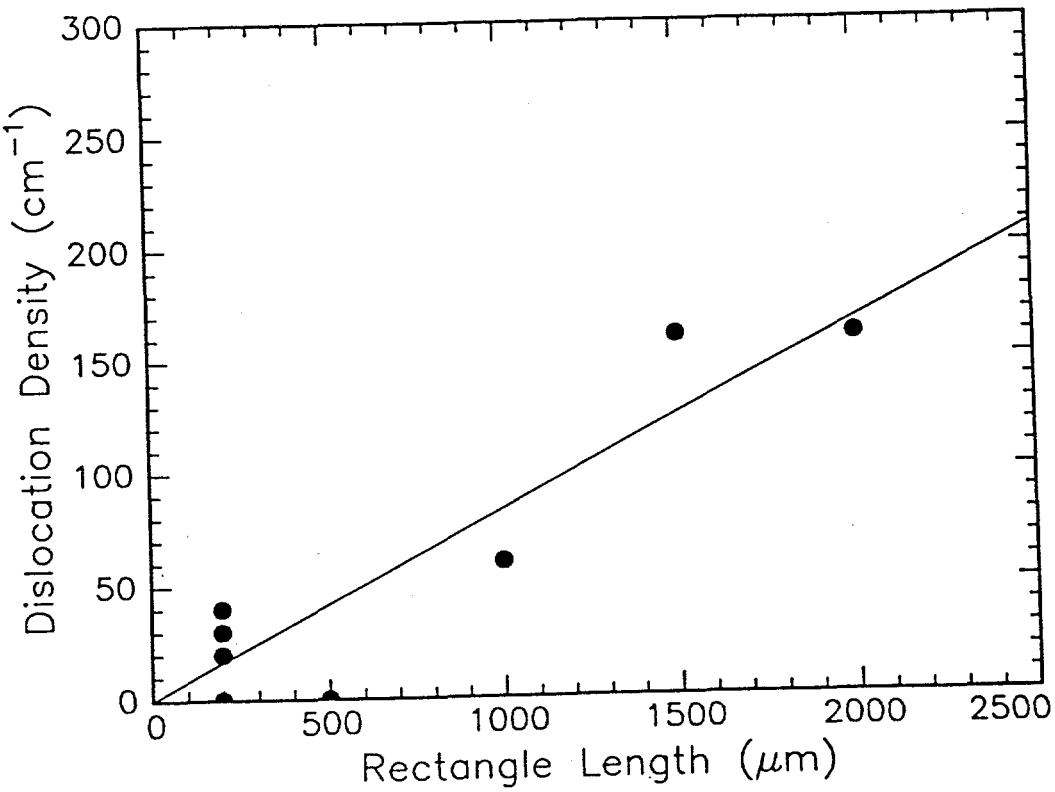

Figure 8.6: A plot of β misfit dislocation density vs. rectangle size.

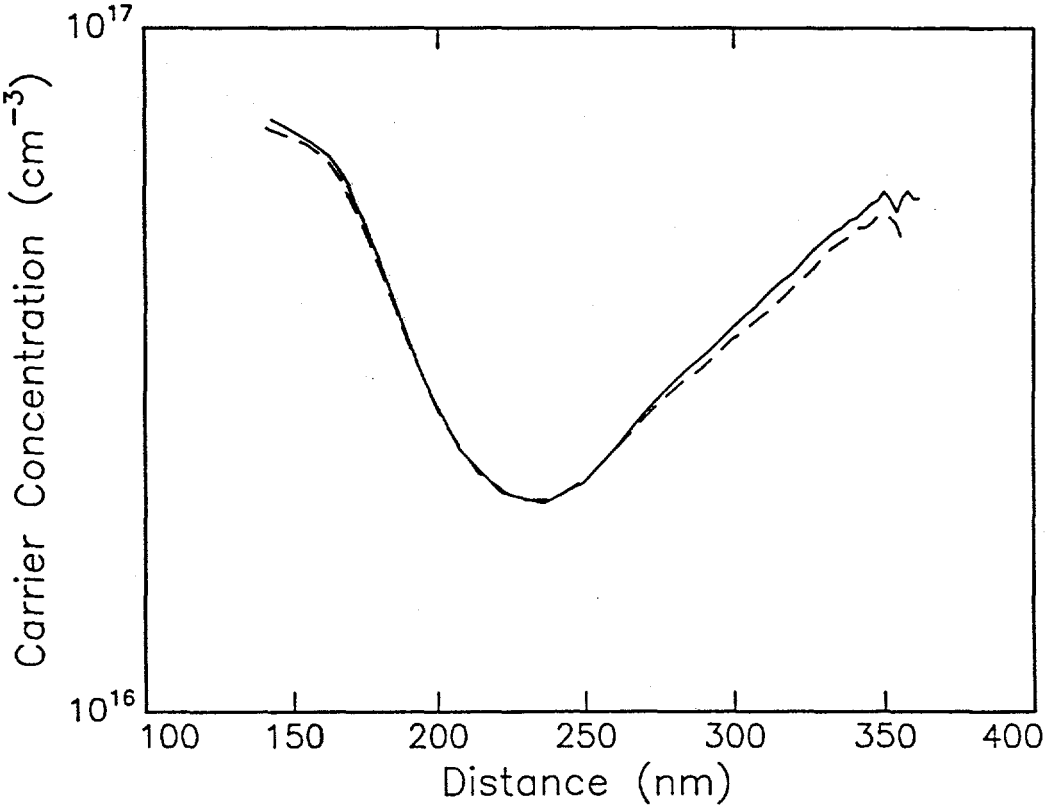

Figure 8.7: Capacitance/voltage characteristics of two rectangular diodes.

than the type 1 peak.

The DLTS spectra for a complete set of rectangular diodes, all at the same measurement conditions, are shown in Figure 8.9. On the vertical axis is the DLTS signal, normalized to remove the differences among the contact areas ($\Delta C/C$). The peak labeled A has roughly the same peak height for all of the diodes. The activation energy of 0.49 ± 0.02 eV and emission cross section of 3×10^{14} cm^2 corresponds to the trap known as M4 [BDBJ86,IHI88]. The size of the peak labeled BC on the other hand depends on the diode geometry. Although it is small and essentially constant for diodes 1 through 4, the peak height increases in rectangles 5 through 8.

The average ($\Delta C/C$) of the peak BC (the mean of 4 sets of diodes of each size and direction) has been plotted versus the [1$\bar{1}$0] rectangle dimension in Figure 8.10. The signal generally increases with rectangle size with a least squares fit slope of $4.5 \pm 1.1 \times 10^{-3}$ cm^{-1}. An intercept of $2.8 \pm 1.1 \times 10^{-4}$ was also calculated - which corresponds to a capacitance transient of a trap whose density is independent of rectangle dimension. The correlation coefficient is 0.860 for this fit. At a reverse bias of -1.0 V instead of the usual -2.0 V, the intensity of peak BC dropped off considerably, indicating that the defect lies in the material near the heterojunction and not near the diode surface.

Figure 8.11 is a plot of BC $\Delta C/C$ versus the [110] direction rectangle lengths. The peak intensity is not influenced by the rectangle dimension in this case, indicating that β dislocations do not contribute to the BC peak in the DLTS spectra. The line drawn through the data is a least squares fit of only the four data points corre-

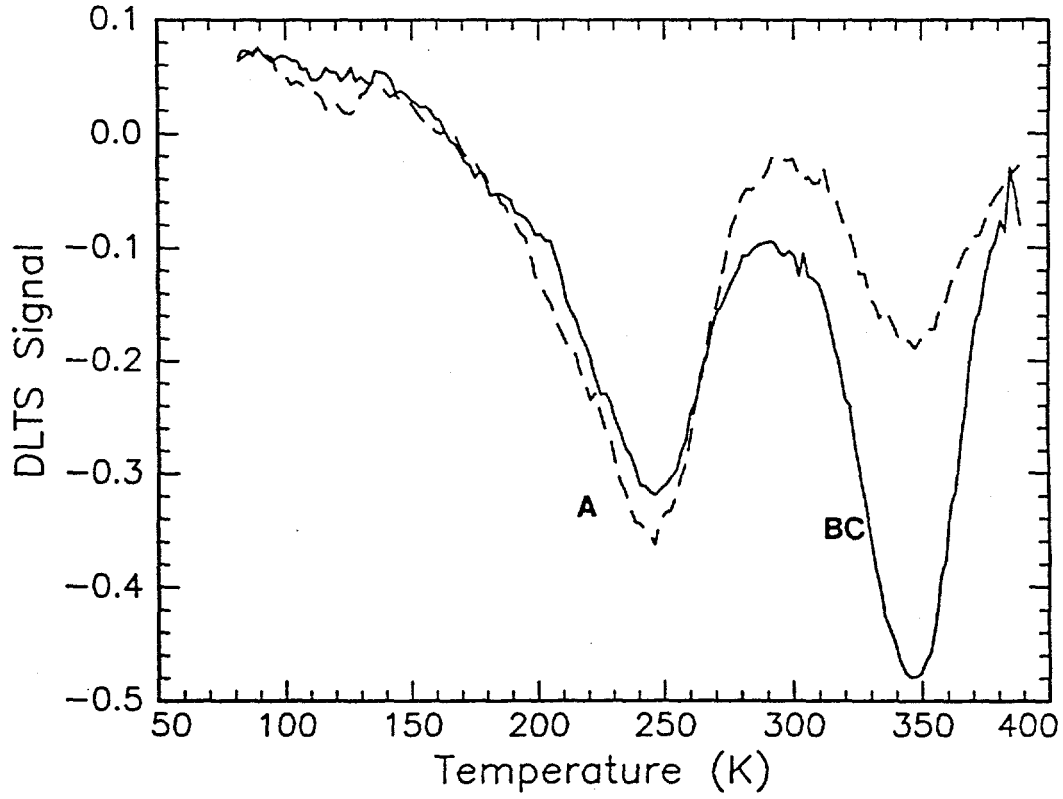

Figure 8.8: DLTS spectra of the same two rectangular diodes as in Figure 8.7.

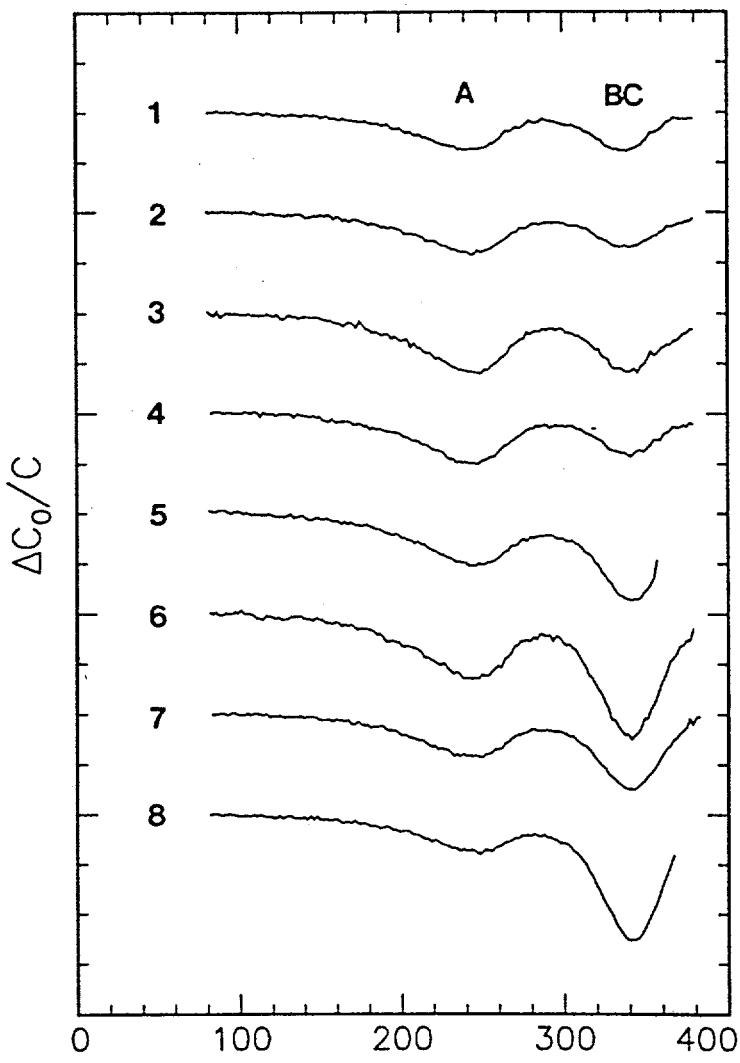

Figure 8.9: DLTS spectra of a complete set of 8 rectangular diodes.

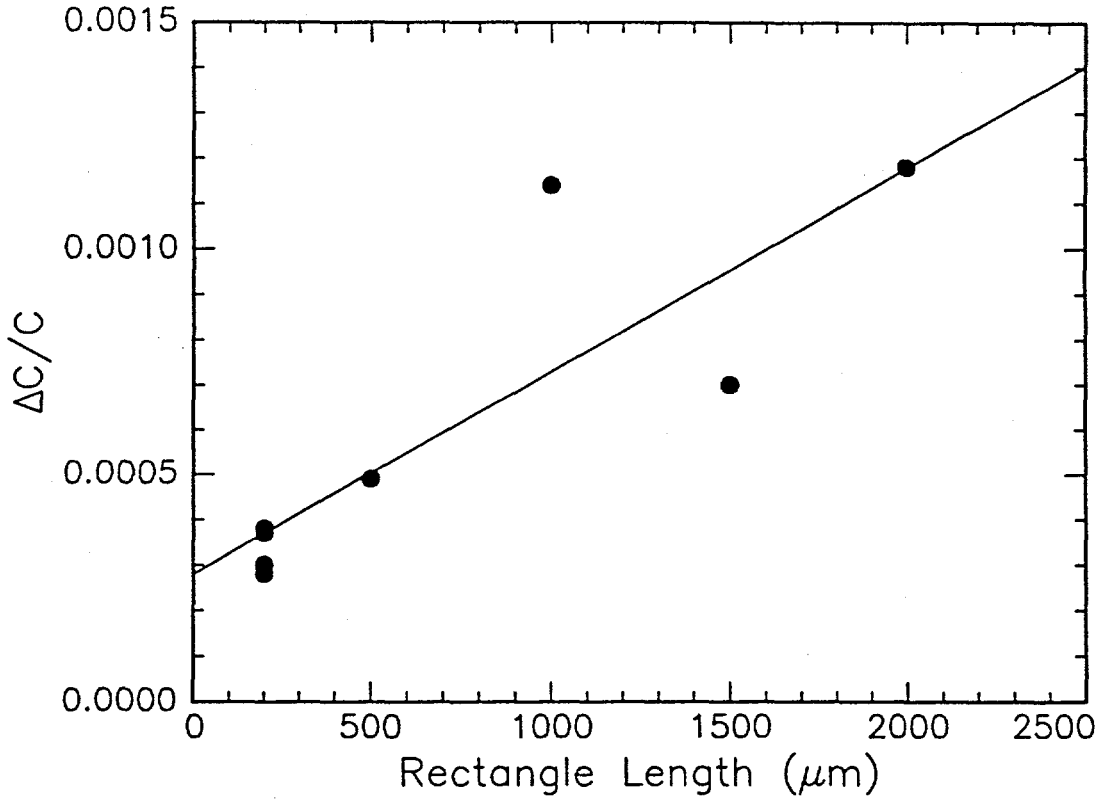

Figure 8.10: A plot of the average DLTS signal vs. rectangle dimension lying in the α direction.

sponding to the rectangles with varying lengths in the [110] direction and constant widths in the [1$\bar{1}$0] direction (rectangles 1 through 4).

There is a small but significant difference in the peak position of BC when a large signal from a rectangle 8 is compared with a small peak from a rectangle such as 4. The activation energy when BC is large is 0.58 ± 0.03 eV and 0.73 ± 0.02 eV when it is small. The emission cross sections are 2×10^{-16} and 3×10^{-14} cm^2, respectively. We denote the two traps as B at 0.58 eV and C at 0.73 eV. In addition, since the peak intensities did not change appreciably with emission rate, the capture cross sections are temperature independent. Figure 8.12 is an activation energy plot of traps B and C. The characteristics of trap C are consistent with those of trap EL2 described in the literature [SLM$^+$87,IMT80].

The argument connecting dislocation core states to the DLTS signal is indirect at this point. It has been established that the misfit dislocation density does increase, in general, with rectangle size and that the DLTS signal varies with the dimensions of some rectangles as well. However, to confirm the connection, a more direct experiment was carried out as follows: after recording the DLTS spectra for a set of rectangles, the contacts were removed and the misfit dislocation density was measured by CL. Figure 8.13 is a plot of $\Delta C/C$ versus the corresponding ρ_α under the contacts. The expected linear relationship is seen, with a slope of $2.0 \pm 0.4 \times 10^{-6}$ cm and an intercept of $3.6 \pm 0.1 \times 10^{-4}$. The regression coefficient is 0.869, virtually the same as the fit in Figure 8.9. One of these diodes, 4, was found to possess no dark line defects at all, although a small BC peak was found. This fact is consistent with the inference that the peak is composed of two traps, only one

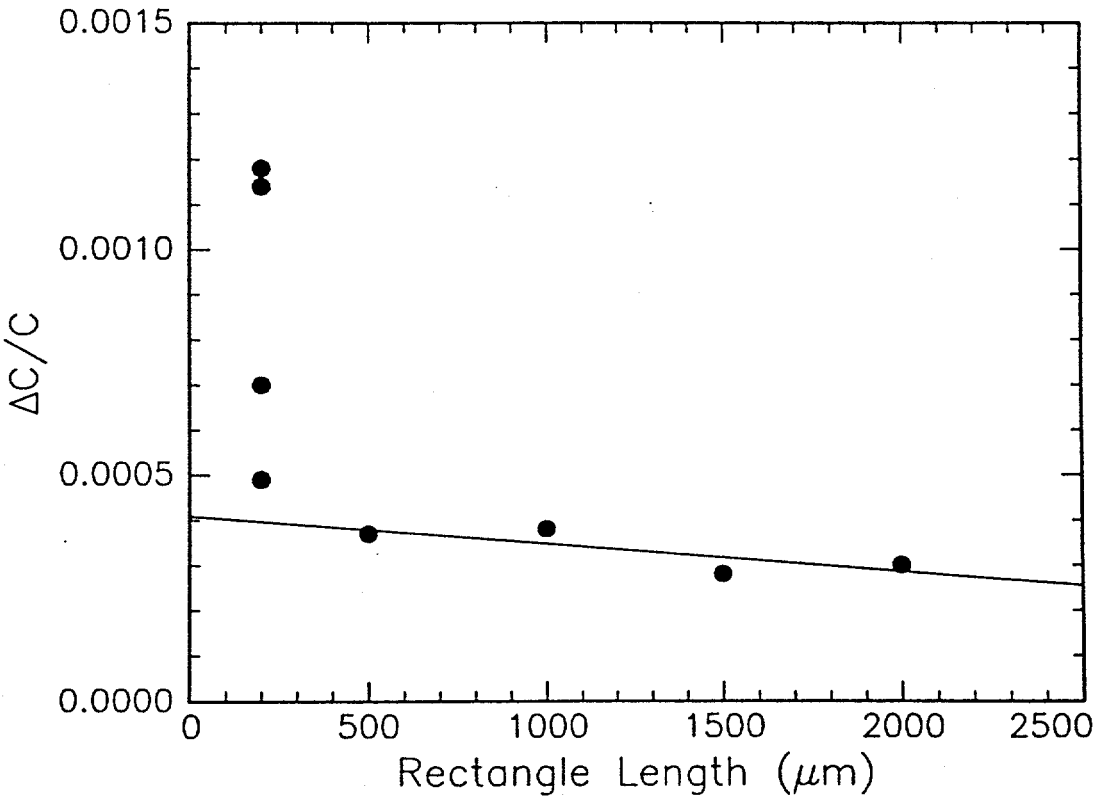

Figure 8.11: A plot of the average DLTS signal vs. rectangle dimension lying in the β direction.

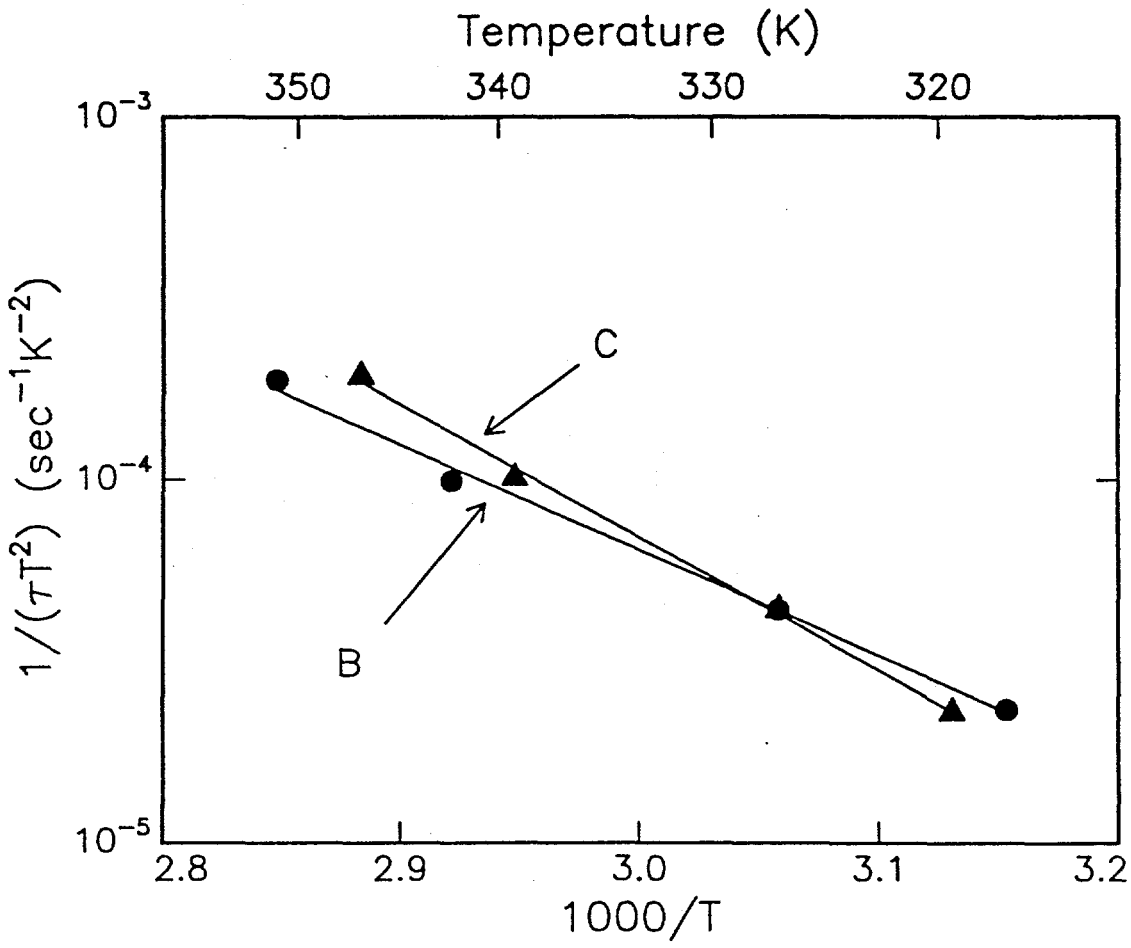

Figure 8.12: DLTS activation energies of traps B and C.

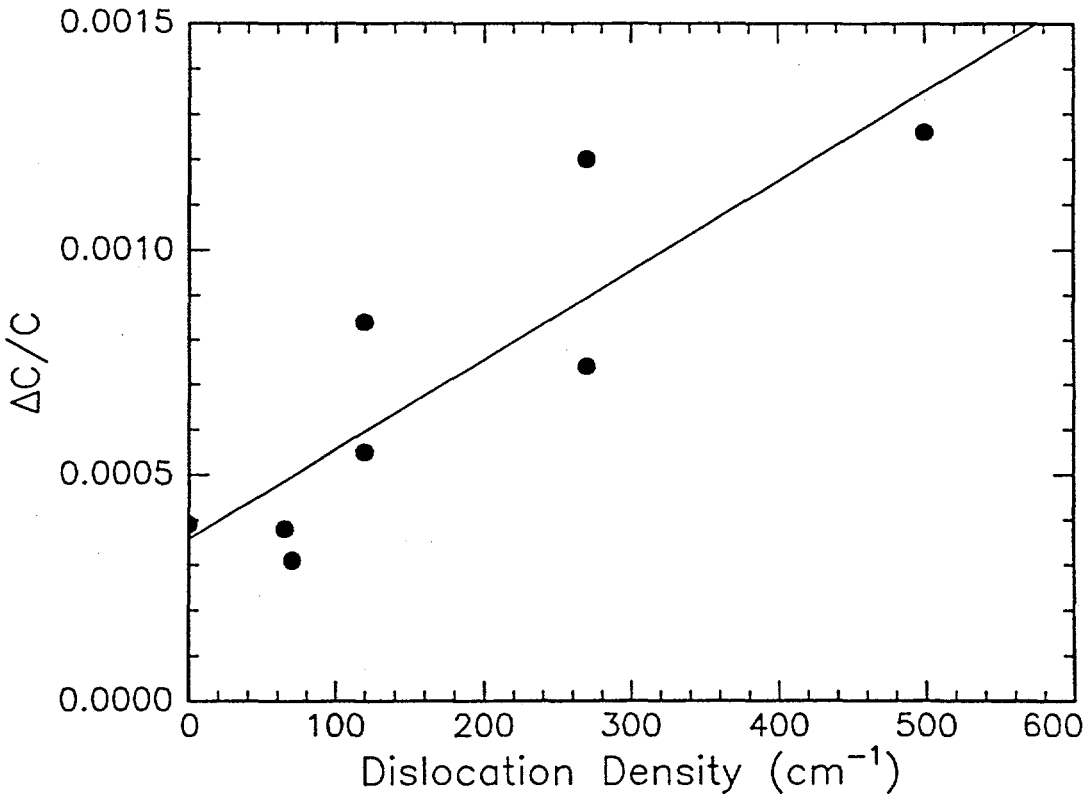

Figure 8.13: A plot of the DLTS signal vs. the α misfit dislocation density.

of which (B) varies with linear defect density. The other, C, is a point defect-like trap that is independent of rectangle dimensions.

The trap B capture kinetics was studied by measuring the DLTS signal at a time constant of 0.086 s and a constant temperature of 343 K (the peak maximum) and various filling pulse times. A diode was selected that had an unusually large B peak so that the C peak would have little effect on the overall trends. Figure 8.14 is a plot of the DLTS signal, in arbitrary units, versus the pulse filling time, t_{fill} on logarithmic scale. The clear linear relationship between peak intensity and $log(t_{fill})$ for over 4 orders of magnitude of t_{fill} implies that these traps are configured as interacting linear arrays [Wos89,Fig78].

8.5 Discussion

8.5.1 Misfit Dislocation Density

The density of dislocations found in the diode interfaces is much lower than those found in comparable material and pattern dimensions in other works [FWP+89, WAAH90a]. The slope of the dislocation densities versus dimension plots is determined by the density of misfit dislocation nucleation sources on the wafer surface. The nucleation source density, g_i, is defined as the number of sites per unit area that create a misfit dislocation in direction $\pm i$. The number of dislocations that cross a unit length that is perpendicular to i (the misfit dislocation density ρ_i) is $\frac{1}{2} g_i \times L$. where L is the length of the isolated region measured parallel to direction i. The factor of one half is necessary since only that fraction of dislocation glide segments travel in the correct direction. The nucleation densities found in this material,

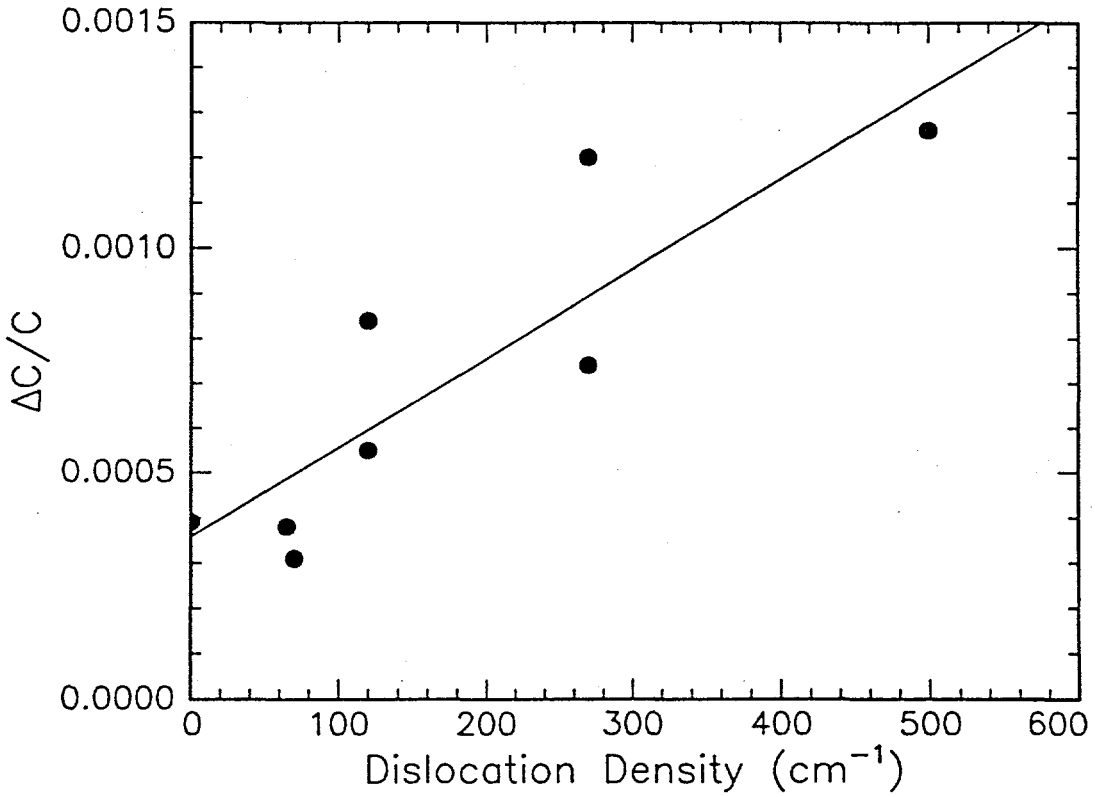

Figure 8.13: A plot of the DLTS signal vs. the α misfit dislocation density.

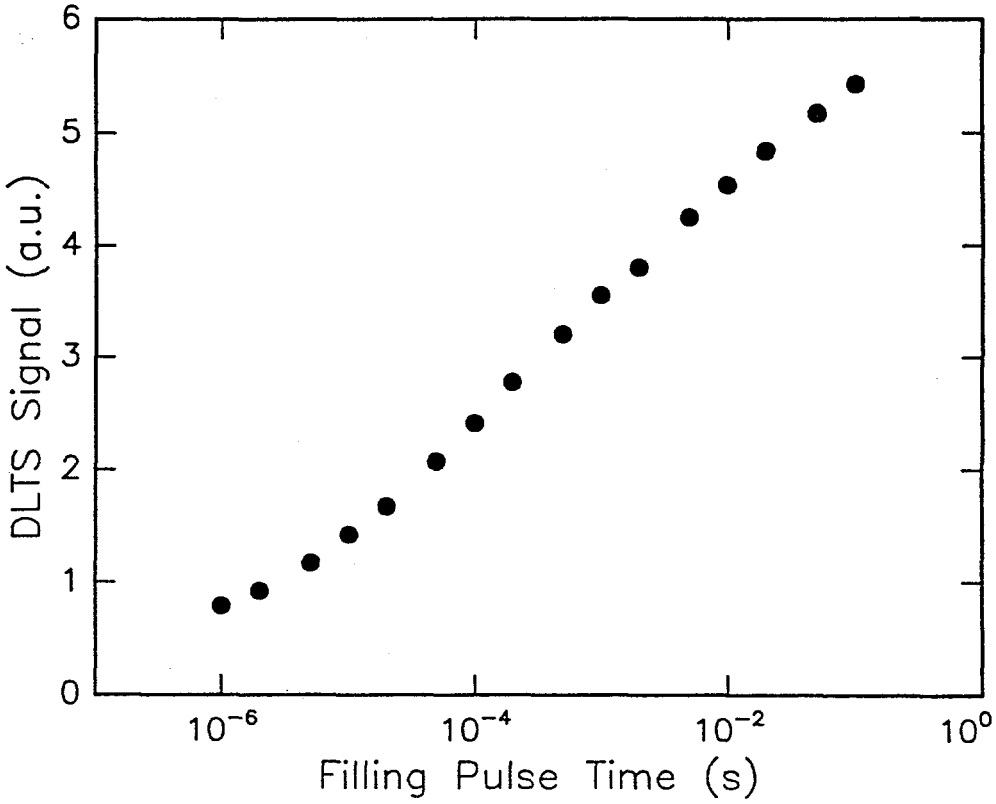

Figure 8.14: DLTS Signal vs. filling pulse time.

g_α=5600 cm^{-2} and g_β=1700 cm^{-2}, are much lower than that found by Fitzgerald et al. in MBE InGaAs of comparable thickness and composition, g_α=50,000 cm^{-2} and g_β=20,000 cm^{-2} for substrates with etch pit densities of 10^4 cm^{-2} [FWP+89]. Watson et al. studied OMVPE InGaAs grown under the same conditions as the diode material (except for doping level) [WAAH90a]. They found nucleation densities of $g_\alpha = g_\beta$=48,000 cm^{-2}. In more recent work, the nucleation densities were reduced to less than about g_α=g_β=2500 cm^{-2} by improving processing and cleaning techniques before epitaxial growth [WAAH90b]. Improved cleaning enhanced the CL signal in these epitaxial layers presumably by removing surface contaminants on the GaAs surface before growth and at the same time removed surface flaws such as foreign particles that act as misfit nucleation sources.

While reduced nucleation densities are advantageous for device applications, the low g_i's found in the present patterned material hinders more precise correlations between DLTS signal and misfit dislocation density. Not only is the signal smaller for a given diode area, but the percent variation in the number of dislocations under the contact is larger. Larger dislocation densities can be created by simply making longer rectangular mesas; however, the mean misfit dislocation path length and the misalignment of the substrate surface and mesa sides would limit the maximum density.

8.5.2 Trap Energy and Kinetics

Trap B possesses many of the same properties as the dislocation related trap ED1 described by Wosinski [Wos89]. Wosinski's dislocations were induced by plastic

deformation of GaAs crystals which also created large numbers of point defects such as EL2. Because misfit dislocations are formed by glide in low mismatch epitaxial layers, the point defect densities in the rectangular diodes should not change with size. In addition, since the misfit dislocation densities are far from the values expected to fully relax the films, the epitaxial layer strain in each diode is essentially the same. Although trap C does interfere with the measurement of the concentration of trap B, unlike defects in plastic deformation studies, its DTLS peak height does not, presumably, change with dislocation density.

The trap energy of B, $E_c - E_t = 0.58 \pm 0.03$ eV, measured from the conduction band edge, is smaller than the value of ED1 found by Wosinski of 0.68 ± 0.01 eV [Wos89]. If they are indeed the same trap, the difference may be due to the fact that ED1 occurred along side a very large EL2 peak. Although Wosinski used a fitting routine to extract the peak positions, it is possible that two overlapping peaks (such as B and C) were fit as one. Only for the largest DLTS peaks was the activation energy found to be constant at 0.58 eV in this work. The measured activation energy was found to vary with peak intensity as the ratio of the two peaks, B and C, changed.

Another possible reason for the energy difference may be due to the fact that the dislocations in this work are located at a heterojunction with an conduction band offset of about 0.048 eV and a bandgap difference of about 0.095 eV [Ada82, SE87]. For instance, if the dislocation energy level in the bandgap is tied to the valence band edge and the active partial dislocation lies in the InGaAs then the measured trap energy could be expected to be smaller than the GaAs energy by the

InGaAs/GaAs bandgap difference, giving Wosinski's E_c-E_t=0.58 eV, the same as trap B. Although a misfit dislocation minimizes the strain energy in the epitaxial layer if it lies precisely at the interface, calculations show that the other (non-strain relieving) Burgers vector components would tend to drive the dislocation into the more compliant InGaAs. The expected position of the misfit dislocation supports of the above argument.

The electron capture of B shown in Figure 12 changes slope at a filling pulse time of about 5×10^{-6} s. At pulse times around 1×10^{-6} s the curve flattens out, apparently because trap C, with a different capture cross section, has a peak intensity comparable to B. No signal saturation occurs for the trap B even at pulse times of 1×10^{-1} s (the maximum possible filling pulse available with the DLTS instrument).

Non-interacting traps are expected to generate a DLTS peak signal as in Equation 8.4. Plotting the DLTS signal height versus $log(t_{fill})$ for such a trap must show a drop from 95% of the saturation value to 5% in about 1.5 orders of magnitude in t_{fill}, independent of the value of τ_c. Wosinski and Figielski showed that if the trap levels are arranged in a linear array, then Coulombic repulsion of the captured carriers influences the probability of capture of future ones and that the DLTS signal is approximately proportional to $ln(t_{fill})$ as Equation 8.10 indicates [Wos89,Fig78]. The capture rate data for B follows this trend for almost 5 orders of magnitude.

The slope in Figure 8.13 connects the DLTS signal directly to the dislocation density as $(\Delta C/C)/\rho_\alpha$. Its value, $2.0 \pm 0.4 \times 10^{-6}$ cm, should be equal to the ratio of the slopes of Figures 8.10 and 8.5, eliminating the rectangle dimension. This is

in fact true; the calculated ratio, $1.6 \pm 0.4 \times 10^{-6}$ cm, agrees well the Figure 8.13 slope.

Given the material characteristics and the misfit dislocation nucleation rate, an estimate of the density of traps per unit length of dislocation is made. The usual relation between DLTS signal and trap concentration was modified to account for the fact that all of the defects lie in one plane in the diode depletion region, and are not dispersed throughout that region. The result, Equation 8.13, can be used to extract the interface trap density from the peak signal intensity. The trap density in turn is related to the α dislocation nucleation source density, g_α, by

$$N_t = \frac{1}{2} g_\alpha \eta_t \xi L_\alpha, \tag{8.14}$$

where η_t is the number of traps per length of dislocation, ξ is the fraction of traps that are filled during the filling pulse and L_α is the rectangle length. Only α dislocations are assumed to contribute. The number of traps per unit length of dislocation may be found by combining Equations 8.13 and 8.14:

$$\eta_t = \frac{N_D W^2}{\xi x_I} \times \frac{\left(\frac{\Delta C/C}{L}\right)}{\left(\frac{1}{2} g_\alpha\right)}. \tag{8.15}$$

The term in parentheses in the numerator is simply the slope in Figure 8.10. The term in parentheses in the denominator is the slope in Figure 8.5. The factor ξ may be estimated by noting that the DLTS peak signal in Figure 8.14 almost doubles from 1×10^{-3} s to the maximum filling pulse time. Assuming that the dislocations are about 27% filled ($f \approx 0.27$ based on Equation 8.7) at that point, the slope in Figure 8, taken at $t_{fill} = 1 \times 10^{-3}$ s, corresponds to a ξ of about one half of that, or 0.13. Inserting $N_D = 7 \times 10^{16}$ cm^{-3}, $W = 240 \times 10^{-7}$ cm, $x_I =$

150×10^{-7} cm and the measured slope values yields a minimum η_t of about 3.2×10^7 cm^{-1}. The corresponding spacing between traps is about 0.3 nm, relatively close to the expected spacing of 0.4 nm between dangling bonds in an undissociated 60° shuffle set dislocation. Although the values of several of the factors are questionable, the estimate of η_t from Equation 8.15 indicates that the majority of traps sites are not eliminated by bond reconstruction at the misfit dislocation core (or at the cores of its constituent partials).

Wosinski speculated that the dislocation energy level he detected was due to β dislocations since it is known that the glide velocities of only β's are influenced by the Fermi level in GaAs [Wos89,DCC89]. Calculations by Jones et al. support this view; they indicate that dissociated β dislocations in GaAs form levels that fall in the mid-gap region and above while α dislocations were estimated to produce electron energy levels near the valence band - if in the bandgap region at all [JOM81]. However, the experimental evidence in this paper shows that only α dislocations form any significant concentration of electron traps in the bandgap. In support of this finding, Zozime and Schroter, studying dislocations in InP, found that α dislocations created many more trap states than β dislocations [ZS90].

Since α dislocations give rise to a DLTS signal in these devices while β dislocations do not, it may be concluded that the configuration of the dislocation core is responsible. If deep levels are caused by impurities or other point defects that simply congregate around the linear defect (because of the strain field), then both dislocation types (with identical long range strain fields) would be expected to possess identical DLTS signatures.

The precise structure that gives rise to the deep level states cannot be discerned here, although it is well established that 60° dislocations in III-V materials (both gliding and static) are for the most part dissociated into 30° and 90° partial dislocations. During motion, the partial dislocations are most likely in the glide set configuration. However, Alexander has proposed that when static, one of the partial dislocations may absorb a row of vacancies or interstitials to become a shuffle set dislocation [Ale79]. Specifically, an As(g) partial would convert to a Ga(s) one. If so, then this may explain the discrepancy between the quantum mechanical model of Jones et al. (based on two glide set partials) and the present experimental results [JOM81].

The devices fabricated in this study are only majority carrier devices. Acceptor-like traps cannot be measured. It is also important to note that both α and β misfit dislocations have similar CL contrasts, meaning that both act as effective electron-hole recombination centers in the material studied. The experiment presented here does not shed any light on this important aspect of dislocation electron states. However, this technique can be extended to p-n junction devices. It would then be possible to study both electron and hole traps in the n-type InGaAs/GaAs heterojunction.

8.6 Conclusions

The density and core type of misfit dislocations, formed at mildly mismatched InGaAs grown by OMVPE on GaAs substrates was controlled by varying the dimensions of rectangular mesas etched on the substrate before growth. DLTS ex-

periments performed on Schottky diodes fabricated on those rectangles reveal an n-type majority carrier deep level trap at 0.58 eV below the conduction band. The trap concentration increases with increasing rectangle dimension only for devices oriented so that the density of α misfit dislocations increases with rectangle length. Since the preparation, composition, and strain are essentially the same for each diode, it is concluded that the trap is caused by misfit dislocations. The logarithmic dependence of the intensity of the DLTS peak with fill time for this trap strengthens the view that the trap found is indeed related to defects that are in close proximity to one another such as at dislocation cores sites, and is not caused by isolated defects.

Since only α type dislocations give rise to trap energy levels, and since both α and β types have identical strain fields outside their cores, it is concluded that the deep level is due to the dislocation core itself, and not to impurity gettering.

Calculations indicate that virtually all of the core atoms contribute to the defect density, indicating that core reconstruction does not significantly reduce the potential trap sites at the dislocation core.

Chapter 9

Summary

9.1 Strained Layers on Ion-Damaged Substrates

Lattice mismatched InGaAs, MBE grown on selectively ion damaged GaAs substrates leads to a unique degree of strain release at a 400°C growth temperature. Misfit dislocations form for the most part along only the $[1\bar{1}0]$ direction in the interface plane and therefore relieve strain in only one direction. The ion damaged edges nucleate a large number of misfit dislocations but it is still an insufficient number to reach the expected equilibrium density (about three times higher). Calculations show that the difference cannot be explained by dislocation interactions or frictional forces and must reflect nucleation difficulties. Growth at 500°C does reduce the misfit density, but at the cost of no longer confining the gliding misfit dislocations.

Material grown on selectively etched substrates nucleated misfits in only the $[1\bar{1}0]$ direction as well. Increasing the growth temperature also reduced the misfit

dislocation density. The reason for the temperature dependence may be related to the edge profile and is currently being studied.

The reason that misfits nucleate at etched or ion damaged edges in only the $[1\bar{1}0]$ direction may be explained by assuming that only α dislocations can glide in the n-type material and that they relieve strain in only that direction. It is shown that the few misfit dislocations that do form in the [110] direction can do so by glide of α threading dislocations.

9.2 Misfit Dislocation Glide in Continuous Strained Layers

The misfit dislocation density in strained, continuous, OMCVD InGaAs layers can be significantly reduced by patterning and etching the GaAs substrate before growth. The etch depth needed to isolate misfit dislocations in $In_{0.04}Ga_{0.96}As$ is about 250 nm for a 300 nm thick epitaxial layer and 450 nm for a 600 nm thick layer. Isolation occurs at a trench depth of about 500 nm for 300 nm thick $In_{0.08}Ga_{0.92}As$. Three isolation regimes are seen, depending on the etch depth. In regime I, the shallowest depths, some dislocations can glide across the trenches, reaching adjacent islands. In regime II, dislocations are stopped, but are blocked only after gliding down into the trenches where they come to rest at the far side. In regime III, dislocations stop at the edge of the mesas because the strained epitaxial layer thins down below the critical thickness at the trench wall, preventing the misfit gliding segment from getting through. However, epitaxial layer discontinuity, or near discontinuity at large trench depths is not necessary to prevent the glide of misfit dislocations. Continuous layers in regime II material

can stop virtually all of the dislocations from crossing from one isolated region to another.

Analysis of the system free energy as a function of misfit dislocation position near a trench wall reveals that the transition from regimes I to II is determined by the trench wall angle. Sharp wall slopes which are present in the deeper trench regime II substrates, can block the passage of misfit dislocations in spite of the epitaxial layer continuity.

9.3 Thermal Stability of Strained Layers on Patterned Substrates

Annealing strained epitaxial layers grown on patterned substrates induces new misfit dislocations to form by the apparent nucleation of half-loops that glide along the interface, leaving a strain relieving dislocation behind. These dislocations nucleate for the most part only at edges created by the patterning and etching before epitaxial growth.

OMCVD InGaAs epitaxial layers grown on patterned GaAs substrates possess a very small misfit dislocation density, and even after severe annealing for up to 300 s at 800°C the defect density is less than 1500 cm^{-1}. Though their density increases with annealing, the misfit dislocation density remains well below the density found in unpatterned substrates. The MBE grown epitaxial layers are much less stable; misfit dislocations nucleate in much greater numbers in MBE material at all of the temperatures studied.

The misfit dislocation nucleation properties of OMCVD grown material is found

to depend on the trench depth. Films deposited on patterned substrates with deeper trenches (greater than 0.5 μm) are more stable, apparently because a thinning of the epitaxial layer occurs at the edges of these trenches. A thinner layer means less strain energy is available in the region where the misfit dislocations apparently nucleate. Furthermore, if the layer thickness locally falls below the critical thickness, the propagation of misfit dislocations is inhibited.

The reason that MBE material is less stable than OMCVD grown samples is not epitaxial layer topology. OMCVD material that was etched to expose the InGaAs/GaAs interface (and thereby *mimic* an MBE grown profile) is no less stable than unetched material. The different dopants used in the two growth processes or the difference in concentrations of other defects may cause the different nucleation properties of these materials.

9.4 ZnSe on Patterned GaAs Substrates

Scanning CL images of ZnSe/GaAs interfaces show that only β misfit dislocations form in epitaxial layers grown at 440°C by OMCVD. This is counter to the typical results seen in the InGaAs/GaAs system, where α misfit dislocations predominate. Misfit dislocations were not visible in ZnSe epitaxial layers grown at temperatures below 440°C.

The relationship between the average misfit dislocation density and mesa size is not linear, as it is with the InGaAs/GaAs system. The sub-linear behavior, and the variation of misfit dislocation density with measurement position on the mesas, are consistent with glide segment blocking by other, randomly distributed, defects.

9.5 Electronic Deep Level States Caused by Misfit Dislocations

The density and core type of misfit dislocations, formed at mildly mismatched InGaAs grown by OMCVD on GaAs substrates was controlled by varying the dimensions of rectangular mesas etched on the substrate before growth. DLTS experiments performed on Schottky diodes fabricated on those rectangles reveal an n-type majority carrier deep level trap at 0.58 eV below the conduction band. The trap concentration increases with increasing rectangle dimension only for devices oriented so that the density of α misfit dislocations increases with rectangle length. Since the preparation, composition, and strain are essentially the same for each diode, it is concluded that the trap is caused by misfit dislocations. The logarithmic dependence of the intensity of the DLTS peak with fill time for this trap strengthens the view that the trap found is indeed related to defects that are in close proximity to one another such as at dislocation cores sites, and is not caused by isolated defects.

Since only α type dislocations give rise to trap energy levels, and since both α and β types have identical strain fields outside their cores, it is concluded that the deep level is due to the dislocation core itself, and not to impurity gettering.

Calculations indicate that virtually all of the core atoms contribute to the defect density, indicating that core reconstruction does not significantly reduce the potential trap sites at the dislocation core.

Bibliography

[AAS+88] Y. Ashizawa, S. Akbar, W. J. Schaff, L. F. Eastman, E. A. Fitzgerald, and D. G. Ast. Influence of lattice misfit on heterojunction bipolar transistors with lattice-mismatched InGaAs bases. *Journal of Applied Physics*, 64:4065, 1988.

[ABB72] M. S. Abrahams, J. Blanc, and C. J. Buiocchi. Like-sign asymmetric dislocations in zinc-blende structure. *Applied Physics Letters*, 21:185, 1972.

[ABW85] G. Abstreiter, H. Brugger, and T. Wolf. Strain-induced two-dimensional electron gas in selectively doped Si/SiGe superlattices. *Physical Review Letters*, 54:2441, 1985.

[Ada82] S. Adachi. Materials parameters of ingaasp and related binaries. *Journal of Applied Physics*, 53:999, 1982.

[AHLS79] H. Alexander, P. Haasen, R. Labusch, and W. Schroter. Forward. *Journal of Physics, Paris*, 40, 1979.

[Ale79] H. Alexander. Models of the dislocation structure. *Journal de Physique, Colloquium C6*, 40:1, 1979.

[BDBJ86] P. K. Bhattacharya, S. Dhar, P. Berger, and F. Juang. Electrical and optical properties of deep levels in MOVPE grown GaAs. *Applied Physics Letters*, 49:470, 1986.

[BS85] J. L. Batstone and J. W. Steeds. TEM and CL characterization of dislocations in OMCVD ZnSe. *Insitute of Physics Conference Series*, 76:383, 1985.

[BYC+89] K. J. Beernink, P. K. York, J. J. Coleman, R. G. Waters, J. Kim, and C. M. Wayman. Characterization of InGaAs-GaAs strained-layer

lasers with quantum wells near the critical thickness. *Applied Physics Letters*, 55:2167, 1989.

[CFST86] M. Cocito, P. Franzosi, G Salviati, and F. Taiariol. Cathodoluminescence study of defects in III-V substrates and structures. *Scanning Electron Microscopy*, page 1299, 1986.

[Cho83] A. Y. Cho. Growth of III-V semiconductors by molecular beam epitaxy and their properties. *Thin Solid Films*, 100:291, 1983.

[CSM89] C. B. Cooper, S. Salimian, and H. F. Macmillan. Reactive ion etch characteristics if thin InGaAs and AlGaAs stop-etch layers. *Journal of Electronic Materials*, 18:619, 1989.

[Cul78] B. D. Cullity. *Elements of X-ray Diffraction.* Adison-Wesley Publishing Co., 1978.

[DAC+89] A. V. Drigo, A. Aydinli, A. Carnera, F. Genova, C. Rigo, C. Ferrari, P. Franzosi, and G. Salviati. On the mechanisms of strain release in molecular-beam-epitaxy-grown InGaAs/GaAs single hetreostructures. *Journal of Applied Physics*, 66:1975, 1989.

[DC87] B. C. De Cooman. *Contribution to the Study of Extended Defects in GaAs and Related Compounds.* Ph.D. dissertation, Cornell University, 1987.

[DCC89] B. C. De Cooman and C. B. Carter. Dislocation configurations in semi-insulating, n-type and p-type GaAs deformed at 150 c. *Philosophical Magazine A*, 60:245, 1989.

[DT87] B. W. Dodson and J. Y. Tsao. Relaxation of strained-layer semiconductor structures via plastic flow. *Applied Physics Letters*, 51:1325, 1987.

[FAA+88] E. A. Fitzgerald, D. G. Ast, Y. Ashizawa, S. Akbar, and L. F. Eastman. Dislocation structure, formation and minority carrier recombination in AlGaAs/InGaAs/GaAs heterojunction bipolar transistors. *Journal of Applied Physics*, 64:2473, 1988.

[FAI+90] S. F. Fang, K. Adomi, S. Iver, H. Morkoc, H. Zabel, C. Choi, and N. Otsuka. Gallium arsenide and other compound semiconductors on silicon. *Journal of Applied Physics*, 68:R31, 1990.

[Fig78] T. Figielski. Recombination at dislocations. *Solid State Electronics*, 21:1403, 1978.

[Fit88] E. A. Fitzgerald. The effect of substrate growth area on misfit and threading dislocation densities in mismatched heterostructures. *Journal of Vacuum Science and Technology*, B7:782, 1988.

[Fit89] E. A. Fitzgerald. *The properties, control, and elimination of misfit dislocations in semiconductor heterostructures.* Ph.D. dissertation, Cornell University, 1989.

[FJ90] B. A. Fox and W. A. Jesser. Investigation of the asymmetric misfit dislocation morphology in epitaxial layers with the zinc-blende structure. *Journal of Applied Physics*, 68:2739, 1990.

[FTdM+91] H. H. Farrell, M. C. Tamargo, J. L. de Miguel, F. S. Turco, D. M. Hwang, and R. E. Nahory. Designer interfaces in II-IV/III-V polar heteroepitaxy. *Journal of Applied Physics*, 69:7021, 1991.

[FWP+89] E. A. Fitzgerald, G. P. Watson, R. E. Proano, D. G. Ast, P. D. Kirchner, G. D. Pettit, and J. M. Woodall. Nucleation mechanisms and the elimination of misfit dislocations at mismatched interfaces by a reduction in growth area. *Journal of Applied Physics*, 65:2220, 1989.

[FXM+90] E. A. Fitzgerald, Y. H. Xie, J. Michel, P. E. Freeland, and B. E. Weir. Reduction of defect density in heteroepitaxial GeSi grown on patterned Si substrates. In B. W. Dodson, L. J. Schowalter, J. E. Cunningham, and F. H. Pollak, editors, *Layered Structures - Heteroepitaxy, Superlattices, Strain, and Metastability*, volume 160, page 59. Materials Research Society, 1990.

[GCB+89] M. Grundmann, J. Christen, D. Bimberg, A. Fischer-Colbrie, and R. Hull. Misfit dislocations in pseudomorphic InGaAs quantum wells: Influence on lifetime and diffusion of excess excitons. *Journal of Applied Physics*, 66:2214, 1989.

[Ger79] E. Gerlach. Scattering of charge-carriers by dislocations. *Journal de Physique, Colloquium C6*, 40:47, 1979.

[GFD88] P. L. Gourley, I. J. Fritz, and L. R. Dawson. Controversy of critical thickness for InGaAs/GaAs strained layer epitaxy. *Applied Physics Letters*, 52:377, 1988.

[GJM75] Gibbons, Johnson, and Mylroie. *Projected Range Statistics, 2nd ed.* Halsted Press, 1975.

[GK90] P. J. Goodhew and P. Kightley. The creation of misfit dislocations; a study of InGaAs alloys on GaAs substrates. In *Materials Research Society Fall Meeting Abstracts*, page 81, 1990.

[GL65] H. C. Gatos and M. C. Lavine. Chemical behavior of semiconductors: Etching characteristics. In A. F. Gibson and R. E. Burgess, editors, *Progress in Semiconductors, Vol. 9.* Temple Press Books Ltd., London, 1965.

[GLB+89] M. Grundmann, U. Lienert, D. Bimberg, A. Fischer-Colbrie, and J. N. Miller. Anisotropic and inhomogeneous strain relaxation in pseudomorphic InGaAs/GaAs quantum wells. *Applied Physics Letters*, 55:1765, 1989.

[GLB+90] M. Grundmann, U. Lienert, D. Bimberg, A. Fischer-Colbrie, and J. N. Miller. Erratum: Anisotropic and inhomogeneous strain relaxation in pseudomorphic InGaAs/GaAs quantum wells. *Applied Physics Letters*, 57:2034, 1990.

[GPG+91] A. Gustafsson, M. E. Pistol, M. Gerling, L. Samuelson, M. R. Leys, and H. Titze. Dislocations in mismatched layers of GaAsP in between GaP as observed by low-temperature cathodoluminescence. *Journal of Applied Physics*, 70:1660, 1991.

[HBB86] S. D. Hersee, E. Barbier, and R. Blondeau. A study of the orientation dependence of Ga(Al)As growth by MOVPE. *Journal of Crystal Growth*, 77:310, 1986.

[HBG+86] H. Heinecke, A. Brauers, F. Grafahrend, C. Plass, N. Putz, K. Werner, M. Weyers, H. Luth, and P. Balk. Selective growth of GaAs in the MOMBE and MOCVD systems. *Journal of Crystal Growth*, 77:303, 1986.

[HCDP90] M. A. Haase, H. Cheng, J. M. Depuydt, and J. E. Potts. Characterization of p-type ZnSe. *Journal of Applied Physics*, 67:448, 1990.

[HF90] J. P. Hirth and X. Feng. Critical layer thickness for misfit dislocation stability in multilayer structures. *Journal of Applied Physics*, 67:3343, 1990.

[HH90] S. Hildebrandt and W. Hergert. Unified theoretical description of the CL, EBIC, PL, and LBIC contrast profile area of an individual surface parallel dislocation. *Physica Status Solidi (a)*, 119:689, 1990.

[HHN+65] P. B. Hirsch, A. Howie, R. B. Nicholson, D. W. Pashley, and M. J. Whelan. *Electron Microscopy of Thin Crystals.* Butterworth, Sevenoaks, 1965.

[HL82] J. P. Hirth and J. Lothe. *The Theory of Dislocations.* John Wiley and Sons, 1982.

[Hou90] D. C. Houghton. Nucleation rate and glide velocity of misfit dislocations in SiGe/Si heterostructures. *Applied Physics Letters*, 57:2124, 1990.

[Hou91] D. C. Houghton. Strain relaxation kinetics in SiGe/Si heterostructures. *Journal of Applied Physics*, 70:2136, 1991.

[HS78] W. Hagen and H. Strunk. A new type of source generating misfit dislocations. *Applied Physics*, 17:85, 1978.

[HS85] D. B. Holt and F. M. Saba. The cathodoluminescence mode of the scanning electron microscope: A powerful microcharacterization technique. *Scanning Electron Microscopy*, page 1023, 1985.

[Hu91] S. M. Hu. Misfit dislocations and critical thickness of heteroepitaxy. *Journal of Applied Physics*, 69:7901, 1991.

[IHI88] D. E. Ioannou, Y. J. Huang, and A. A. Iliadis. Deep states and misfit dislocations in indium-doped GaAs layers grown by molecular beam epitaxy. *Applied Physics Letters*, 52:2258, 1988.

[IMT80] T. Ishida, K. Maeda, and S. Takeuchi. A study of deformation-produced deep levels in n-GaAs using deep level transient capacitance spectroscopy. *Applied Physics*, 21:257, 1980.

[IMW91] K. Ismail, B. S. Meyerson, and P. J. Wang. High electron mobility in modulation-doped Si/SiGe. *Applied Physics Letters*, 58:2117, 1991.

[JLSM87] J. Jeong, J. C. Lee, T. E. Schlesinger, and A. G. Milnes. Study of n-InGaAs/n-GaAs heterostructure epilayers. *Journal of Vacuum Science and Technology B*, 5:792, 1987.

[Joh86] N. M. Johnson. Deep-level transient spectroscopy: characterization and identification of electronic defects. *Optical Engineering*, 25:698, 1986.

[JOM81] R. Jones, S. Oberg, and S. Marklund. Structure and energy level calculations of dislocations in gallium arsenide. *Philosophical Magazine*, 43:839, 1981.

[KCH+88] K. L. Kavanagh, M. A. Capano, L. W. Hobbs, J. C. Barbour, P. M. J. Maree, W. Schaff, J. W. Mayer, D. Pettit, J. M. Woodall, J. A. Stroscio, and R. M. Feenstra. Asymmetries in dislocation densities, surface morphology, and strain of GaInAs/GaAs single heterostructures. *Journal of Applied Physics*, 64:4843, 1988.

[KCHE80] H. Kroemer, W. Y. Chien, J. S. Harris, and D. D. Edwall. Measurement of isotype heterojunction barriers by C-V profiling. *Applied Physics Letters*, 36:295, 1980.

[KFG+90] J. F. Klem, W. S. Fu, P. L. Gourley, E. D. Jones, T. M. Brennan, and J. A. Lott. Role of substrate threading dislocation density in relaxation of highly strained InGaAs/GaAs quantum well structures. *Applied Physics Letters*, 56:1350, 1990.

[KFS88] Y. Kohama, Y. Fukuda, and M. Seki. Determination of the critical layer thickness of SiGe/ Si heterostructures by direct observation of misfit dislocations. *Applied Physics Letters*, 52:380, 1988.

[KG70] A. Kelly and G. W. Groves. *Crystallography and crystal defects.* Addison-Wesley, 1970.

[KHG89] C. A. King, J. L. Hoyt, and J. F. Gibbons. Bandgap and transport properties of SiGe by analysis of nearly ideal Si/SiGe/Ssi heterojunction bipolar transistors. *IEEE Transactions on Electron Devices*, 36:2093, 1989.

[KNJ+91] T. I. Kamins, K. Nauka, R. D. Jacowitz, S. S. Laderman, J. L. Hoyt, D. B. Noble, and J. F. Gibbons. p-n junction diodes in selective Si/SiGe epitaxial layers. In *Electronic Materials Conference*, 1991.

[KP87] J. Kleiman and R. M. Park. Determination of the onset of plastic deformation in ZnSe layers grown on (100) GaAs by molecular-beam epitaxy. *Journal of Applied Physics*, 61:2067, 1987.

[KSK+86] K. Kamon, M. Shimazu, K. Kimura, M. Mihara, and M. Ishii. Selective growth of AlGaAs embedded in etched grooves on GaAs by low-pressure OMVPE. *Journal of Crystal Growth*, 77:297, 1986.

[KTM86] K. Kamon, S. Takagishi, and H. Mori. Selective embedded growth of AlGaAs by low-pressure oganometallic vapor phase epitaxy. *Japanese Journal of Applied Physics*, 25:L10, 1986.

[Lan74] D. V. Lang. Deep-level transient spectroscopy: A new method to characterize traps in semiconductors. *Journal of Applied Physics*, 45:3023, 1974.

[LBT91] W. Q. Li, P. K. Bhattacharya, and R. L. Tober. Improved performance of strained InGaAs/GaAs photodiodes grown on patterned GaAs substrates by molecular beam epitaxy. *Applied Physics Letters*, 58:1931, 1991.

[LS80] R. Labusch and W. Schroter. Electrical properties of dislocations in semiconductors. In F. R. N. Nabarro, editor, *Dislocations in Solids, Volume 5*. North-Holland Publishing Co., New York, 1980.

[LTLA89] S. Y. Lin, D. C. Tsui, H. Lee, and D. Ackley. Conduction-band offset in strained AlGaAs/InGaAs/ GaAs pseudomorphic structures. *Applied Physics Letters*, 55:2211, 1989.

[Mat75a] J. W. Matthews. Coherent interfaces and misfit dislocations. In J. W. Matthews, editor, *Epitaxial Growth, Part B*. Academic Press, New York, 1975.

[Mat75b] J. W. Matthews. Defects associated with the accommodation of misfit between crystals. *Journal of Vacuum Science and Technology*, 12:126, 1975.

[MB74] J. W. Matthews and A. E. Blakeslee. Defects in epitaxial multilayers. *Journal of Crystal Growth*, 27:118, 1974.

[MBM76] J. W. Matthews, A. E. Blakeslee, and S. Mader. Use of misfit strain to remove dislocations from epitaxial thin films. *Thin Solid Films*, 33:253, 1976.

[MIIN83] S. Miyazawa, Y. Ishii, S. Ishida, and Y. Nanishi. Direct observation of dislocation effects on threshold voltage of a GaAs field-effect transistor. *Applied Physics Letters*, 49:853, 1983.

[MML70] J. W. Matthews, S. Mader, and T. B. Light. Accommodation of misfit across the interface between crystals of semiconducting elements or compounds. *Journal of Applied Physics*, 41:3800, 1970.

[MSIT84] K. Maeda, K. Suzuki, M. Ichihara, and S. Takeuchi. Electron-beam irradiation enhanced dislocation glide in GaAs observed by transmission electron microscopy. *Journal of Applied Physics*, 56:554, 1984.

[Nab67] F. R. N. Nabarro. *Theory of Crystal Dislocations.* Dover Publications, 1967.

[ND85] R. J. Nelson and N. K. Dutta. Review of IngaAsP/InP laser structures and comparison of their performance. In W. T. Tsang, editor, *Semiconductors and Semimetals, Vol. 22, Lightwave Communications Technology.* Academic Press, 1985.

[NHK+90] D. B. Noble, J. L. Hoyt, C. A. King, J. F. Gibbons, T. I. Kamins, and M. P. Scott. Reduction in misfit dislocation density by the selective growth of SiGe/Si in small areas. *Applied Physics Letters*, 56:51, 1990.

[Nye85] J. F. Nye. *Physical Properties of Crystals.* Oxford University Press, New York, 1985.

[OAZ74] G. H. Olsen, M. S. Abrahams, and T. J. Zamerowski. Asymmetric cracking in III-V compounds. *Journal of the Electrochemical Society*, 121:1650, 1974.

[oDiCC79] Hünfeld Conference on Dislocations in Covalent Crystals. *Journal de Physique, Colloquium C6*, 40:1, 1979.

[OKWO89] Y. Ohmachi, Y. Kadota, Y. Watanabe, and H. Okamoto. High quality GaAs in Si and its application to a solar cell. In *Materials Research Society Symposia Proceedings*, volume 144, page 297, 1989.

[OO89] A. Okamoto and K. Ohata. Growth condition dependence for GaAs selective epitaxial growth by molecular-beam epitaxy. *Journal of Electronic Materials*, 18:111, 1989.

[PB85] R. People and J. C. Bean. Calculation of critical thickness versus lattice mismatch for GeSi/Si strained layer heterostructures. *Applied Physics Letters*, 47:322, 1985.

[PCMS87] J. E. Potts, H. Cheng, S. Mohapatra, and T. L. Smith. Effect of elastic strain on the energy band gap in heteroepitaxially grown ZnSe. *Journal of Applied Physics*, 61:333, 1987.

[Pea91] T. J. Pearsall. Strained-layer superlattices. In T. P. Pearsall, editor, *Semiconductors and Semimetals, Vol. 32, Strained-Layer Superlattices: Materials Science and Technology.* Academic Press, 1991.

[PK79] J. R. Patel and L. C. Kimmerling. Dislocation defect states in silicon. *Journal de Physique, Colloquium C6*, 40:67, 1979.

[PLS79] J. Petroff, R. A. Logan, and A. J. Savage. Nonradiative recombination at dislocations in III-V compound semiconductors. *Journal of Microscopy*, 118:255, 1979.

[RBS+90] J. Ren, K. A. Bowers, B. Sneed, D. L. Dreifus, J. W. Cook, Jr., J. F. Schetzina, and R. M. Kolbas. ZnSe light-emitting diodes. *Applied Physics Letters*, 57:1901, 1990.

[Rea54] W. T. Read. Theory of dislocations in germanium. *Philosophical Magazine*, 45:775, 1954.

[REC+87] L. P. Ramberg, P. M. Enquist, Y. K. Chen, F. E. Najjar, L. F. Eastman, E. A. Fitzgerald, and K. L. Kavanaugh. Lattice-strained heterojunction InGaAs/GaAs bipolar structures: recombination properties and performance. *Journal of Applied Physics*, 61:1234, 1987.

[Rei78] L. Reimer. Scanning electron microscopy - present state and trends. *Scanning*, 1:3, 1978.

[SB84] G. J. Sonek and J. M. Ballantyne. Reactive ion etching of GaAs using BCl_3. *Journal of Vacuum Science and Technology B*, 4:653, 1984.

[SCB87] A. Scherer, H. G. Craighead, and E. D. Beebe. Gallium arsenide and aluminum gallium arsenide reactive ion etching in boron trichloride/argon mixtures. *Journal of Vacuum Science and Technology B*, 5:1599, 2987.

[Sch90] D. K. Schroder. *Semiconductor Material and Device Characterization.* John Wiley and Sons, New York, 1990.

[SE87] W. J. Schaff and L. F. Eastman. MBE growth and materials and device characterization of strained layer GaInAs/GaAs for application

to MODFETs. In *European Materials Research Society Meeting*, volume 16, page 295, 1987.

[Sha81] D. W. Shaw. Localized GaAs etching with acidic hydrogen peroxide solutions. *Journal of the Electrochemical Society*, 128:874, 1981.

[SLM+87] M. Skowronski, J. Lagowski, M. Milshtein, C. H. Kang, F. P. Dabowski, A. Hennel, and H. C. Gatos. Effect of plastic deformation on electronic properties of GaAs. *Journal of Applied Physics*, 62:3791, 1987.

[STFE91] W. J. Schaff, P. J. Tasker, M. C. Foisy, and L. F. Eastman. Device applications of strained-layer epitaxy. In T. P. Pearsall, editor, *Semiconductors and Semimetals, Vol. 33, Strained-Layer Superlattices: Materials Science and Technology.* Academic Press, 1991.

[STII81] J. Shirafuji, A. Tamura, M. Inoue, and Y. Inuishi. Influence of lattice mismatch on properties of InGaAsP layers epitaxially grown on InP substrates. *Journal of Applied Physics*, 52:4704, 1981.

[Sze81] S. M. Sze. *Physics of Semiconductor Devices.* John Wiley and Sons, New York, 1981.

[TGHR90] C. G. Tuppen, C. J. Gibbens, M. Hockly, and S. G. Roberts. Misfit dislocation multiplication processes in SiGe alloys for $x < 0.15$. *Applied Physics Letters*, 56:54, 1990.

[UKYK81] O. Ueda, S. Komiya, S. Yamakoshi, and T. Kotani. TEM observation of dark defects appearing in InGaAsP/ InP double-heterostructure light emitting diodes aged at high temperature. *Japanese Journal of Applied Physics*, 20:1201, 1981.

[vdM63] J. H. van der Merwe. Crystal interfaces. part i. semi-infinite crystals. *Journal of Applied Physics*, 34:117, 1963.

[vdMJ88] J. H. van der Merwe and W. A. Jesser. An exactly solvable model for calculating critical misfit and thickness in epitaxial superlattices: layers of equal elastic constants and thicknesses. *Journal of Applied Physics*, 63:1509, 1988.

[Veg21] L. Vegard. Die konstitution der mischkristalle und die raumfüllung der atome. *Z. Phys.*, 5:17, 1921.

[WAAH90a] G. P. Watson, D. G. Ast, T. J. Anderson, and Y. Hayakawa. The control and properties of misfit dislocations in OMCVD grown epitaxial layers. In J. E. Lait and I. V. Samarasekera, editors, *Proceedings of the F. Weinberg Symposium on Solidification Processing*, page 382. The Canadian Institute of Mining and Metallurgy, Pergamon Press, 1990.

[WAAH90b] G. P. Watson, D. G. Ast, T. J. Anderson, and Y. Hayakawa. The isolation of misfit dislcoations in OMCVD grown, strained InGaAs epitaxial layers. In *Electronic, Optical and Device Properties of Layered Structures*, page 267. Material Research Society, Extended Abstract (EA-21), Nov. 1990.

[WC90] G. J. Whaley and P. I. Cohen. Relaxation of strained InGaAs during molecular beam epitaxy. *Applied Physics Letters*, 57:144, 1990.

[Wen89] S. L. Weng. Experimental studies of misfit dependence of critical layer thickness in pseudomorphic InGaAs single-strained quantum-well structures. *Journal of Applied Physics*, 66:2217, 1989.

[WHJM91] J. E. Williams, L. S. Heath, H. R. Jen, and K. Meehan. Nonplanar MOVPE growth on reactive ion etched substrates. In *Fifth Biennial Workshop on Organometallic Vapor Phase Epitaxy*, 1991.

[Wie89] C. R. Wie. Relaxation and rocking-curve broadening of strained (Ga,In)As single layers on (001) GaAs. *Journal of Applied Physics*, 65:2267, 1989.

[Wos89] T. Wosinski. Evidence for the electron traps at dislocations in GaAs crystals. *Journal of Applied Physics*, 65:1566, 1989.

[WTA+90] G. P. Watson, M. O. Thompson, D. G. Ast, A. Fischer-Colbrie, and J. Miller. The isolation and nucleation of misfit dislocations in strained epitaxial layers grown on patterned, ion-damaged GaAs. *Journal of Electronic Materials*, 19:975, 1990.

[YH86] B. G. Yacobi and D. B. Holt. Cathodoluminescence scanning electron micrscopy of semiconductors. *Journal of Applied Physics*, 59:R1, 1986.

[YH90] B. G. Yacobi and D. B. Holt. *Cathodoluminecence Microscopy of Inorganic Solids.* Plenum Press, New York, 1990.

[YMY+87] T. Yuasa, M. Mannoh, T. Yamada, S. Naritsuka, K. Shinozaki, and M Ishii. Characteristics of molecular-beam epitaxially grown pair-groove-substrate GaAs/AlGaAs multiquantum-well lasers. *Journal of Applied Physics*, 62:764, 1987.

[Zip85] C. L. Zipfel. Light emitting diode reliability. In W. T. Tsang, editor, *Semiconductors and Semimetals, Vol. 22, Lightwave Communications Technology*. Academic Press, 1985.

[ZS90] A. Zozime and W. Schroter. Deep levels associated with α and β dislocations in n-type InP. *Applied Physics Letters*, 57:1326, 1990.